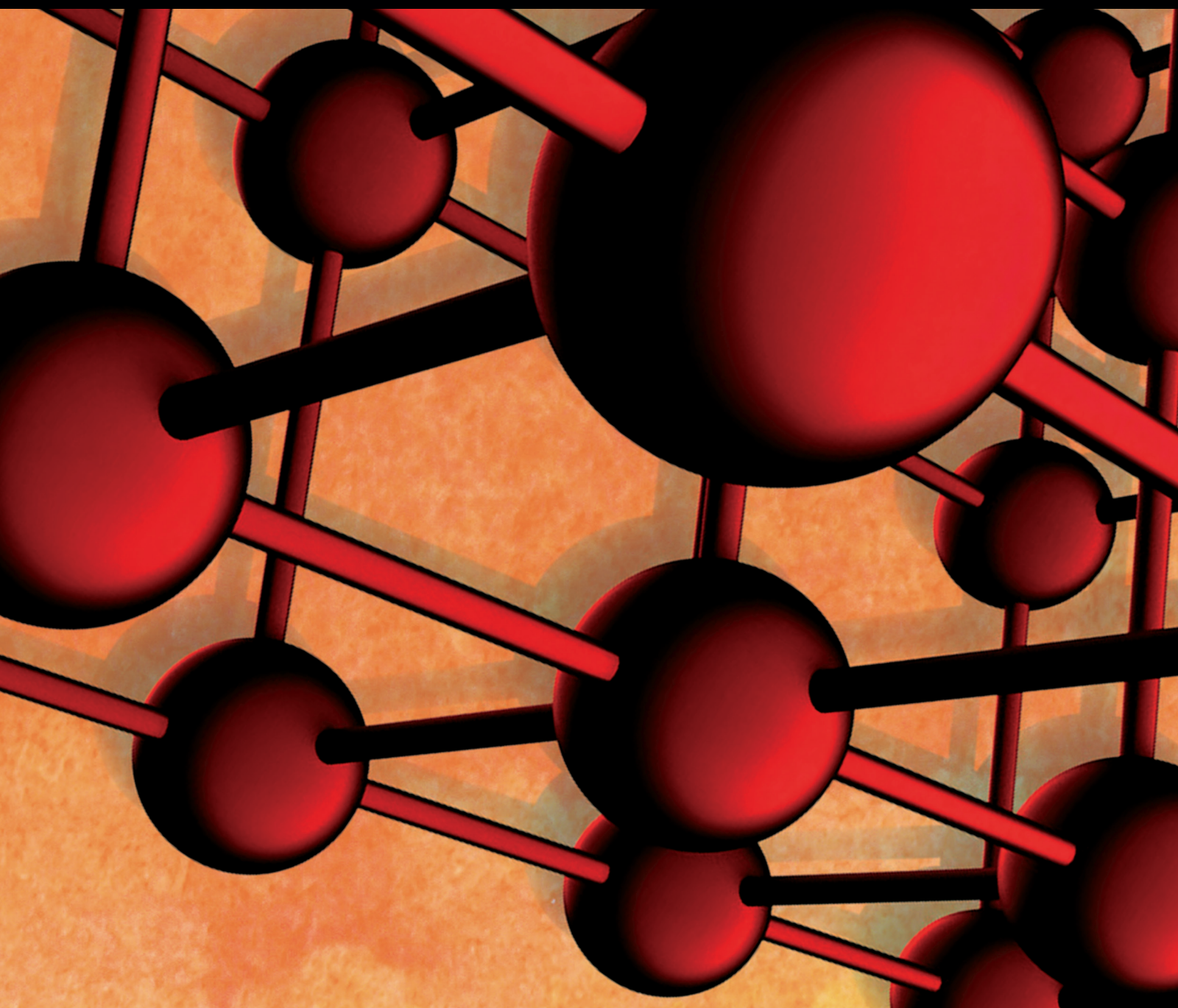


Advances in Materials Science and Engineering

Mechanics, Fatigue, and Fracture of Structural Joints

Lead Guest Editor: Dariusz Rozumek

Guest Editors: Roberto Brighenti, Zbigniew Marciniak, and Marek Smaga





Mechanics, Fatigue, and Fracture of Structural Joints

Advances in Materials Science and Engineering

Mechanics, Fatigue, and Fracture of Structural Joints

Lead Guest Editor: Dariusz Rozumek

Guest Editors: Roberto Brighenti, Zbigniew Marciniak,
and Marek Smaga



Copyright © 2019 Hindawi. All rights reserved.

This is a special issue published in “Advances in Materials Science and Engineering.” All articles are open access articles distributed under the Creative Commons Attribution License, which permits unrestricted use, distribution, and reproduction in any medium, provided the original work is properly cited.

Editorial Board

- Antonio Abate, Germany
H.P.S Abdul Khalil, Malaysia
Michael Aizenshtein, Israel
Hamed Akhavan, Portugal
Jarir Aktaa, Germany
Amelia Almeida, Portugal
Rajan Ambat, Denmark
K. G. Anthymidis, Greece
Santiago Aparicio, Spain
Raul Arenal, Spain
Alicia E. Ares, Argentina
Farhad Aslani, Australia
Apostolos Avgeropoulos, Greece
Renal Backov, France
Markus Bambach, Germany
Amit Bandyopadhyay, USA
Massimiliano Barletta, Italy
Stefano Bellucci, Italy
Avi Bendavid, Australia
Brahim Benmokrane, Canada
Jamal Berakdar, Germany
Jean-Michel Bergheau, France
G. Bernard-Granger, France
Giovanni Berselli, Italy
Patrice Berthod, France
Michele Bianchi, Italy
Hugo C. Biscaia, Portugal
Antonio Boccaccio, Italy
Susmita Bose, USA
H.-G. Brokmeier, Germany
Steve Bull, UK
Gianlorenzo Bussetti, Italy
Jose M. Cabrera, Spain
Antonio Caggiano, Germany
Veronica Calado, Brazil
Marco Cannas, Italy
Paolo Andrea Carraro, Italy
Victor M. Castaño, Mexico
Michelina Catauro, Italy
Robert Černý, Czech Republic
Jose Cesar de Sa, Portugal
Daolun Chen, Canada
Wensu Chen, Australia
Francisco Chinesta, France
Er-Yuan Chuang, Taiwan
Gianluca Cicala, Italy
Francesco Colangelo, Italy
Marco Consales, Italy
María Criado, Spain
Gabriel Cuello, France
Lucas da Silva, Portugal
Narendra B. Dahotre, USA
João P. Davim, Portugal
Angela De Bonis, Italy
Abílio De Jesus, Portugal
Luca De Stefano, Italy
Francesco Delogu, Italy
Luigi Di Benedetto, Italy
Aldo Di Carlo, Italy
Maria Laura Di Lorenzo, Italy
Marisa Di Sabatino, Norway
Luigi Di Sarno, Italy
Ana María Díez-Pascual, Spain
Guru P. Dinda, USA
Nadka Tzankova Dintcheva, Italy
Hongbiao Dong, China
Mingdong Dong, Denmark
Frederic Dumur, France
Stanislaw Dymek, Poland
Kaveh Edalati, Japan
Philip Eisenlohr, USA
Claude Estournès, France
Luis Evangelista, Norway
Michele Fedel, Italy
Isabel J. Ferrer, Spain
Paolo Ferro, Italy
Dora Foti, Italy
Massimo Fresta, Italy
Pasquale Gallo, Japan
Germà Garcia-Belmonte, Spain
Santiago Garcia-Granda, Spain
Carlos Garcia-Mateo, Spain
Georgios I. Giannopoulos, Greece
Ivan Giorgio, Italy
Antonio Gloria, Italy
Vincenzo Guarino, Italy
Daniel Guay, Canada
Gianluca Gubbiotti, Italy
Jenö Gubicza, Hungary
Xuchun Gui, China
Benoit Guiffard, France
Ivan Gutierrez-Urrutia, Japan
Hiroki Habazaki, Japan
Simo-Pekka Hannula, Finland
Akbar Heidarzadeh, Iran
David Holec, Austria
Satoshi Horikoshi, Japan
David Houivet, France
Rui Huang, USA
Yi Huang, UK
Michele Iafisco, Italy
Erdir Ibrahim, UK
Saliha Ilcan, Turkey
Md Mainul Islam, Australia
Iliya Ivanov, USA
Hom Kandel, USA
kenji Kaneko, Japan
Fuat Kara, Turkey
Katsuyuki Kida, Japan
Akihiko Kimura, Japan
Soshu Kirihara, Japan
Paweł Kłosowski, Poland
Jan Koci, Czech Republic
Fantao Kong, China
Ling B. Kong, Singapore
Lingxue Kong, Australia
Pramod Koshy, Australia
Hongchao Kou, China
Alexander Kromka, Czech Republic
Andrea Lamberti, Italy
Luciano Lamberti, Italy
Fulvio Lavecchia, Italy
Marino Lavorgna, Italy
Laurent Lebrun, France
Joon-Hyung Lee, Republic of Korea
Pavel Lejcek, Czech Republic
Cristina Leonelli, Italy
Ying Li, USA
Yuanshi Li, Canada
Yuning Li, Canada
Guang-xing Liang, China
Barbara Liguori, Italy

Jun Liu, China
Meilin Liu, Georgia
Shaomin Liu, Australia
Yunqi Liu, China
Zhiping Luo, USA
Fernando Lusquiños, Spain
Peter Majewski, Australia
Georgios Maliaris, Greece
Muhamamd A. Malik, UK
Dimitrios E. Manolakos, Greece
Necmettin Maraşlı, Turkey
Enzo Martinelli, Italy
Alessandro Martucci, Italy
Yoshitake Masuda, Japan
Bobby Kannan Mathan, Australia
Roshan Mayadunne, Australia
Mamoun Medraj, Canada
Shazim A. Memon, Kazakhstan
Philippe Miele, France
A. E. Miroshnichenko, Australia
Hossein Moayedi, Vietnam
Sakar Mohan, India
Jose M. Monzo, Spain
Michele Muccini, Italy
Alfonso Muñoz, Spain
Roger Narayan, USA
Rufino M. Navarro, Spain
Miguel Navarro-Cia, UK
Ali Nazari, Australia
Behzad Nematollahi, Australia
Luigi Nicolais, Italy
Peter Niemz, Switzerland
Hiroshi Noguchi, Japan
Chérif Nouar, France
Olanrewaju Ojo, Canada
Dariusz Oleszak, Poland
Laurent Orgéas, France
Togay Ozbakkaloglu, UK
Nezih Pala, USA
Marián Palcut, Slovakia
Davide Palumbo, Italy
Gianfranco Palumbo, Italy
A. Maria Paradowska, Australia
Zbyšek Pavlík, Czech Republic
Matthew Peel, UK
Alessandro Pegoretti, Italy
Gianluca Percoco, Italy
Claudio Pettinari, Italy
Giorgio Pia, Italy
Silvia M. Pietralunga, Italy
Daniela Pilone, Italy
Teresa M. Piqué, Argentina
Candido Fabrizio Pirri, Italy
Marinos Pitsikalis, Greece
Alain Portavoce, France
Simon C. Potter, Canada
Ulrich Prah, Germany
Viviana F. Rahhal, Argentina
Carlos R. Rambo, Brazil
Shahed Rasekh, Portugal
Manijeh Razeghi, USA
Paulo Reis, Portugal
Yuri Ribakov, Israel
Aniello Riccio, Italy
Anna Richelli, Italy
Antonio Riveiro, Spain
Marco Rossi, Italy
Sylvie Rossignol, France
Pascal Roussel, France
Fernando Rubio-Marcos, Spain
Francesco Ruffino, Italy
Mark H. Rummeli, China
Pietro Russo, Italy
Antti Salminen, Finland
F.H. Samuel, Canada
MariaGabriella Santonicola, Italy
Hélder A. Santos, Finland
Carlo Santulli, Italy
Fabrizio Sarasini, Italy
Michael J. Schütze, Germany
Raffaele Sepe, Italy
Kenichi Shimizu, USA
Fridon Shubitidze, USA
Mercedes Solla, Spain
Donato Sorgente, Italy
Charles C. Sorrell, Australia
Andres Sotelo, Spain
Costas M. Soukoulis, USA
Damien Soulat, France
Adolfo Speghini, Italy
Antonino Squillace, Italy
Koichi Sugimoto, Japan
Baozhong Sun, China
Sam-Shajing Sun, USA
Youhong Tang, Australia
Kohji Tashiro, Japan
Miguel Angel Torres, Spain
Laszlo Toth, France
Achim Trampert, Germany
Tomasz Trzepieciński, Poland
Matjaz Valant, Slovenia
Luca Valentini, Italy
Ashkan Vaziri, USA
Lijing Wang, Australia
Rui Wang, China
Zhongchang Wang, Portugal
Lu Wei, China
Jörg M. K. Wiezorek, USA
Jiang Wu, China
Guoqiang Xie, China
Dongmin Yang, UK
Zhonghua Yao, China
Hemmige S. Yathirajan, India
Yee-wen Yen, Taiwan
Wenbin Yi, China
Ling Yin, Australia
Tetsu Yonezawa, Japan
Hiroshi Yoshihara, Japan
Belal F. Yousif, Australia
Lenka Zajíčková, Czech Republic
Michele Zappalorto, Italy
Gang Zhang, Singapore
Jinghuai Zhang, China
Li Zhang, China
Meng Zhang, USA
Mikhail Zheludkevich, Germany
Wei Zhou, China
You Zhou, Japan
Hongtao Zhu, Australia
F. Javier Fernández Fernández, Spain
J. A. Fonseca de Oliveira Correia, Portugal

Contents

Mechanics, Fatigue, and Fracture of Structural Joints

Dariusz Rozumek , Roberto Brighenti, Zbigniew Marciniak, and Marek Smaga
Editorial (2 pages), Article ID 8707038, Volume 2019 (2019)

Optimization of Structure Parameters of Airfield Jointed Concrete Pavements under Temperature Gradient and Aircraft Loads

Bangshu Xu, Wanzhi Zhang , Jie Mei, Guangyao Yue, and Laihua Yang
Research Article (11 pages), Article ID 3251590, Volume 2019 (2019)


Numerical Investigation of Distribution Laws of Shear Force in Box Girder Webs

Xingwei Xue , Chao Zang , Junlong Zhou , and Hai Zhang 
Research Article (14 pages), Article ID 9865989, Volume 2019 (2019)


Mechanical Properties Optimization of Friction Stir Welded Lap Joints in Aluminium Alloy

Antonio Viscusi , Antonello Astarita , and Umberto Prisco 
Research Article (9 pages), Article ID 3832873, Volume 2019 (2019)

Prediction of Fatigue Life of Welded Joints Made of Fine-Grained Martensite-Bainitic S960QL Steel and Determination of Crack Origins

Tomasz Ślęzak 
Research Article (9 pages), Article ID 9520801, Volume 2019 (2019)



Effects of Stem Cutting in Rice Harvesting by Combine Harvester Front Header Vibration

Zhong Tang , Haotian Zhang, Yuepeng Zhou, and Yu Li
Research Article (15 pages), Article ID 6834269, Volume 2019 (2019)

Effects of Welded Mechanical Heterogeneity on Interface Crack Propagation in Dissimilar Weld Joints

Fu-qiang Yang , He Xue , Ling-yan Zhao , and Xiu-rong Fang 
Research Article (10 pages), Article ID 6593982, Volume 2019 (2019)

Failure Analysis on 42CrMo Steel Bolt Fracture


Guo Hongfei, Jianwei Yan , Ru Zhang, Zhihui He, Zengqi Zhao, Ting Qu, Ming Wan, Jingshun Liu, and Congdong Li 
Research Article (8 pages), Article ID 2382759, Volume 2019 (2019)

Effect of PWHT on the Carbon Migration and Mechanical Properties of 2205DSS-Q235 LBW Joint

Fujun Cao  and Chengchao Du 
Research Article (10 pages), Article ID 6090464, Volume 2018 (2019)

Editorial

Mechanics, Fatigue, and Fracture of Structural Joints

Dariusz Rozumek ¹, **Roberto Brighenti**², **Zbigniew Marciniak**¹ and **Marek Smaga**³

¹*Opole University of Technology, Opole, Poland*

²*University of Parma, Parma, Italy*

³*Technische Universität Kaiserslautern, Kaiserslautern, Germany*

Correspondence should be addressed to Dariusz Rozumek; d.rozumek@po.opole.pl

Received 16 April 2019; Accepted 16 April 2019; Published 5 May 2019

Copyright © 2019 Dariusz Rozumek et al. This is an open access article distributed under the Creative Commons Attribution License, which permits unrestricted use, distribution, and reproduction in any medium, provided the original work is properly cited.

For centuries, engineering structures have been made for people's life everyday needs, such as buildings, transportation, construction equipment, infrastructures, and plants. To achieve the desired functionality, usually simple individual members are connected with each other to get the final complex desired structure. Depending on the design requirements, the structural elements can be connected in a nonpermanent or permanent manner. To ensure an adequate safety level and optimal structural joints durability, construction node tests and simulations are required to determine the effect of the various factors influencing the durability and strength of the joints. The types of different connections that have been developed and proposed to date is very huge; joints represent a crucial part of complex structures, and the consequence of their collapse can be the loss of human lives and economic resources.

Studies and research outcomes carried out in this field are necessary to guide the development of new and advanced standards for a better design and improved safety level of structural joints, leading to beneficial effects in all the technologies where connection of structural elements is required.

This special issue aims to gather the most recent research advancements in the field of structural joints, with particular emphasis on their safety and reliability. In the analysis of joints, the study of initiation and fatigue crack growth in metallic permanent structural connections is of primary interest, but studies related to any other engineering material employed in bearing joint applications are also well fitted with the aim and scope of this special issue.

Over the last year, we have received and analyzed 39 submitted research works by outstanding international

scientists. The papers submitted by the authors have been subjected to the rigorous journal peer-review process. During the intensive process of reviews and in-depth discussions, 8 articles were accepted for the publication, while other documents were rejected mainly due to the discrepancy to the topic of the special issue. Accepted papers, after passing the positive review process as well as the editorial processes, will be published in this special issue of *Advances in Materials Science and Engineering* entirely devoted to the mechanics of structural joints.

The topics considered in the accepted papers include several aspects influencing the performance of structural joints such as the effects of factors affecting the fatigue life and crack initiation in welded joints, the influence of geometric effects (notches, fillets, etc.) on the fatigue crack growth, mechanical properties optimization, the effect of all the various factors (physical, chemical, and environmental) on the lifetime of welds, mechanics of joints made of nonmetallic materials such as concrete and polymers, whose investigation has been performed by adopting theoretical, numerical, and experimental approaches.

Conflicts of Interest

The Guest Editorial team of this special issue declares that there are no conflicts of interest or private agreements with companies regarding our work for this special issue. They have no financial relationships through employment, consultancies, and either stock ownership or honoraria, with the industry.

Acknowledgments

We thank the reviewers who assisted us in the review process providing useful comments and proposing constructive improvements to the articles. We are grateful to all authors for their excellent contributions to this special issue.

*Dariusz Rozumek
Roberto Brighenti
Zbigniew Marciniak
Marek Smaga*

Research Article

Optimization of Structure Parameters of Airfield Jointed Concrete Pavements under Temperature Gradient and Aircraft Loads

Bangshu Xu,¹ Wanzhi Zhang¹,¹ Jie Mei,¹ Guangyao Yue,¹ and Laihua Yang²

¹Research Center of Geotechnical and Structural Engineering, Shandong University, Jinan 250061, China

²China Railway 12th Bureau Group Co., Ltd., Taiyuan 030024, China

Correspondence should be addressed to Wanzhi Zhang; zwzwanzhi@163.com

Received 6 November 2018; Accepted 25 March 2019; Published 24 April 2019

Guest Editor: Roberto Brighenti

Copyright © 2019 Bangshu Xu et al. This is an open access article distributed under the Creative Commons Attribution License, which permits unrestricted use, distribution, and reproduction in any medium, provided the original work is properly cited.

Daily changing temperature causes significant thermal stress in concrete pavement. Tensile stress obtained can exceed flexural tensile strength when the concrete slabs are subjected to large temperature gradient and traffic loads, resulting in pavement damages. In this paper, maximum tensile stresses in concrete slabs with different slab sizes, thicknesses, and length to width (L/W) ratios were investigated by using the finite element (FE) method. The important parameters in the design of concrete pavement are the flexural tensile strength and the fatigue limit. By analyzing the comparison results between the maximum tensile stress and the fatigue limit, the optimum slab size and the critical thickness were determined. The results indicate that the maximum tensile stress obtained is higher for larger slab size with thin thickness. Furthermore, to reduce cutting work and the amount of dowel bars, the optimum slab sizes of the regional airport concrete pavement are recommended as $4\text{ m} \times 4\text{ m}$ to $6\text{ m} \times 6\text{ m}$. The critical thicknesses of $4\text{ m} \times 4\text{ m}$ slab and $6\text{ m} \times 6\text{ m}$ slab are determined as 28.2 cm and 34.7 cm, respectively, based on the most unfavorable coupling between positive and negative temperature gradients and the Boeing 737–800 aircraft load. Moreover, the maximum tensile stress increases as the L/W ratio increases. When the slab length is less than 6 m, it is better to use square slab in airport jointed concrete pavement (JCP).

1. Introduction

In the recent years, concrete pavements are preferred because of their high strength, good durability, less maintenance, and ease of procurement. In China, approximately 90% of civil airport pavements are constructed with Portland cement concrete (PCC) [1, 2]. Airport concrete pavement, as a sheet and large area structure exposed to natural environment, bears the long-term damage from the external environment, such as atmospheric temperature, humidity, and solar radiation [3–5] and aircraft repeated loads [6], resulting in cracks, voids, and other defects [7]. Especially in the environment of large temperature difference between day and night, it is important to have a better understanding of the response of concrete pavement within its design life. Therefore, in the design of airport concrete pavement, airport authorities are interested in

selecting the preferred pavement design considering environmental factors and performance requirements.

PCC pavements expand and contract in the horizontal plane under temperature changes. Meanwhile, PCC pavements show upward curling or downward curling under the influence of temperature gradients [8–10]. However, these movements will be restrained or resisted by self-weight of concrete slabs and friction between slab and layer below it, inducing significant thermal stresses in concrete slabs [11–13]. For JCP, the thermal stress magnitude is directly related to the structural parameters and the constraints of the concrete slab. Tian et al. studied the effect of the base types and the conditions of constraint between the slab and the base on the thermal stress [14]. The findings imply that the thermal stress in the slab of lean concrete base is the largest. Moreover, when the contact state between the slab

and the base changes from continuous to smooth, the thermal stress decreases significantly. Nam et al. proposed that subsurface conditions and joint/crack width affect the behavior and response of JCP [15]. It is noted that the slab tends to have smaller voids with the decreased subgrade modulus, and the longitudinal stress in its bottom edge increases as the crack width becomes tighter. Moreover, when concrete slabs are subjected to the combined action of the large temperature gradient and traffic loads, critical stresses may be developed. Many researchers have reported different slab sizes considering various factors. Huang suggested the sizes of concrete slabs are in the range of 15–30 ft (4.6–9.1 m) for JCP depending on the type of aggregate and climate [16]. Wei et al. suggested that the critical slab size of rural road concrete pavement was $2\text{ m} \times 2\text{ m}$ considering the combined effect of 15°C temperature difference and 100 kN axes load [17]. Chattaraj and Pandey investigated critical stresses of square slabs of different sizes under dual wheel load using the FE method [18]. They proposed that critical stresses are drastically reduced for smaller slab size. A number of studies related to thicknesses of concrete slabs and L/W ratios have also been conducted. Al-Nasra and Wang [19] and Nam et al. [15] have also revealed that the thicker slab has a greater fluctuation in the edge vertical movement. Vishwakarma and Ingle studied the effect of different sizes and L/W ratios of concrete slabs on their critical stresses under temperature load, traffic load, and combined effect of temperature and traffic loads [20]. They concluded that the tensile stress increases with the increase in the slab length and width. Tensile stresses for L/W ratio 1.25 or below are almost the same. However, when L/W ratio exceeds 1.25, there is considerable increase in the maximum edge stress.

The objectives of the present studies are to evaluate the critical stresses and deformations of concrete slabs considering different structural parameters and combined effects of various temperature and traffic loads. The optimum slab sizes, thicknesses, and L/W ratios of regional airport JCP related to environmental temperature and aircraft loads still need to be investigated. It is especially important for environment temperature occurring in Northeast China significantly influencing tensile stresses of concrete slabs. Therefore, field temperature and strain tests of a regional airport concrete pavement in Northeast China were performed. In order to analyse in detail distributions of maximum tensile stresses of different slab sizes, thicknesses, and L/W ratios under the most unfavorable load-bearing positions, we applied three-dimensional (3-D) analyses using the FE method. Here, based on the comparison results between the maximum tensile stress and the fatigue limit, the optimum slab size and the critical thickness are determined and the square slab is recommended. The obtained results can be helpful in design of new regional airport JCP and assessment of their load in countries with big temperature amplitudes.

2. Field Experiment

2.1. Temperature and Strain Tests. Based on a regional airport concrete pavement project in Northeast China,

distribution laws of temperature and strain fields in concrete slabs were monitored by embedding semiconductor temperature sensors and vibration wire strain sensors. Figure 1 shows the cross section of the pavement structure and the layout of the temperature and strain sensors. The airport pavement is composed of concrete slabs, cement-treated base (CTB), crushed-stone base (CSB), and subgrade (Table 1). The temperature and strain sensors are placed inside the concrete slab. The guideline of CACC (China Airport Construction Group Corporation) recommends that the reinforced concrete cover depth should not be less than 50 mm in the design of airport reinforced concrete pavements [21]. Therefore, the embedded temperature and strain sensors are placed at a distance of 60 mm from the surface and bottom of the concrete slab. The temperature and strain sensors are installed in the centre of the slab. In Figure 1(a), four temperature sensors (T60/T140/T220/T300, the number represents its depth) are arranged in the vertical direction and the vertical spacing is 80 mm. In Figure 1(b), two strain sensors are arranged at the surface and bottom, respectively, of which one (S60-1/S300-1) is in the transverse direction and the other (S60-2/S300-2) is in the longitudinal direction and the vertical spacing is 240 mm.

The temperature and strain data were collected continuously and automatically by using “Wireless transmission module JMTX-2014” and “DSC software platform.” Data acquisition time was from August 1, 2016, to November 3, 2016, and the data acquisition interval was set to 1 h.

2.2. Distribution Laws of Temperature and Strain Fields.

From August to November, the natural climate conditions in Northeast China change from midsummer to early winter and the ambient temperature significantly decreases. It is important to understand the behavior of concrete slabs under the environmental load including temperature gradient and environmental strain. Therefore, the temperature and strain data of a typical day with maximum temperature difference between day and night in August and November were adopted. The data are used to analyze the daily temperature variations, temperature gradient distributions along the depth, and the incremental relationships between strain and temperature.

2.2.1. Temperature Field Distributions. Figure 2 presents daily temperature variations over different months. The temperature fluctuation curves in the concrete slab are similar to sine function curves. The surface temperature exhibits extreme fluctuations. An increase in the depth successively decreases the amplitude of the temperature fluctuation. Figure 3 shows temperature gradient distributions along the depth over different months. Temperature distributions along the slab depth are nonlinear. The temperature gradients considerably vary at different times within a day. As shown in Figures 2 and 3, the maximum positive temperature difference between surface and bottom is approximately observed at 3 p.m. while the maximum negative temperature difference occurs at

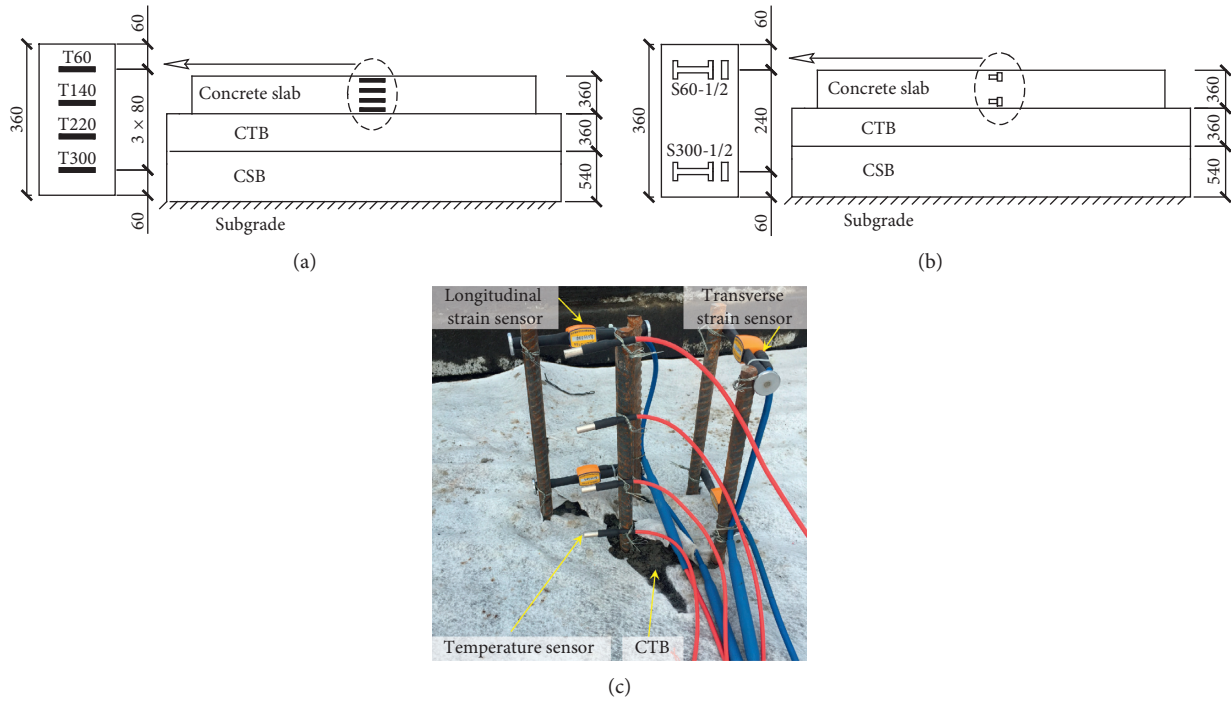


FIGURE 1: Pavement structure and layout of (a) temperature sensors (unit: mm) and (b) strain sensors (unit: mm). (c) Field layout of temperature and strain sensors.

TABLE 1: Structure parameters of airport pavement layers.

Pavement layers	Slab size (m)	Thickness (m)
Concrete slab	5 × 4.5	0.36
CTB	19 × 14	0.36
CSB	19 × 14	0.54
Subgrade	19 × 14	7.00

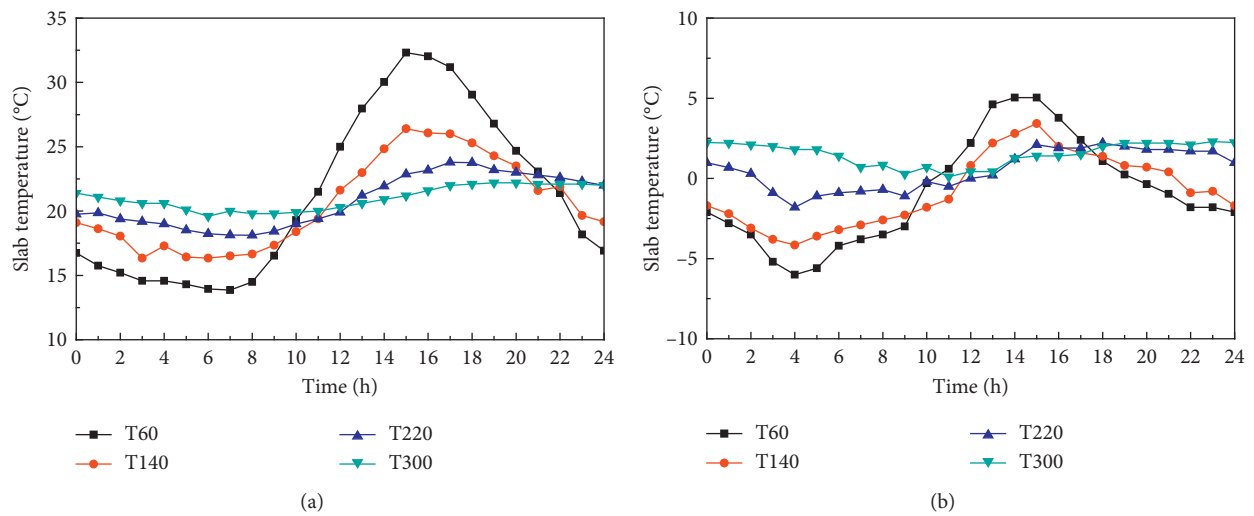


FIGURE 2: Temperature daily fluctuation curves in the concrete slab over different months. (a) August 14th. (b) November 2nd.

approximately 4 a.m. The maximum positive and negative temperature differences and corresponding temperature gradients are listed in Table 2.

2.2.2. *Strain Field Distributions.* Figure 4 shows the temperature-strain increment relationships in a typical day over different months. The hysteresis of temperature data

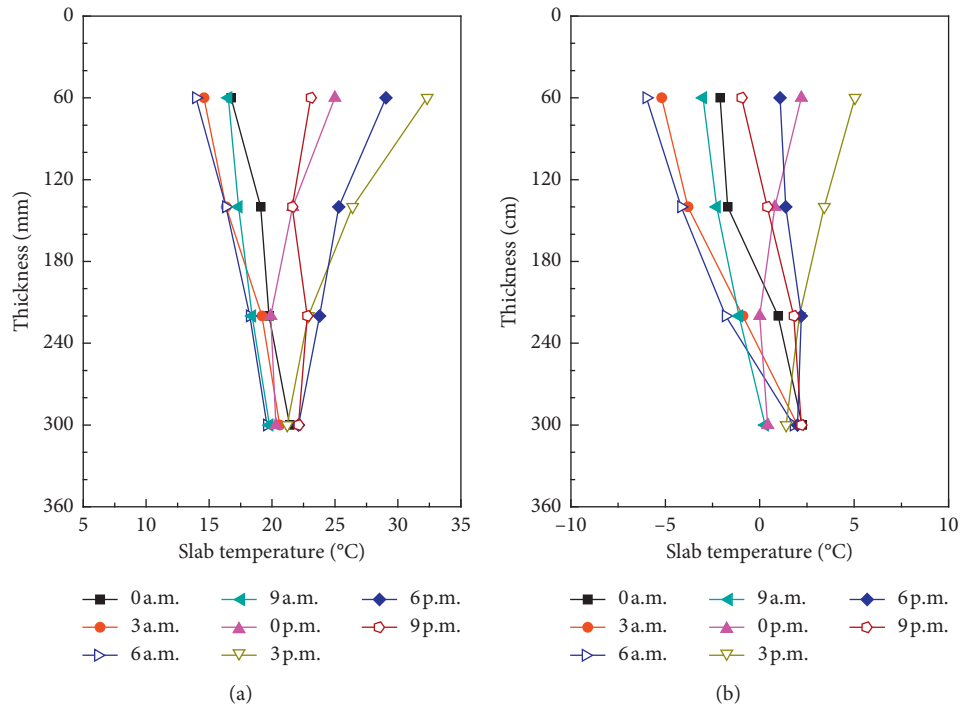


FIGURE 3: Nonlinear temperature gradient distribution in the concrete slab over different months. (a) August 14th. (b) November 2nd.

TABLE 2: Maximum temperature differences and temperature gradients in the concrete slab over different months.

Date	Positive		Negative	
	Temperature difference (°C)	Temperature gradient (°C.cm ⁻¹)	Temperature difference (°C)	Temperature gradient (°C.cm ⁻¹)
August 14 th	12.1	0.50	-7.8	-0.33
November 2 nd	4.6	0.19	-9.8	-0.41

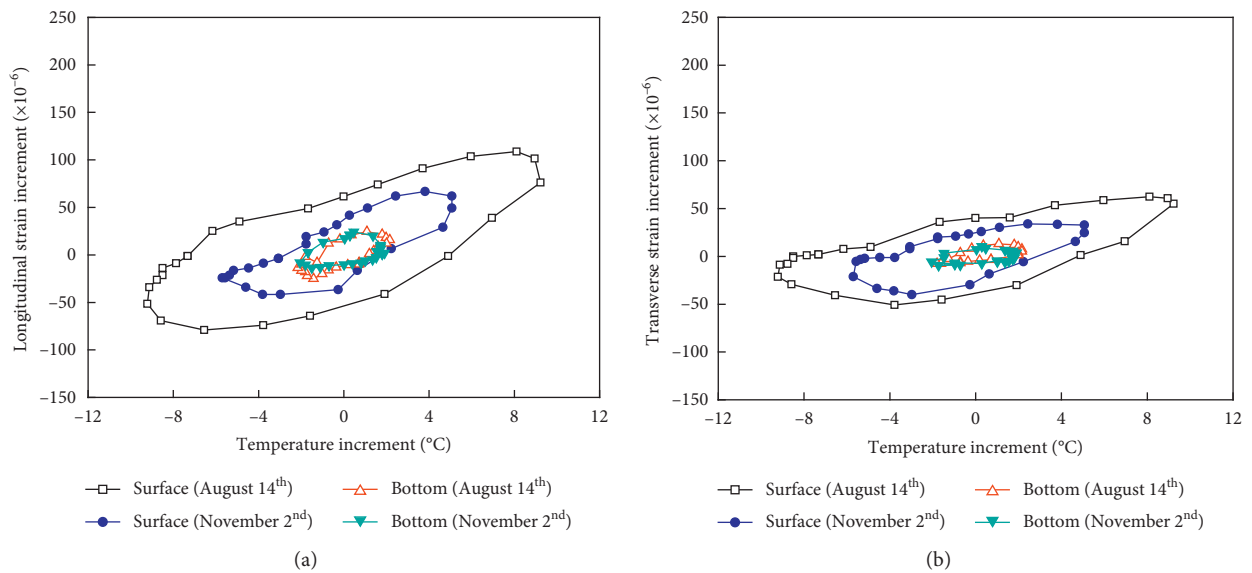


FIGURE 4: Relationships between the measured temperature-strain increments. (a) Longitudinal temperature-strain increments. (b) Transverse temperature-strain increments.

versus strain data is evident, and the paths of temperature increase and decrease do not coincide. When the increment of temperature is identical, a slight difference is observed between the longitudinal and transverse strain increments and the increment of transverse is smaller. The temperature-strain increment hysteresis loops of the bottom are significantly smaller than that of the surface due to the effect of slab thickness. The size of the temperature-strain increment hysteresis loops varies in different months under the influence of environment temperature.

3. Modeling and Validation of FE Model

3.1. Model and Mesh. To analyze the mechanical behaviors of concrete pavement given the measured temperature gradients, the 3-D FE model with nine concrete slabs was developed by using the FE software ABAQUS (Figure 5). In the numerical simulation, multilayer structures of pavement, self-weight, two different joint types (dowel joint and key joint), and the interlayer contact surfaces were modelled. The dowel joint has dowel bars, and the key joint has tension bars at the mid-depth of concrete slabs. The 27-node solid elements (C3D27R) was used to discretize the pavement layers and dowel bars and tension bars, which were widely used in related researches and recommended by the ABAQUS program for plane stress analysis [22–24]. Each node of the C3D27R element has three degrees of freedom (U_x , U_y , and U_z). The C3D27R was used such that the accuracy of the mechanical calculation is not evidently affected when the element meshes are distorted in numerical analysis.

3.2. Pavement Layers and Material Parameters. The sizes of pavement layers are listed in Table 1. According to geological exploration data and geotechnical tests, the material parameters of pavement layers are summarized in Table 3. The coefficient of thermal expansion (CTE) used in the FE analysis was estimated by backcalculation by using the measured temperature-strain increment data (Figure 4). The first-order polynomial of the least squares method is used to obtain the average of CTE of the concrete mixture. In this study, the CTE is $9.86 \times 10^{-6}/^\circ\text{C}$.

3.3. Temperature Field in the FE Models. From the temperature measurement results (Figure 3), the nonlinear distribution of temperature is not negligible in the numerical analysis. Choubane and Tia proposed that the temperature nonlinear distribution throughout the whole depth of concrete slab can be adequately described by quadratic function as follows [25]:

$$T(z) = A + Bz + Cz^2, \quad (1)$$

where A , B , and C are coefficients and z is the distance from the slab surface.

The temperature gradients of $50^\circ\text{C}\cdot\text{m}^{-1}$ and $-41^\circ\text{C}\cdot\text{m}^{-1}$ were applied. Equation (1) was used to fit the nonlinear distribution of positive and negative temperature gradients in concrete slabs based on the temperature data measured at

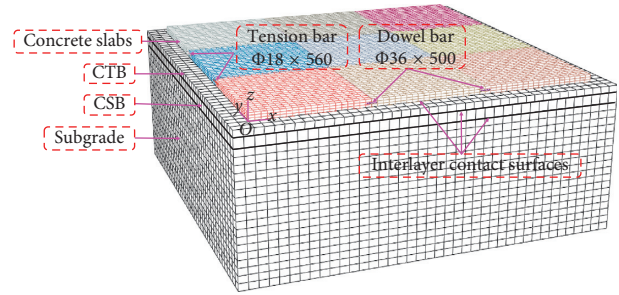


FIGURE 5: 3-D FE model for test slabs (unit: mm).

6 a.m. and 3 p.m. (Figure 3). In the FE models, it is assumed that the temperature of the whole base is a fixed value, which is the bottom temperature of the concrete slab at the corresponding time.

3.4. Interlayer Contact Relations and Boundary Conditions. The isotropic Coulomb friction model is used to simulate the tangential bond slip between the pavement layers. The airport pavement test section is a new concrete pavement, and thus, the contact between each layer is good. In the FE models, the friction coefficient is set to 1, and this implies that the layers are continuous. The normal contact between layers is set to the hard contact. Meanwhile, according to the researches of Tian et al. and Nam et al. [14, 15], the smaller the joint width of adjacent slabs, the larger the stress in the concrete pavement under the same temperature load. Therefore, the two adjacent slabs are simulated as full contact.

The symmetrical boundary condition is set in x -axis, and the free boundary condition is set in y -axis for the concrete slabs. The bottom of the subgrade layer is modelled as fixed with respect to the x , y , and z directions. The sides of the CTB, CSB, and subgrade are x - and y -axes symmetrical boundary conditions. Dowel bars were arranged in the transverse joints (dowel joints), and tension bars were placed in the longitudinal joints (key joints).

3.5. Model Validation. Based on the temperature and strain data and the elastic thin plate theory, the measured stresses of the test slab are calculated as follows [26]:

$$\sigma_x = -\frac{E}{1-\nu^2}(\varepsilon_x + \nu\varepsilon_y) - \frac{E\alpha T(z)}{1-\nu}, \quad (2)$$

$$\sigma_y = -\frac{E}{1-\nu^2}(\varepsilon_y + \nu\varepsilon_x) - \frac{E\alpha T(z)}{1-\nu}, \quad (3)$$

where σ_x is the longitudinal stress (MPa); σ_y is the transverse stress (MPa); E is Young's modulus (MPa); ν is Poisson's ratio; ε_x is the longitudinal strain ($\mu\varepsilon$); ε_y is the transverse strain ($\mu\varepsilon$); α is the CTE ($1/^\circ\text{C}$); and $T(z)$ is the temperature at the depth of z in the slab ($^\circ\text{C}$).

Figure 6 presents a comparison between the computed stresses predicted by using the FE models and the measured stresses calculated by using equations (2) and (3). Here, S-measured and S-computed represent the measured stresses

TABLE 3: Material properties used in numerical analysis.

Structural components	Elastic modulus (E) (MPa)	Poisson's ratio (ν)	Density (ρ) (kg/m ³)
Concrete slab	34000	0.20	2400
CTB	2550	0.25	2200
CSB	1800	0.30	2200
Subgrade	150	0.35	1900
Dowel bar	200000	0.30	7850
Tension bar	200000	0.30	7850

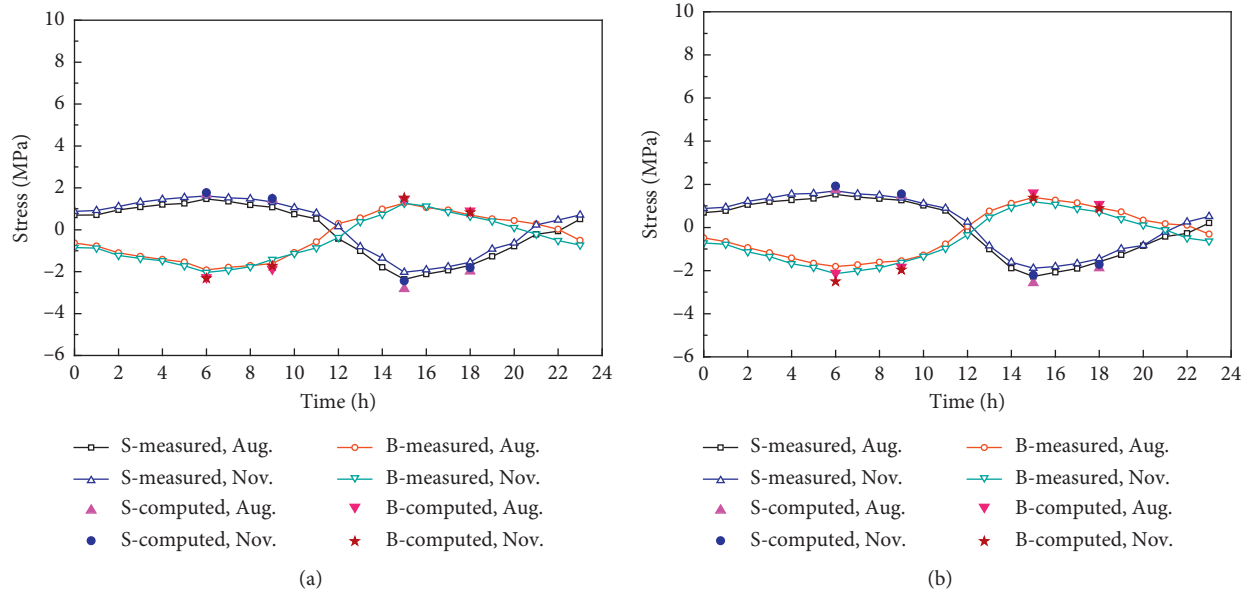


FIGURE 6: Measured and computed stresses in the concrete slab. (a) Stresses in the longitudinal direction. (b) Stresses in the transverse direction.

and computed stresses on the surface, respectively; B-measured and B-computed represent the measured stresses and computed stresses at the bottom, respectively. The results identify that the FE analysis results are in good agreement with the measured results in terms of the stress amplitude. The maximum difference of tensile stresses obtained by the two methods is 0.33 MPa in the longitudinal direction and 0.22 MPa in the transverse direction. Meanwhile, the maximum difference of compressive stresses is -0.41 MPa in the longitudinal direction and -0.37 MPa in the transverse direction. So, the FE method can effectively predict the mechanical properties of the concrete pavement.

4. Calculation Conditions considering the Temperature and Aircraft Loads

4.1. Aircraft Dynamic Load. The aircraft dynamic load is related to the sliding speed, the pavement roughness rating, and the lift of the wing. Lv et al. proposed an aircraft dynamic load coefficient model based on the International Roughness Index (IRI) [27]:

$$K' = 1 + 11.5c_0IRI\sqrt{v} - \frac{1 + 11.5c_0IRI\sqrt{v_0}}{v_0^2}v^2, \quad (4)$$

where K' is the aircraft dynamic load coefficient; $c_0 = 10^{-3} \text{ m}^{-0.5} \cdot \text{s}^{0.5}$; v is the sliding speed; and v_0 is the instantaneous speed of aircraft taking-off.

The formula for solving the aircraft dynamic load is as follows:

$$F = K'G, \quad (5)$$

where F is the aircraft dynamic load and G is the aircraft static load (i.e., the maximum ramp weight).

The maximum allowable aircraft type is Boeing 737-800 in the design of the regional airport concrete pavement. Zhang et al. suggested that when $K' = 1$, the dynamic load is equal to the maximum ramp weight and the maximum ramp weight multiplied by $K' = 1.15$ is used as the maximum take-off weight of the Boeing 737-800 aircraft for the fatigue strength of the concrete pavement [28]. Commonly, the fatigue strength of the concrete material is much lower than the ultimate compressive strength [29]. Therefore, the maximum take-off weight (1.15 times the maximum ramp weight) is used as the dynamic load in the stress analysis of the concrete slabs based on the fatigue limit criterion, fully meeting the static strength requirements. The maximum dynamic load and related parameters of the B737-800 aircraft are listed in Table 4. Since the main landing gears

TABLE 4: Load and structure parameters of the B737-800 aircraft.

Related parameters	Value
Maximum aircraft dynamic load (kN)	790.04
Main landing gear number	2
Main landing gear configuration	Single axle dual wheel
Main landing gear distance (m)	5.72
Main landing gear wheelbase (m)	0.86
Tire pressure	1.47
Wheel seal area (m ²)	0.13
Wheel seal length (m)	0.43
Wheel seal width (m)	0.30

support 95% of the aircraft load, the aircraft load is assigned without considering the nose landing gear in the FE Models. Figure 7(a) shows a schematic illustration of the wheel configuration of the Boeing 737-800 aircraft, and Figure 7(b) shows the ground shape of the aircraft wheel, which is approximately composed of a rectangle and two semicircles.

4.2. Coupling of the Temperature and Aircraft Loads. Because the measured temperature is the temperature inside the concrete slab, the temperature difference between the surface and the bottom of the concrete slab is bigger. In numerical analysis, the positive and negative temperature gradients between the surface and the bottom of the concrete slab are set to $\pm 50^\circ\text{C}\cdot\text{m}^{-1}$ and $\pm 60^\circ\text{C}\cdot\text{m}^{-1}$, respectively.

When considering the combined effects of the temperature and aircraft loads, the most unfavorable load positions of the concrete slab are different. Related researches indicated that the longitudinal middle edge of the concrete slab is the most unfavorable area given positive temperature gradient and traffic load. However, the slab corner is the most unfavorable area given negative temperature gradient and traffic load [30, 31]. In this study, analysis is performed for two cases: (a) combined actions of positive temperature gradients and the single axle dual wheel load on the longitudinal middle edge of the concrete slab; (b) combined actions of negative temperature gradients and the single axle dual wheel load on concrete slab corner. Uniform area load is assigned in gravity direction to represent the single axle dual wheel load.

4.3. FE Model Calculation Cases. Because the width of the main landing gear of the Boeing 737-800 aircraft is 6.58 m, the main landing gear acts on separated slabs when the slab size is less than $3\text{ m} \times 3\text{ m}$, while the main landing gear acts on a single slab when the slab size is more than $6\text{ m} \times 6\text{ m}$. Figure 8 shows distributions of the single axle dual wheel load on concrete slabs with different sizes, only the case of slab longitudinal middle edge as shown in Figure 8. In addition, pavement design guidelines [21, 32] recommend that the thicknesses of concrete slab should not be less than 20 cm and the L/W ratios of slab should be 1~1.25. Vishwakarma and Ingle presented that most of the concrete pavements have a thickness below 35 cm [33]. They have also concluded that the critical stresses of the concrete slab

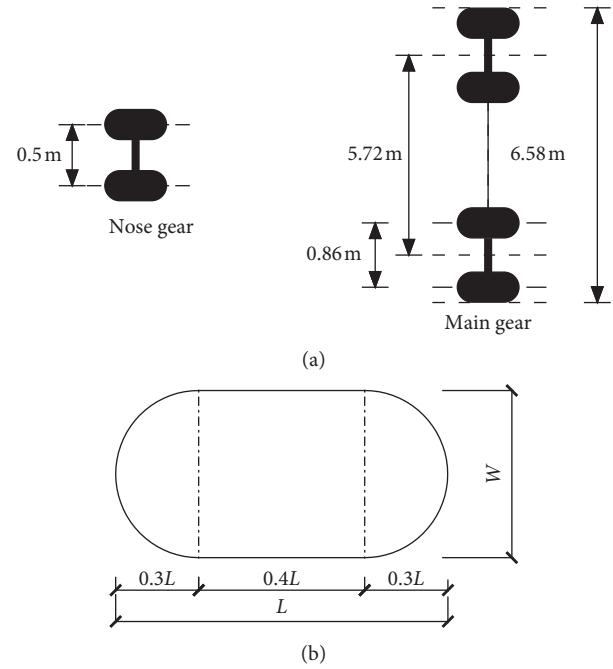


FIGURE 7: Wheel configuration of the Boeing 737-800 aircraft. (a) Landing gear. (b) Wheel ground shape.

for L/W ratio 1.25 or below are almost the same [20]. In this study, to optimize structural parameters of regional airport JCP, given the combined effect of large temperature gradient and aircraft loads, 144 numerical models were developed, as shown in Table 5.

5. Analysis of Results and Discussion

5.1. Determination of the Fatigue Limit. In the CACC guideline, equation (6) is used to analyze the fatigue life of concrete pavement. In addition, the NCHRP1 26 fatigue function (equation (7)) was recommended in the research report of the research and application of new technology for large military transportation airport pavement engineering construction conducted by the Tongji University. Equation (8) expresses the stress-strength ratio:

$$l_g(N) = 14.048 - 15.117e, \quad (6)$$

$$l_g(N) = \begin{cases} 4.284 - 1.7136e, & e > 1.25, \\ 2.8127e^{-1.2214}, & e \leq 1.25, \end{cases} \quad (7)$$

$$e = \frac{\sigma}{f}, \quad (8)$$

where N is the fatigue life of the pavement slab; e is the stress-strength ratio; σ is the maximum tensile stress (MPa); and f is the flexural tensile strength (MPa).

According to the design requirements of the regional airport in Northeast China, the passenger handling capacity is 400,000 person times in a year. The maximum passenger volume of the Boeing 737-800 aircraft is 189 people. Therefore, the annual take-off times of the Boeing 737-800

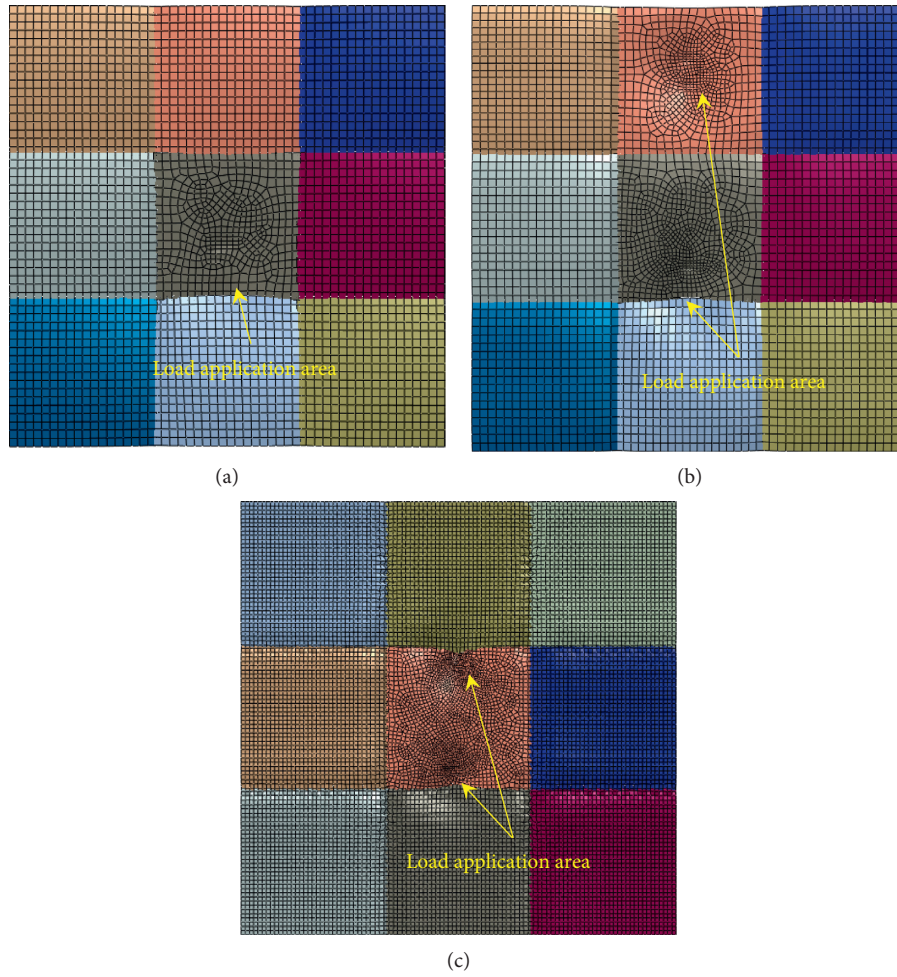


FIGURE 8: Distributions of the single axle dual wheel load on the concrete slabs with different sizes. (a) Load acting on separated slabs. (b) Load acting on adjacent slabs. (c) Load acting on a single slab.

TABLE 5: Statistics of numerical models.

Slab size	Thickness (cm)	L/W	Temperature gradient ($^{\circ}\text{C}\cdot\text{m}^{-1}$)	Loading position
2 m \times 2 m				
3 m \times 3 m	20	1.00		
4 m \times 4 m	25	1.05		
5 m \times 5 m	30	1.10		
6 m \times 6 m	35	1.15	50, -50, 60, -60	Longitudinal middle edge of slab or slab corner
7 m \times 7 m	40	1.20		
8 m \times 8 m		1.25		
9 m \times 9 m				
Total				144 models

aircraft are determined as 2117 times. The designed service life of the airport pavement is 30 years, and thus $N = 2117 \times 30 = 63,510$ times. When compared with the results of stress-strength ratio as obtained by equations (6) and (7), the lower value is used that is $e = 0.61$. In this study, the flexural tensile strength of the concrete is 5.5 MPa. Thus, the fatigue limit of the concrete pavement is 3.3 MPa.

5.2. Optimization Analysis of Slab Size. Figure 9 shows the maximum tensile stresses computed by FE models of different slab sizes and thicknesses, given the unfavorable

coupling of the temperature gradients ($\pm 60^{\circ}\text{C}\cdot\text{m}^{-1}$) and the Boeing 737-800 aircraft load. The flexural tensile strength ($\sigma = 5.5$ MPa) and the fatigue limit ($f = 3.3$ MPa) of the concrete slabs are also denoted in Figure 9. The slab size has a significant influence on the maximum tensile stresses. The maximum tensile stresses are found to be increasing with the increase of the slab size. Compared with the maximum tensile stresses in 2 m \times 2 m slab, those in 9 m \times 9 m slab increase by 2.36 MPa under the combined effect of $60^{\circ}\text{C}\cdot\text{m}^{-1}$ and the slab edge load and 2.17 MPa under the combined effect of $-60^{\circ}\text{C}\cdot\text{m}^{-1}$ and the slab corner load, respectively.

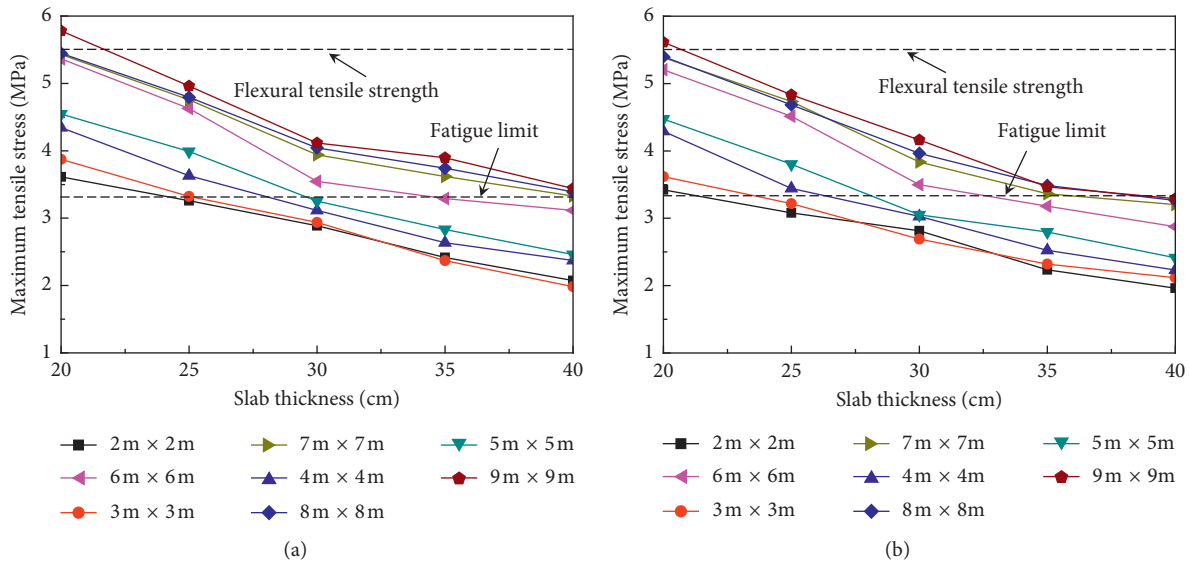


FIGURE 9: Maximum tensile stress given the combined effects of different temperature gradients and the aircraft load. (a) $60^{\circ}\text{C}\cdot\text{m}^{-1}$ and slab edge load. (b) $-60^{\circ}\text{C}\cdot\text{m}^{-1}$ and slab corner load.

On the one hand, when the slab size is larger than $7\text{ m} \times 7\text{ m}$, the maximum tensile stresses are more than the fatigue limit under the combined effect of $60^{\circ}\text{C}\cdot\text{m}^{-1}$ and the slab edge load and more than or slight less than the fatigue limit under the combined effect of $-60^{\circ}\text{C}\cdot\text{m}^{-1}$ and the slab corner load, respectively. On the other hand, the maximum tensile stresses in $2\text{ m} \times 2\text{ m}$ slab and $3\text{ m} \times 3\text{ m}$ slab are less. However, from the construction viewpoint, a decrease in the slab size inevitably increased the work of cutting joint and the amounts of materials such as dowel bars and tension bars. Consequently, the optimum slab sizes of the regional airport concrete pavement in Northeast China are recommended as $4\text{ m} \times 4\text{ m}$ to $6\text{ m} \times 6\text{ m}$.

It also shows a sudden increase in the maximum tensile stress of $6\text{ m} \times 6\text{ m}$ slab. This is because wheel is placed exactly at the edge for this width of slab. Thus, when the width of the concrete slab is close to the width of the main landing gear, the single axle dual wheel load acting on the key joints of both sides will easily cause greater tensile stress.

5.3. Optimization Analysis of Slab Thickness. As shown in Figure 9, the slab thicknesses also have a significant effect on the maximum tensile stress. The maximum tensile stress gradually decreases as the thickness of concrete slab increases. When the slab size is $9\text{ m} \times 9\text{ m}$, the maximum tensile stress in a 40 cm thick slab decreases by 2.34 MPa compared to that in a 20 cm thick slab under the combined effect of $60^{\circ}\text{C}\cdot\text{m}^{-1}$ and the slab edge load and by 2.22 MPa under the combined effect of $-60^{\circ}\text{C}\cdot\text{m}^{-1}$ and the slab corner load, respectively. This is because the maximum tensile stress is related to the bending stiffness of the concrete slab. An increase in the bending stiffness decreases the maximum tensile stress [20, 33]. Moreover, the bending stiffness of the concrete slab is proportional to the third power of the slab

thickness. Thus, an increase in the slab thickness increases the bending stiffness. The bending stiffness is expressed as follows [34]:

$$D = \frac{Eh^3}{12(1 - \nu^2)}, \tag{9}$$

where D is the bending stiffness ($\text{N}\cdot\text{m}$) and h is the slab thickness (m).

The concrete slabs with different sizes have different critical thicknesses under the same combined effect of the temperature gradient and aircraft loads. Figure 10 shows the critical thicknesses of concrete slabs, given the combined effects of different temperature gradients ($\pm 50^{\circ}\text{C}\cdot\text{m}^{-1}$ or $\pm 60^{\circ}\text{C}\cdot\text{m}^{-1}$) and the Boeing 737-800 aircraft load. Obviously, for the concrete slab with same size, the larger the temperature gradient, the larger the critical thickness required. The critical thicknesses of $4\text{ m} \times 4\text{ m}$ slab and $6\text{ m} \times 6\text{ m}$ slab are 28.2 cm and 34.7 cm , respectively, under the combined effect of $60^{\circ}\text{C}\cdot\text{m}^{-1}$ and the slab edge load. However, the critical thicknesses of $4\text{ m} \times 4\text{ m}$ slab and $6\text{ m} \times 6\text{ m}$ slab are 27.4 cm and 33.1 cm , respectively, under the combined effect of $-60^{\circ}\text{C}\cdot\text{m}^{-1}$ and the slab corner load. Thus, with respect to the combined effects of $\pm 60^{\circ}\text{C}\cdot\text{m}^{-1}$ and the Boeing 737-800 aircraft load, the critical thicknesses of $4\text{ m} \times 4\text{ m}$ slab and $6\text{ m} \times 6\text{ m}$ slab are determined as 28.2 cm and 34.7 cm , respectively.

5.4. Optimization Analysis of L/W Ratios. Figure 11 shows variations of maximum tensile stresses for different L/W ratios under the combined effects of $60^{\circ}\text{C}\cdot\text{m}^{-1}$ and the slab edge load or $-60^{\circ}\text{C}\cdot\text{m}^{-1}$ and the slab corner load. The maximum tensile stress increases with the increase of the L/W ratio for the same width of concrete slab. This is because temperature stress gets added to aircraft load stress that enhances the total stress in the concrete slab. When the slab

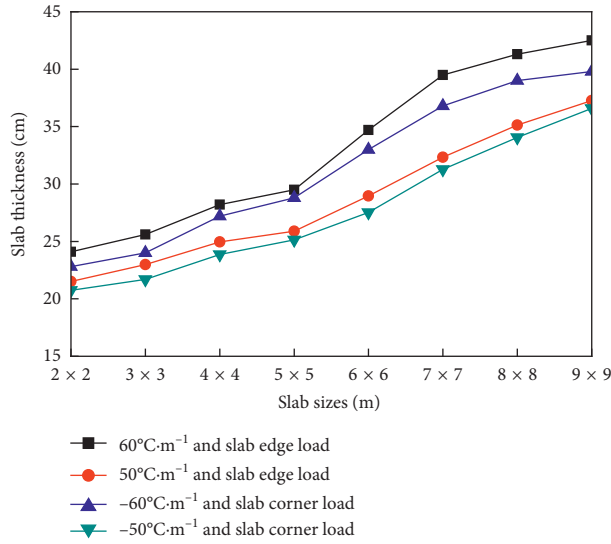


FIGURE 10: Critical thicknesses of concrete slabs given the combined effects of different temperature gradients and the aircraft load.

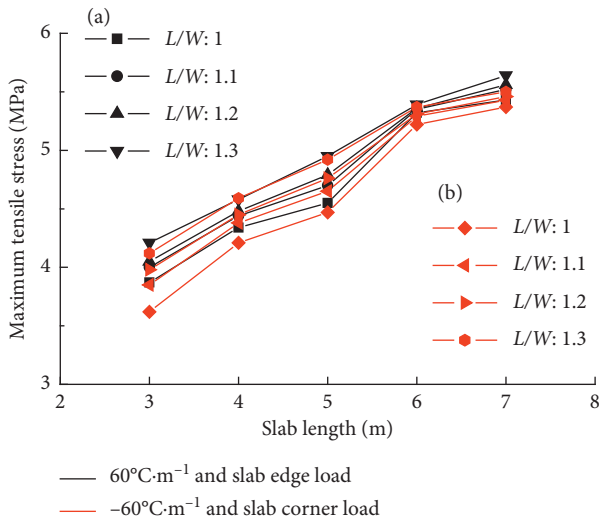


FIGURE 11: Variations of stresses for different L/W ratios due to the combined effects of different temperature gradients and the aircraft load.

length is less than 6 m, the maximum tensile stress in the slab for $L/W = 1.3$ increases by 0.50 MPa compared to that in the slab for $L/W = 1$. But, for the slab with a length of 6 m or 7 m, different L/W ratios have a slight effect on the maximum tensile stress. Consequently, when the slab length is less than 6 m, it is better to use square slab in airport JCP.

6. Conclusions

In order to optimize the structure parameters such as slab size, thickness, and L/W ratio of regional airport JCP, 3-D FE models were developed by using ABAQUS. The effects of different slab sizes, thicknesses, and L/W ratios on the maximum tensile stresses were investigated. In the numerical model, FE simulations of the environment gradient and Boeing 737–800 aircraft loads were modelled. Moreover, the

environmental load was based on findings from the field temperature gradient. By analyzing the comparison results between the maximum tensile stress and the fatigue limit of the concrete slab, the following significant conclusions are made:

- (1) The maximum tensile stresses alter largely as the structure parameters of JCP vary. The maximum tensile stress obtained is higher for larger slab size with thin thickness.
- (2) With respect to the combined effects of the temperature and aircraft loads, unfavorable load-bearing positions, and construction factors, the optimum slab sizes of the regional airport concrete pavement are recommended as 4 m × 4 m to 6 m × 6 m.
- (3) The critical thicknesses of 4 m × 4 m slab and 6 m × 6 m slab are determined as 28.2 cm and 34.7 cm, respectively, based on the comparison and analysis of calculation results of 60°C·m⁻¹ and the slab edge load and -60°C·m⁻¹ and the slab corner load.
- (4) When the slab length is less than 6 m, it is better to use square slab in regional airport JCP.
- (5) Combined action of temperature gradient and aircraft loads induces higher stress. The larger the temperature gradient, the larger the critical thickness required. Hence, temperature load should not be neglected in the design of regional airport JCP where large temperature variations occur.

Data Availability

The figure data used to support the findings of this study have been deposited in the Figshare repository (https://figshare.com/articles/Academic_data/7379813). The table data used to support the findings of this study have been deposited in the Figshare repository (https://figshare.com/articles/Table_data/7379831).

Conflicts of Interest

The authors declare that there are no conflicts of interest.

Authors' Contributions

Bangshu Xu and Wanzhi Zhang conceived and designed the experiments. Wanzhi Zhang and Guangyao Yue analyzed the data and made numerical simulation. Wanzhi Zhang and Jie Mei wrote the paper. Laihua Yang contributed experimental sites.

Acknowledgments

This research was supported by the National Nature Science Foundation of China (Grant no. 50909056).

References

- [1] X. Ma, F. J. Ni, and X. Y. Gu, "Structure design method of composition airfield pavement," *Journal of Traffic and Transportation Engineering*, vol. 10, no. 2, pp. 36–40, 2010.

- [2] M. Q. Jin, "Research on typical diseases analysis and treatment technology of airport cement concrete pavement," Master's thesis, Chang'an University, Xi'an, China, 2015.
- [3] S.-M. Kim and J.-H. Nam, "Measurements and experimental analysis of temperature variations in Portland cement concrete pavement systems," *Road Materials and Pavement Design*, vol. 11, no. 3, pp. 745–771, 2010.
- [4] Y. Qin and J. E. Hiller, "Simulating moisture distribution within concrete pavement slabs: model development and sensitivity study," *Materials and Structures*, vol. 47, no. 1-2, pp. 351–365, 2014.
- [5] Y. Qin and J. E. Hiller, "Modeling the temperature and stress distributions in rigid pavements: impact of solar radiation absorption and heat history development," *KSCE Journal of Civil Engineering*, vol. 15, no. 8, pp. 1361–1371, 2011.
- [6] S.-H. Kim, J.-Y. Park, and J.-H. Jeong, "Effect of temperature-induced load on airport concrete pavement behavior," *KSCE Journal of Civil Engineering*, vol. 18, no. 1, pp. 182–187, 2014.
- [7] D. H. Chen and M. Won, "Field investigations of cracking on concrete pavements," *Journal of Performance of Constructed Facilities*, vol. 21, no. 6, pp. 450–458, 2007.
- [8] O. M. Jensen and P. F. Hansen, "Influence of temperature on autogenous deformation and relative humidity change in hardening cement paste," *Cement and Concrete Research*, vol. 29, no. 4, pp. 567–575, 1999.
- [9] J. H. Jeong and D. G. Zollinger, "Environmental effects on the behavior of jointed plain concrete pavements," *Journal of Transportation Engineering*, vol. 131, no. 2, pp. 140–148, 2005.
- [10] H. J. Oh, Y. K. Cho, Y. Seo, and S.-M. Kim, "Experimental analysis of curling behavior of continuously reinforced concrete pavement," *Construction and Building Materials*, vol. 128, pp. 57–66, 2016.
- [11] H. M. Westergaard, "Analysis of stresses in concrete pavements due to variations of temperature," *Highway Research Board Proceedings*, vol. 6, pp. 201–215, 1927.
- [12] P. Mackiewicz, "Thermal stress analysis of jointed plane in concrete pavements," *Applied Thermal Engineering*, vol. 73, no. 1, pp. 1169–1176, 2014.
- [13] M. Belshe, M. S. Mamlouk, K. E. Kaloush, and M. Rodezno, "Semperature gradient and curling stresses in concrete pavement with and without open-graded friction course," *Journal of Transportation Engineering*, vol. 137, no. 10, pp. 723–729, 2011.
- [14] B. Tian, L. Quan, and K. M. Niu, "Structural experiment and theoretical analysis of thermal curling in JPCP with different base types," *China Journal of Highway and Transport*, vol. 27, no. 6, pp. 17–26, 2014.
- [15] B. H. Nam, J. H. Yeon, and Z. Behring, "Effect of daily temperature variations on the continuous deflection profiles of airfield jointed concrete pavements," *Construction and Building Materials*, vol. 73, pp. 261–270, 2014.
- [16] Y. H. Huang, *Pavement Analysis and Design*, Pearson Education Inc., Hoboken, NJ, USA, 2nd edition, 2004.
- [17] Y. Wei, S. M. Liang, K. He, and J. L. Feng, "Slab-size optimization of rural road concrete pavement considering the combined effect of temperature gradient and traffic load," *Engineering Mechanics*, vol. 32, no. 7, pp. 111–142, 2015.
- [18] R. Chattaraj and B. B. Pandey, "Short panelled concrete pavement in built-up area," *Indian Highways*, vol. 42, no. 1, pp. 5–12, 2014.
- [19] M. Al-Nasra and L. R. L. Wang, "Parametric study of slab-on-grade problems due to initial warping and point loads," *ACI Structural Journal*, vol. 91, no. 2, pp. 198–210, 1994.
- [20] R. J. Vishwakarma and R. K. Ingle, "Effect of panel size and radius of relative stiffness on critical stresses in concrete pavement," *Arabian Journal for Science and Engineering*, vol. 43, no. 10, pp. 5677–5687, 2018.
- [21] China Airport Construction Group Corporation (CACC), *Specifications for Airport Cement Concrete Pavement Design, MH/T5004-2010*, China Communication Press, Beijing, China, 2010.
- [22] Z. F. Zhou and J. M. Ling, "Finite element model of airport rigid pavement structure based on ABAQUS," *Journal of Traffic and Transportation Engineering*, vol. 19, no. 3, pp. 39–44, 2009.
- [23] H. J. Oh, S.-M. Kim, W. Chung, Y. H. Lee, and Y. K. Cho, "Effect of joint type on rigid airfield pavement behavior," *KSCE Journal of Civil Engineering*, vol. 18, no. 8, pp. 1389–1396, 2014.
- [24] Dassault Systèmes Simulia Corp, *ABAQUS User's Manual, Version 6.13-1*, Dassault Systèmes Simulia Corp., Providence, RI, USA, 2013.
- [25] B. Choubane and M. Tia, "Analysis and verification of thermal-gradient effects on concrete pavement," *Journal of Transportation Engineering*, vol. 121, no. 1, pp. 75–81, 1995.
- [26] S. P. Timoshenko and S. Woinowsky-Krieger, *Theory of Plates and Shells*, McGraw-Hill Book Co. Inc., New York, NY, USA, 1959.
- [27] Y. Z. Lv, Q. Dong, C. F. Hu, M. S. Li, and J. G. Zhang, "Study on the relationship between aircraft dynamic load and international roughness index," *Journal of China and Foreign Highway*, vol. 33, no. 3, pp. 74–77, 2013.
- [28] X. M. Zhang, Q. Dong, Y. Z. Lv, H. X. Xue, and Z. C. Sun, "Mechanical responses of edge of rigid airport pavement under aircraft loadings," *Journal of Nanjing University of Aeronautics and Astronautics*, vol. 45, no. 5, pp. 693–699, 2013.
- [29] K. Dyduch, M. Szerszeń, and J.-F. Destrebecq, "Experimental investigation of the fatigue strength of plain concrete under high compressive loading," *Materials and Structures*, vol. 27, no. 9, pp. 505–509, 1994.
- [30] K. Kim and S. Chun, "Evaluation of internally cured concrete pavement using environmental responses and critical stress analysis," *International Journal of Concrete Structures and Materials*, vol. 9, no. 4, pp. 463–473, 2015.
- [31] B. Qu, X.-Z. Weng, J. Zhang et al., "Analysis on the deflection and load transfer capacity of a prefabricated airport prestressed concrete pavement," *Construction and Building Materials*, vol. 157, pp. 449–458, 2017.
- [32] American Association of State Highway, and Transportation Officials, *AASHTO Guide for Design of Pavement Structures*, American Association of State Highway, Washington, DC, USA, 1993.
- [33] R. J. Vishwakarma and R. K. Ingle, "Simplified approach for the evaluation of critical stresses in concrete pavement," *Structural Engineering and Mechanics*, vol. 61, no. 3, pp. 389–396, 2017.
- [34] Z. K. Yao, *Highway Design Manual—Pavement*, China Communications Press, Beijing, China, 2006.

Research Article

Numerical Investigation of Distribution Laws of Shear Force in Box Girder Webs

Xingwei Xue , Chao Zang , Junlong Zhou , and Hai Zhang 

School of Civil Engineering, Shenyang Jianzhu University, Shenyang 110168, China

Correspondence should be addressed to Hai Zhang; h Zhang@sjzu.edu.cn

Received 22 November 2018; Revised 1 February 2019; Accepted 18 February 2019; Published 18 March 2019

Guest Editor: Roberto Brighenti

Copyright © 2019 Xingwei Xue et al. This is an open access article distributed under the Creative Commons Attribution License, which permits unrestricted use, distribution, and reproduction in any medium, provided the original work is properly cited.

To study the shear force distribution laws of a box girder with a single-box multichamber (SB-MC) configuration for different supporting conditions, numbers of webs, stiffness of end diaphragm, and web thickness values, a box girder with SB-MC was numerically simulated using three-dimensional finite element model. According to the comparison results of web shear force, the concept of η , a shear-increased coefficient for webs, was introduced. The results show that supporting conditions and chambers have a significant impact on the shear-increased coefficient η , and end diaphragm must be set up in the 3D finite element model when calculating η . Nonlinear analysis shows that in the elastic phase, the shear-increased coefficient η basically does not change, but in the cracking stage, the coefficient η of each web changes with the degree of web cracking, and side-webs (S-Webs) reach the ultimate load first. The variation of the web thickness hardly affects the distribution of the shear force, so the method to adjust the web thickness of S-Web was proposed according to the result of shear-increased coefficient η to improve the shear resistance of the box girder.

1. Introduction

Box girder is an important type of bridge structure. For box girder, many scholars have conducted research on shear lag, effective width [1–5], and live load distribution factors [6–8]. There are multiple webs in the cross section of a single-box and multichamber (SB-MC) box girder, and their spatial mechanical behavior is complicated. The laws of their shear distribution have important significance and value to effectively ensure the excellent work of the web.

To study the shear resistance, failure modes, and internal force redistribution of box-shaped bridges, the finite element model of the box girder was established and numerically analyzed [9]. This study revealed the effects of factors such as the shear-span ratio, concrete strength, stirrup ratio, and web thickness on the failure modes and shear capacity of the box girder.

The shear resistance of the box girder was experimentally analyzed [10]. The results show that it is unsafe to use the equivalent I-beam to calculate the shear capacity of the box girder. Then, methods based on the modified pressure field theory were compared with the experimental results, including the double-section method, single-section method,

simplified analysis method, and finite element method. The conclusion is that the analysis methods based on the modified pressure field theory could better predict the shear capacity of box beams.

A comparative analysis of the shear design codes of various countries was carried out, and the influence of various influencing factors on the calculation of shear capacity of different national codes was analyzed [11].

There were few results on the shear distribution in the webs of the box girder with SB-MC, so the regular processing method [12–14] is each web equally shares the shear force in the shear calculations of the box girder. However, a preliminary study showed that the shear force is not evenly distributed in webs because of factors such as the supporting conditions, number of webs, stiffness of end diaphragm, and web thickness.

Since the finite element software performed well in civil engineering simulations, many practical projects were calculated and analyzed using this method, and the results proved to be positive [15–17]. This study uses the MIDAS/FEA software to calculate and analyze the models of the SB-MC box girder under various conditions. Based on the summary of actual sharing of shear forces of each web, the

laws of shear distribution of the box girder are obtained, and related design suggestions are proposed.

2. Research on the Shear Distribution of the Box Girder

2.1. Extraction Method of the Shear Force in Webs with the Three-Dimensional Finite Element Model. The stress analysis of a box girder is relatively complicated. With the conventional theory for the box girder, only the analysis results under specific conditions of a typical section can be obtained. It is difficult to obtain the effects of factors such as the change in internal force of the full bridge section and the difficulty in reflecting different supporting conditions. The main goal of this party is to use the software Midas/FEA to build a linear elastic three-dimensional finite element models of the single-box multichamber (SB-MC) box girder under the action of self-weight of the bridge and second-stage dead load in different cases, such as different supporting conditions, number of webs, stiffness of end diaphragm, and web thickness (Figure 1).

Using the function sum of internal forces in specific location in the software to extract the shear forces in each web is varied with the support conditions, numbers of webs, stiffness of end diaphragm, and web thicknesses. Then, the shear distribution of the web could be obtained.

The three-dimensional finite element model can well reflect the mechanical behavior of the structure, but in general, the postprocessing of the three-dimensional finite element analysis only provides the displacement, stress, and strain. The internal forces such as bending moment, axial force, and shear force are difficult to obtain. To study the distribution laws of the shear force in the SB-MC box girder, it is necessary to extract the shear values of each web of the box girder model in a specific section using the function sum of internal forces in specific location.

Taking the box girder with a single box and three chambers as an example, the sum of the internal forces in the specified section of the box girder was extracted. The main process is as follows: first, in the postprocessing after the model analysis, the objective section of the box girder was obtained by a flat surface, which is established by three points and intersects the box girder (Figure 2(a)).

Then, the objective section was selected by the function sum of internal forces in specific location. Finally, the sum of the internal forces in the selected section can be outputted by clicking Text. The exported internal forces mainly contain F_x (axial force in the X direction), F_y (shear force in the Y direction), F_z (shear force in the Z direction), M_x (bending moment around the X -axis), M_y (bending moment around the Y -axis), and M_z (bending moment around the Z -axis), as shown in Figure 3.

The research on shear distribution of webs need to extract the shear force of each web and section. Before the sum of the internal forces V_i of web, only the area of the objective web that requires the extraction of shear force was activated. Then, in the sum of internal forces, the result is the internal forces of the objective web, i.e., the shear force of the objective web can be accessed, as shown in Figure 2(b). If the sum of the internal

forces V_i of the section needs to be extracted, the entire section of the girder needs to be activated (Figure 2(a)).

2.2. Models to Analyze the Shear Distribution of Webs. This study mainly extracts the shear values shared by all webs of the SB-MC box girder under different conditions of support cases, numbers of webs, and web thicknesses; then, we summarize the shear distribution laws of the web.

The basic parameters of the box girder are span: 25 m; beam height: 1.60 m; roof thickness: 20 cm; and floor thickness: 20 cm. The middle segment of the girder is 10 m long, the segment with widening webs is 2.5 m long, the segment with widened webs is 5.0 (4.6, 4.4, 4.0, 3.8, and 3.5) m long, and end diaphragm is 0.0 (0.4, 0.8, 1.0, 1.2, and 1.5) m long. The variables studied are the support conditions, web thickness, the stiffness of end diaphragm, and number of webs. The analysis model corresponding to each variable is described as follows.

2.2.1. Models with Different Support Cases. The cross section of the box girder has a single box and five chambers, whose roof width is 20.4 m, floor width is 15.4 m, the thickness of end diaphragm is 1.2 m, and center distance between two adjacent chambers is 300 cm. The thickness of the web linearly changes from 40 cm to 60 cm. Models with different support conditions are introduced as follows:

- (1) Model SPT-2 used two bearings, whose center distance is 14.2 m, as shown in Figure 4(a)
- (2) Model SPT-3 used three bearings, whose center distance is 7.1 m, as shown in Figure 4(b)
- (3) Model SPT-4 used four bearings, whose center distance is 4.7 m, as shown in Figure 4(c)

2.2.2. Models with Different Numbers of Chambers. The cross section of the box girder has a single box and five chambers, whose roof width is 20.4 m, and the floor width is 15.4 m. The thickness of the web linearly changes from 40 cm to 60 cm, and double bearings were used for this model with a center distance of 14.2 m.

Four models were comparatively analyzed: the box girder with a single box and two chambers (three webs with a web spacing of 740 cm, which corresponds to model CHB-2), the box girder with a single box and three chambers (four webs with a web spacing of 483 cm, which corresponds to model CHB-3), the box girder with a single box and four chambers (five webs with a web spacing of 385 cm, which corresponds to model CHB-4), and the box girder with a single box and five chambers (six webs with a web spacing of 300 cm, which corresponds to model CHB-5).

2.2.3. Models with Different Thicknesses of the Web. Based on model CHB-4, a comparative analysis of four models with the web thickness as the variable was performed using a three-bearing form with a support distance of 7.1 m. The four models are introduced as follows: model WebThk-35(55), with various web thicknesses of 35–55 cm; model

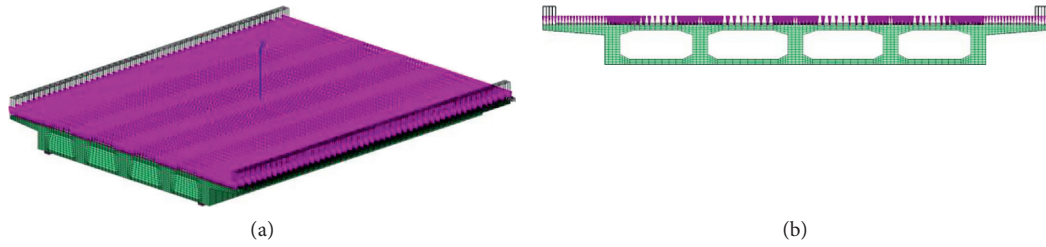


FIGURE 1: (a) 3D FE model and action. (b) Section of the girder.

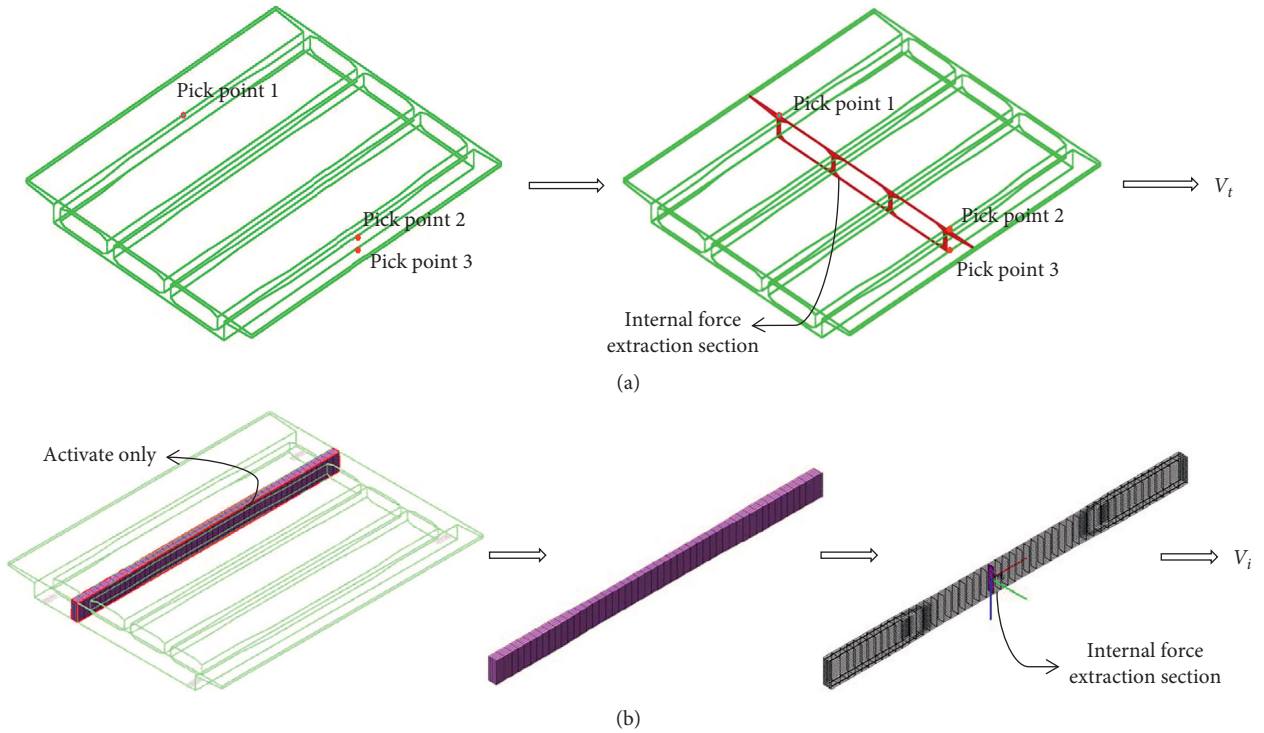


FIGURE 2: Selection of internal force extraction section. (a) Extraction of internal shear force V_t in section. (b) Extraction of internal shear force V_i in web.

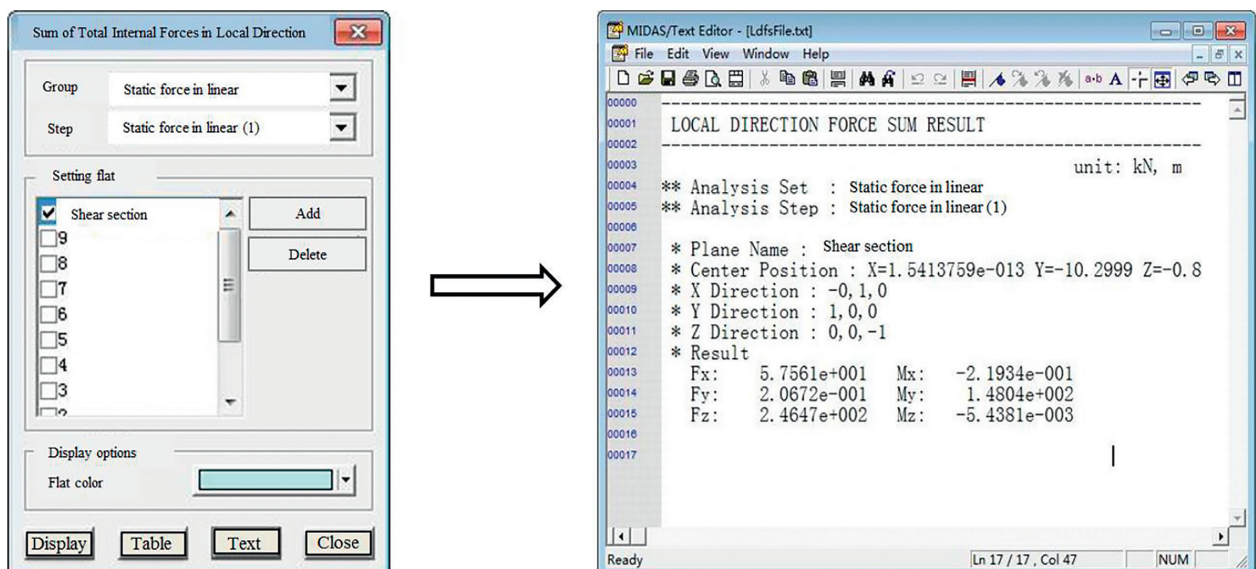


FIGURE 3: Sum of internal forces in specific location.

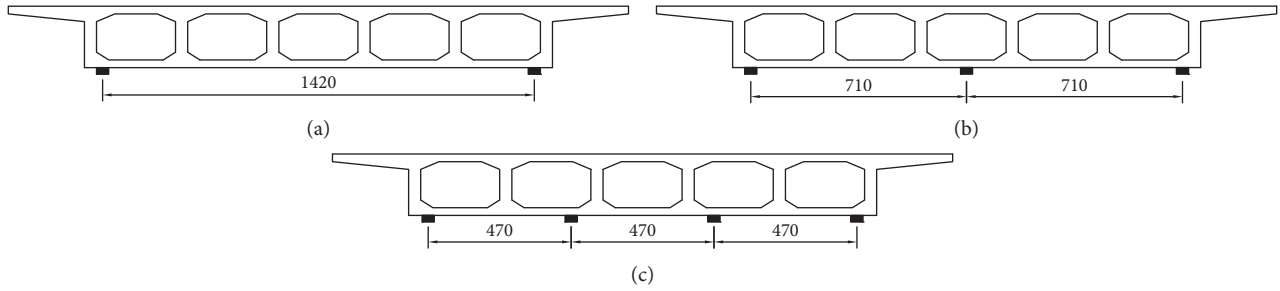


FIGURE 4: Layout of the bearings in different models (unit: cm). (a) Model SPT-2. (b) Model SPT-3. (c) Model SPT-4.

WebThk-40(60), with web thickness of 40–60 cm; model WebThk-45(65) with web thickness of 45–65 cm; and model WebThk-50(70) with web thickness of 50–70 cm.

2.2.4. Models with Different Stiffnesses of End Diaphragm. In order to obtain the influence of stiffness of end diaphragm on the shear force distribution, six analytical models, model DPH-0, model DPH-0.4, model DPH-0.8, model DPH-1.0, model DPH-1.2, and model DPH-1.5, are proposed, corresponding to thicknesses of 0.0 m, 0.4 m, 0.8 m, 1.0 m, 1.2 m, and 1.5 m, respectively.

2.3. Results and Discussion to Analyze the Shear Distribution of Webs. The names of each web are stipulated with a single-box five-chamber configuration as an example (Figure 5). The two outermost webs are named side-webs (S-Webs), the webs close to S-Webs are called secondary side-webs (SS-Webs), and middle-webs (M-Webs) are at the center of the cross section.

Twenty groups of cross sections of the box girder were taken at intervals of $(1.3 + 18 \times 1.0 + 1.3)$ m from the midpoint of the bridge midspan to both sides of the bearing along the portrait direction of the bridge to analyze the shear distribution of each web in the portrait direction.

2.3.1. Shear Distribution of Webs with Different Support Cases. Model SPT-2, model SPT-3, and model SPT-4 are the models of the box girder with different bearing spacings, whose form of cross section is single box and five chamber. The roof width of the box girder is 20.4 m, the floor width is 15.4 m, and the center distance of chambers is 300 cm.

According to the conventional design method, the shearing force shared by each web is averaged using formula (1). However, a preliminary study showed that the shear force is not evenly distributed in each web; this paper defined the shear-increased coefficient η of each web, which characterizes the ratio of the actual shear force value of each web to the mean value of the webs, as shown in formula (2):

$$V_a = \frac{V_t}{N_f}, \quad (1)$$

$$\eta = \frac{V_i}{V_a}, \quad (2)$$

where V_a is the nominal shear value equally distributed to each web (MPa); V_t is the shear value of the full section of the girder (MPa); N_f is the number of webs; and V_i is the shear value of single web (MPa).

From the 20 groups of cross sections in Figure 5, the shear forces shared by the S-Webs, SS-Webs, and M-Webs of the box girder in model SPT-2, model SPT-3, and model SPT-4 were extracted. The variation of the shear values and shear-increased coefficient η of each web from model SPT-2 to model SPT-4 along the portrait directions of the girder is shown in Figures 6(a)–6(f).

The average value curve shows $\eta = 1.0$. As observed in Figure 6,

- (1) The shear forces shared by each web of the box girder are not evenly distributed, and the shear-increased coefficient η of both SS-Webs and M-Webs is less than 1.0. However, the shear-increased coefficient η of S-Webs is more than 1.0, which is unsafe in bridge design.
- (2) In model SPT-2, the shear-increased coefficient η of S-Webs is 1.58 in the midspan and 1.64 in the sections at the bearings, and the increase of these values is remarkable compared with the mean of 1.0. In addition, the shear-increased coefficient η of S-Webs in model SPT-3 and model SPT-4 is 1.31 and 1.27 in the section at the bearings, respectively, which cannot be ignored in the design.

The shear force shared by each web with double bearings is most different because the web near the bearings directly bears the reaction force from the bearings. According to Saint-Venant's principle, the shear-increased coefficient η of each web gradually decreases from the bearings to the midpoint of the bridge.

2.3.2. Shear Distribution of Webs with Different Numbers of Chambers Cases. Model CHB-2, model CHB-3, model CHB-4, and model CHB-5 are the models of the box girder with different numbers of chambers, which used double bearings with a center distance of 14.2 m. The roof width of the box girder is 20.4 m, the floor width is 15.4 m, and its center distance of the chambers is 300 cm. Models CHB-2 to CHB-5 are described in detail in Section 2.2.2.

It can be seen from the calculation results that all shear-increased coefficients η of S-Webs in models CHB-2 to

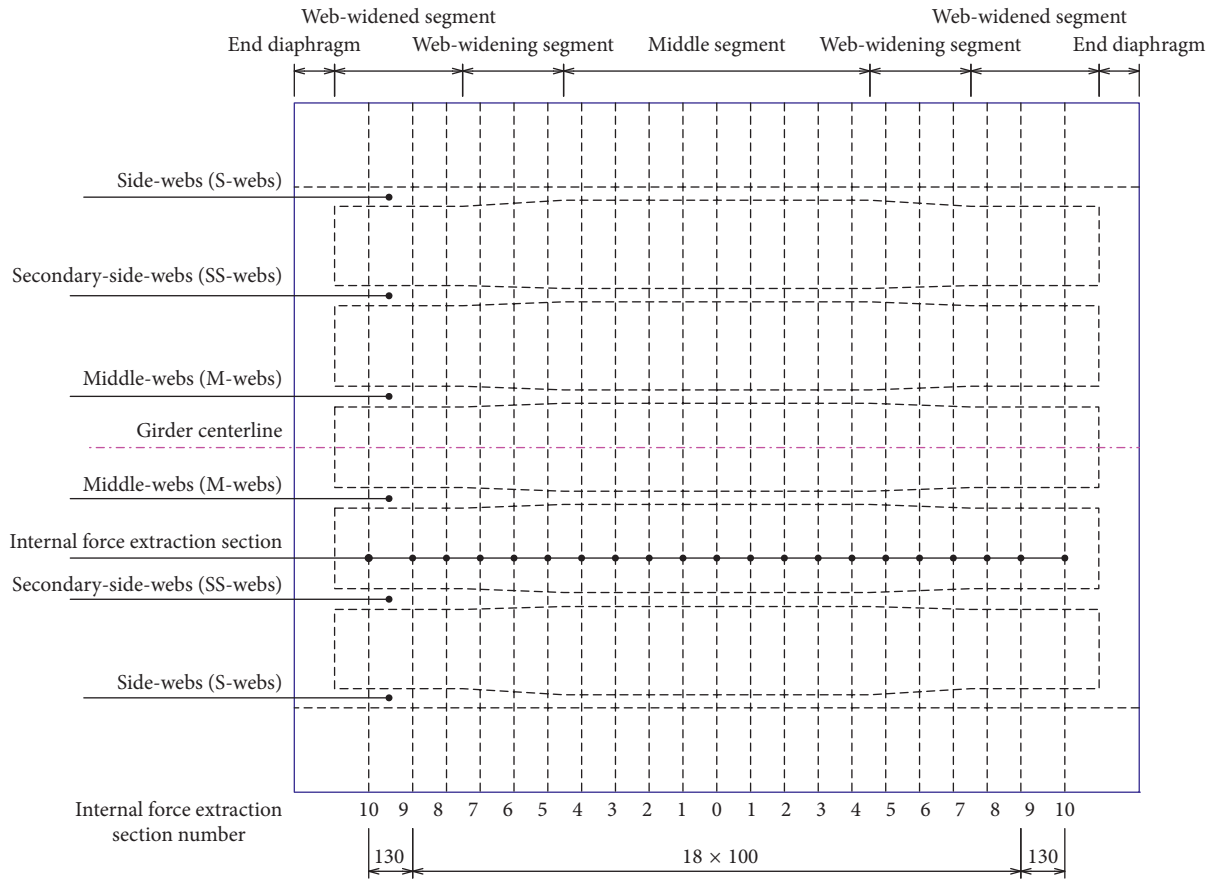


FIGURE 5: Main beam structure and web naming (unit: cm).

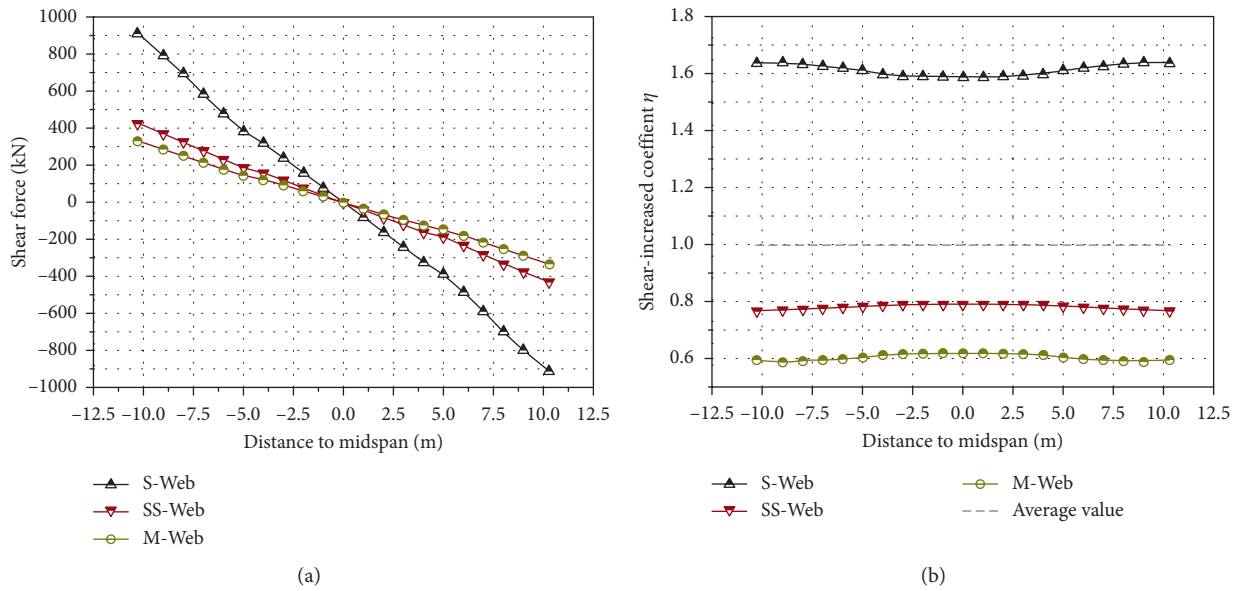


FIGURE 6: Continued.

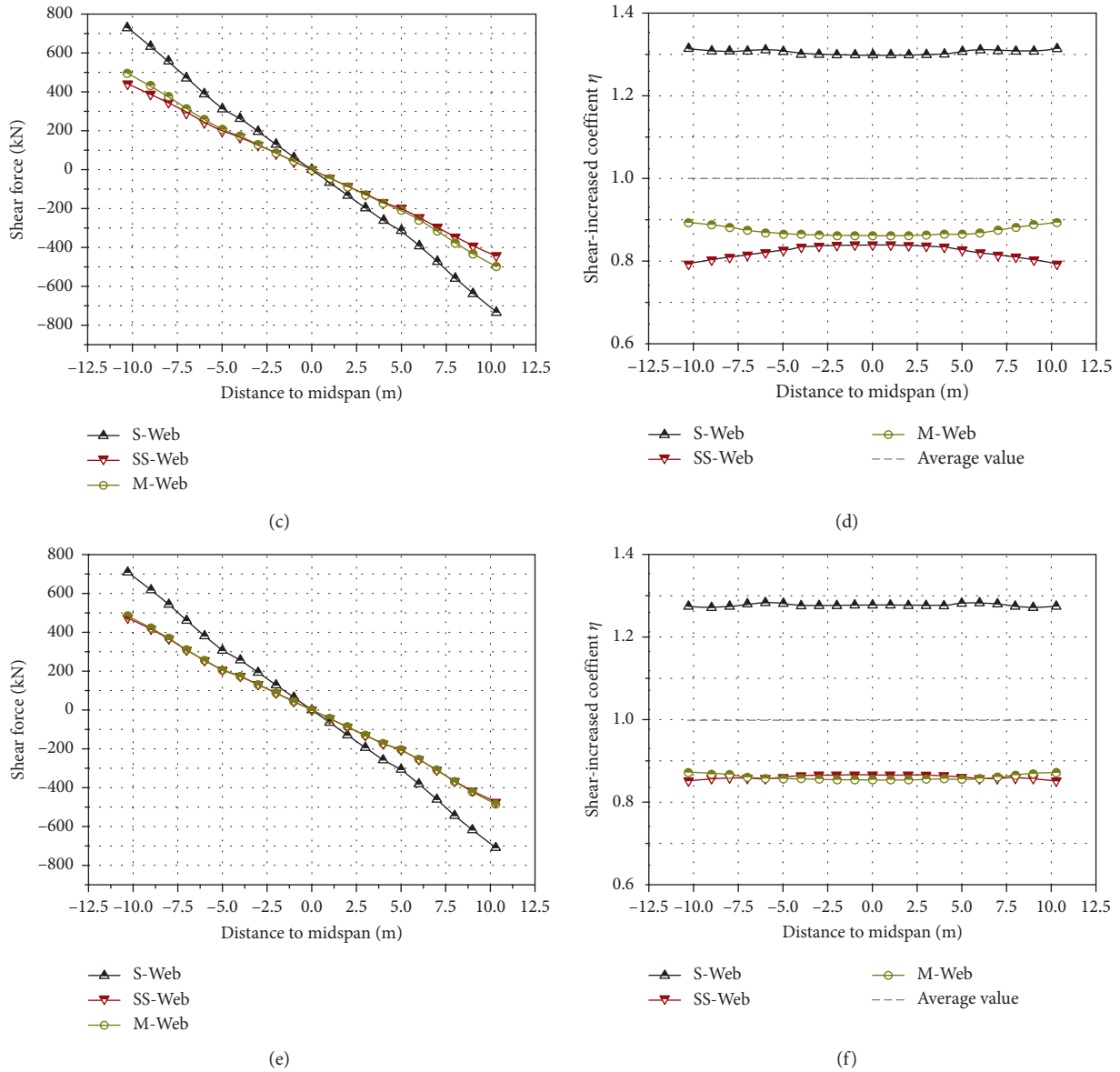


FIGURE 6: Shear distribution and shear-increased coefficient η of the webs with different support cases. (a) Shear value of each web in model SPT-2. (b) Shear-increased coefficient of each web η in model SPT-2. (c) Shear value of each web in model SPT-3. (d) Shear-increased coefficient of each web η in model SPT-3. (e) Shear value of each web in model SPT-4. (f) Shear-increased coefficient of each web η in model SPT-4.

CHB-5 are greater than 1.0, and their values for SS-Webs and M-Webs are less than 1.0. As shown in Figure 7, with the increase in number of webs, the shear-increased coefficient η of S-Webs increases. In contrast, the shear-increased coefficient η of SS-Webs and M-Webs decreases with the increase in number of webs.

2.3.3. Shear Distribution with Different Thicknesses of the Web Cases. Model WebThk-35(55), model WebThk-40(60), model WebThk-45(65), and model WebThk-50(70) are the models of the box girder with different web thicknesses, whose cross-sectional forms are a single box with four chambers, three bearings, and a center distance of 7.1 m. The roof width of the box girder is 20.4 m, and the floor width is

15.4 m. Models WebThk-35(55) to WebThk-50(70) are described in Section 2.2.3. The results of different thicknesses of the web are shown in Figure 8.

The shear distribution results are as follows: the largest shear value is assigned to S-Webs, and the shear-increased coefficient η of S-Webs in models WebThk-35(55) to WebThk-50(70) is greater than 1.0. As shown in Figure 8, the shear-increased coefficient η values differ by less than 1%. Therefore, the effect of the web thickness on the shear distribution of the web is unremarkable.

2.3.4. Shear Distribution with Different Stiffnesses of End Diaphragm Cases. Both ends of the box beam are generally provided with end diaphragms of a certain thickness.

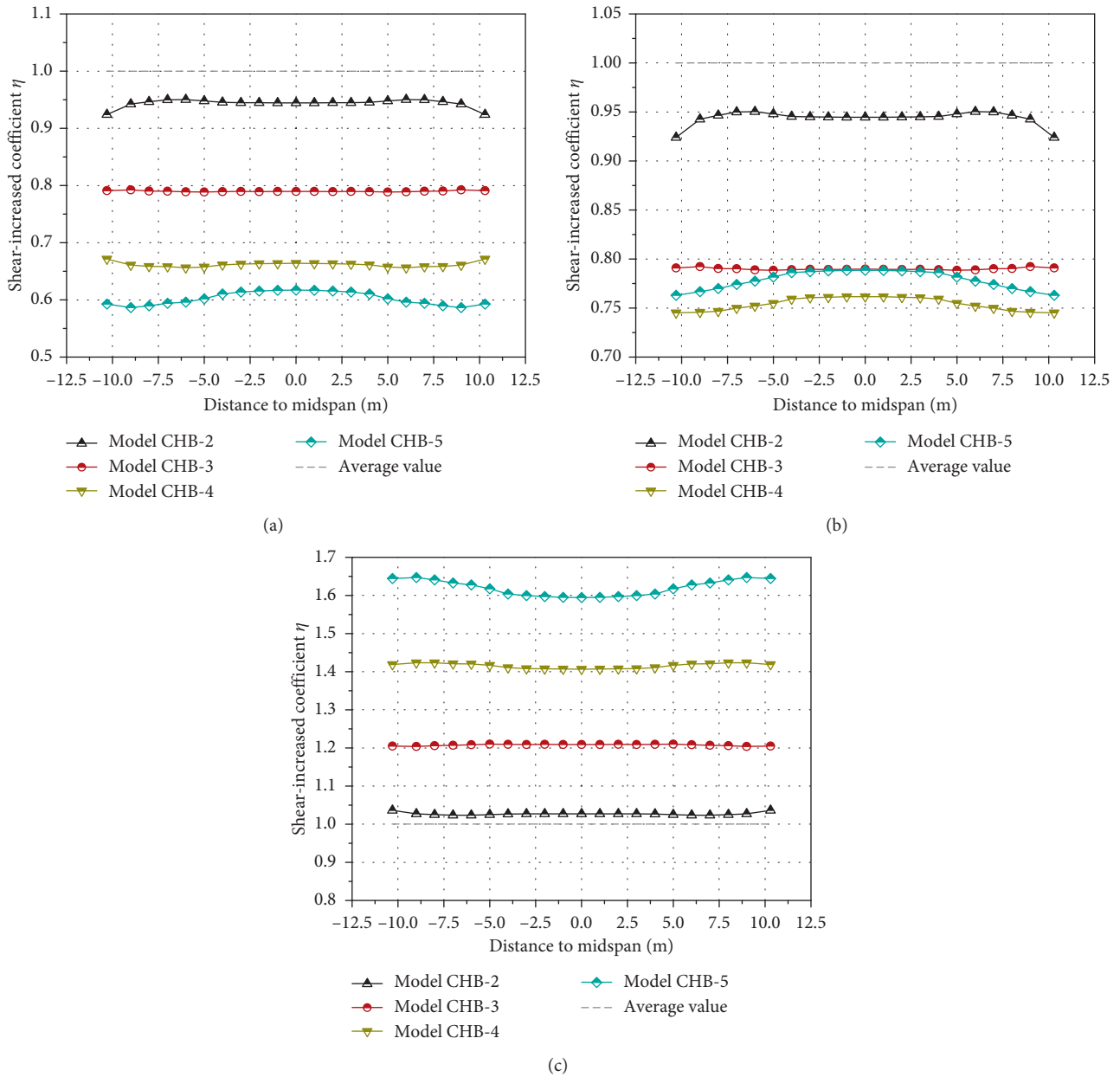


FIGURE 7: Shear-increased coefficient η with different numbers of chambers cases. (a) Shear-increased coefficient η of M-Webs. (b) Shear-increased coefficient η of SS-Webs. (c) Shear-increased coefficient η of S-Webs.

A certain number of supports are arranged below the end of the box beam, and the reaction force at the support has a longitudinal and transverse effect on the main beam. End diaphragms at the end of the box beam can play a transverse role against the reaction force of support, and at the same time, due to the action of end diaphragm, the reaction force of support can be transmitted to the webs relatively uniform. Therefore, whether end diaphragms are set or not, the stiffness of end diaphragm to the shear-increase coefficient η is worthy of further study. Six models of end diaphragms were studied in the effects of stiffness. Calculations prove that

- (1) When end diaphragms are not set, the shear-increased coefficient η of the S-Webs is the largest,

reaching 1.37 at the internal forces extraction section 10 and 1.24 at the middle of the span (corresponding to internal forces extraction section 0).

- (2) After end diaphragms are set, the shear-increased coefficient η of the S-Webs is rapidly decreased. For example, for section 10, when the thickness of end diaphragms is 0.4 m, the shear-increased coefficient η of the S-Webs is 1.12, which is reduced by 18.2% with respect to the case where end diaphragms are not provided.
- (3) Within the range of thicknesses commonly used for end diaphragms, that is, in the range of 1.0~1.5 m, the shear-increased coefficient η of the S-Webs is not obvious, and the difference is less than 1% (Figure 9).

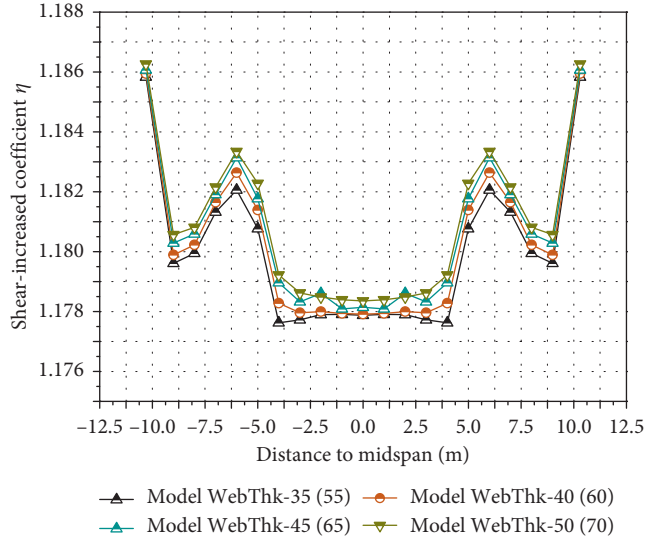


FIGURE 8: Shear-increased coefficient η with different thicknesses of the web cases.

3. Analysis of the Shear Failure of the SB-MC Box Girder

For the uneven distribution of shear force in the webs of an SB-MC box girder, a three-dimensional nonlinear model was established. Through the nonlinear analysis from loading to failure, we attempt to find the effect of the uneven distribution shear on the damage process of the webs and the redistribution of shear values in the webs.

3.1. Finite Element Model for the Nonlinear Analysis of the SB-MC Box Girder

3.1.1. Constitutive Tensile Relationship of Concrete Material. The nonlinear properties of the concrete material are considered in the Midas/FEA analysis to determine the causes of cracking. The total strain crack model in the concrete material parameters is a type of discrete crack model, which finds the crack behavior according to a fixed crack model or a rotating crack model. Once determined, the cracking direction does not change in any case for the fixed crack model; although less widespread, it was successfully applied in some problems of reinforced concrete structures [18–20]. In comparison, the rotating crack model requires no knowledge of past cracking states, so its calculation process is much simpler and convergent [21–23]. In this study, the rotating crack model was selected.

Based on fracture energy theory, a parabolic hardening-softening model is used in the total stress cracking model, which depends on three parameters of compressive strength f_c , compressive fracture energy G_c , and characteristic element length h , as shown in Figure 10.

The strain corresponding to 1/3 of the maximum compressive strength f_c is shown in equation (3), and the strain corresponding to the maximum compressive strength f_c is shown in equation (4):

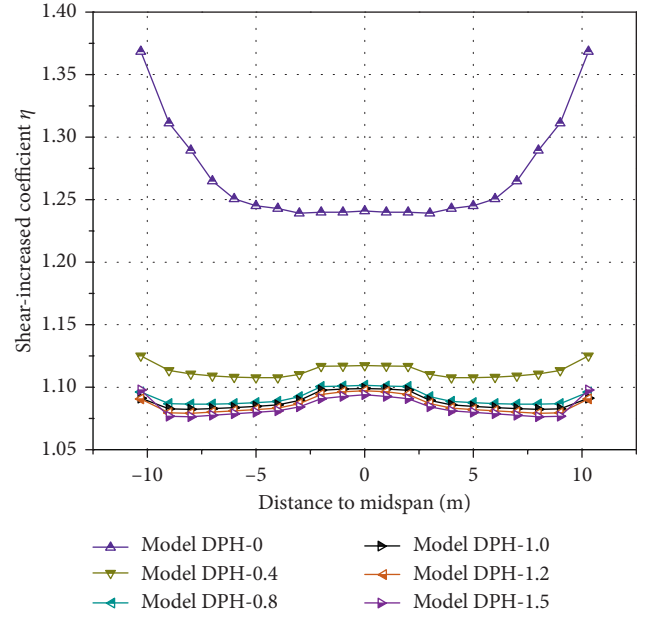


FIGURE 9: Shear-increased coefficient η with different stiffnesses of end diaphragm cases.

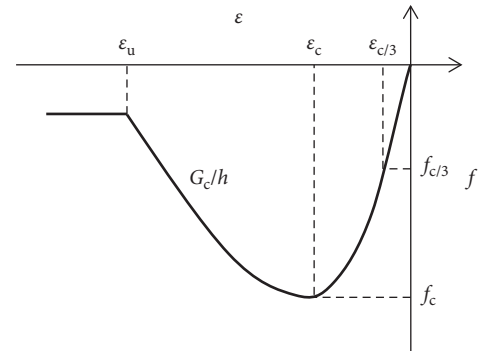


FIGURE 10: Compressive model with parabolic hardening-softening.

$$\varepsilon_{c/3} = \frac{1}{3} \frac{f_c}{E}, \quad (3)$$

$$\varepsilon_c = -\frac{4}{3} \frac{f_c}{E}. \quad (4)$$

As can be seen from the above formula, the values are independent of cell size and compressive fracture energy. Thus, the ultimate strain at the softening end position of the compression zone is shown in the following equation:

$$\varepsilon_u = \varepsilon_c - \frac{3}{2} \frac{G_c}{hf_c}. \quad (5)$$

A linear softening model is used in the total stress cracking model, which exhibits softening when the tensile strength of the base material is exceeded, as shown in Figure 11.

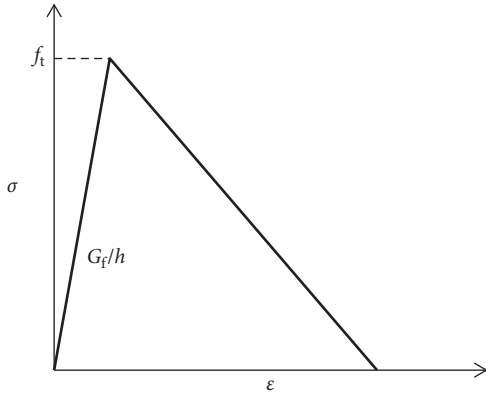


FIGURE 11: Tensile model with linearized softening.

The major constitutive equations for the linearized softening tensile model are shown in the following equations:

$$\begin{aligned} \varepsilon_{u-\min}^{cr} &= \frac{f_t}{E}, \\ f_t &= \sqrt{2\left(\frac{G_f E}{h}\right)}, \end{aligned} \quad (6)$$

where G_f is the tensile fracture energy of concrete, E is the elastic modulus of concrete, h is the crack width, f_t is the tensile stress in the concrete, and $\varepsilon_{u-\min}^{cr}$ is the minimum ultimate crack strain.

3.1.2. Constitutive Relationship of the Steel Bar. The von Mises model is widely used in the analysis of metallic materials. The von Mises model in MIDAS/FEA requires the definition of the hardening curve of the material yield stress $f_{y,r}$. Tri-fold line stress-strain model of the hot-rolled steel bar was used to generate the constitutive model of the steel bar, as shown in Figure 12.

3.1.3. Bonding Model of Reinforced Concrete. Because the slippage between concrete and steel in reinforced concrete structures is impressed by cracks, a bond-slip model based on the deformation theory of plasticity can be used to simulate this effect. Assuming that the tangential direction is nonlinear and the normal direction of materials is linear elasticity, the bond-slip model can be expressed as follows:

$$t_n = k_n \Delta u_n, \quad (7)$$

$$t_t = f_t(dt). \quad (8)$$

By determining the right side of equations (7) and (8) for the relative displacement, the tangent stiffness is as follows:

$$\begin{bmatrix} D_{11} = k_n & D_{12} = 0 \\ D_{21} = 0 & D_{22} = \frac{\partial f_t}{\partial d_t} \end{bmatrix}. \quad (9)$$

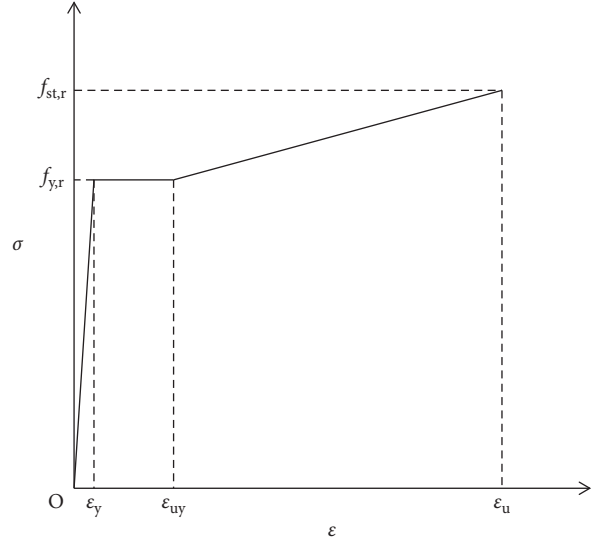


FIGURE 12: Stress-strain curve of hot-rolled steel.

3.1.4. A Model for Calculation. The object of nonlinear analysis is a box girder with a single box and four chambers. The basic parameters of the box girder are introduced as follows. Its span is 25 m, the beam height is 1.60 m, the roof and floor are 20 cm thick, and the thickness of the web from its midspan to the side-span is 40–60 cm in a linear gradient relationship. The middle segment of the girder is 10 m long, the segment with widening webs is 2.5 m long, the segment with widened webs is 3.8 m long, and end diaphragm is 1.2 m long. The distance between the chambers is 300 cm, the width of the roof is 20.4 m, and the width of the floor is 15.4 m. The model used double bearings with a bearing spacing of 14.2 m.

The stirrups are 12 mm in diameter, and the diameter of longitudinal steel bars of the bottom plate, the top plate, and the other is 32 mm, 16 mm, and 12 mm, respectively. Reinforcement configuration of the stirrups and longitudinal steel bars is shown in Figure 13.

The shear-span ratio of the model is 2.0. To avoid the stress concentration at the areas for loading and supporting, elastic blocks were used in the corresponding position, as shown in Figure 13. The sum of the applied vertical loads on a single loaded block is 70500 kN. Because the roof of the model is 20.4 m wide and the elastic block for loading is 0.475 m wide, the surface pressure applied to the surface of the elastic blocks is approximately 7275.5 kN/m². The displacement criterion was used as the convergence condition and a modified Newton–Raphson iteration method was used to analyze the model in nonlinearity.

3.2. Results and Discussion of the Nonlinear Analysis

3.2.1. Curves of Load-Displacement. The vertical displacements of each web in the underside of the beam at the midspan were first extracted, as shown in Figure 14. Through the function multistep isosurface in the post-processing of MIDAS/FEA, the crack development process

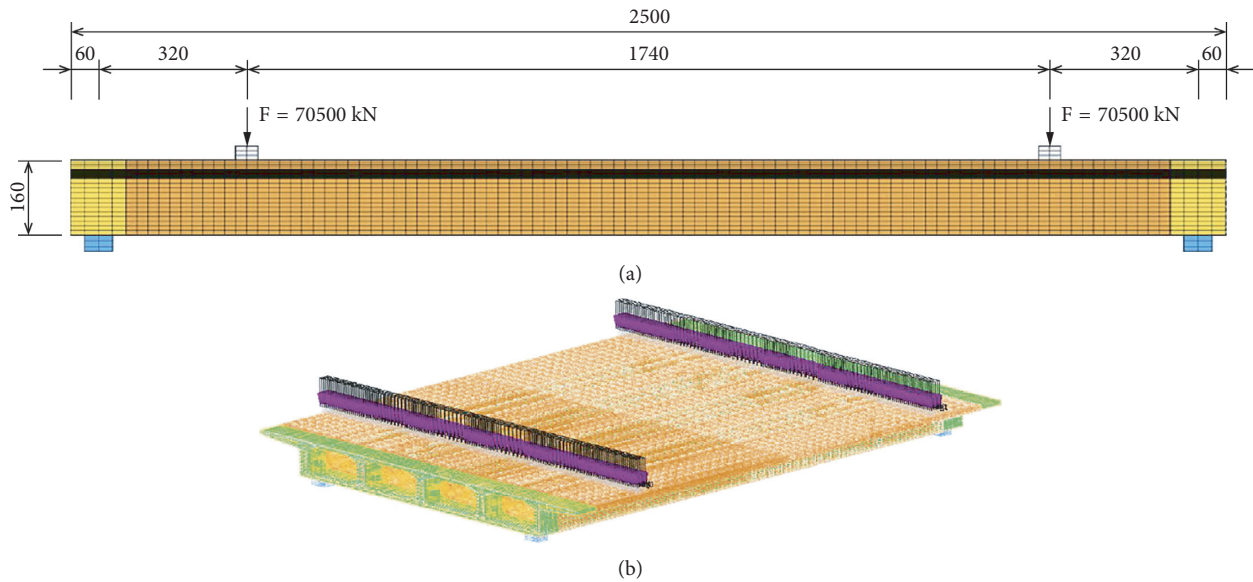


FIGURE 13: Model of the box girder (unit: cm). (a) Elevation of the model. (b) Finite element of steel bar.

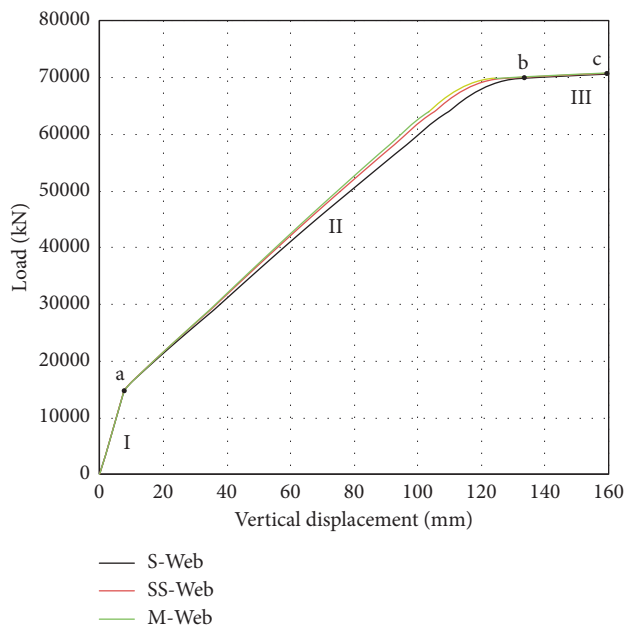


FIGURE 14: Load-displacement curves at midspan.

of the box girder with a single box and four chambers was extracted according to the load step. The failure mode and cracking development of the beam are shown in Figures 15 and 16.

Figure 14 shows the following: (1) the entire loading process went through three phases (Stage I, Stage II, and Stage III) and three feature points (a, b, and c). In Stage I, corresponding to section 0-a in Figure 14 for the elastic stage, the displacement increases linearly with the load; after the cracking characteristic point a (load factor is 0.22), the girder enters the cracking stage, corresponding to Stage II, as seen in Figure 16, the S-Webs firstly crack (Figure 16(a)), and then the SS-Webs and M-Webs sequentially crack

(Figures 16(b) and 16(c)). As the load increases, the degree of cracking of the girder increases (Figures 15 and 16(d)). After reaching point b, the girder enters Stage III (the stirrups in shear span (corresponding to sections 8, 9, and 10, as seen Figure 5) and longitudinal rebars in the midsole plate yield) and further reaches the shear capacity.

3.2.2. Shear Force Redistribution during Loading. MIDAS/can extract not only the internal force of a solid element in the elastic phase but also the cracking phase. Under each load step, the shear force of the S-Webs, SS-Webs, and M-Webs of section no. 9 (Figure 5) was extracted, and the shear-increased coefficient η was calculated. Figure 17(a) shows the variation of the shear-increased coefficient η with loading during the whole process. Figure 17(b) clearly shows the change of the shear-increased coefficient η when the loading force was from 10000 to 30000 kN before and after cracking. The characteristics of the change in the shear-increased coefficient η are summarized as follows:

- (1) In the elastic phase I (corresponding to oa), the shear-increased coefficient η remains basically unchanged and is 1.25, 0.84, and 0.81 to S-Web, SS-Web, and M-Web, respectively.
- (2) When loaded to point a, S-Web first cracks; its shear-increased coefficient η reduces to 1.19, but the shear-increased coefficient η of SS-Web and M-Web increase to 0.9 and 0.82, respectively.
- (3) With the further loading, the girder continues to crack, and the difference of the shear-increased coefficient η among the webs is gradually reduced. When loaded to the bearing capacity of 70500 kN, the shear-increased coefficient η of S-Web, SS-Web, and M-Web is 1.09, 0.95, and 0.93, respectively.

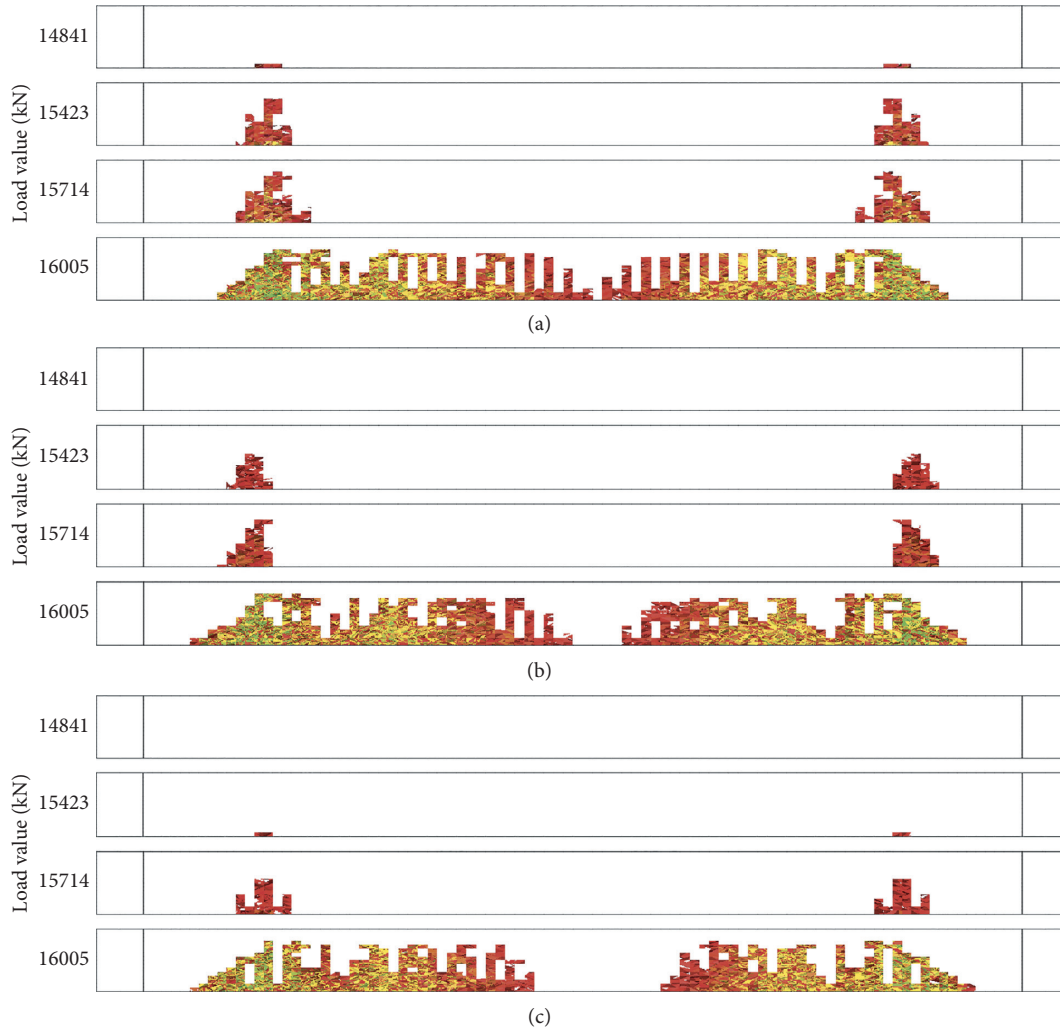


FIGURE 15: Crack distribution of webs. (a) Crack distribution of S-Webs. (b) Crack distribution of SS-Webs. (c) Crack distribution of M-Webs.

The distribution of the shear-increased coefficient η in each web is a process of redistribution with the change of structural stiffness.

4. Design Measures considering the Laws of Shear Distribution

Through the comparative analysis of the results of the elastic model, we can preliminarily conclude that the shear distribution of webs in a box girder with a single box and multiple chambers is greatly affected by the supporting conditions and number of chambers, but shear-increased coefficient η is not sensitive to web thickness; the shear value shared by the S-Webs is larger than those shared by the SS-Webs and M-Webs. Therefore, the even distribution of shear force of the full section to each web in the design is unsafe to S-Webs. Nonlinear analysis shows that in the elastic phase, shear-increased coefficient η basically does not change, and coefficient η of each web changes with the degree of its cracking in the cracking stage, and S-Webs reach the ultimate load first.

The shear bearing capacity of the box girder is greatly affected by the thickness of its web [11]. Because the S-Webs have absorbed more shear force than the other webs, the shear-increased coefficient η is hardly affected by the web thickness and the main beam in the conventional design is generally in a nonshear crack state; this study proposes the design idea that according to the calculation result of shear-increased coefficient η , the S-Webs are thickened accordingly. This change may make the shear strength of each web match its shear resistance, and the webs almost simultaneously reach their shear capacity.

The formula can be expressed as

$$t_s = \eta_0 \cdot t_{s0}, \quad (10)$$

where t_s is the S-Webs thickness adjusted according to η_0 ; η_0 is the shear-increased coefficient calculated under the average web thickness, and t_{s0} is the average thickness of the webs before adjustment.

Model WebThk-40(60) of the box girder with a single box and four chambers is used as an example. The thickness of the web linearly changes from 40 cm at the

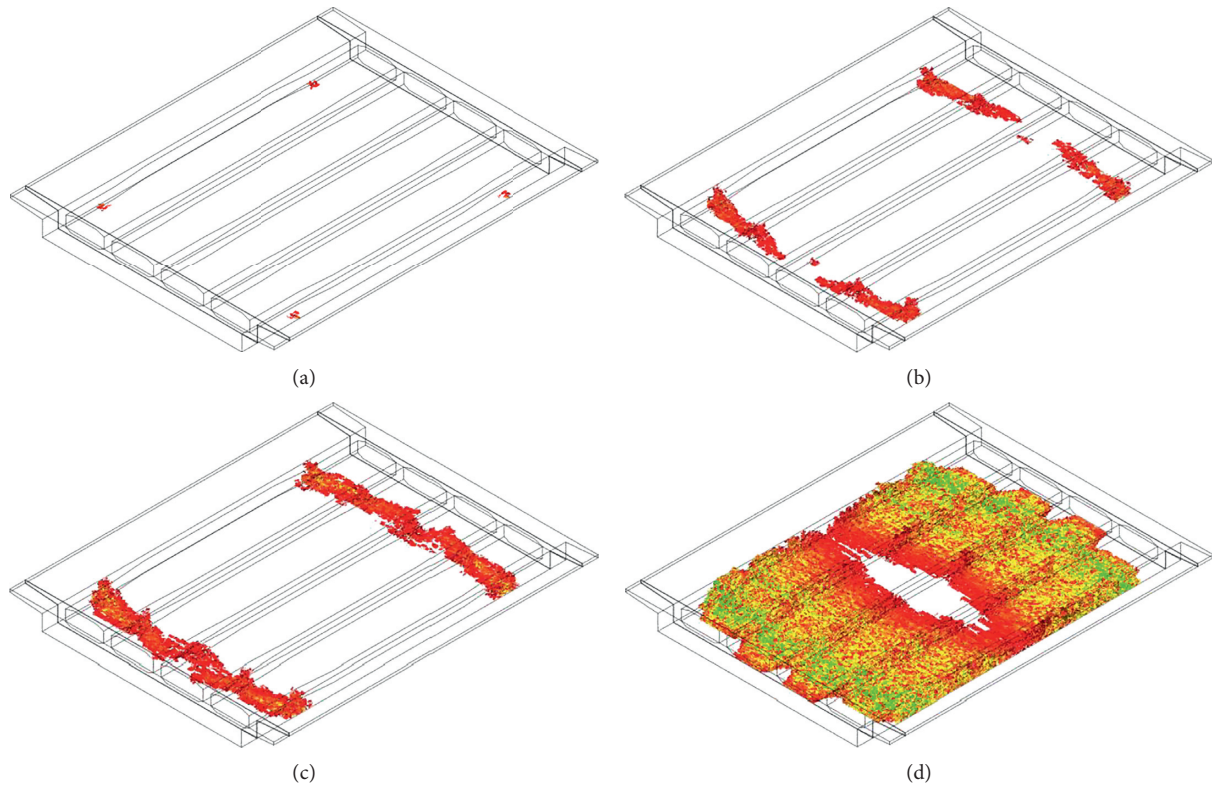


FIGURE 16: Crack distribution of girder. (a) Load value: 14841 kN. (b) Load value: 15423 kN. (c) Load value: 15714 kN. (d) Load value: 16005 kN.

middle segment to 60 cm at the widened webs segment. The shear-increased coefficient η of the S-Webs is 1.19, and the η of the SS-Webs and M-Webs is 0.83 and 0.97, respectively. According to the calculation results of η_0 , the thickness of the S-Webs is adjusted in $40 \times \eta_0 = 47.6$ cm and $60 \times \eta_0 = 71.4$ cm. According to the conventional web thickness value, the thickness of the S-Webs is changed to 50 cm and 70 cm, which is 1.25 times of the original thickness. For the webs with shear-increased coefficient η_0 less than 1.0, the web thickness is not adjusted.

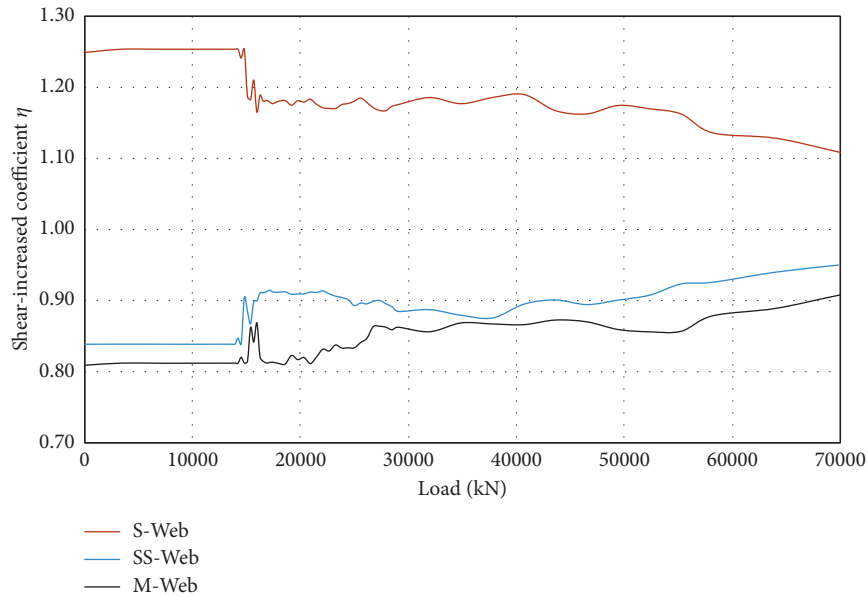
After the optimal design of S-Web thickness was obtained, the shear-increased coefficient $\eta_s = 1.24$ of S-Webs was again extracted, which matches the time value 1.24 of the adjusted thickness to the original thickness, in the same time matches the shear resistance of the S-Webs. On the other hand, η_s for the SS-Webs and M-Webs is 0.80 and 0.93, respectively, which matches their thickness and shear resistance. Therefore, the adjusted webs in the shear distribution are reasonable and safe.

5. Conclusions

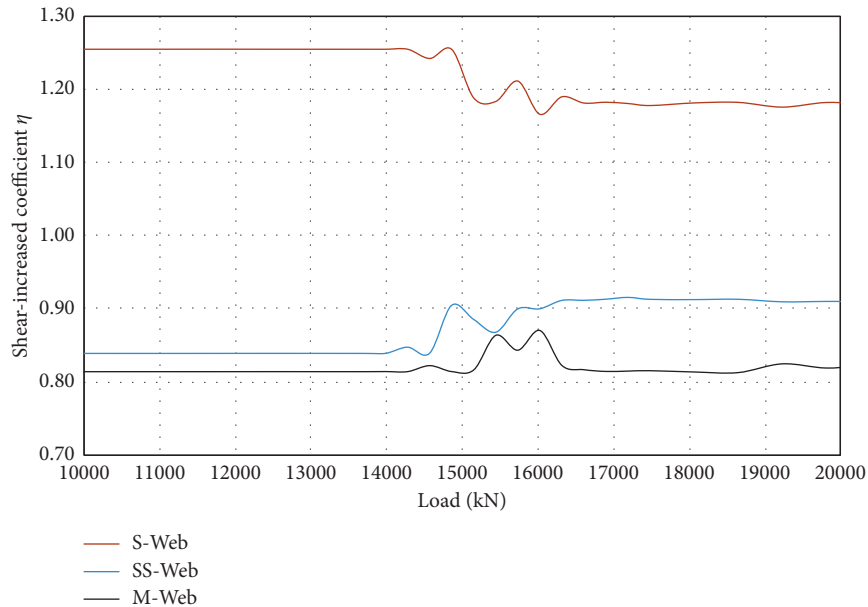
In this paper, in the elastic model, the shear distribution of the SB-MC box girder was examined for different support conditions, the number of webs, the stiffness of end diaphragm, and the thickness of the web. In addition, the problem of shear redistribution was also studied in the nonlinear model. Finally, according to the shear-increased coefficient η of the S-Web, the method of structural

optimization design is proposed. The main conclusions are as follows:

- (i) The Midas/FEA software, with great postprocessing capabilities, can easily and quickly extract the internal forces of models for a comparative analysis.
- (ii) The laws of shear distribution of the elastic model of the SB-MC box girder are as follows:
 - (1) All the calculation conditions show that the S-Webs have more or less shared shear force greater than the average value. This means that it is not safe or even dangerous to design according to all webs bearing the average shear force.
 - (2) When calculating the shear-increased coefficient η using a three-dimensional model, the end diaphragm must be built and included in the three-dimensional model; within the range of thicknesses commonly used for end diaphragms, that is, in the range of 1.0~1.5 m, the shear-increased coefficient η of the S-Webs is not obvious.
 - (3) Support conditions have an obvious influence on the shear distribution. The less support corresponds to the greater shear-increased coefficient η . In the model SPT-2, the shear-increased coefficient η of the S-Webs reaches 1.64. In addition, the number of the chambers is also an important factor affecting the coefficient



(a)



(b)

FIGURE 17: Shear-increased coefficient η of webs in section 9 with load. (a) Shear-increased coefficient η of webs (load: 0~70500 kN). (b) Shear-increased coefficient η of webs (load: 10000~20000 kN).

η , and the irregularity of the shear distribution increases with the chamber number of the girder; the coefficient η of the S-Webs even reaches 1.65 in model CHB-5.

- (4) The change in web thickness has little effect on the shear distribution of the box girder.
- (iii) Nonlinear analysis shows that in the elastic phase, shear-increased coefficient η basically does not change, the coefficient η value of each web changes with the degree of web cracking in the cracking stage, and S-Webs reach the ultimate load first.

- (iv) The concept of the shear-increased coefficient η of the web was proposed, and the method to adjust the S-Web thickness according to the calculation result of η_0 was introduced, which basically makes the shear forces of each web simultaneously reach their shear resistance; thus, the advanced shear failure in webs is prevented.

Data Availability

The data used to support the findings of this study are available from the corresponding author upon request.

Conflicts of Interest

The authors declare that there are no conflicts of interest regarding the publication of this paper.

Acknowledgments

The authors acknowledge the financial support from the project of the National Key R&D Program of China (grant nos. 2018YFC0809600 and 2018YFC0809606) and the MOE Key Lab of Disaster Forecast and Control in Engineering of Jinan University (grant no. 20180930004).

References

- [1] G. P. Zhou, A. Q. Li, J. H. Li, M. Duan, B. F. Spencer, and L. Zhu, "Beam finite element including shear lag effect of extra-wide concrete box girders," *Journal of Bridge Engineering*, vol. 20, no. 11, 2018.
- [2] F. Gara, G. Ranzi, and G. Leoni, "Simplified method of analysis accounting for shear-lag effects in composite bridge decks," *Journal of Constructional Steel Research*, vol. 67, no. 10, pp. 1684–1697, 2011.
- [3] F. Gara, G. Ranzi, and G. Leoni, "Partial interaction analysis with shear-lag effects of composite bridges: a finite element implementation for design applications," *Advanced Steel Construction*, vol. 7, no. 1, pp. 1–16, 2011.
- [4] L. H. Reginato, J. L. P. Tamayo, and I. B. Morsch, "Finite element study of effective width in steel-concrete composite beams under long-term service loads," *Latin American Journal of Solids and Structures*, vol. 15, no. 8, 2018.
- [5] P. F. Boules, S. S. F. Sameh, and M. M. Bakhoum, "Shear lag effects on wide U-section pre-stressed concrete light rail bridges," *Structural Engineering and Mechanics*, vol. 68, no. 1, 2018.
- [6] I. Mohseni, Y. K. Cho, and J. Kang, "Live load distribution factors for skew stringer bridges with high-performance-steel girders under truck loads," *Applied Science*, vol. 8, no. 10, p. 1717, 2018.
- [7] A. A. Semendary, E. P. Steinberg, K. K. Walsh, and E. Barnard, "Live-load moment-distribution factors for an adjacent precast prestressed concrete box beam bridge with reinforced UHPC shear key connections," *Journal of Bridge Engineering*, vol. 22, no. 11, article 04017088, 2017.
- [8] E. Hughs and R. Idriss, "Live-load distribution factors for prestressed concrete, spread box-girder bridge," *Journal of Bridge Engineering*, vol. 11, no. 5, pp. 573–581, 2006.
- [9] X. Y. Li, "Numerical analysis and simplified calculation on shearing performance of box bridge," Thesis, Tongji University, Shanghai, China, 2007.
- [10] F. Zhi, "Experimental studies of the shear strength and size effect of reinforced concrete thin-walled box girders," *China Civil Engineering Journal*, vol. 45, no. 7, 2012.
- [11] Q. Ding, "Research on the shear resistance of box girder and the shear distribution of web," Thesis, Chang'an University, Xi'an, China, 2012.
- [12] Z. Zheng and J. Guo, "A computer method of calculating the transversal internal force in box girder bridge," *Journal of Fuzhou University*, vol. 3, no. 1, 1995.
- [13] S. S. Wu, "Experimental research and spatial mechanics behavior analysis of wide box girder," Thesis, Chongqing Jiaotong University, Chongqing, China, 2011.
- [14] W. Zhang, "Research and application of the grillage method used on multi-room wide girder bridge," Thesis, Wuhan University of Technology, Wuhan, China, 2014.
- [15] X. W. Xue, J. L. Zhou, X. D. Hua, and H. Li, "Analysis of the generating and influencing factors of vertical cracking in abutments during construction," *Advances in Materials Science and Engineering*, vol. 2018, Article ID 1907360, 13 pages, 2018.
- [16] J. Y. Lu, L. N. Yan, Y. Tang, and H.-H. Wang, "Study on seismic performance of a stiffened steel plate shear wall with slits," *Shock and Vibration*, vol. 2015, Article ID 689373, 16 pages, 2015.
- [17] S. J. Choi, S. W. Lee, and J. H. J. Kim, "Impact or blast induced fire simulation of bi-directional PSC panel considering concrete confinement and spalling effect," *Engineering Structures*, vol. 149, pp. 113–130, 2017.
- [18] M. Soltani, X. An, and K. Maekawa, "Computational model for post cracking analysis of RC membrane elements based on local stress-strain characteristics," *Engineering Structures*, vol. 25, no. 8, pp. 993–1007, 2003.
- [19] F. J. Vecchio, D. Lai, W. Shim, and J. Ng, "Disturbed stress field model for reinforced concrete: validation," *Journal of Structural Engineering*, vol. 127, no. 4, pp. 350–358, 2001.
- [20] R. Cerioni, I. Iori, E. Michelini, and P. Bernardi, "Multi-directional modeling of crack pattern in 2D R/C members," *Engineering Fracture Mechanics*, vol. 75, no. 3-4, pp. 615–628, 2008.
- [21] Y. J. Li and T. Zimmerman, "Numerical evaluation of the rotating crack model," *Computers & Structures*, vol. 69, no. 4, pp. 487–497, 1998.
- [22] C. Balkaya and E. Kalkan, "Nonlinear seismic response evaluation of tunnel form building structures," *Computers & Structures*, vol. 81, no. 3, pp. 153–165, 2003.
- [23] C. Balkaya and E. Kalkan, "Three-dimensional effects on openings of laterally loaded pierced shear walls," *Journal of Structural Engineering*, vol. 130, no. 10, pp. 1506–1514, 2004.

Research Article

Mechanical Properties Optimization of Friction Stir Welded Lap Joints in Aluminium Alloy

Antonio Viscusi , Antonello Astarita , and Umberto Prisco 

Department of Chemical, Materials and Production Engineering, University of Napoli Federico II, Piazzale Tecchio 80, 80125 Napoli, Italy

Correspondence should be addressed to Umberto Prisco; umberto.prisco@unina.it

Received 7 November 2018; Revised 18 January 2019; Accepted 28 January 2019; Published 17 February 2019

Guest Editor: Dariusz Rozumek

Copyright © 2019 Antonio Viscusi et al. This is an open access article distributed under the Creative Commons Attribution License, which permits unrestricted use, distribution, and reproduction in any medium, provided the original work is properly cited.

This work focuses on the influence of the rotational and travel speed on the strength of AA 2024 T3 friction stir welded lap joints. Tensile tests were carried out on minispecimens extracted from different welding zones. A central composite design was applied to identify the relative importance of the variable factors' effects and their interaction on yield/ultimate strength and elongation for both the heat affected-zone (HAZ) and nugget zone. Surface methods and gradient algorithms were used to optimize the yield strength of the joints. Shear and microhardness tests were executed to achieve a more complete mechanical characterization.

1. Introduction

The feasibility of replacing the riveting process with friction stir welding (FSW) technology in the assembly of fuselage skin-stiffener panels was the objective of several scientific papers in the last decades [1–6]. The potential of FSW to result in significantly lower assembly times and manufacturing costs, yet higher productivity, cannot be overemphasized. However, commercial applications of this process require addressing issues such as strength analysis and design as well as optimizing the manufacturing process parameters for more reliable welds with minimum distortion [7, 8]. One of the many experimental strategies used to determine the process parameters as well as to optimize the process is defined “by trial” and relies on the researcher’s technical and theoretical process knowledge [9]. This strategy consists of a sequential procedure wherein the value of just one parameter among the set of parameters identified in the previous experiment is varied. This specific parameter is the one that mostly influences the process response while keeping fixed the level of the other parameters [10]. Such an approach has at least two disadvantages: it lacks objectivity in determining mathematical relations between process inputs and response variables and it also lacks efficiency and

accuracy in optimizing the surface response through trials [11]. Another experimental strategy is the “one factor per time approach,” wherein the researcher subsequently varies the levels of each factor within its range while keeping fixed at the base level the other factors [12]. Obviously, this approach lacks information about the factors’ interactions, but it enables estimating main factors’ effects. In any event, the one factor per time approach is less accurate and less efficient than the statistical approach [13]. Many studies of experimental strategies prove that the correct experimental strategy for problems involving more than one factor and data points affected by experimental errors must be taken from design of experiments (DOE) techniques if the aim is to remove objective results from experimental data [14]. These techniques allow maximum conclusive information to be drawn from minimum work, time, energy, money, or other limited resources. So, DOE aims to maximize information per run by choosing a reduced number of input sample points. Moreover, it enables developing a robust process, i.e., a process that minimizes the influence of noise variables [15]. Data organized by DOE allow the most powerful use of analysis of variances, since main factor and interaction effects can be estimated to determine their significance. Another considerable advantage of using these techniques

involves combining DOE with response surface methodologies (RSMs), more efficiently to evaluate the effectiveness of investigative trade-offs [16]. One of the most important advantages of using DOE techniques is extrapolation [17]. This property is significant because it allows optimum prediction even if “optimum” lies outside the initial design range, and the number of runs must be reduced to achieve optimum. Good predictive properties allow DOE association with other complex mathematical methods without compromising accuracy and assuring the method of steepest ascent. This method is a viable technique for sequentially moving toward the optimum response [18]. A comprehensive recitation of additional advantages of these DOE techniques is beyond the scope of this paper. Several papers deal with the influence of process parameters on properties of FSW joints [19–22]; in particular, it was adopted a DOE to investigate such influence [23]. From the literature, it is also evident that the main process parameters that need to be investigated are the rotational speed and travel speed [24–26]. In particular, it was proved that the inverse of travel speed measurements was better than travel speed to fit experimental data [27]. Therefore, this study examined the strength of FSW aluminium alloy lap joints in two different welding zones: HAZ and nugget zone. Aiming to test separately the tensile strength of HAZ and nugget zone, minispecimens from both these zones were subjected to shear and microhardness tests. The process parameters optimization issue was approached using central factorial design, response surface methods, and gradient algorithms.

2. Materials and Methods

AA 2024 T3 sheets were used as the bottom and the top sheet of the lap joints. The nominal weight percent composition (major alloying additions) of AA 2024 is 4.4% Cu, 1.5% Mg, 0.6% Mn, and the rest is aluminium. Sheets' thickness is 1.27 mm. The ultimate tensile strength (UTS) of the AA 2024 T3 base metal is 475 MPa. As for the welding process parameters, the inverse of travel speed (TS^{-1}) ranged from 0.155 to 0.533 s/mm and the rotational speed (RS) ranged from 950 to 2222.5 rpm. Plunge depth was fixed to 2.11 mm, tilt angle to zero degree, and travel angle to one degree.

Nine different TS^{-1} -RS combinations were used for obtaining 13 welds in this study; five combinations were derived by 2^2 factorial design with five centre points, and the remaining four combinations were obtained by using the steepest ascent algorithm. One tool configuration equipped with a pin consisting of a threaded frustum of the cone was used; the lower and the upper diameters are 2.77 mm and 5.06 mm, respectively, with a length of 2.03 mm. The shoulder diameter is 12.04 with a concavity of 7° . Two different machines were used to perform FSW lap and overlap joints with single pass. A controlled numerical machine (CNM) was employed to perform the set of runs concerned with the central factorial design featured by high heat generation (hot runs); a vertical milling machine was used to carry out the set of runs concerned with the steepest algorithm featured by low heat generation (cold runs).

Both the top and bottom sheets, 152.40 mm long and 2.54 mm thick, were positioned as shown in Figure 1. Sheets were degreased prior to welding using acetone as a cleaner. After the FSW process, an optical specimen was taken out from each run; microscope observations of the cross sections were carried out to identify the exact position of the welding zones. At the same time, the cross sections of the welds were observed and analysed by image processing software to identify the position of the hook defects and measure the grain size. According to ASTM E 112, the grain size number is determined by using the general intercept method. For this purposes, standard metallographic polishing procedures were used with modified Keller's reagent. Thanks to the aforementioned analyses, it was possible to remove three minitensile specimens from both the nugget and heat-affected zones for each run by using a minimilling machine.

Minitensile testing was carried out by following design of experiments. Figure 2 shows the minitensile specimen drawing with its geometrical dimensions. It is worth to note that smaller is the specimen higher are the mechanical properties recorded; experimental results of minitensile samples refer to local properties of the material which exceed the global ones [28]. Each sample was pulled out from the lap joints; then, it was refined and polished on both sides by using abrasive papers of $30\ \mu\text{m}$ and $12\ \mu\text{m}$ removing exceeding material and leading the thickness from 1 mm to 0.50 mm. Abrasive papers of $9\ \mu\text{m}$ and $3\ \mu\text{m}$ were used to eliminate the surface scratches; finally, a diamond suspension of $1\ \mu\text{m}$ was used to create a like-mirror surface. The waiting time between the welding and the minitensile testing was typically 150 h. The minitensile testing was performed through a minitensile testing machine by imposing a strain rate equal to $10^{-3}\ \text{s}^{-1}$. The ultimate strength, the yield strength, and the elongation of the weld were measured. The last property was evaluated by using the Epsilon ONE optical high-precision extensometer, which is a noncontact device able to measure accurately the strain of this type of minitensile specimen at the narrow section.

The mechanical characterization of the lap joints obtained by FSW technology also included shear testing and microhardness measurements. The strength of the lap joints loaded nominally in overlap shear was examined, even though in this case, 150 h elapsed before shear testing was carried out. All the specimens tested were 25.4 mm wide, 127 mm long, and 2.54 mm thick (Figure 3), manufactured using a shear machine, and ground on both sides by milling. Three specimens for each run were tested, and the failure loads were averaged. All overlap shear tests were performed using the same strain rate used in the tensile testing. The maximum loads (failure loads) were recorded for each specimen. Each weld was sectioned and polished so the hardness could be measured using a digital Vickers hardness tester. The centre of the welds was tested throughout the cross section with 1 mm spacing between data points; all welding zones down to the base material were involved.

As for the experiments design, the central composite design (CCD), able to fit the response surface through a quadratic regression model, was used in this study. CCD contains an embedded factorial or fractional factorial design

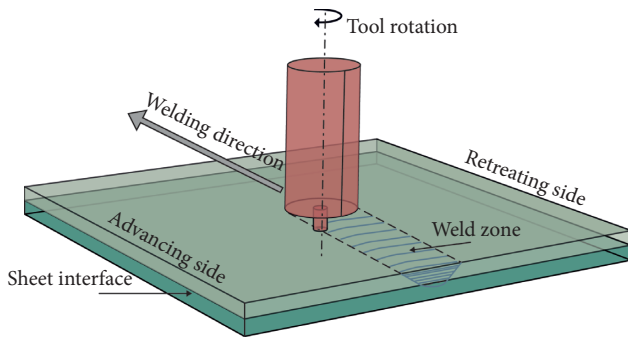


FIGURE 1: Schematic of friction stir welding.

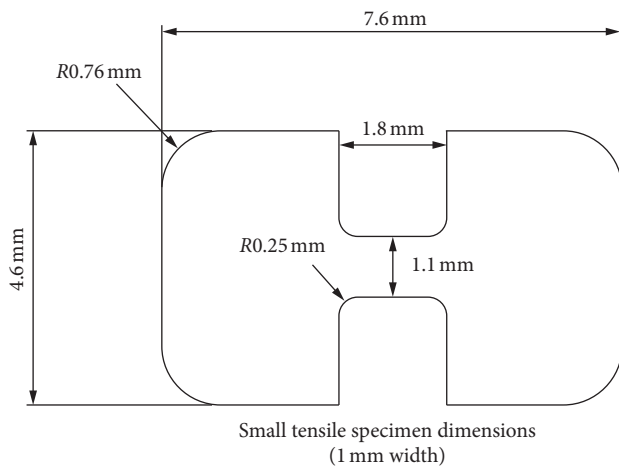


FIGURE 2: Minitensile specimen drawing.

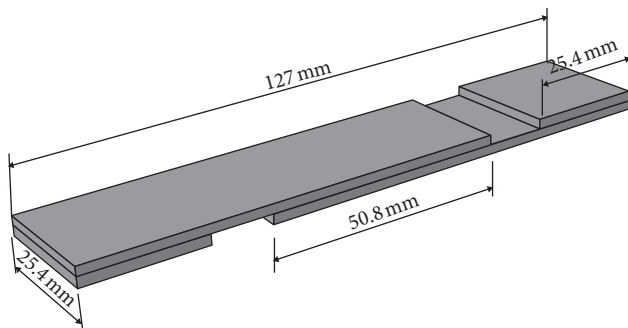


FIGURE 3: Shear specimens drawing.

with centre points that are augmented with a group of “star points.” The importance of the centre points is that they allow for a curvature estimation [29]. The CCD could be implemented more easily with a sequential procedure: firstly, a factorial design with centre points should be performed to estimate the significance of the main factor effects and interaction effects, and above all to prove or to reject the presence of a curvature. Then, if the presence of the curvature is proved, the “star points” procedure can be performed. According to the aforementioned procedure, a 2² factorial design with five centre points and three repeated measurements was carried out to perform tensile testing for the nugget zone and for the heat-affected zone. The experimental table is summarized (Table 1).

TABLE 1: Table data for two factorial designs with five centre points.

Runs order	rpm	s/mm
1	1377.5	0.267
7	2222.5	0.267
6	1377.5	0.533
5	2222.5	0.533
2	1800.0	0.400
3	1800.0	0.400
4	1800.0	0.400
9	1800.0	0.400
8	1800.0	0.400

To avoid systematic errors, the whole set of experiments has been randomized. To perform an ANOVA in every possible case, even in the case of heteroskedasticity of data (i.e., not constant variance), a weighted ANOVA was carried out [30]. Such analysis requires repeated measurements for each run. Experimental data of yield strength, ultimate strength, and elongation are analysed and plotted separately. MINITAB, one of the most common statistical software packages, was used to define the DOE table and to perform a weighted ANOVA as well as residuals analysis. Experiments included repeats of the response, whose measurements allowed variability analysis in response data through a weighted regression. Such a method is suitable for handling data with different variances.

3. Results and Discussion

Experimental data of yield strength are shown in Table 2. An important point is that the column called WGTS_ADJ contains weights, i.e., an estimate of the reciprocal variance of the mean. These weights are due to the analysis of variability that is shown in Table 3. This analysis calculates and stores the standard deviations of the repeated responses detecting differences or dispersion effects across factor settings. This analysis even allows weights to be stored to perform a weighted ANOVA.

This analysis shows that only two effects could be considered significant: rpm with a *p* value of 0.094 and the inverse of the travel speed with a *p* value of 0.055; the interaction effect seems not to be noticeable. Neither curvature could be considered significant. The weighted ANOVA related to the experimental data of yield strength is shown in Table 4. The regression model has been reduced by removing the interaction effect since a previous analysis proved its negligibility; in fact, the value of *F* related to the interaction effect is 0.09 corresponding to a *p* value of 0.782.

The analysis shows a curvature *p* value of 0.145 that cannot be able to prove its presence and a main effect *p* value of 0.040 that ensures a significant influence; specifically, the *p* value related to rpm is 0.0045, and the *p* value related to TS⁻¹ is 0.0055. Both the values can be considered significant. Regression model coefficients are estimated as shown in Table 4. Aiming to prove the model adequacy, residuals analysis was performed that is not here reported for the sake of brevity. Such an analysis verified the hypothesis made on the residuals; i.e., residuals can be assumed to be normally

TABLE 2: Yield strength experimental responses.

rpm	s/mm	Ys1	Ys2	Ys3	Ys4	Std. Ys	Dim	Avg. Ys	WGTS_ADJ
1377.5	0.267	372	365	353	—	9.609	3	363.333	0.0390
2222.5	0.267	361	323	356	—	20.648	3	346.667	0.0084
1377.5	0.533	349	319	368	—	24.705	3	345.333	0.0059
2222.5	0.533	402	345	249	343	63.373	4	334.750	0.0011
1800.0	0.400	353	356	326	—	16.523	3	345.000	0.0063
1800.0	0.400	356	374	320	—	27.495	3	350.000	0.0063
1800.0	0.400	360	366	348	—	9.165	3	358.000	0.0063
1800.0	0.400	342	357	397	338	26.938	4	358.500	0.0084
1800.0	0.400	355	343	392	—	25.541	3	363.333	0.0063

TABLE 3: Results of yield strength analysis of variability.

Regression estimated effects and coefficients for natural log of std. Ys ratio (coded units)							
Term	Effect	Effect	Coef.	SE coef.	<i>T</i>	<i>p</i>	
Constant	—	—	3.0796	0.1407	21.89	0.0	
rpm	0.8733	2.395	0.4367	0.2118	2.06	0.094	
s/mm	1.0527	2.865	0.5264	0.2118	2.49	0.055	
rpm * s/mm	0.1084	1.115	0.0542	0.2118	0.26	0.808	
$R^2 = 72.04\%$			$R^2(\text{adj}) = 55.26\%$				
Analysis of variance for natural log of std. Ys							
Source	DF	Seq. SS	Adj. SS	Adj. MS	<i>F</i>	<i>p</i>	
Main effects	2	6.319	5.900	2.950	5.981	0.047	
2-Way interactions	1	0.032	0.032	0.032	0.070	0.808	
Residual error	5	2.465	2.465	0.493	—	—	
Curvature	1	0.130	0.130	0.130	0.222	0.661	
Pure error	4	2.335	2.335	0.583	—	—	
Total	8	8.816	—	—	—	—	

TABLE 4: Results of yield strength weighted analysis of variance.

Estimated effects and coefficients for avg. Ys (coded units)							
Term	Effect	Coef.	SE coef.	<i>T</i>	<i>p</i>		
Constant	—	346.718	3.953	87.71	0.0		
rpm	-15.948	-7.974	3.004	-2.65	0.0045		
s/mm	-17.026	-8.513	3.413	-2.49	0.0055		
Ct Pt	—	8.469	4.903	1.73	0.45		
$S = 0.533470$		$R^2 = 73.27\%$		$R^2(\text{adj}) = 57.24\%$			
Analysis of variance for avg. Ys (coded units)							
Source	DF	Seq. SS	Adj. SS	Adj. MS	<i>F</i>	<i>p</i>	
Main effects	2	3.051	3.709	1.855	6.52	0.040	
Curvature	1	0.849	0.850	0.850	2.98	0.145	
Residual error	5	1.423	1.422	0.285	—	—	
Lack of fit	1	0.031	0.030	0.030	0.09	0.782	
Pure error	4	1.393	1.392	0.348	—	—	
Total	8	5.327	—	—	—	—	
Estimated coefficients for avg. Ys using data in uncoded units							
Term	Coef.						
Constant	406.30						
rpm	-0.019						
s/mm	-64.01						
Ct Pt	8.47						

distributed with null average and constant standard deviation. Moreover, the regression model fits the data very well since the high *p* value related to the lack of fit (0.782) is just a consequence of the interaction term omission. Experimental data of ultimate strength are shown in Table 5. The analysis of variability related to the experimental data of ultimate strength is shown in Table 6.

It can be seen that only two effects could be considered significant: rpm with a *p* value of 0.059 and the inverse of the travel speed with a *p* value of 0.006; the interaction effect seems not to be noticeable. Either curvature could be considered significant. The weighted ANOVA related to the experimental data of ultimate strength is shown in Table 7. The regression model presented has been reduced by

TABLE 5: Ultimate strength experimental responses.

rpm	s/mm	Us1	Us2	Us3	Us4	Std. US	Dim	Avg. US	WGTS_ADJ
1377.5	0.267	502.0	480.0	484.0	—	11.719	3	488.667	0.0324
2222.5	0.267	431.0	432.5	460.2	—	16.443	3	441.233	0.0081
1377.5	0.533	444.6	419.5	478.0	—	29.348	3	447.367	0.0026
2222.5	0.533	435.6	452.0	285.0	392	75.160	4	391.150	0.0008
1800.0	0.400	491.0	501.4	449.0	—	27.743	3	480.467	0.0046
1800.0	0.400	496.6	492.5	428.6	—	38.131	3	472.567	0.0046
1800.0	0.400	456.0	485.7	483.3	—	16.498	3	475.000	0.0046
1800.0	0.400	475.7	451.8	494.0	—	21.162	3	473.833	0.0046
1800.0	0.400	472.0	466.8	514.0	—	25.881	3	484.267	0.0046

TABLE 6: Results of ultimate strength analysis of variability.

Regression estimated effects and coefficients for natural log of std. US ratio (coded units)						
Term	Effect	Effect	Coef.	SE coef.	<i>T</i>	<i>p</i>
Constant	—	—	3.2266	0.0909	35.48	0.0
rpm	0.6428	1.902	0.3214	0.1317	2.44	0.059
s/mm	1.2221	3.394	0.6111	0.1317	6.64	0.006
rpm * s/mm	0.3041	1.355	0.1520	0.1317	1.15	0.301
	$R^2 = 87.80\%$		$R^2(\text{adj}) = 80.48\%$			
Analysis of variance for natural log of std. US						
Source	DF	Seq. SS	Adj. SS	Adj. MS	<i>F</i>	<i>p</i>
Main effects	2	6.6109	5.8970	2.9485	15.46	0.007
2-Way interactions	1	0.2540	0.2540	0.2540	1.33	0.301
Residual error	5	0.9537	0.9537	0.1907	—	—
Curvature	1	0.0037	0.0037	0.0037	0.02	0.907
Pure error	4	0.9500	0.9500	0.2375	—	—
Total	8	7.8187	—	—	—	—

TABLE 7: Results of ultimate strength weighted analysis of variance.

Estimated effects and coefficients for avg. US (coded units)						
Term	Effect	Coef.	SE coef.	<i>T</i>	<i>p</i>	
Constant	—	442.97	2.973	148.99	0.0	
rpm	-48.23	-24.12	1.860	-12.96	0.0	
s/mm	-43.49	-21.75	2.798	-7.77	0.001	
Ct Pt	—	34.26	3.629	9.44	0.0	
	$S = 0.3170$	$R^2 = 97.93\%$	$R^2(\text{adj}) = 96.68\%$			
Analysis of variance for avg. US (coded units)						
Source	DF	Seq. SS	Adj. SS	Adj. MS	<i>F</i>	<i>p</i>
Main effects	2	14.7680	23.677	11.838	117.76	0.0
Curvature	1	8.9605	8.9605	8.9605	89.13	0.0
Residual error	5	0.5027	0.5027	0.1005	—	—
Lack of fit	1	0.0464	0.0464	0.0464	0.41	0.558
Pure error	4	0.4563	0.4563	0.1141	—	—
Total	8	24.2317	—	—	—	—
Estimated coefficients for avg. US using data in uncoded units						
Term	Coef.					
Constant	611.11					
rpm	-0.057					
s/mm	-163.52					
Ct Pt	34.26					

removing the interaction effect since a previous analysis proved its negligibility. In fact, the value of *F* related to the interaction effect is 0.41 corresponding to a *p* value of 0.558.

The analysis shows a significant curvature *p* value, whose value is less than 0.001, a main effect *p* value less than 0.001 ensuring a huge significant influence; specifically, the *p* value related to rpm is less than 0.001 and the *p* value related to

TS^{-1} is 0.001. Both the effects can be considered very significant. Regression model coefficients are estimated as shown in Table 7. It was also performed a residuals analysis that seems to verify the hypothesis made on the residuals, so they can be assumed to be normally distributed with null average and constant standard deviation. By the way, the regression model cannot fit well the data, even if the *p* value

related to the lack of fit is very high, since the adopted design cannot allow second-order estimate effects being significant in this case.

As for the nugget zone, a 2^2 factorial design with two centre points and three repeated measurements was carried out for the elongation. Experimental data of yield strength are shown in Table 8.

In this case, a simple ANOVA was carried out since the analysis of variability did not show any significant effect. Reliance on this consideration would deem the weights negligible. The ANOVA related to the experimental data of elongation is shown in Table 9.

The analysis shows a curvature p value of 0.070 that proves its presence; the main effect p value is 0.051; specifically, the p value related to rpm is 0.037 which is significant. The p value related to TS^{-1} is 0.198, which is not significant. The residuals can be assumed to be normally distributed, with null average and constant standard deviation. An important point is that the high p value related to the curvature proves even a lack of fit of the regression model. Looking data of ultimate strength, yield strength, and elongation relative of the analysis of variance, it can be seen that the influence effects are not significant.

Regarding the optimization of the response surface related to the yield strength, which is the main mechanical property of interest, an algorithm of steepest ascent to the yield strength response of the nugget zone was proposed. Assuming that $x_1 = x_2 = \dots = x_k = 0$, where $i = 1, 2, \dots, k$ identifies the factors and $[-1; 0; 1]$ are the coded variables identifying the lower, the centre, and the upper level of the factors, respectively, the algorithm procedure can be described according to the following procedure: defining the step length for one of the process variables and the step length of the other variables can be defined by using equation (1). Finally, turning the step length Δx_i from the coded variable into natural variables.

This algorithm can be applied only when the regression model is of the first order and does not include interactions. Runs obtained by implementing the aforementioned algorithm are shown in Table 10:

$$\Delta x_i = \frac{\beta_i}{\beta_j \Delta x_j}, \quad \text{with } i = 1, 2, \dots, k, \quad i \neq j. \quad (1)$$

The results are similar to those expected, and this ascertainment guarantees the reliability of the previous analysis. The average of the yield strength has increased from a value of 363.33 MPa (point: 1377.5 rpm; 0.267 s/mm) to values of 399.25 MPa (point: 1250 rpm; 0.241 s/mm) and 395.8 MPa (point: 1150 rpm; 0.213 s/mm). The region where the two last points are set is the optimum region; a new investigation using a central composite design would have been necessary to determine the exact position of the yield strength optimum point. Following the next steps of the steepest path, the yield strength decreases, which suggests that the steepest path is leaving from the optimum region. A similar behaviour is acted also by the ultimate strength, but steepest yield strength of the nugget zone path is even one of the improvement directions of yield and ultimate strength of

TABLE 8: Elongation experimental responses.

rpm	s/mm	El1	El2	El3	Std. El	Dim	Avg. El
1377.5	0.267	31.5	30.5	32.0	0.764	3	31.333
2222.5	0.267	9.0	9.0	15.0	3.464	3	11.000
1377.5	0.533	23.0	30.5	27.5	3.775	3	27.000
2222.5	0.533	11.5	4.5	9.0	3.547	3	8.333
1800.0	0.400	33.6	25.0	32.0	4.574	3	30.200
1800.0	0.400	26.0	28.0	31.0	2.517	3	28.333

the heat-affected zone. Seemingly, the mechanical properties of the HAZ improve markedly when the process gets colder and colder.

As for the shear testing, the results showed averaged failure loads, since three specimens were tested for each run. In Table 11, a summary of averaged failure loads is presented.

According to the tensile testing results, the runs corresponding to the first two steepest ascent algorithms show the best performances for yield strength, especially the run (1150 rpm; 0.213 s/mm) which had an averaged failure load of 10125.16 N. Those failures occur always in the nugget zone explaining the correlation between tensile and shear testing.

Vickers microhardness measurements, which were carried out from the centre of the welding along the cross section passing through HAZ, TMAZ, and nugget zone, are shown in Figure 4.

The results reveal a switch of the best mechanical behaviour zones, from welds showing better hardness performances in the nugget zone to welds showing better hardness performances in the HAZ. Looking at the welds carried out by setting rpm equal to 1050 and TS^{-1} equal to 0.184 s/mm and the ones obtained with rpm equal to 1150 and TS^{-1} equal to 0.213 s/mm (Figure 4), the switch in hardness performances confirms the results already obtained with tensile testing. In fact, as well as tensile testing has held up when the runs get very cold (namely, the following runs: rpm = 950; $TS^{-1} = 0.155$ s/mm, rpm = 1050; $TS^{-1} = 0.184$ s/mm), improved mechanical behaviour in the HAZ exceeds nugget zone performance. Thus, microhardness testing confirms the same trend of tensile testing.

Optical investigations included the study of the oxide film; this kind of defect, which is a feature for friction stir welding technology, is commonly called hook defect because of its shape. Hook defects must be taken seriously since they represent cross-section thinning, and for this reason, they may explain shear testing results [31]. Hook's distances are shown in Table 12.

This study does not contain statistical evidence for hook's distance and shear tests correlation; in fact, a linear regression analysis showed a very low coefficient of determination ($R^2 = 0.102$ and $R^2(\text{adj}) = 0$) and a very high ANOVA p value ($F = 0.68$; p value = 0.44).

As for the grain size number of the nugget zone, the results are shown in Table 13.

It can be seen a decrease in grain size for runs featured by high heat generation. A regression analysis between grain size estimates and heat index was carried out as proof. Heat index is considered as a measurement of heat

TABLE 9: Results of elongation analysis of variance (nugget zone).

Estimated effects and coefficients for avg. El (coded units)						
Term	Effect	Coef.	SE coef.	T	p	
Constant	—	19.417	0.5612	34.60	0.018	
rpm	-19.500	-9.750	0.5612	-17.37	0.037	
s/mm	-3.500	-1.750	0.5612	-3.12	0.198	
rpm * s/mm	0.833	0.417	0.5612	0.74	0.593	
Ct Pt	—	9.850	1.089	9.04	0.070	
S = 0.619324		R ² = 99.82%	R ² (adj) = 99.09%			
Analysis of variance for avg. El (coded units)						
Source	DF	Seq. SS	Adj. SS	Adj. MS	F	p
Main effects	2	179.25	149.80	74.90	195.26	0.051
2-Way interactions	1	0.256	0.211	0.211	0.55	0.593
Curvature	1	31.37	31.37	31.37	81.80	0.070
Residual error	1	0.384	0.384	0.384	—	—
Pure error	1	0.384	0.384	0.84	—	—
Total	5	211.26	—	—	—	—
Estimated coefficients for avg. El using data in uncoded units						
Term	Coef.					
Constant	71.56					
rpm	-0.026					
s/mm	-23.51					
rpm * s/mm	0.0074					
Ct Pt	9.85					

TABLE 10: Yield strength, ultimate strength, and elongation experimental responses performed along the steepest ascent direction (summarized data for nugget and HAZ).

rpm	s/mm	Avg. YS	Avg. US	Avg. El
<i>Nugget</i>				
1250	0.241	399.25	511.8	28.75
1150	0.213	395.8	507.9	26.36
1050	0.184	339.33	453	25.25
950	0.155	368.67	475.6	25.23
<i>HAZ</i>				
1250	0.241	370	482.3	19.8
1150	0.213	368	474.5	20.17
1050	0.184	386	491	21.4
950	0.155	405.7	506.25	21.45

TABLE 11: Shear testing results of averaged failure loads.

rpm	s/mm	Shear testing results (N)
950	0.155	7433.596
1050	0.184	7531.358
1150	0.213	10125.16
1250	0.241	8394.355
1377.5	0.533	5708.624
1377.5	0.267	7768.978
1800	0.25	7001.34
2222.5	0.533	6682.956
2222.5	0.267	4074.074

generated during welding, as the higher the index, the higher is the heat generated. It was defined by using the following equation:

$$HI = \frac{rpm^2}{(\text{inch}/\text{min}) \times 10000} \quad (2)$$

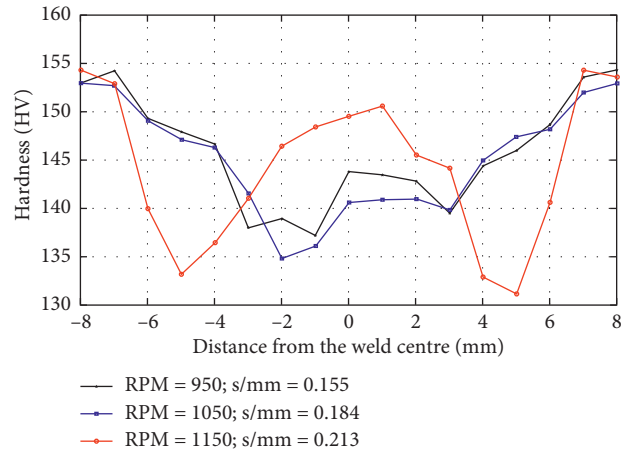


FIGURE 4: Vickers microhardness measurement results.

TABLE 12: Minimum hook distances measured on advancing (AS) and retreating (RS).

rpm	s/mm	Loaded AS thickness (mm)	Loaded RS thickness (mm)
950	0.155	0.12	0.12
1050	0.184	0.11	0.12
1150	0.213	0.114	0.116
1250	0.241	0.09	0.12
1377.5	0.533	0.074	0.12
1377.5	0.267	0.032	0.12
2222.5	0.533	0.044	0.12
2222.5	0.267	0.08	0.12

The coefficient of determination presented a high value ($R^2 = 0.68$, $R^2(\text{adj}) = 0.63$), which suggests a good correlation between the two parameters, as well the analysis of variance as

TABLE 13: ASTM grains size number versus heat index regression.

rpm	s/mm	G	HI
950	0.155	8.54	5.710
1050	0.184	8.60	8.350
1150	0.213	8.66	11.664
1250	0.241	8.72	15.749
1377.5	0.267	8.78	42.841
1377.5	0.533	8.84	21.421
1800	0.25	8.90	54.864
2222.5	0.267	8.96	55.762

proof of a significant influence of the heat index on grain size showing a p value of 0.012. In other words, these analyses seem to ensure this assertion: “As big is the heat generation as big is the grain size in the Nugget Zone.” The mechanical behaviour of the welds is explained by regression analysis between hardness Vickers tests and grain size. Such an analysis revealed a lack of correlation between the two properties, thus disagreeing with the Hall–Petch rule. So, the causes of the mechanical behaviour should be found in the differences of the weld microstructure; i.e., different temporal thermal profiles produce different precipitate compositions, where some are more hardened than others [22, 32, 33].

4. Conclusions

In this study, a procedure to optimize the mechanical behaviour of friction stir welded joints was developed. The yield strength was chosen as a factor of interest, and its response was optimized by using a response surface method. This method, which consisted of a central composite design and a subsequent steepest ascent algorithm, provided for optimal yield strength surface. Tensile tests on base metal specimens were conducted with benchmarking measures obtained from processed samples proving the high performance of FSW technology. The best performances, which were evaluated choosing the minimum value between HAZ and nugget zone ratio for both yield and ultimate strength, were found under these welding conditions: rpm = 1250 and $TS^{-1} = 0.241$ s/mm. Shear testing confirmed the results provided by tensile tests. Hook’s defect was studied, and the grain size of the nugget zone was estimated.

Data Availability

The data used to support the findings of this study are included within the article.

Conflicts of Interest

The authors declare that they have no conflicts of interest.

References

- [1] V. M. Magalhães, C. Leitão, and D. M. Rodrigues, “Friction stir welding industrialisation and research status,” *Science and Technology of Welding and Joining*, vol. 23, no. 5, pp. 400–409, 2017.
- [2] X. Liu, S. Lan, and J. Ni, “Analysis of process parameters effects on friction stir welding of dissimilar aluminum alloy to advanced high strength steel,” *Materials & Design*, vol. 59, pp. 50–62, 2014.
- [3] R. Nandan, T. Debroy, and H. Bhadeshia, “Recent advances in friction-stir welding-process, weldment structure and properties,” *Progress in Materials Science*, vol. 53, no. 6, pp. 980–1023, 2008.
- [4] Y. S. Sato, M. Urata, and H. Kokawa, “Parameters controlling microstructure and hardness during friction-stir welding of precipitation-hardenable aluminum alloy 6063,” *Metallurgical and Materials Transactions A*, vol. 33, no. 3, pp. 625–635, 2002.
- [5] A. Ali, M. W. Brown, C. A. Rodopoulos, and S. Gardiner, “Characterization of 2024-T351 friction stir welding joints,” *Journal of Failure Analysis and Prevention*, vol. 6, no. 4, pp. 83–96, 2006.
- [6] M. W. Mahoney, C. G. Rhodes, J. G. Flintoff, W. H. Bingel, and R. A. Spurling, “Properties of friction-stir-welded 7075 T651 aluminum,” *Metallurgical and Materials Transactions A*, vol. 29, no. 7, pp. 1955–1964, 1998.
- [7] R. Nandan, G. G. Roy, T. J. Lienert, and T. Debroy, “Three-dimensional heat and material flow during friction stir welding of mild steel,” *Acta Materialia*, vol. 55, no. 3, pp. 883–895, 2007.
- [8] H. J. Liu, H. Fujii, M. Maeda, and K. Nogi, “Tensile properties and fracture locations of friction-stir-welded joints of 2017-T351 aluminum alloy,” *Journal of Materials Processing Technology*, vol. 142, no. 3, pp. 692–696, 2003.
- [9] R. F. Gunst, “Response surface methodology: process and product optimization using designed experiments,” *Technometrics*, vol. 38, no. 3, pp. 284–286, 1996.
- [10] J. Antony, “Simultaneous optimisation of multiple quality characteristics in manufacturing processes using taguchi’s quality loss function,” *International Journal of Advanced Manufacturing Technology*, vol. 17, no. 2, pp. 134–138, 2001.
- [11] T. V. Sibalija and V. D. Majstorovic, “An integrated approach to optimise parameter design of multi-response processes based on Taguchi method and artificial intelligence,” *Journal of Intelligent Manufacturing*, vol. 23, no. 5, pp. 1511–1528, 2010.
- [12] M. J. Anderson, “A new method for non-parametric multivariate analysis of variance,” *Austral Ecology*, vol. 26, no. 1, pp. 32–46, 2001.
- [13] W. B. Schaufeli, M. Salanova, V. González-romá, and A. B. Bakker, “The measurement of engagement and burnout: a two sample confirmatory factor analytic approach,” *Journal of Happiness Studies*, vol. 3, no. 1, pp. 71–92, 2002.
- [14] N. Alagumurthi, K. Palaniradja, and V. Soundararajan, “Optimization of grinding process through design of experiment (DOE)-a comparative study,” *Materials and Manufacturing Processes*, vol. 21, no. 1, pp. 19–21, 2006.
- [15] W. Chen, J. K. Allen, K.-L. Tsui, and F. Mistree, “A procedure for robust design: minimizing variations caused by noise factors and control factors,” *Journal of Mechanical Design*, vol. 118, no. 4, p. 478, 1996.
- [16] G. Vicente, A. Coteron, M. Martinez, and J. Aracil, “Application of the factorial design of experiments and response surface methodology to optimize biodiesel production,” *Industrial Crops and Products*, vol. 8, no. 1, pp. 29–35, 1998.
- [17] B. K. Rout and R. K. Mittal, “Parametric design optimization of 2-DOF R-R planar manipulator-A design of experiment approach,” *Robotics and Computer-Integrated Manufacturing*, vol. 24, no. 2, pp. 239–248, 2008.

- [18] A. E. Bryson and W. F. Denham, "A steepest-ascent method for solving optimum programming problems," *Journal of Applied Mechanics*, vol. 29, no. 2, p. 247, 1962.
- [19] M. Jones, P. Heurtier, C. Desrayaud, F. Montheillet, D. Allehaux, and J. Driver, "Correlation between microstructure and microhardness in a friction stir welded 2024 aluminium alloy," *Scripta Materialia*, vol. 52, no. 8, pp. 693–697, 2005.
- [20] G. Liu, L. E. Murr, C.-S. Niou, J. C. McClure, and F. R. Vega, "Microstructural aspects of the friction-stir welding of 6061-T6 aluminum," *Scripta Materialia*, vol. 37, no. 3, pp. 355–361, 1997.
- [21] G. D'Urso and C. Giardini, "The influence of process parameters and tool geometry on mechanical properties of friction stir welded aluminum lap joints," *International Journal of Material Forming*, vol. 3, no. 1, pp. 1011–1014, 2010.
- [22] Y. S. Sato, M. Urata, H. Kokawa, and K. Ikeda, "Hall-Petch relationship in friction stir welds of equal channel angular-pressed aluminium alloys," *Materials Science and Engineering: A*, vol. 354, no. 1-2, pp. 298–305, 2003.
- [23] P. M. G. P. Moreira, T. Santos, S. M. O. Tavares, V. Richter-Trummer, P. Vilaça, and P. M. S. T. de Castro, "Mechanical and metallurgical characterization of friction stir welding joints of AA6061-T6 with AA6082-T6," *Materials & Design*, vol. 30, no. 1, pp. 180–187, 2009.
- [24] L. Commin, M. Dumont, J.-E. Masse, and L. Barrallier, "Friction stir welding of AZ31 magnesium alloy rolled sheets: influence of processing parameters," *Acta Materialia*, vol. 57, no. 2, pp. 326–334, 2009.
- [25] W. Zhang, Y. Shen, Y. Yan, and R. Guo, "Dissimilar friction stir welding of 6061 Al to T2 pure Cu adopting tooth-shaped joint configuration: microstructure and mechanical properties," *Materials Science and Engineering: A*, vol. 690, pp. 355–364, 2017.
- [26] R. S. Mishra and Z. Y. Ma, "Friction stir welding and processing," *Materials Science and Engineering: R: Reports*, vol. 50, no. 1-2, pp. 1–78, 2005.
- [27] A. Murphy, M. Price, R. Curran, and P. Wang, "Integration of strength and process modeling of friction-stir-welded fuselage panels," *Journal of Aerospace Computing, Information, and Communication*, vol. 3, no. 4, pp. 159–176, 2006.
- [28] A. V. Sergueeva, J. Zhou, B. E. Meacham, and D. J. Branagan, "Gage length and sample size effect on measured properties during tensile testing," *Materials Science and Engineering: A*, vol. 526, no. 1-2, pp. 79–83, 2009.
- [29] M. Ahmadi, F. Vahabzadeh, B. Bonakdarpour, E. Mofarrah, and M. Mehranian, "Application of the central composite design and response surface methodology to the advanced treatment of olive oil processing wastewater using Fenton's peroxidation," *Journal of Hazardous Materials*, vol. 123, no. 1–3, pp. 187–195, 2005.
- [30] W. S. Cleveland and S. J. Devlin, "Locally weighted regression: an approach to regression analysis by local fitting," *Journal of the American Statistical Association*, vol. 83, no. 403, pp. 596–610, 1988.
- [31] W. Li, J. Li, Z. Zhang, D. Gao, W. Wang, and C. Dong, "Improving mechanical properties of pinless friction stir spot welded joints by eliminating hook defect," *Materials & Design (1980–2015)*, vol. 62, pp. 247–254, 2014.
- [32] N. Dialami, M. Chiumenti, M. Cervera, and C. Agelet de Saracibar, "Challenges in thermo-mechanical analysis of friction stir welding processes," *Archives of Computational Methods in Engineering*, vol. 24, no. 1, pp. 189–225, 2016.
- [33] M. M. Attallah, C. L. Davis, and M. Strangwood, "Microstructure-microhardness relationships in friction stir welded AA5251," *Journal of Materials Science*, vol. 42, no. 17, pp. 7299–7306, 2007.

Research Article

Prediction of Fatigue Life of Welded Joints Made of Fine-Grained Martensite-Bainitic S960QL Steel and Determination of Crack Origins

Tomasz Ślęzak 

Military University of Technology, Faculty of Mechanical Engineering, Institute of Machine Building, Ul. Gen. W. Urbanowicza 2, 00-908 Warsaw, Poland

Correspondence should be addressed to Tomasz Ślęzak; tomasz.slezak@wat.edu.pl

Received 23 November 2018; Accepted 16 January 2019; Published 4 February 2019

Guest Editor: Dariusz Rozumek

Copyright © 2019 Tomasz Ślęzak. This is an open access article distributed under the Creative Commons Attribution License, which permits unrestricted use, distribution, and reproduction in any medium, provided the original work is properly cited.

Due to growing requirements connected with the utilization of advanced structures, nowadays the modern design processes are developed. One of the crucial issues considered in these processes is proper design of the joints against fatigue in order to fulfill a stated life of operation. In this study, the method of fatigue life prediction based on the criterion of permissible strain range in the notch root is presented. An engaged simplified model of fatigue life prediction was previously developed for mild and carbon steels. The evaluation made during the research has proven that this method can also be used for S960QL high-strength steel characterized by entirely different properties and structure. A considered theoretical model demonstrates satisfactory correlation with experimental data and safely describes the fatigue life of weldments. Furthermore, the predicted fatigue life of studied steel without welds shows great comparability with experimental data. The limit value of the strain range in the notch root was estimated. Below this value of strain, the fatigue life of welded joints is infinite, theoretically. Finally, the impact of the surface imperfections on the fatigue crack initiation was revealed. For paternal material, the origins of cracking were discovered at the places of nonmetallic scale particles. In welded joints, the fatigue cracks initiated at the whole length of the fusion line.

1. Introduction

Individual members of more complex structures are connected to each other in the nodes utilizing different techniques. Design requirements define whether this junction has to be demountable or permanent. The permanent manner of joining is obvious in the case of fabrication of the large and complex structures like bridges and other civil engineering constructions, heavy vehicle frames, pipeline systems, or cranes, exemplary. These types of structures require realization of numerous joints, and the welding is adequate to ensure an optimal efficiency of fabrication with proper finance outcome. The use of welding allows to reduce the thickness of structural elements decreasing the total weight of structure together with the number of employed consumables and finally influencing the reduction of fabrication costs. For these reasons, this connecting technique is widespread. Nevertheless, it has to be remembered that the

junctions are the points weakening a structure and the most probable places of failure initiation. The above-mentioned structures are served in condition of alternating loads, and thus, the fatigue is predicted to be the major cause of rupture. This phenomenon is directly related to the changes of geometric shape, microstructure, and stress distribution occurring during the welding process. For these reasons, the highest probability where the crack origins occur is in the nearest vicinity of the weldments where numerous notches are discovered.

The complexity of this matter causes that different methods of prediction of the fatigue strength and fatigue life have hitherto been developed. The most popular is a division into three main approaches, namely, stress-, strain-, and energy-based.

The nominal stress approach is based on the assumption of overall elastic behaviour. The stress is computed in the considered section, and the effect of the macrogeometric

shape of the component, notches, and residual stresses are taken under account. Nevertheless, the local influence of the welded joints on the stress value is disregarded. For the reason of its simplicity, this method is the most widely used approach to design welded structures against fatigue [1–5].

In the case when nominal stresses cannot be determined with sufficient accuracy due to component complexity, the structural hot-spot stress approach should be engaged. This method takes into account all factors resulting in the increase of stress in the vicinity of the junction and works by extrapolating a reference stress value at the weld toes, with the stress gradient effect being accounted for through ad hoc compiled design curves [6, 7]. Two or three measures have to be realized at different distances from the weld toe in order to compute the value of stress in the weld toe. In the case of stress calculated on the plate surface, according to [1], it can be determined using extrapolation of the following equations:

$$\sigma_{hs} = 1.67 \cdot \sigma_{0.4t} - 0.67 \cdot \sigma_{1.0t}, \quad (1)$$

$$\sigma_{hs} = 2.52 \cdot \sigma_{0.4t} - 2.24 \cdot \sigma_{0.9t} + 0.72 \cdot \sigma_{1.4t}. \quad (2)$$

The parameter t is the thickness of the considered component and $\sigma_{0.4t}$ is the stress measured at the distance of $0.4t$ from the toe. The hot-spot stress approach is very often engaged during finite element analysis (FEA) of welded components. Moreover, novel numerical methods are being developed and, in this regard, distinctive or unique structure cases are considered [8–12]. Nevertheless, this approach is also insufficient in more complex cases due to the assumption of an elastic stress range with linear change. Therefore, the welded joints of these structures are designed against fatigue using the effective notch stress approach [13–19], which is the most advanced fatigue design method being recommended by IIW [1]. This approach is based on the statement that stresses in the notch bottom are determined in the weld toe/root rounded with a fictive radius of 1 mm or 0.5 mm when the thickness of welded component is larger than 5 mm or less, respectively. The idea behind this method is that the mechanical local behaviour of the material in the notch bottom is similar to the behaviour of an unnotched or slightly notched, miniaturized, and axially loaded specimen extracted from this area [20].

Described approaches can be successfully employed if the high-cycle fatigue strength in infinite life is taken under consideration. These instances are characterized by the presence of elastic stresses. Only the notch stress approach can be extended into a finite-life range where the plastic microstrains cause crack initiation and their development. The influence of plastic strains is more substantial in the range of a low-cycle fatigue obtained under high and very high loads.

This paper presents the results of research conducted on development of the simplified model of fatigue life prediction of welded joints utilized from a fine-grained high-strength structural steel. Initially, there is consideration of the matter of adoption of the existing description for HSS steel and its extension on welded joints. The experimental verification was carried out, and the fractographic studies of fatigue crack initiation were also presented.

2. Prediction of Fatigue Life

The description of fatigue behaviour in the low-cycle range has to consider the plastic component. This crucial reason causes that the strain- and energy-based approaches of fatigue life prediction are most suitable, in comparison with stress-based methods. The most common formula describes this relationship is the Morrow design rule (3):

$$\varepsilon_a = \varepsilon_{ael} + \varepsilon_{apl} = \frac{\sigma'_f}{E} (2N_f)^b + \varepsilon'_f (2N_f)^c. \quad (3)$$

The above rule defines the dependence between strain amplitude ε_a divided into elastic and plastic components and pertinent fatigue life N_f . The coefficients σ'_f and ε'_f together with exponents b and c are determined during fatigue tests performed under the strain mode.

Alternative simplified solution of this problem was proposed by Manson [21]:

$$\Delta\varepsilon_a = \Delta\varepsilon_{ael} + \Delta\varepsilon_{apl} = 3.5 \frac{R_m}{E} (N_f)^{-0.12} + \varepsilon_{fra}^{0.6} (N_f)^{-0.6}, \quad (4)$$

where only three material properties are used: ultimate strength R_m , yield modulus E , and ductility ε_{fra} defined as

$$\varepsilon_{fra} \approx \ln \frac{100}{100 - Z}, \quad (5)$$

where Z is a percent area reduction.

Other version of relationships (3) and (4) is an equation developed by Langer [22]:

$$\varepsilon_a = \varepsilon_{ael} + \varepsilon_{apl} = \frac{Z_{-1}}{E} + 0.25 \cdot (N_f)^{-0.5} \ln \frac{100}{100 - Z}, \quad (6)$$

where Z_{-1} is the fatigue strength under fully reversed loading.

In the publication [23], authors proposed a new formula developed on the basis of relationships (3)–(6) with some modifications. Firstly, Z_{-1} is replaced in Equation (6) by $0.55R_m$ because according to [24] $Z_{-1} = \gamma R_m$ and $\gamma = 0.55$ is a coefficient depended on the material type. For steel, it is equal from 0.4 up to 0.55, and on the basis of results presented in [23], the maximum value has been chosen. Moreover, the influence of cycle asymmetry was also taken under account. According to [24], the plastic strain amplitude ε_{apl} was replaced by the medium plastic strain amplitude ε_{mapl} :

$$\varepsilon_{mapl} = \varepsilon_{apl} \frac{1 + R}{1 - R}. \quad (7)$$

Considered relationships were developed and evaluated for carbon and mild steels with $R_m < 700$ MPa. In the case of high-strength steels that have another microstructure and strengthening mechanism, Z parameter should be replaced by $Z^x = 0.5Z + 15$ [24]. Moreover, in order to define the permissible strain range $\Delta\varepsilon_{per}$ and the permissible fatigue life N_{per} , the partial factors of safety ψ_ε and ψ_N were imposed, defined in Equations (8). The first is related to $\Delta\varepsilon_a$ and the second is related to N_f , respectively:

$$\begin{aligned}\psi_\varepsilon &= \frac{\Delta\varepsilon_a}{\Delta\varepsilon_{\text{per}}}, \\ \psi_N &= \frac{N_f}{N_{\text{per}}}\end{aligned}\quad (8)$$

As a result, the following relationships describing $\Delta\varepsilon_{\text{per}}$ and N_{per} were obtained:

$$\Delta\varepsilon_{\text{per}} = \frac{2}{2 \cdot (\psi_N \cdot N_f)^m + ((1 + R_\varepsilon)/(1 - R_\varepsilon))} \cdot \ln \frac{100}{100 - Z^x} + \frac{1.1R_m}{E}, \quad (9)$$

$$N_{\text{per}} = \left(\frac{1}{\psi_\varepsilon \cdot \Delta\varepsilon_a - ((1.1R_m)/E)} \cdot \ln \frac{100}{100 - Z^x} - \frac{1 + R_\varepsilon}{2 \cdot (1 - R_\varepsilon)} \right)^{1/m}. \quad (10)$$

2.1. Prediction of Low-Cycle Fatigue Life of Welded Joints. In order to describe predicted fatigue life of welded joints, the notch strain approach was proposed. Therefore, the value of elastic-plastic strain range in the notch root $\Delta\varepsilon_{\text{notch}}$ should be specified. In the considered case, the notch is localized at the fusion line of weld. The condition of low-cycle fatigue strength is fulfilled if

$$\Delta\varepsilon_{\text{notch}} \leq \Delta\varepsilon_{\text{per}}, \quad (11)$$

which means that the strain should not exceed the limit value determined for the locally changed material at the notch. The strain range $\Delta\varepsilon_{\text{notch}}$ can be expressed by the product of strain concentration factor α_ε and the nominal strain range $\Delta\varepsilon_N$:

$$\Delta\varepsilon_{\text{notch}} = \alpha_\varepsilon \cdot \Delta\varepsilon_N. \quad (12)$$

According to [23], the strain concentration factor can be calculated using the following formula:

$$\alpha_\varepsilon = \frac{\alpha_k^{[2/(1+n)]} \cdot \bar{\Delta}\sigma_N^{[(1-n)/(1+n)]}}{(\alpha_k \cdot \bar{\Delta}\sigma_N)^{a \cdot (1-n)} \cdot (1 - \bar{\Delta}\sigma_N + (1/\sigma_k))^{1/(1+n)}}, \quad (13)$$

where α_k is the stress concentration factor (weld shape induced), n is the strain-hardening exponent, a is the constant (equal from 0 to 0.5), $\bar{\Delta}\sigma_N = \Delta\sigma_N / ((1 - R_\sigma) \cdot R_\varepsilon)$ is the normalized range of nominal stresses, $\Delta\sigma_N$ is the nominal stress range, and R_σ is the loading stress ratio.

The range of nominal strain $\Delta\varepsilon_N$ was computed using the following dependence:

$$\Delta\varepsilon_N = \frac{\Delta\sigma_N}{E}. \quad (14)$$

In order to determine the dependence describing predicted fatigue life of welded joints and taking into account condition (11), equation (10) was modified. Hitherto strain was replaced by $\Delta\varepsilon_{\text{notch}}$, and two new factors of safety were considered, namely, ψ_{Ff} related to the uncertainty degree of the used theoretical model and ψ_{Mf} related to the sensitivity of the material on cracking connected with the accessibility to supervise the welded structure (15):

$$N_f = \left(\frac{1}{\psi_{\text{Ff}} \cdot \psi_{\text{Mf}} \cdot \Delta\varepsilon_{\text{notch}} - ((1.1R_m)/E)} \cdot \ln \frac{100}{100 - Z^x} - \frac{1 + R_\varepsilon}{2 \cdot (1 - R_\varepsilon)} \right)^{1/m}. \quad (15)$$

3. Experimental Procedure

3.1. Materials. Experimental validation of the model of fatigue life prediction was carried out on fine-grained high-strength structural steel S960QL. The used material was in the form of sheet with a thickness of 6 mm. This steel is produced by liquid-quenching and tempering (Q&T) process which results in bainite-martensitic microstructure. The results obtained during chemical composition measurements and mechanical properties tests are presented in Tables 1 and 2.

The study of the chemical composition has been carried out using scanning electron microscopy equipped with an EDS spectrometer. Mechanical properties were determined on the basis of the results of tensile tests carried out according to [25].

3.2. Welded Joints. The fatigue tests were carried out using two types of butt joints, namely, I-shaped and V-shaped. The geometry of the connected parts before welding is shown in Figure 1.

The welds were made using MAG (metal active gas) welding with shielding gas containing 82% CO₂ and 18% Ar (EN ISO 14175–M21–ArC–18). Wire UNION X96 (EN ISO 16834–A–G Mn4Ni2,5CrMo) with a diameter of 1.2 mm was used to make the welds. The weld type presented in Figure 1(a) was made in a fully robotized way, in contrast to the second where the first run (root side) was made manually and only the second run (face side) using a mechanised method.

3.3. Fatigue Life Test Procedure. Fatigue tests were performed in terms of the low-cycle fatigue (LCF) and carried out for the paternal material and both types of welded joints. The tests were conducted using flat samples prepared on the basis of standard ASTM E606-4 [26]. Test samples were cut from a sheet with a nominal thickness of 6 mm, and their geometry is shown in Figure 2.

It was assumed that the fatigue tests will be performed on the material in the supply condition, which means that the surface of the test samples was not subjected to machining. The aim was to reflect as closely as possible the causes of fatigue crack initiation in real conditions.

Fatigue tests were carried out using an Instron 8808 hydraulic pulsator equipped with a dynamic extensometer. Two different gauges with the length of 25 mm and 50 mm were used during fatigue tests of the paternal material and welded joints, respectively. The tests were conducted in the strain mode controlled with the value of the total strain amplitude ε_a with a sinusoidal waveform. The values of amplitude ε_a fit in the range of 0.30% to 1.5% for the paternal material and from 0.15% to 0.40% for the joints. The value of the strain ratio R_ε of 0.1 and an average strain rate of $\dot{\varepsilon} = 10^{-2} \cdot \text{s}^{-1}$ were adopted. The failure criterion was a 25% decrease of maximum load.

TABLE 1: Chemical composition of S960QL steel.

	C	Si	Mn	Cr	Mo	Ni	Al	V	Cu
Own measurement	0.18	0.36	1.19	0.23	0.66	0.06	0.11	0.03	0.19
According to the certificate	0.18	0.28	1.13	0.22	0.67	0.08	0.08	0.03	0.18

TABLE 2: Mechanical properties of S960QL steel.

	E (MPa)	$R_{p0.2}$ (MPa)	R_m (MPa)	A (%)	Z (%)
Own measurement	2.20×10^5	974	1070	14.2	45.6
According to the certificate	—	997	1069	13.0	—

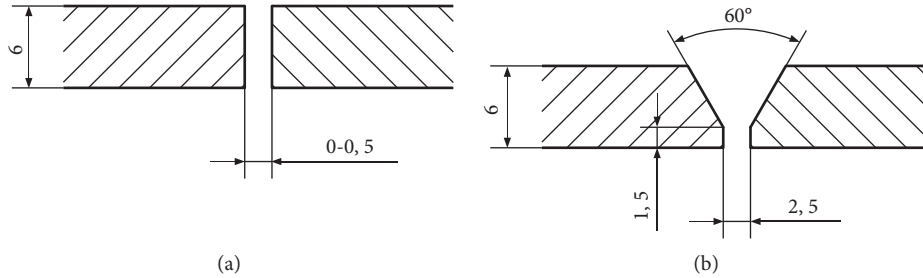


FIGURE 1: Geometry of welded elements prior to the implementation of joints: I-shaped (a) and V-joints (b).

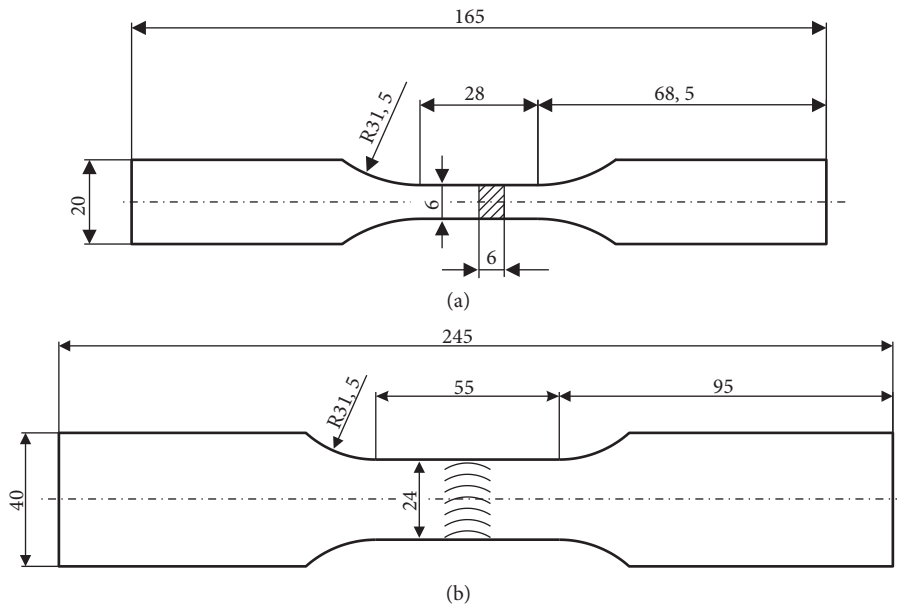


FIGURE 2: Dimensions of samples used in fatigue tests conducted on the paternal material (a) and welded joints (b).

4. Results and Discussion

4.1. Fatigue Test Results. In order to validate the developed theoretical model of fatigue life prediction, firstly, the fatigue tests were conducted on the paternal material—steel S960QL. Examination was carried out under six different total strain amplitudes: 0.30%, 0.40%, 0.50%, 0.75%, 1.0%, and 1.5%. Obtained results are shown in Table 3.

Based on these results and taking into account that the dependence $\sigma_a = f(\epsilon_{apl})$ expressed by (16) in the log-log scale is similar to linear function, the hardening exponent n for examined steel was determined. Its value is equal to 0.0769:

$$\sigma_a = K' \cdot (\epsilon_{apl})^n. \quad (16)$$

Secondly, the fatigue tests on the welded joints were conducted. Examination was carried out under five different total strain amplitudes, namely, 0.15%, 0.20%, 0.25%, 0.30%, and 0.40%. Obtained results are shown in Table 4.

4.2. Comparison of the Fatigue Life Prediction Model with Experimental Results. At the beginning, the theoretical ϵ_{per} - N_{per} curve for S960QL steel was determined based on formula (10). In calculations, the values of parameters R_m , E ,

TABLE 3: Results of fatigue tests for S960QL steel.

Load ε_a (%)	ε_{apl} (%)	ε_{ael} (%)	N_f (cycles)	σ_a (MPa)
0.30	0.0097	0.2903	11863	603
	0.0066	0.2934	10488	597
0.40	0.0669	0.3331	5731	680
0.50	0.1184	0.3816	1867	754
	0.1377	0.3623	1688	771
0.75	0.3178	0.4322	583	814
	0.3227	0.4273	612	811
1.00	0.5380	0.4620	272	834
	0.5400	0.4600	262	846
1.50	1.0080	0.4920	140	842

TABLE 4: Results of fatigue tests for welded joints of S960QL steel.

Load ε_a (%)	Joint type	ε_{apl} (%)	ε_{ael} (%)	N_f (cycles)	σ_a (MPa)
0.15	I	0.0027	0.1473	6858	306
	I	0.0013	0.1487	5195	309
	V	0.0012	0.1488	13851	290
	V	0.0012	0.1488	7036	311
0.20	I	0.0029	0.1971	3160	413
	I	0.0025	0.1975	2444	421
	V	0.0015	0.1985	1892	445
	V	0.0020	0.1980	1755	400
0.25	I	0.0026	0.2474	1298	536
	I	0.0025	0.2475	914	545
	I	0.0063	0.2437	1610	534
	V	0.0020	0.2480	1095	534
0.30	V	0.0040	0.2460	1418	478
	I	0.0087	0.2913	772	604
	I	0.0088	0.2912	969	610
	V	0.0074	0.2926	553	652
0.40	V	0.0085	0.2915	699	624
	I	0.0323	0.3677	268	740
	V	0.0425	0.3575	178	788
	V	0.0330	0.3670	274	713

and Z (to calculate Z^x) have been taken from Table 2 and $R_\varepsilon = 0.1$ from the experiment conditions. It is proposed to take a value of material exponent $m = 0.6$ [24]. The factor of safety was assumed to be equal to 1.0 because this dependence describes theoretical relation between strain and fatigue life. The final results are presented on the graph (Figure 3).

In Figure 3, two curves are presented. The first curve was plotted on the basis of the developed model of permissible fatigue life expressed by equation (10). The second curve was obtained from registered experimental data and expressed by the Morrow curve (3). Additionally, the results of fatigue life for tested samples are placed. The presented graphs show a proper correlation between the adopted theoretical model for describing the fatigue life of the S960QL steel with the results obtained in the experimental way.

In order to establish the N_f function concerning the welded joints of S960QL steel (15), determination of stress concentration factor α_k is crucial. Three methods were considered, namely, Jewdokimow's, Lawrance's, and Ushirokawa-Nakayama's, and the first was recommended as

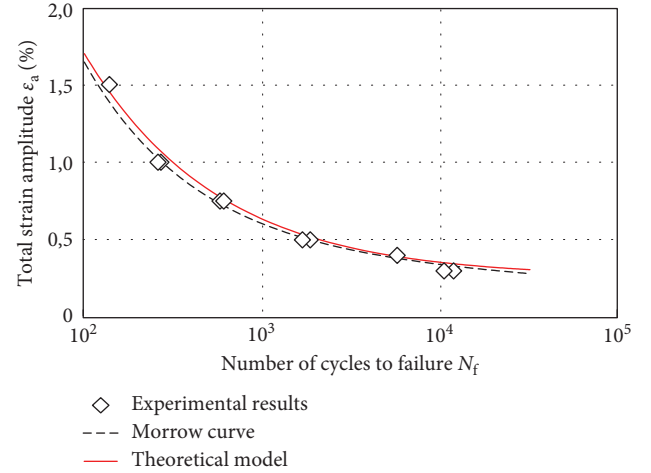


FIGURE 3: Comparison of the developed theoretical model with experimental results.

the most severe [27]. Measurements of the radius in the notch root ρ were performed which reached the value of 0.5–1.1 mm. Because the measurements were made locally in random cross-sections, $\rho = 0.5$ mm was taken under further consideration. Then, the values of α_k factor have equalled approximately 1.93 in the case of I-shaped weld and from 1.61 up to 1.81 for V-shaped weld, and the worst values of $\alpha_k = 1.93$ and $\alpha_k = 1.81$ were adopted, respectively. Moreover, the stress range $\Delta\sigma_N$ was taken as a double value of strain amplitude σ_a (Table 4) and n exponent from equation (16). Loading stress ratio R_σ was determined individually in each test taking into account the maximum and minimum values of recorded stresses from the middle cycle of the fatigue life. Material constant $a = 0.5$ was taken. The strain range $\Delta\varepsilon_N$ was calculated according to equation (14). Obtained results are presented in Table 5 and shown on the plot (Figure 4).

On the basis of the developed plot (Figure 4), it can be stated that the elaborated theoretical model of prediction of the fatigue life describes it in a simple and safe way. Moreover, the assumed fatigue strength criterion based on the maximum strain in the notch root was proper for the case of welded joints made of high-strength steel. The analysis made on the basis of results obtained for $N_f > 1000$ cycles leads to the conclusion that influence of R_ε in this range is negligible. For presented results, the most important advantage is that predicted values are slighter than the results obtained during fatigue tests. Furthermore, final equation (17) describing the dependence of the predicted fatigue life of S960QL steel-welded joints N_f versus the strain range in the notch root $\Delta\varepsilon_{notch}$ was elaborated:

$$N_f = \left(\frac{0.475}{1.725 \cdot \Delta\varepsilon_{notch} - 5.36 \cdot 10^{-3}} - 0.61 \right)^{1.67}. \quad (17)$$

The experimental research results and the theoretical values are characterized by noticeable good correlation particularly under lower values of strain $\Delta\varepsilon_{notch}$. Determined values of strain bring about the fatigue life no lower than 5000 cycles. It can be probably caused by the significant reduction or even partial cessation of plastic strains in the

TABLE 5: Results of calculations of the strain range $\Delta\epsilon_{\text{notch}}$.

Load ϵ_a (%)	Joint type	$\Delta\sigma_N$ (MPa)	R_σ (-)	$\bar{\Delta}\sigma_N$ (-)	α_ϵ (-)	$\Delta\epsilon_N$ (%)	$\Delta\epsilon_{\text{notch}}$ (%)
0.15	I	611	-0.02	0.616	2.09	0.278	0.58
	I	618	+0.03	0.651	2.16	0.281	0.61
	V	579	-0.19	0.500	1.74	0.264	0.46
	V	622	+0.33	0.953	2.51	0.283	0.71
0.20	I	826	-0.09	0.780	2.41	0.376	0.91
	I	841	-0.11	0.778	2.40	0.383	0.92
	V	890	-0.135	0.805	2.22	0.405	0.90
	V	800	+0.13	0.944	2.49	0.364	0.91
0.25	I	1072	-0.02	1.082	3.16	0.488	1.54
	I	1090	-0.21	0.925	2.74	0.496	1.36
	I	1067	-0.16	0.944	2.79	0.486	1.35
	V	1068	-0.17	0.937	2.48	0.486	1.20
	V	956	-0.14	0.861	2.32	0.435	1.01
0.30	I	1207	-0.24	0.999	2.93	0.550	1.61
	I	1219	-0.40	0.894	2.66	0.555	1.48
	V	1302	-0.47	0.909	2.42	0.593	1.43
	V	1248	-0.41	0.909	2.42	0.568	1.37
0.40	I	1479	-0.63	0.932	2.75	0.00673	1.85
	V	1425	-0.58	0.926	2.45	0.00649	1.59
	V	1576	-0.77	0.914	2.43	0.00718	1.74

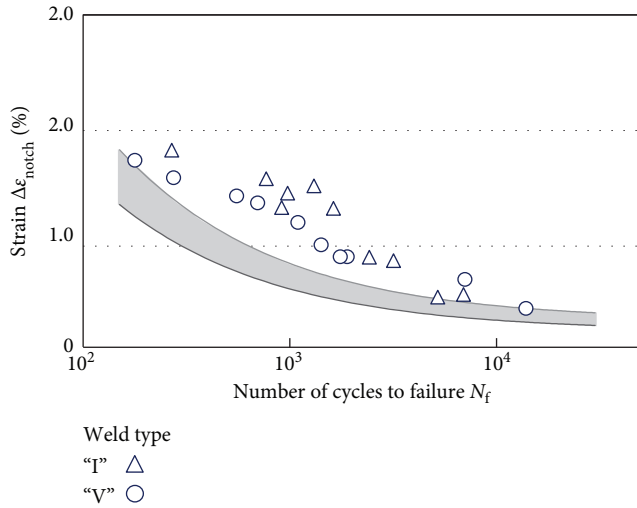


FIGURE 4: Comparison of the results obtained for the developed theoretical model of fatigue life prediction with experimental data. Grey area is the range of predicted fatigue life defined by equation (14) and obtained for different values of safety factors.

notch root. However, a limit value of the strain range in the notch root $\Delta\epsilon_{\text{notch}}$ for which an unlimited fatigue life takes place can be determined taking into account the issue $N_f \rightarrow \infty$:

$$\Delta\epsilon_{\text{notch}} = \lim_{N_f \rightarrow \infty} \left[\frac{1}{\psi_{Ff} \cdot \psi_{Mf}} \left(\frac{1}{(N_f)^m + ((1 + R_\epsilon)/(2 \cdot (1 - R_\epsilon)))} \cdot \ln \frac{100}{100 - Z^x} + \frac{1.1R_m}{E} \right) \right]. \quad (18)$$

The limit value of $\Delta\epsilon_{\text{notch}}$ calculated using formula (18) equals $3.11 \cdot 10^{-3}$. The predicted value of stress range $\Delta\sigma$ was determined using this strain, specific for S960QL steel, and it

amounts to at least 300 MPa. This value was computed under the statement that the maximum strain concentration factor α_ϵ equals 2.2 and was determined for $\epsilon_a = 1.5 \cdot 10^{-3}$.

4.3. Fractographic Investigation on Fatigue Crack Initiation.

The studies of fatigue crack surfaces were conducted using the scanning electron microscope JEOL JSM-6610, and the observations were realized by SE (secondary electrons) and BSE (backscattered electrons) detectors. Both the paternal material and welded joint samples are explored (Figures 5 and 6).

In Figures 5(a) and 5(b) are presented the exemplary fatigue fractures resulting from fatigue tests conducted at the total strain amplitude $\epsilon_a = 0.3\%$ and 1.5% , respectively. Although these tests were carried out under significantly different loading levels, the mechanism of crack initiation is similar. The process of cracking has started from the surface and propagated into the material. Magnified pictures placed on the right side indicate that there are numerous origins caused simultaneously by crack development in many places. The initiation of fatigue cracks proceeded in local strains and stress concentrations within the rolled-in hard and brittle scale particles the surface of the material (indicated by yellow arrows). Individual initial cracks join together into the much greater cracks which propagate into deeper parts of the material affected by fatigue.

Representative examples of fatigue fractures received from examined welded joints are presented in Figures 6(a) and 6(b). These pictures were made for the samples, both I-shaped (a) and V-shaped (b), tested at the total strain amplitude $\epsilon_a = 0.2\%$. All received results of the study on crack initiation are similar, namely, the fractures initiated in the notch root, and in considered welded joints, they have been at the surface in the vicinity of fusion line. Detailed studies, presented in magnified pictures, have revealed that

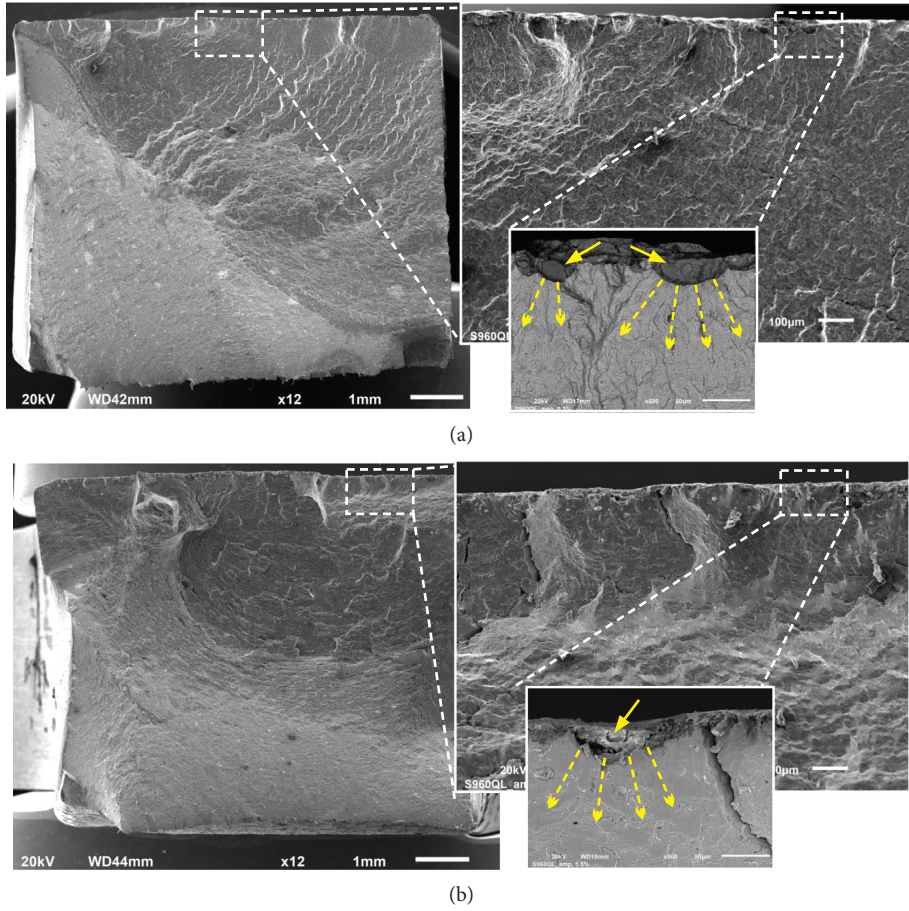


FIGURE 5: The pictures of fatigue fractures have been observed during fractographic investigation. Samples made of S960QL steel tested under total strain amplitude: (a) $\epsilon_a = 0.3\%$ and (b) $\epsilon_a = 1.5\%$.

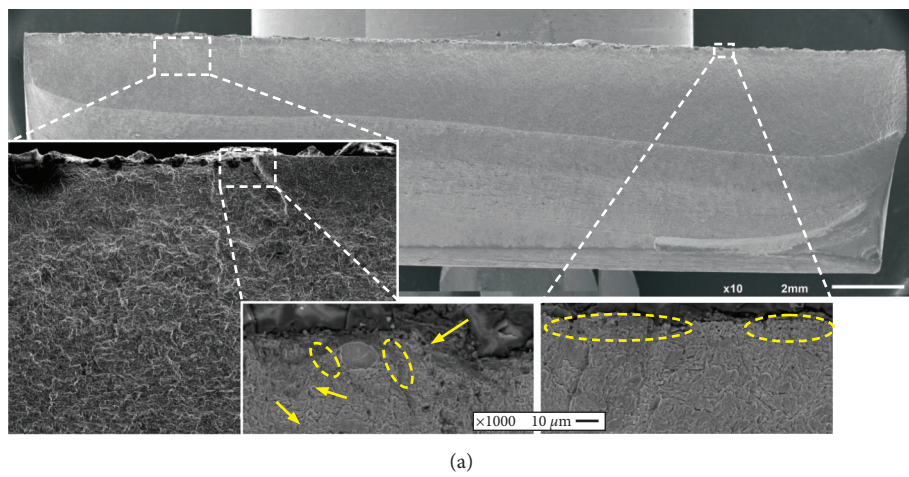


FIGURE 6: Continued.

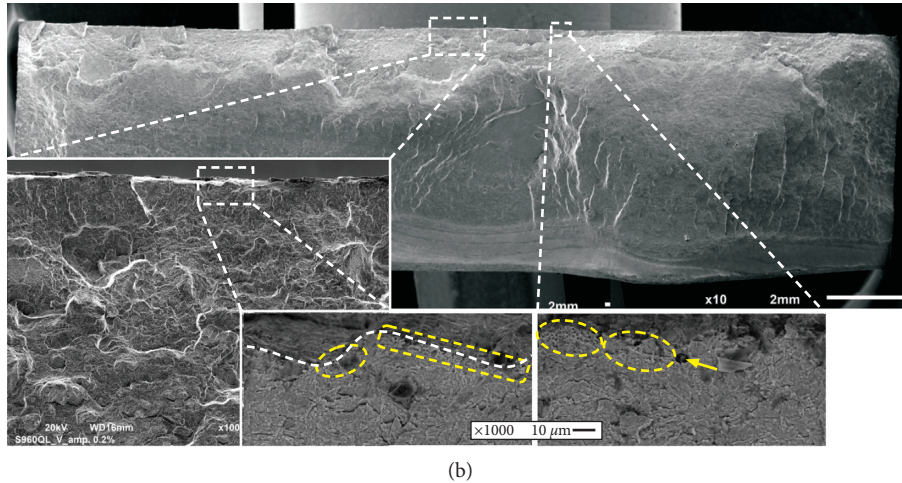


FIGURE 6: The pictures of fatigue fractures have been observed during fractographic investigation. Samples of weldments made of S960QL steel tested under the total strain amplitude $\varepsilon_a = 0.2\%$: (a) I-shaped and (b) V-shaped welds.

there were no dominating origins of fatigue cracks, and the initiation in both cases occurred over almost the entire length of the fusion line. It should be emphasized that the cracks in all researched V-shaped welded joints have propagated from the root side. The cracking process was probably affected by the presence of numerous micropores (surrounded regions) and inclusions, rare but existing (indicated by arrows). These imperfections in the microscale have caused local weakness of the welded material independently from the adverse microstructural changes. Moreover, the shape of the fusion line is also undesirable because it is wavy causing an additional strain concentration (Figure 6(b), the white dashed line in the nether picture).

5. Conclusions

In this paper, a method of the fatigue life prediction based on the criterion of permissible strain range in the notch root was developed. This model was verified for welded joints made of high-strength steel S960QL. Moreover, the fatigue crack initiation stage was investigated by fractographic analysis and the origins were revealed. From the obtained results and observations made, the following conclusions can be drawn:

- (1) The simplified model of fatigue life prediction which was previously developed for mild and carbon steels can also be engaged for fine-grained bainitic-martensitic HSS steels.
- (2) The method of fatigue life prediction based on the criterion of permissible strain range in the notch root indicates satisfactory correlation with experimental data and safely describes the fatigue life of weldments made of S960QL.
- (3) The estimated limit value of the strain range in the notch root $\Delta\varepsilon_{\text{notch}}$ equals $3.11 \cdot 10^{-3}$, resulting in the stress range $\Delta\sigma$ of 300 MPa.
- (4) The direct impact of the surface imperfections on the fatigue cracks initiation was revealed. In the case of

paternal material, the origins of cracking were discovered at the places of rolled-in hard and brittle scale particles. In welded joints, the fatigue cracks initiated at the whole length of the fusion line.

Data Availability

The data underlying the findings of this study and other more detailed information are available from the author upon request.

Conflicts of Interest

The author declares that there are no conflicts of interest regarding the publication of this paper.

Acknowledgments

The author is grateful to Prof. Lucjan Śniezek for advice and guidance and also to Janusz Torzewski, Ph.D., who have supported the realization of fatigue tests. The execution of fatigue tests was financially supported by the Faculty of Mechanical Engineering through the internal academic grant (RMN 08-878). The processing charge was also financed by this faculty.

References

- [1] A. Hobbacher, *Recommendations for Fatigue Design of Welded Joints and Components*, International Institute of Welding, Paris, France, 2008.
- [2] I. Al Zamzami and L. Susmel, "On the accuracy of nominal, structural, and local stress based approaches in designing aluminium welded joints against fatigue," *International Journal of Fatigue*, vol. 101, pp. 137–158, 2017.
- [3] T. Shiozaki, N. Yamaguchi, Y. Tamai, J. Hiramoto, and K. Ogawa, "Effect of weld toe geometry on fatigue life of lap fillet welded ultra-high strength steel joints," *International Journal of Fatigue*, vol. 116, pp. 409–420, 2018.
- [4] W. Hiramoto, W. Jiang, X. Zhao, and S. T. Tu, "Fatigue life of a dissimilar welded joint considering the weld residual stress:

- experimental and finite element simulation,” *International Journal of Fatigue*, vol. 109, pp. 182–190, 2018.
- [5] C. Cui, Q. Zhang, Y. Bao, J. Kang, and Y. Bu, “Fatigue performance and evaluation of welded joints in steel bridges,” *Journal of Constructional Steel Research*, vol. 148, pp. 450–456, 2018.
- [6] D. Kang, C. M. Sonsino, and W. Fricke, *Fatigue Assessment of Welded Joints by Local Approaches*, Woodhead Publishing Limited, Cambridge, UK, 2007.
- [7] E. Niemi, W. Fricke, and S. J. Maddox, *Fatigue Analysis of Welded Components: Designer’s Guide to The Structural Hot-Spot Stress Approach*, Woodhead Publishing Limited, Cambridge, UK, 2006.
- [8] L. Rong, L. Yuqing, J. Bohai, M. Wang, and Y. Tian, “Hot spot stress analysis on rib–deck welded joint in orthotropic steel decks,” *Journal of Constructional Steel Research*, vol. 97, pp. 1–9, 2014.
- [9] Y. Kim, J. S. Oh, and S. H. Jeon, “Novel hot spot stress calculations for welded joints using 3D solid finite elements,” *Marine Structures*, vol. 44, pp. 1–18, 2015.
- [10] I. A. Zamzami and L. Susmel, “On the use of hot-spot stresses, effective notch stresses and the point method to estimate lifetime of inclined welds subjected to uniaxial fatigue loading,” *International Journal of Fatigue*, vol. 117, pp. 432–449, 2018.
- [11] N. Osawa, N. Yamamoto, T. Fukuoka, J. Sawamura, H. Nagai, and S. Maeda, “Study on the preciseness of hot spot stress of web-stiffened cruciform welded joints derived from shell finite element analyses,” *Marine Structures*, vol. 24, no. 3, pp. 207–238, 2011.
- [12] M. H. Sawamura, S. M. Kim, Y. N. Kim et al., “A comparative study for the fatigue assessment of a ship structure by use of hot spot stress and structural stress approaches,” *Ocean Engineering*, vol. 36, no. 14, pp. 1067–1072, 2009.
- [13] C. M. Sonsino, W. Fricke, F. de Bruyne, A. Hoppe, A. Ahmadi, and G. Zhang, “Notch stress concepts for the fatigue assessment of welded joints -background and applications,” *International Journal of Fatigue*, vol. 34, no. 1, pp. 2–16, 2012.
- [14] T. Nykänen, H. Mettänen, T. Björk, and A. Ahola, “Fatigue assessment of welded joints under variable amplitude loading using a novel notch stress approach,” *International Journal of Fatigue*, vol. 101, pp. 177–191, 2017.
- [15] L. Bertini, F. Frendo, and G. Marulo, “Fatigue life assessment of welded joints by two local stress approaches: the notch stress approach and the peak stress method,” *International Journal of Fatigue*, vol. 110, pp. 246–253, 2018.
- [16] K. Rother and W. Fricke, “Effective notch stress approach for welds having low stress concentration,” *International Journal of Pressure Vessels and Piping*, vol. 147, pp. 12–20, 2016.
- [17] C. Morgenstern, C. Sonsino, A. Hobbacher, and F. Sorbo, “Fatigue design of aluminium welded joints by the local stress concept with the fictitious notch radius of $r_f = 1$ mm,” *International Journal of Fatigue*, vol. 28, no. 8, pp. 881–890, 2006.
- [18] C. M. Sorbo, “A consideration of allowable equivalent stresses for fatigue design of welded joints according to the notch stress concept with the reference radii $r_{ref} = 1.00$ and 0.05 mm,” *Welding in the World*, vol. 53, no. 3-4, pp. R64–R75, 2009.
- [19] R. Sołtysiak and D. Boroński, “Strain analysis at notch root in laser welded samples using material properties of individual weld zones,” *International Journal of Fatigue*, vol. 74, pp. 71–80, 2015.
- [20] D. Radaj, “Review of fatigue strength assessment of non-welded and welded structures based on local parameters,” *International Journal of Fatigue*, vol. 18, no. 3, pp. 153–170, 1996.
- [21] S. S. Manson, *Fatigue: a Complex Subject-Some Simple Approximations*, NASA, Washington, DC, USA, 1965.
- [22] S. Kocańda and A. Kocańda, *Niskocyklowa Wytrzymałość Zmęczeniowa Metali*, in Polish, PWN, Warszawa, Poland, 1989.
- [23] C. Goss, S. Kłysz, and W. Wojnowski, *Problemy Niskocyklowej Trwałości Zmęczeniowej Wybranych Stali I Połączeń Spawanych*, in Polish, Wydawnictwo ITWL, Warszawa, Poland, 2004.
- [24] N. A. Machutow, A. P. Gusienkow, and M. M. Galenin, *Raszczoty Prochnosti Elementow Konstrukcij Pri Malocyklowom Nagruzhenii*, in Russian, Metodicheskie ukazania, Moscow, Russia, 1987.
- [25] ISO 6892-1: Metallic Materials–Tensile Testing–Part 1: Method of Test at Room Temperature.
- [26] ASTM E 606-04, *Standard Practice for Strain-Controlled Fatigue Testing*, ASTM, West Conshohocken, PA, USA, 2005.
- [27] K. Ida and T. Uemura, “Stress concentration factor formulae widely used in Japan,” *Fatigue & Fracture of Engineering Materials and Structures*, vol. 19, no. 6, pp. 779–786, 1996.

Research Article

Effects of Stem Cutting in Rice Harvesting by Combine Harvester Front Header Vibration

Zhong Tang , Haotian Zhang, Yuepeng Zhou, and Yu Li

School of Agricultural Equipment Engineering, Jiangsu University, Zhenjiang 212013, Jiangsu, China

Correspondence should be addressed to Zhong Tang; tangzhong2012@126.com

Received 19 October 2018; Accepted 10 January 2019; Published 3 February 2019

Guest Editor: Dariusz Rozumek

Copyright © 2019 Zhong Tang et al. This is an open access article distributed under the Creative Commons Attribution License, which permits unrestricted use, distribution, and reproduction in any medium, provided the original work is properly cited.

In order to reveal the reason of stem cutting in rice harvesting by combine harvester front header, stem cutting principle of the front header was developed. Based on the structural models and the parameters of each part of header, the first eight-order constrained modal simulation analysis was carried out to obtain the vibration response frequency. The front header was produced and used to be tested for restraint experimental modal in the rice field. The rice stem cutting state of the header cutter was analyzed by carrying out the vibration test of the no-load rotation state and rice harvesting state in the field. According to the cutting diagram of the stalk in the header, the angle of the cutting surface and length distribution of the short stalk were analyzed with compound state of forward and vertical vibration. The results showed the mean and variance amplitude of front header were similar to length distribution of the short stalk. The mean length 23.60 mm of the repeatedly cut stems was inextricably linked to the up and down vibration amplitude 25.36 mm of the header. The stem cutting surface angles 38°, 44°, and 62° were for different forward speed and cutting areas on the cutting diagram. The above studies reveal the intrinsic nature between header vibration and length distribution of the cutting stem.

1. Introduction

There are always short rice stalks in the grains after rice is harvested from the field. This problem seriously affects the processing and rice grains' quality in the later stage. The cause of short rice stalks has become a current research topic. The vibration behaviors of many structures are generally identified by the method of analyzing the experimental modalities [1, 2]. The relationship between stem cutting and vibration state has received considerable amount of attention. This is a difficult research to reveal the intrinsic nature between header vibration and short rice stem by investigating the vibration state of rice harvesting machinery.

There is strong vibration at the front header of rice combine harvester, which is induced by the dynamic load and the road surface [3, 4]. Vibration of the cutting platform causes reduction of frame lifetime and driver's comfort and also affects the working precision of the machine. There were many research results on vibration of the combine harvester header [5]. The experimental assessment of the most relevant vibration

properties of a combine harvester cutting platform was carried out by Ebrahimi et al. [6]. Chuan-Udom developed 3 types of new cutter bar drivers to reduce the vibration of rice combine harvester [7]. Fukushima et al. revealed that the harmonic frequency components varied with an increase in the width of the interspace although the highest harmonic frequency in the simulation was three times as high as the crank wheel rotation frequency [8, 9]. There are many reasons for front header vibration, such as dynamic loading excitation, natural frequency resonance, and vibration transfer response. Yu et al., took 4LZ-4.6 full-feed harvester's header as research object and adopted the cumulative damage rule to obtain the fatigue life of the header frame [10]. When the excitation frequency was in an integer multiple of the natural frequency of the structure, the vibration of the structure would be excited. Fukushima et al. constructed a dynamic model of the knife driving system to forecast the vibration characteristics of the knife driving system [9]. The vibration occurred at joint of the link arm, and the drive knife was three times as high as the driving frequency.

For the vibration and imbalance problems of the harvester header, the dynamics simulation of the header of the small combine harvester was carried out by Kong et al. [11]. The speed curves of the cutter and the transverse conveyer chain were obtained through dynamic simulation. In order to enhance the process stability of adjusting the height of the header during the operation of combine harvester, a height adaptive adjustment system for the header was developed [12]. Li et al. established a three-dimensional model of the 4LZ-2.0 rice-wheat combine harvester header frame in Solidworks and introduced the model into the ABAQUS finite element analysis software to establish a finite element model [13]. Through the analysis of the modal parameters, the vibration form of the header frame and the weak link of the structure under the excitation frequency were obtained [14]. There were much more studies focused on cutter bar of header. Although many solutions to reduce the vibration of header were also proposed, the vibration in rice cutting process was more obvious and serious. Gao et al. tested the vibration of crawler-type combine harvester in field harvesting condition and indicated that harvesting status caused significant vibration [15]. In order to reduce the vibration of the header in harvesting, Li et al. established a three-dimensional model and performed a finite element modal analysis of the header and bridge of the combine harvester [16]. He carried out reliability optimization design of the wheat harvester header structure [17]. Based on the analysis of the principle of the hydraulic system of the traditional rice harvester, the targeted upgrade was carried out, and the test was verified on test bench. According to the principle of combine harvester, Lu et al. designed a double-cutter double-roller full-track regenerative rice harvester structure [18].

On the contrary, overhigh speed led to too much vibration on the header and caused the reel index to increase header loss. Vibration on the cutter bar driver was measured in some studies at the header's drive axial speed from 250 to 400 rpm. The reel, front auger, and chain conveyer moved along the rice combine harvester's moving direction and caused the relatively low vibration which was compared to that caused by the cutter bar driver [19]. The head structure was optimized by using Pro/E to model and using Matlab to make numerical calculation, and a three-dimensional head model with quality, cross-sectional area, and reliability optimization was established [20]. In order to reduce the harvest loss caused by the vibration of the header during the harvesting process, the motion and dynamic analysis of the cutting transmission system were carried out. The differential equations of the system horizontal vibration were established and solved [21].

Many research results are also obtained. However, for the field working mode of the header, the influence of header vibration on stem cutting and the morphological characteristics left on stalk cut surface was rarely studied. Research results in this area are of great significance for the design of the rice combine harvester header structure.

The objective of this study was to determine vibration behavior of front head of rice combine harvester, structural model, and stem cutting principle of header platform. The

designed header structure was manufactured, and a restraint experimental modal test of the header was carried out in rice field. According to the stalk cutting diagram of the header under the horizontal movement of the cutting head and the horizontal movement of the header, the angle of the cutting surface of the stalk generated during the cutting process of the header and the intrinsic essential relationship between the short stalk and the vibration of the header were analyzed.

2. Materials and Methods

2.1. Structure of Front Header. Front header is an important part of rice harvesting to achieve stem cutting and collection [22]. The stalk cut by header is transported from header to threshing cylinder by conveying house. The front header of rice combine harvester consists of header platform, cutting bar, combine auger, pentagon reel, and conveying house. The front header is shown in Figure 1.

As shown in Figure 1, the harvesting process of front header consists of three steps. The first step was to shift stems with pentagon reel, and then the stems were guided into header platform. The second step was to cut stems by cutting bar, and then the stems were separated from root. The third step was to collect and compress the stems, and the stems were fed to threshing cylinder by conveying chain [23]. That is, the function of the front header was the initial preparation work for subsequent grain threshing. In rice harvesting process, there are always short rice stalks in the grains after rice is harvested from the field.

As shown in Figure 1, the pentagon reel radius is 500 mm. The rod number is 5, and the reel eccentric distance is 60 mm. Reel shaft inner and outer diameters of the tube are 36 mm and 42 mm, respectively. Reel wheel speed is 35 r/min. The combine auger diameter is 300 mm, helical blade height is 100 mm, pitch is 460 mm, the speed of feeding auger is 150 r/s, gap between the helical blade and floor is 20 mm, and clearance between helical blade and rear side of cutting table is 25 mm. The spiral cylinder of the cutting table is provided with 11 telescopic fingers. The cutter driving wheel speed is 411 r/min.

2.1.1. Pentagon Reel. The pentagon reel could adjust the movement direction of stem while the combine harvester was going forward. The pentagon reel performed circular motion under rotating condition. So, the trajectory of pentagon reel was a combination of circular motion and linear motion. Structural model of pentagon reel is shown in Figure 2. While the pentagon reel was running, the reel teeth should be always vertically downward. Only in this way, the stem could be pushed into header platform. The method of ensuring the reel teeth being vertically downward was based on the principle of planar four-bar linkage [24].

As shown in Figure 2(b), the O point on pentagon reel was selected as the research object and set as the coordinate origin. The vertical direction was the Y coordinate and the horizontal direction was the X coordinate. The trajectory of O point was a combination of circular motion and linear motion. Then, the trajectory equation of O point is shown as follows:

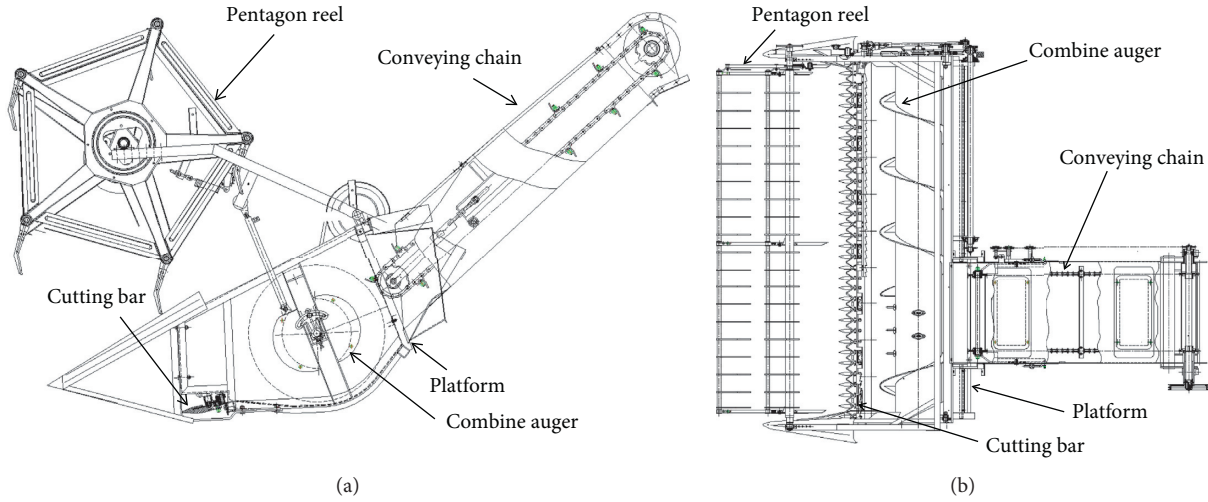


FIGURE 1: Structure and composition of front header. (a) Header main view. (b) Header top view.

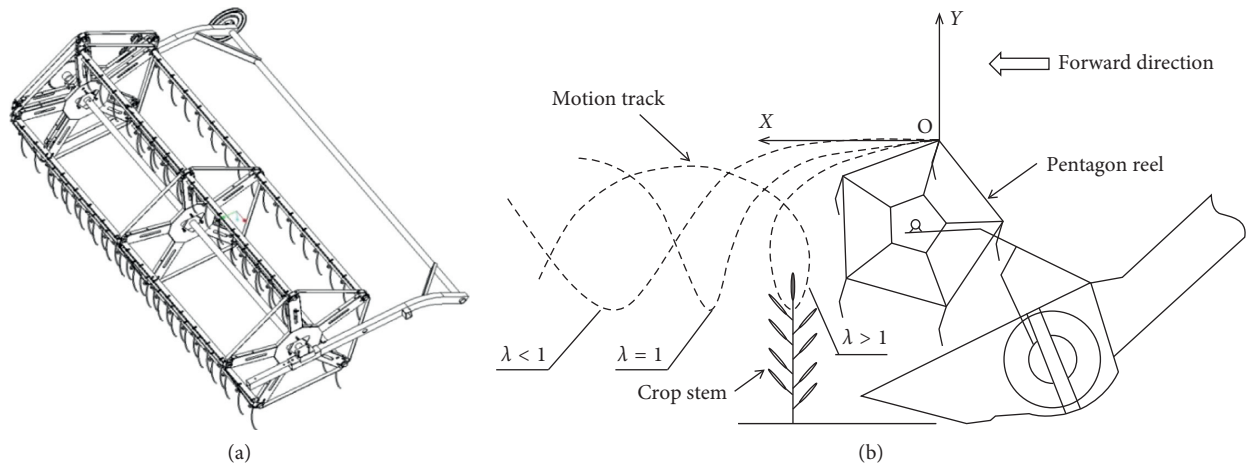


FIGURE 2: Structure and schematic of the pentagon reel. (a) Assembly of the pentagon reel. (b) Trajectory of the pentagon reel.

$$\begin{cases} X = Vt + R \cos \omega t, \\ Y = H - R \sin \omega t + h, \end{cases} \quad (1)$$

where R is the radius of the reel, ω is the rotational velocity, H is the height from the ground to point O , h is the height from the ground to cutting bars, t is the motion time, and V is the forward velocity of the pentagon reel.

Based on the trajectory equation of O point, the velocity of O point could be obtained by equation (1). The motion velocities of O point in X coordinate and Y coordinate are shown as follows:

$$\begin{cases} V_X = \frac{dX}{dt} = -R\omega \sin \omega t + V, \\ V_Y = \frac{dY}{dt} = -R\omega \cos \omega t. \end{cases} \quad (2)$$

If the O point of the pentagon reel had to be toggled and guided toward the stem, the horizontal movements' speed of the O point needs to have a value of X negative. Let λ be the

ratio of V_y to V (V_y/V). When $\lambda > 1$, $\lambda = 1$, or $\lambda < 1$, the trajectory of O point is shown in Figure 2(b).

As shown in Figure 2(b), when the $\lambda > 1$, the trajectory of O point was a long cycloid. The trajectory formed a buckle, and the bat had a rearward horizontal speed at the lower portion of the buckle. So $\lambda > 1$ could let pentagon reel be toggled and guided toward the stem. In order to reduce the impact of the pentagon reel on the stem, the horizontal velocity of the O point should be zero which was the best state. So, the motion velocity of O point at X coordinate should be as follows:

$$V_X = -R\omega \sin \omega t + V = 0. \quad (3)$$

Then, $\sin \omega t = V/(R\omega) = (\cos \omega t)/\lambda$, $\lambda = (\cos \omega t)/(\sin \omega t) = ctg \omega t$. So, $\lambda = ctg \omega t > 1$ was the factor of horizontal velocity of the O point be zero.

2.1.2. Cutting Bar. The cutting bar was composed of a reciprocating cutter and fixed supporting portion which was riveted by a cutter bar, movable blades, and cutter

heads. During the cutting crop stem process, the cutter reciprocated and the front edge of the edge guard divided the stems into small bundles and led to the cutter. The cutter pushed the straw to the fixed blades for cutting during the movement. The structural model of cutting bar is shown in Figure 3.

The drive mechanism of the cutting bar changed the rotary motion into reciprocating motion. The existing mainstream adopted the principle of the pendulum mechanism. The pendulum ring mechanism converted rotary motion into reciprocating motion by a pendulum ring mounted obliquely on the main shaft and through a swinging shaft. Pendulum drive mechanism of cutting bar is shown in Figure 3(b). The law of blade motion had a direct impact on the performance of the cutter. The cutter stroke of the pendulum ring mechanism can be expressed as follows:

$$L = 2Kl \sin \beta, \quad (4)$$

where L is the cutter stroke of the pendulum ring, K is the correction factor (0~1), l is the pendulum length, and β is the pendulum angle.

Drive components of horizontal cutter used a slew ring transmission mechanism. To facilitate specialized production and spare parts supply, the industry standard specifies a spacing of 76.2 mm between adjacent cutters and a horizontal inclination of $6^{\circ}30'$. The length of pendulum bar was 95 mm, the pendulum ring angle was 22° , the average speed of the cutter generally was 0~1.2 m/s, and the cutter driving wheel speed was 411 r/min [25]. The cutter knife was perpendicular to the heading direction of the harvester (reciprocating motion in horizontal direction).

2.1.3. Combine Auger. The function of combine auger was transferring the cut crop stalks to the feeding inlet of conveying house. There were two parts of spiral blades and telescopic teeth to complete stalk collection and delivery. Spiral blades were mounted on the surface of the cylinder body [26]. Structural model of combine auger is shown in Figure 4(a). Telescopic teeth were eccentric retractable grilled fingers. The feeding inlet function of eccentric retractable grilled fingers is shown in Figure 4(b).

As shown in Figure 4, inner diameter, outer diameter and pitch were major parameters of the combine auger. Circumference length of the inner diameter should be longer than the length of crop stalks to avoid the stalks entangled on the cylinder body. The size of the pitch was determined by the ability of the spiral blade to transport the crop stalk. The pitch S of the auger should be as follows:

$$S \leq \pi dt g \alpha, \quad (5)$$

where S is the pitch of the combine auger, d is the diameter of the cylinder body, and α is the spiral angle.

As shown in Figure 4, the telescopic fingers were mounted in the spiral barrel and hinged on a fixed crankshaft. The center of the crankshaft had an eccentricity from the center of the spiral cylinder. The outer end of the finger was connected to the spiral barrel through a ball joint. When the spiral barrel rotated through the rotating shaft, it drove

the fingers to rotate together. However, due to the disagreement between the two fingers, the fingers referred to the telescopic movement relative to the surface of the spiral cylinder.

2.1.4. Assembly of Front Header. The header platform mainly included structural beams and sealing plates. The header platform was the skeleton and base that bore the loads of pentagon reel, cutting bar, and combine auger. The frame bore the loads of pentagon reel, cutting bar, and combine auger. Structural model of the header platform is shown in Figure 5.

The conveying aisle was a bridge connecting the header frame to the threshing cylinder. The conveying aisle mainly consisted of a carrying frame and a conveyer chain. Structural model of conveying aisle is shown in Figure 6.

According to the industry standard for grain combine harvesters, the length, width, and height of the caries were 560 mm, 21 mm, and 21 mm, respectively. The chain spacing was 35.2~46.3 mm, and the chain speed was 3~5 m/s.

Based on the above design and parameters, the header platform, cutting bar, combine auger, pentagon reel, and conveying chain were assembled. Assembly drawing of front header is shown in Figure 7.

As shown in Figure 7, there are many rotating parts on the header, which was prone to vibrate with low frequency mode [27]. The vibration of the header has a great influence on the cutting of rice stems, which brings great difficulty to the precise control of the stalk height during the stalk cutting process.

2.2. Stem Cutting Principle. The forward speed and cutting frequency of cutting knife were the major factors that affected the efficiency of rice stem cutting. The cutter consisted of moving knife and fixed knife. Fixed knife was welded and relatively stationary with the header frame. The cutting frequency of the moving knife depended on the frequency of the crank. Then, the cutting speed of the moving knife is shown as follows:

$$V_p = \frac{ns}{30}, \quad (6)$$

where V_p is the cutting speed of the moving knife, n is the cutter crank speed, and s is the stroke of the moving knife.

The forward distance of the front header by the cutter passed a stroke is shown as follows:

$$H = \frac{\pi V}{\omega}, \quad (7)$$

where V is the forward velocity of the front header and ω is the cutter crank angular velocity.

The advancement distance of the header directly affected the area swept by the movable knife on the ground, which is the cutting diagram of the movable knife. The movement of the cutter was synthesized by the forward movement of the head and the reciprocating cutting motion in the horizontal direction. The cutting diagram of the movable knife is shown in Figure 8.

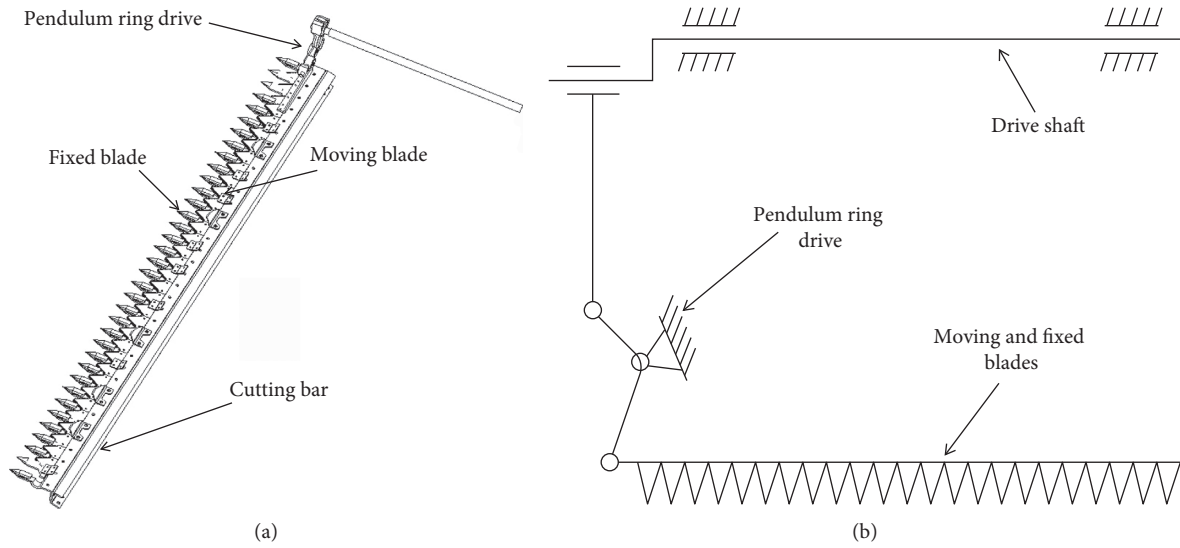


FIGURE 3: Structure and schematic of the cutting bar. (a) Assembly of the cutting bar. (b) Pendulum drive mechanism.

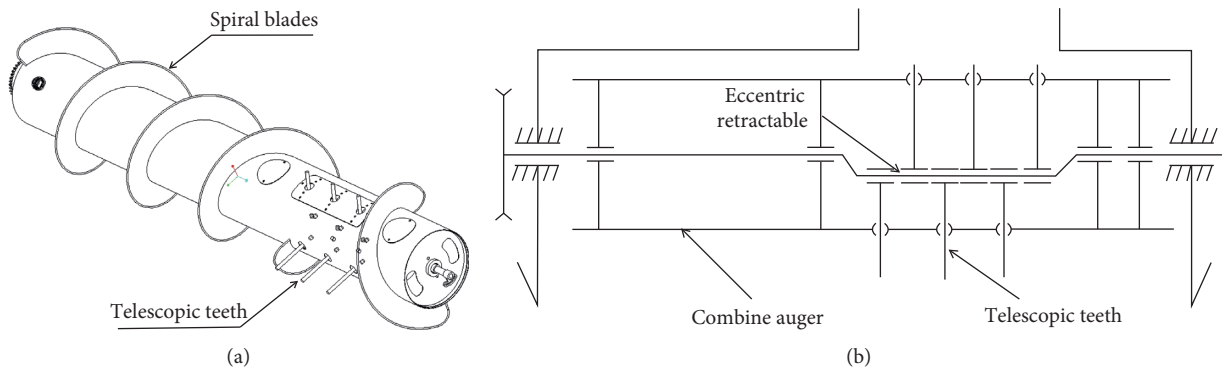


FIGURE 4: Structure and schematic of the combine auger. (a) Assembly of the combine auger. (b) Eccentric retractable gridded fingers.

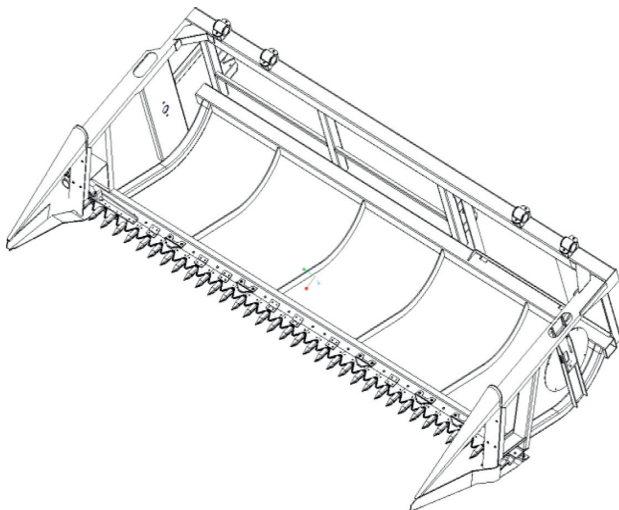


FIGURE 5: Assembly of the header platform.

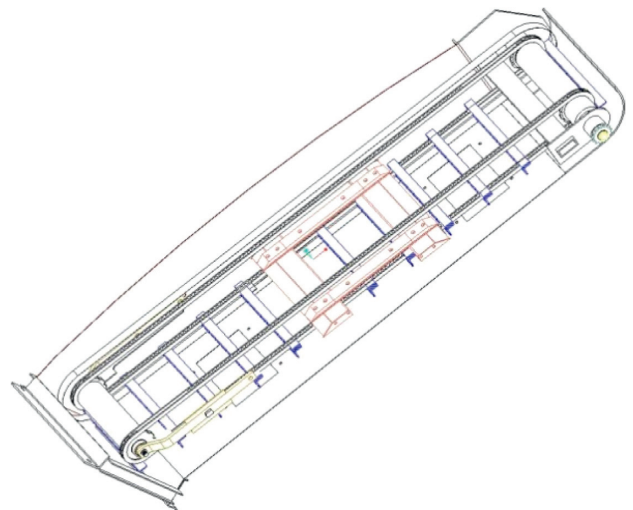


FIGURE 6: Assembly of conveying chain.

As shown in Figure 8, when moving knife was at position 1, the moving knife and fixed knife were at starting position. When the front header forward and the cutter moved to the right, the movable knife reaches the position 2. The trajectory of moving knife was AB and CD. As the front header

forward and the cutter moved to the left, the movable knife reaches the position 3. The trajectory of moving knife was EF and GH. The cutting diagram of movable knife was red shaded area. The red shades from position 1 to position 2 and position 2 to position 3 are visible.

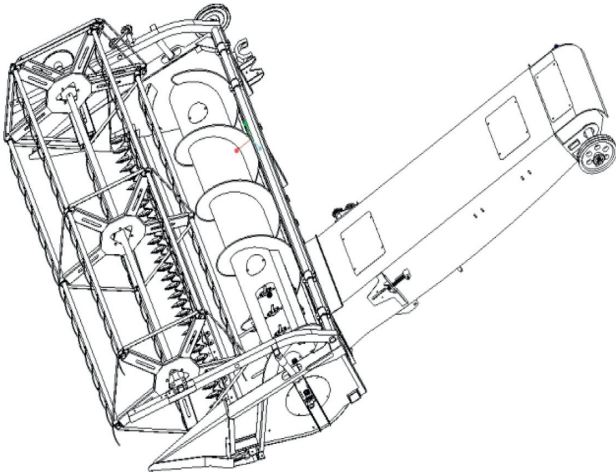


FIGURE 7: Assembly of the front header.

There were three stem cutting areas, zone I, zone II, and zone III. Zone I was the first cutting area of the moving knife; then, zone I was the first cutting area covered by the moving knife from left to right. As the header moved forward, the moving knife would move from right to left and cover an area, which was named as the second cutting area. Zone II was the first and second cutting overlap area of the moving knife. In zone II, the stem would be cut twice. If the header vibrated up and down, zone II showed presence of repeated cuts, which would result in short stalks. The third zone was the leakage cutting zone during the cutter movement. In the area of the leak-cut zone III, the stem would be pushed forward to the next cutting zone for cutting. The Stem oblique cutting principle is shown in Figure 9.

In zone I, the stem would be cut horizontally and the cutting head of the stem would be horizontal (or 90°). The cut horizontally was shown as OA rice stem. In zone II, the stem would be repeatedly cut to produce short stalks. If the header had vibration up and down, the stem would be cut as OB rice stem. In zone III, The missing stalk would be pushed to the next cutting area and the stalk would be cut in a slanted state. The stem would be cut as OC rice stem shown.

2.3. ANSYS Simulation of Front Header. Front header was an assembly device with header platform, cutting bar, combine auger, pentagon reel, and conveying device. The front header's intrinsic mode of dynamic response was an important factor affecting the working state after assembly. The 3D model of the front header was developed by Pro/E and saved as STEP format. Intrinsic modes of front header unit were calculated by ANSYS Workbench [28]. The front header 3D model was gathered and assembled by Pro/E; the assembly model of the front header is shown in Figure 10(a). Then, the 3D model of the front header was imported into ANSYS Workbench and is shown in Figure 10(b).

In order to ensure the free lifting and loading of the front header, the end of the front header was connected to threshing cylinder frame by bearing constraint. The hydraulic cylinder was supported in the middle of the lower side of the conveyer house. The load of the front header was applied to threshing cylinder frame and hydraulic cylinder which were located on

the chassis frame. The two fixed constraint positions A and B beams of the front header were threshing the cylinder frame and hydraulic cylinder on the chassis frame, respectively. The two fixed constraint positions are shown in Figure 11(a).

Front header is mainly welded from Q235 structural steel, angle steel, and square steel. Then, the 3D model was imported into ANSYS Workbench. The material properties selected during ANSYS analysis are elastic modulus $E = 210$ GPa, Poisson's ratio $\mu = 0.33$, density $\rho = 7850$ kg/m³, and yield strength $\sigma_s = 235$ MPa. Because the minimum thickness was 2 mm, the grid size was 2 mm in automatic and swept meshing method. The total number of nodes in the finite element simulation model is 155824. The meshing result is shown in Figure 11(b).

2.4. Experiment Mode of Assembly Front Header. According to the model of header platform, cutting bar, combine auger, pentagon reel, and conveying chain, the front header physical map was processed. The front header of rice combine harvester is shown in Figure 12. The header platform and conveyer aisle were bearer frame. All incentives were applied to the frame. The modality of front header frame was an important factor reflecting the bearing and vibration response of the header.

In order to obtain the experimental mode of header platform and conveyer house, the DH5902 dynamic signal acquisition instrument was used to test the experimental mode. The signal acquisition system and dynamic signal acquisition instrument were produced by Chinese Donghua testing company. The test system consists of vibration signal acquisition system and signal analysis processing system, as shown in Figure 13. The signal acquisition system collected the electrical signal of acceleration on frame under different conditions. Signal acquisition system used the United States of America (PCB) 356A16 type three-component acceleration sensors to test the vibration signals. The methods for testing and analyzing experimental modalities were available in Reference [29].

In order to test the modals of header platform and conveyer aisle, the structure of header platform and conveyer aisle was reduced to a 24-points frame model. The line model is shown in Figure 14(a), and the contour model is shown in Figure 14(b).

The single-input and multi-output method was used to test the modes of header platform and conveyer aisle. Four 356A16 type three-component acceleration sensors were arranged in batches to test the vibration response of 24 points of the header platform. The 13 channels received the excitation signal of the test hammer and the vibration signals of the acceleration sensors.

2.5. Frame Vibration Test of Front Header. In order to analyze the vibration characteristics of the front header in the field, the influence of the vibration characteristics of the header platform with the rice stems cutting was obtained. Two points on the header frame were selected to characterize the vibration of the front header when the rice stem was cut. The vibration of the Point 1 (P1) and Point 2 (P2) represented the cutter bar cutting the rice stem when the header vibrated. Two vibration test points of front header are shown in Figure 15.

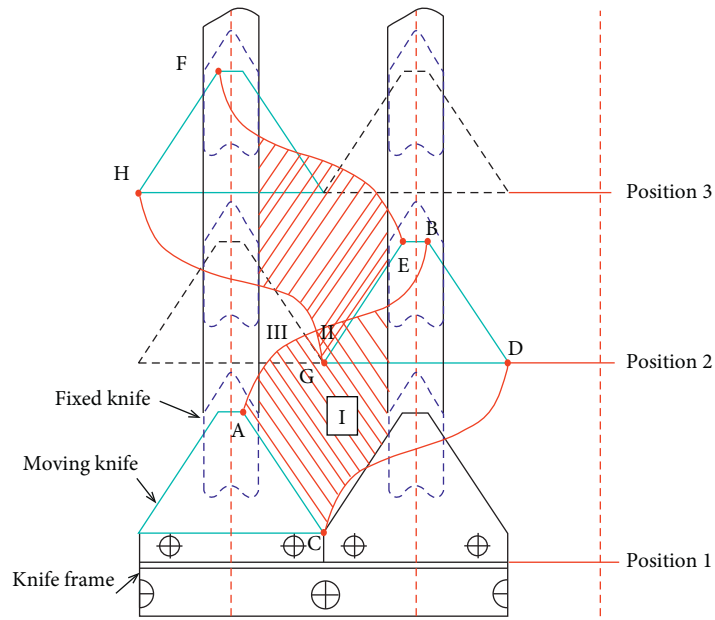


FIGURE 8: Cutting diagram of the movable knife.

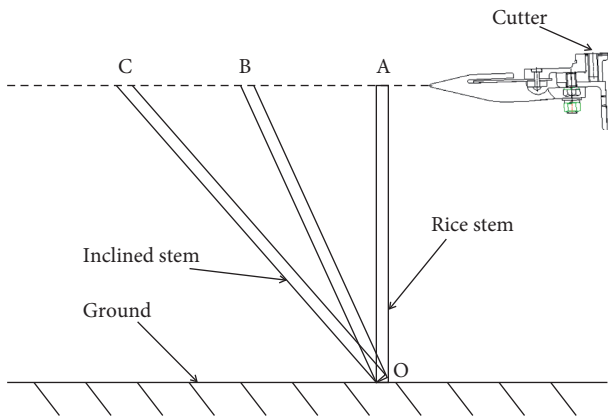
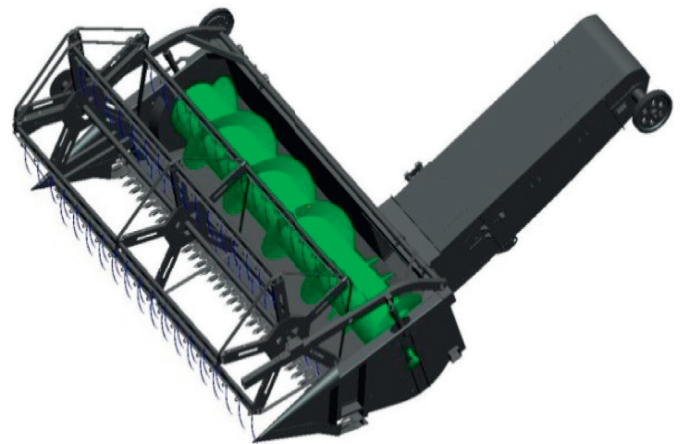


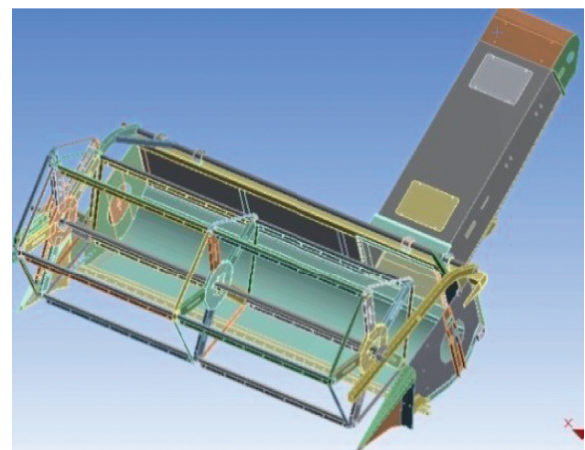
FIGURE 9: Stem oblique cutting principle.

When the combine harvester was working in the field, the vibration of the header at 2 points was tested under the stationary header movement and harvested in the field conditions. The X direction of the test was set to represent the amplitude of the upper and lower vibration of the front header; the Y direction represented the amplitude of the vibration in the left and right direction; the Z direction represented the amplitude of the front and rear vibration.

2.6. Field Rice Stem Cutting Test. In order to study the influence of the header's vibration on cutting the rice stems, the above design parameters were selected and used to test the intrinsic essential relationship between the short stalk and the vibration of the header. The forward speed of the rice combine harvester was set to 0.6~1.0 m/s, and the header used a half-width rice stem cutting method to test the cutting effect of the cutting stalk.



(a)



(b)

FIGURE 10: Assembly device model of the front header. (a) 3D model in Pro/E. (b) Import mode in ANSYS.

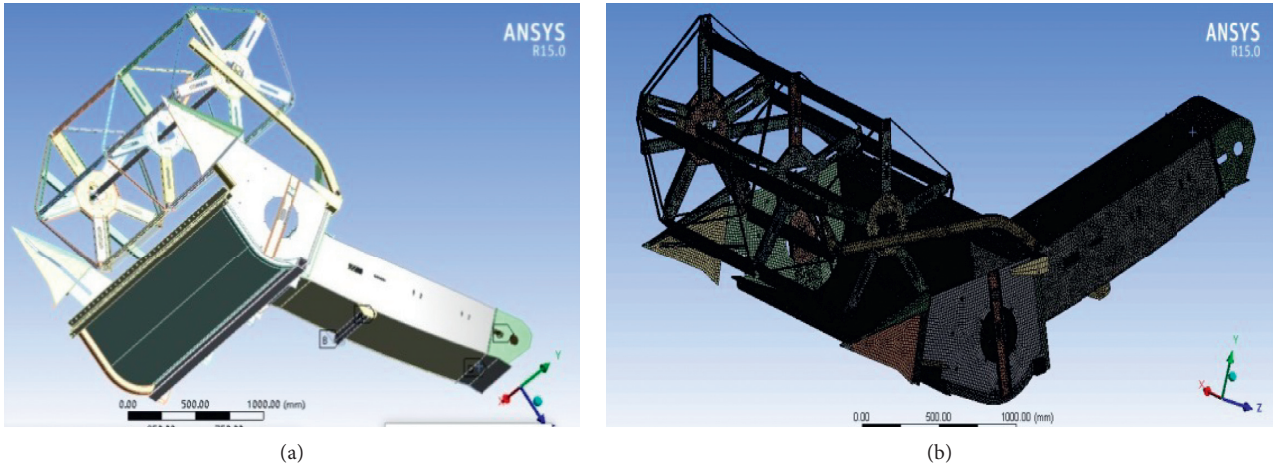


FIGURE 11: (a) Constraint positions at frame beam and (b) mesh model of the front header.



FIGURE 12: Front header physical map.

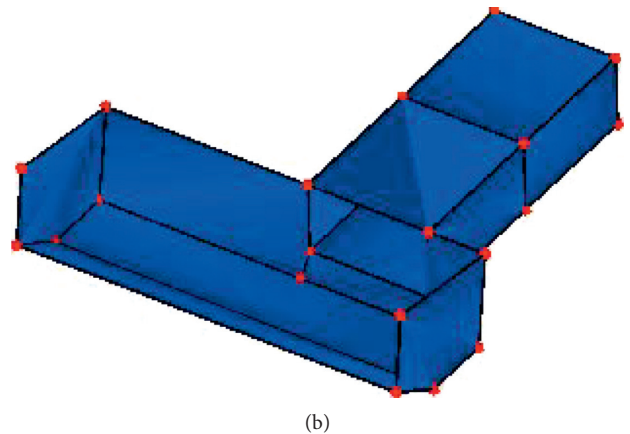
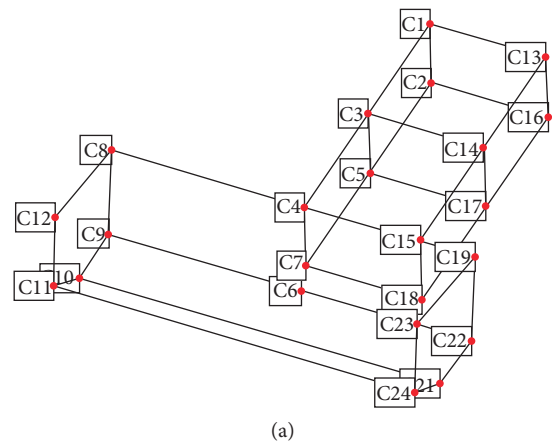


FIGURE 14: Frame model of header platform and conveyer house. (a) Line model. (b) Contour model.

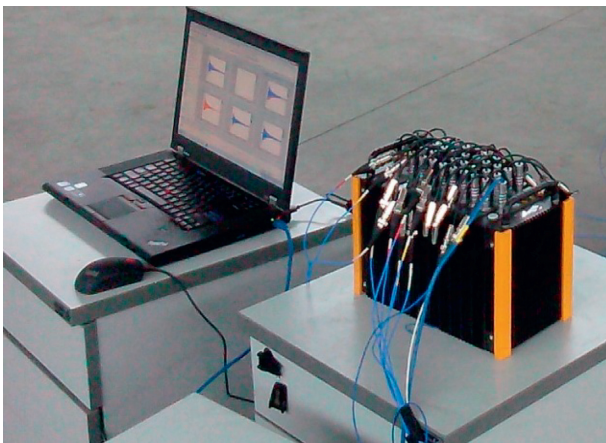


FIGURE 13: Dynamic signal acquisition instrument.

3. Results and Discussion

3.1. *Inherent Modals of Front Header.* In order to obtain a more reasonable structural mode of front header, the

transmission device of front header was deleted. The structure of front header was simplified. The inherent modals of front header were simulated by ANSYS software. The modal shapes under restricted modality are shown in Figure 16. The mode shapes mainly appeared on pentagonal reel and divider.

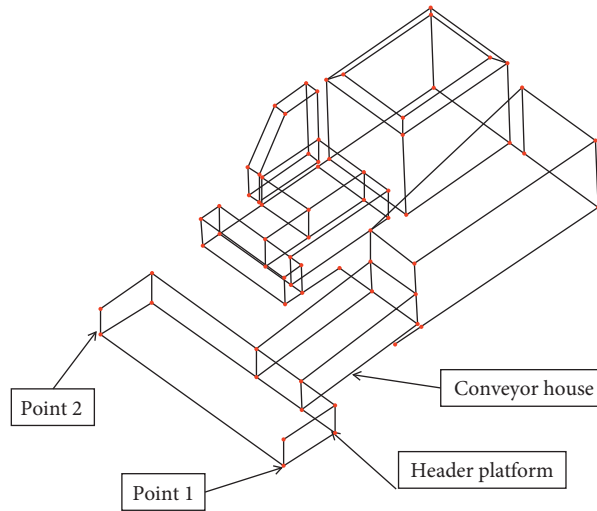


FIGURE 15: Two vibration test points on the front header.

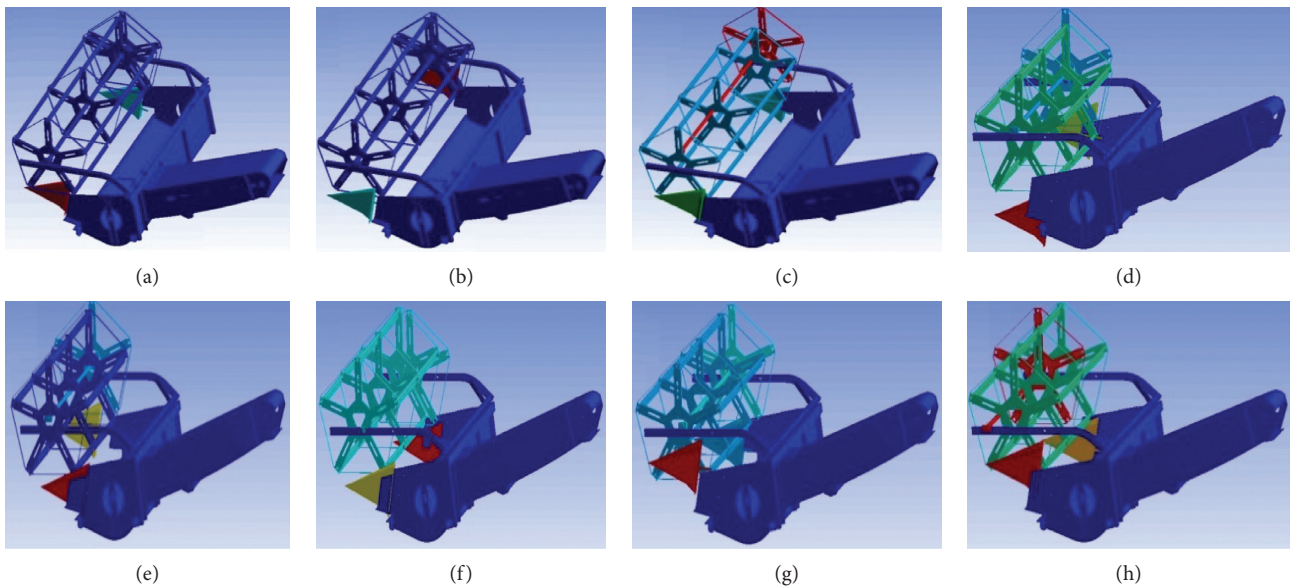


FIGURE 16: Modal shapes under restricted modality. (a) 1st modal shape. (b) 2nd modal shape. (c) 3rd modal shape. (d) 4th modal shape. (e) 5th modal shape. (f) 6th modal shape. (g) 7th modal shape. (h) 8th modal shape.

According to Figure 16, the 1st intrinsic constraint frequency of front header was 5.28 Hz, and its corresponding mode shape was left and right vibration of the divider. The maximum amplitude of the mode shape on divider side was about 10.09 mm. The frequencies from the 2nd inherent frequency to the 8th inherent constraint frequency were 5.64, 20.28, 29.77, 32.36, 33.85, 44.21, and 46.42 Hz, respectively. The modal shapes and amplitude positions are shown in Figure 16. Based on the natural frequency distribution, the vibration mode, mode vibration frequency, and shapes of the front header are shown in Table 1.

According to Figure 16 and Table 1, the frequency of front side plates (divider) at both ends of the header is 5.28–5.64 Hz, and the first natural frequency of the board will cause vibration during the work of the header. In order to avoid the vibration of the two sides of the header, the side plate is replaced with a round steel divider.

3.2. Experiment Mode of Front Header. The signals of acceleration sensors and the hammer were input into the model of software to solve the frequency response curve of the header platform. The conveyer aisle and the steady state diagram of the mode were analyzed by the DH5902 dynamic signal acquisition instrument. Modal mode and modal frequency of header platform and conveyer aisle were obtained by the DH5902 dynamic signal acquisition system. The Modal shapes of the header platform and conveyer aisle are shown in Figure 17.

According to Figure 17, the 1st intrinsic constraint frequency of header platform and conveyer aisle was 23.38 Hz. The corresponding mode shape was up and down vibration of conveyer house. The maximum amplitude of the mode shape on conveyer aisle was 1.76 mm. The frequencies from the 2nd inherent frequency to the 8th inherent constraint frequency were 48.98, 56.45, 78.92, 94.64, 110.75,

TABLE 1: Mode vibration frequency and shape of front header.

Mode frequency order	Natural frequency (Hz)	Maximum amplitude (mm)	Mode vibration shape
1	5.28	10.09	Left and right vibration of the divider
2	5.64	11.64	Left and right vibration of the divider
3	20.28	15.42	Radial vertical vibration of pentagonal reel
4	29.77	16.54	Radial vertical vibration of pentagonal reel
5	32.36	19.39	Left and right vibration of the divider
6	33.85	27.54	Left and right vibration of the divider
7	44.21	18.84	Left and right vibration of pentagonal reel and divider
8	46.42	24.41	Left and right vibration of pentagonal reel and divider

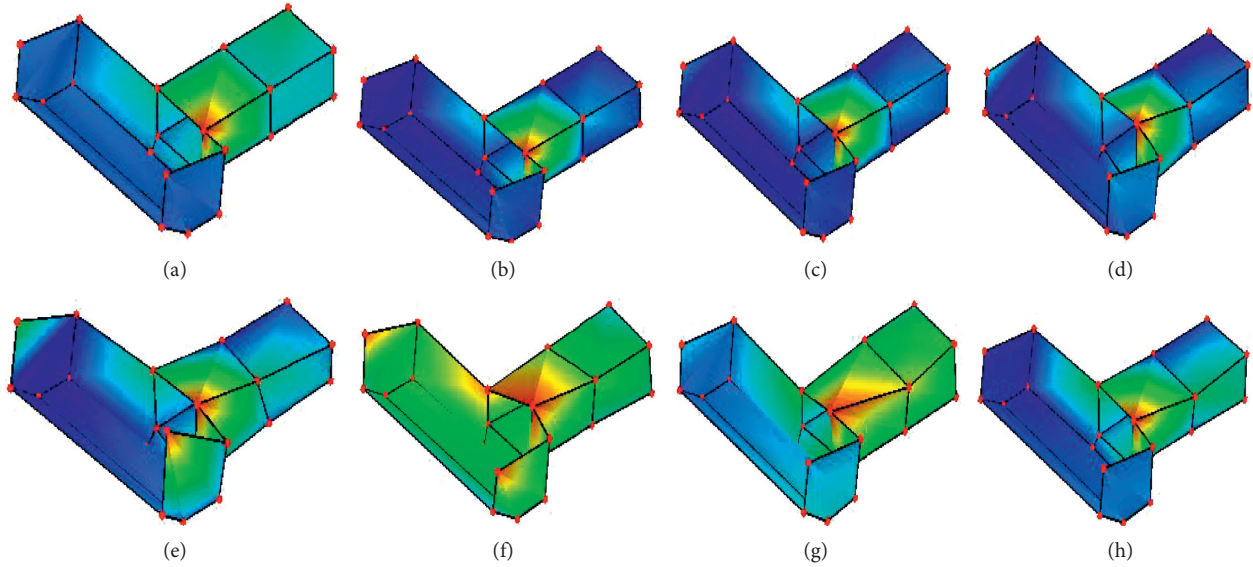


FIGURE 17: Modal shapes of header platform and conveyer house. (a) 1st modal shape. (b) 2nd modal shape. (c) 3rd modal shape. (d) 4th modal shape. (e) 5th modal shape. (f) 6th modal shape. (g) 7th modal shape. (h) 8th modal shape.

144.12, and 185.02 Hz. The modal shapes and amplitude positions are shown in Figure 17. Based on the natural frequency distribution, the vibration mode, the mode vibration frequency, and shapes of header platform and conveyer aisle are shown in Table 2.

In order to compare the natural frequencies of the various parts of front header and the vibration response characteristics at each frequency, the vibration frequency of header platform, cutting bar, combine auger, pentagon reel, and conveying chain was analyzed. The modal shapes of pentagon reel, combine auger, header platform, and conveyer aisle are shown in Figure 18.

The vibration frequency of header platform, cutting bar, combine auger, pentagon reel, and conveying chain were counted and shown in Table 3.

As shown in Table 3, each intrinsic constraint frequency and modal shapes were different. The vibration frequency of the thin plate position was small, such as combine auger, header platform, conveying aisle, and assembly front header. The frame structure had a high natural frequency. Experiment modal frequency of assembly front header was high natural frequency. Then, the response of the low frequency vibration to the frame excitation was not obvious. As shown in Table 3, the intrinsic frequencies 23.38 Hz, 48.98 Hz, 110.75 Hz, and 144.12 Hz were sensitive response frequencies.

3.3. Frame Vibration of Front Header. There were two points which were selected to characterize the vibration of the header front on the header frame during cutting the rice stem. The vibration signals of point 1 in three directions of XYZ are shown in Figure 19.

The maximum and minimum amplitudes, the mean value of the vibration, and the variance of the vibration could be calculated by the vibration signal and the vibration test software. The vibration amplitude test results under various conditions are shown in Table 4.

According to Table 4, the amplitude of point 1 was 18.37~23.49 mm with the mean 0.02~0.04 mm. The average value was less than 0.04 mm, which can be considered that the balance of the vibration was zero. That is to say, the vibration at the static no-load state of the test was steady state. Due to the unstable vibration, the vibration fluctuated greatly, and the variance of the solved vibration mean was 3.07~4.37 mm. The vibration amplitudes of the first point and the second point on the header were not the same. The difference of vibration amplitudes was due to the too long header, which will generate left and right shaking. As shown in Table 4, the vibration of the second point in the front-rear direction was large. The field vibration values of the above headers were similar to those of Reference [30]. As shown in Reference [30], the header vibration was tested during

TABLE 2: Mode vibration frequency and shape of front header.

Mode frequency order	Natural frequency (Hz)	Maximum amplitude (mm)	Mode vibration shape
1	23.38	1.76	Up and down vibration of conveyer house
2	48.98	1.02	Up and down vibration of conveyer house
3	56.45	0.78	Left and right vibration of conveyer house
4	78.92	0.81	Left and right vibration of conveyer house
5	94.64	0.42	Left and right vibration of left frame side panel
6	110.75	1.68	Whole body vibration of header and conveyer frame
7	144.12	1.17	Left and right vibration of conveyer house
8	185.02	0.31	Left and right vibration of conveyer house

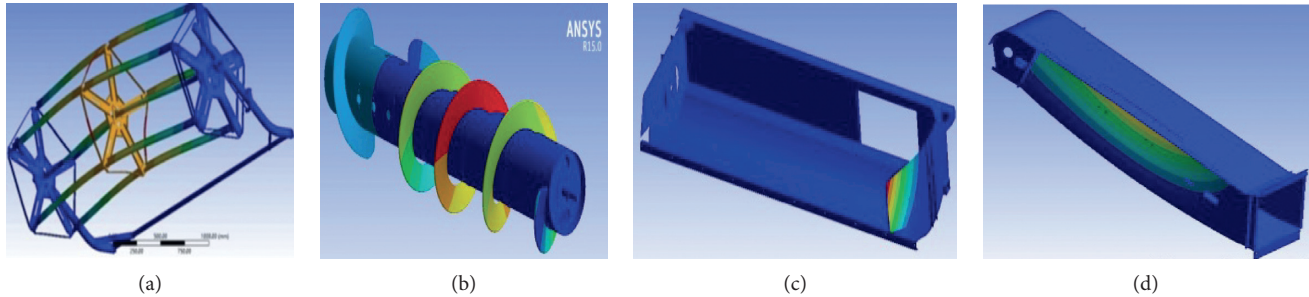


FIGURE 18: Modal shapes under restricted modality. (a) Pentagon reel. (b) Combine auger. (c) Header platform. (d) Conveyer aisle.

TABLE 3: Mode vibration frequency of various parts of front header.

Mode frequency order	Pentagon reel simulation frequency (Hz)	Combine auger simulation frequency (Hz)	Header platform simulation frequency (Hz)	Conveying aisle simulation frequency (Hz)	Simulation frequency of assembly front header (Hz)	Test modal frequency of assembly front header (Hz)
1	20.65	4.96	5.09	8.78	5.28	23.38
2	29.31	5.15	5.13	9.54	5.64	48.98
3	29.81	6.89	12.59	11.42	20.28	56.45
4	35.86	8.34	13.41	13.74	29.77	78.92
5	38.13	14.36	32.27	15.50	32.36	94.64
6	38.18	26.28	33.38	21.12	33.85	110.75
7	39.99	32.18	45.67	21.55	44.21	144.12
8	49.18	63.28	48.55	29.56	46.42	185.02

harvesting in the wheat field. These vibration values were similar features.

When the header worked in the field, the vibration amplitude of the first measuring point on the header in the vertical direction was 25.36 mm, which was significantly higher than no load. However, the vibration of the header in the horizontal and fore-and-rear directions was significantly reduced. When the header worked in the field, the mean value of the vibration increased to 0.12~0.32 mm significantly, but the variance of the mean became smaller. It can be concluded that the vibration of the cutting stalk in the header field was random, and the mean value of the vibration had a tendency to deviate from the origin. However, due to the influence of the stem characteristics, the vibration fluctuation and variance of the mean of the header became smaller. The vibration response of point 2 on the header increased, mainly because the point was far from the trough. When the header was cutting in rice, the vibration amplitude, mean value, and variance of the first and second measurement points were similar.

According to the vibration signals, the vibration analysis software performed FFT (fast Fourier transformation) on the vibration signal to obtain the spectrum of the vibration values. The four orders of vibration frequency are shown in Table 5.

As shown in Table 5, the first-order vibration frequency of the two measuring points was high-frequency. When the header was unloaded, the first-order vibration frequency was 91.79 Hz. The natural frequency of the structure was different. The second-order natural frequency, 31.25 Hz, was closer to the combine auger simulation frequency 32.18 Hz. The third-order natural frequency 15.63 Hz was closer to the conveying aisle simulation frequency 15.50 Hz. Other frequencies are high frequencies, such as 515.63 Hz, 347.63 Hz, and 232.42 Hz. Such high frequency vibrations should be related to the random excitation of the drive sprocket or ground on the header structure. The vibration frequency of the header was significantly higher than the vibration frequency of the header, which was stationary and no load. These vibration frequencies were affected by the random excitation of the ground and the excitation characteristics of the stem cutting.

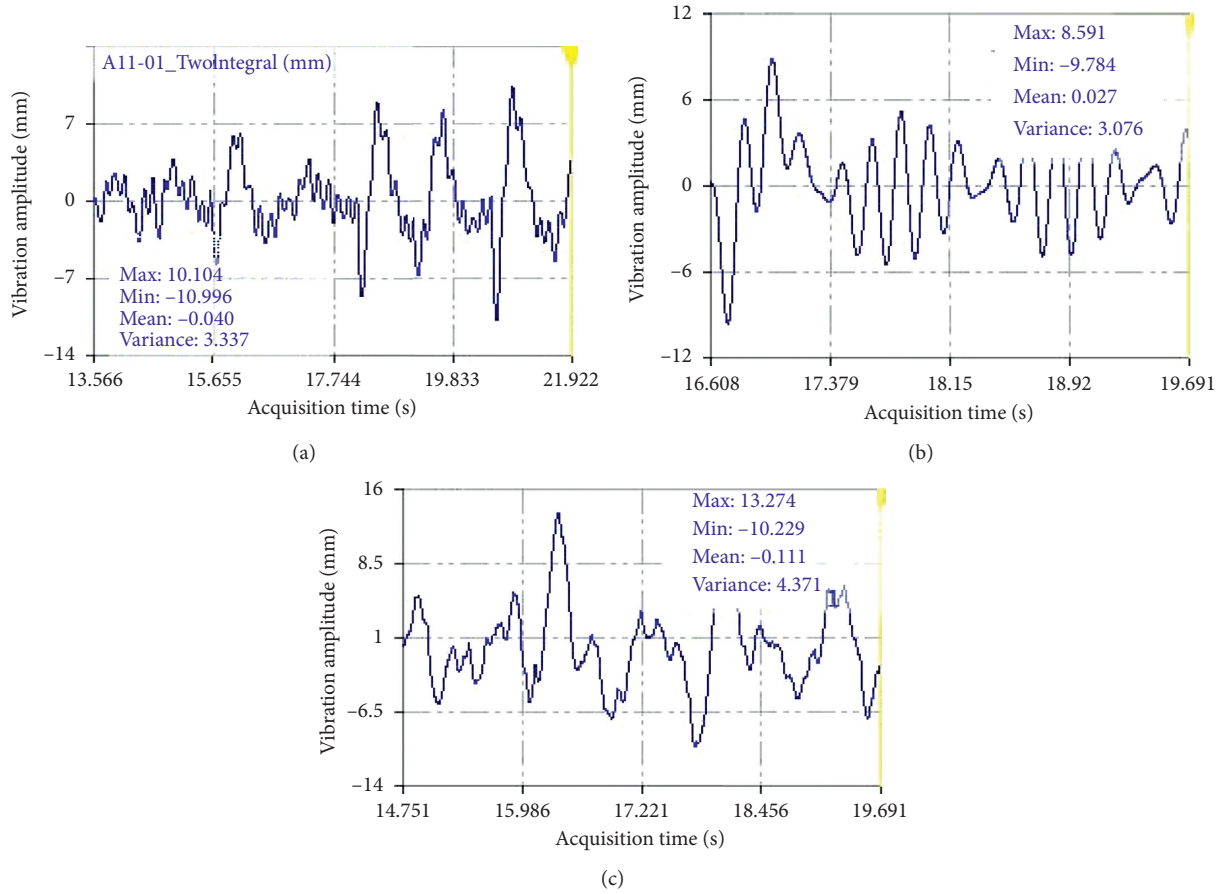


FIGURE 19: Vibration signal of X-Y-Z direction. (a) X direction signal. (b) Y direction signal. (c) Z direction signal.

TABLE 4: Vibration amplitude test results at 2 points.

Test point	Static idling vibration value (mm)				Walking harvesting (mm)			
	Maximum	Minimum	Mean	Variance	Maximum	Minimum	Mean	Variance
1X	10.10	-10.99	-0.04	3.33	13.62	-11.74	0.14	1.64
1Y	8.59	-9.78	-0.02	3.07	6.25	-6.43	0.22	1.48
1Z	13.27	-10.22	0.02	4.37	6.64	-11.40	0.12	1.66
2X	9.34	-12.47	-0.02	3.27	13.34	-10.67	0.18	1.82
2Y	9.90	-17.15	-0.04	3.86	12.48	14.37	0.26	1.64
2Z	18.41	-16.01	0.02	3.48	18.02	16.71	0.32	1.79

TABLE 5: Frequency response test results at 2 points.

Test point	Static idling vibration value (Hz)				Walking harvesting (Hz)			
	1st	2nd	3rd	4th	1st	2nd	3rd	4th
1X	91.79	31.25	15.63	517.57	515.63	347.66	669.92	365.23
1Y	31.25	15.63	91.79	46.87	515.63	541.02	31.25	15.63
1Z	509.76	365.23	91.79	515.63	365.23	513.67	537.11	496.09
2X	91.79	15.63	44.93	1.96	232.42	546.88	582.03	537.11
2Y	91.79	46.86	15.63	31.25	582.03	64.46	546.88	541.02
2Z	91.79	15.63	11.72	751.84	574.22	171.22	582.03	226.56

3.4. Rice Stem Cutting in Field. The cutting stage of the front header was tested at speeds of 0.6, 0.8 and 1.0 m/s. The cutting effects of the stem under different cutting speeds of the header are shown in Figure 20.

When the rice stalks were cut by the header, the height of the stalk and the angle of the cut surface were tested. The short stalks produced by cutting repeatedly were collected. And the length interval and distribution of the short stalks were counted.

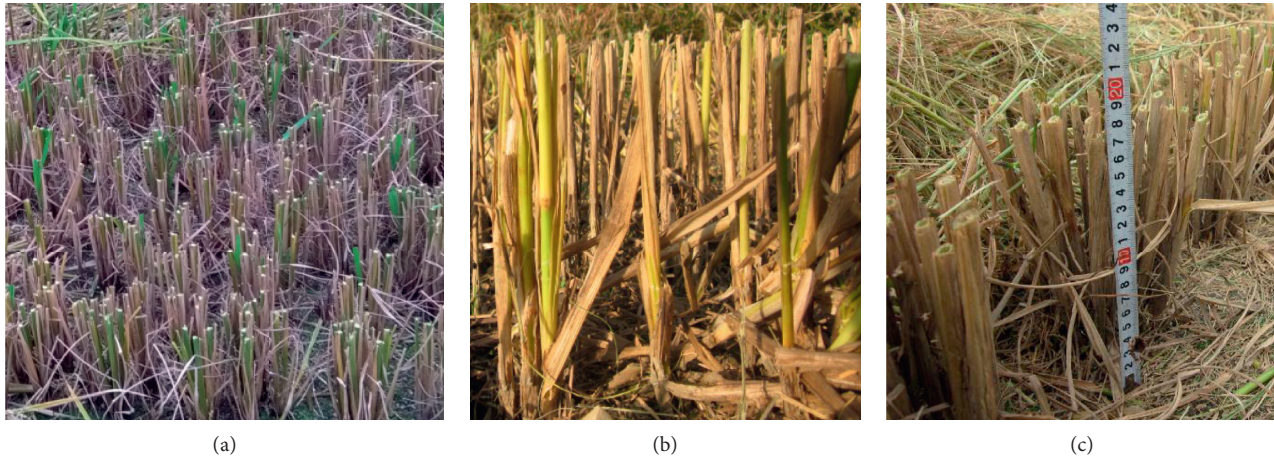


FIGURE 20: Stem cutting effect at different forward speeds: (a) 0.6 m/s, (b) 0.8 m/s, and (c) 1.0 m/s.

As shown in Figure 20(a), when the heading speed is 0.6 m/s, the cut rice stalks are uneven. There are more short stalks on the ground [31]. As shown in Figure 8, the stem cutting will be located in the II region of the cutting map. So, the stem will be repeatedly cut with a forward speed of 0.6 m/s. The reason of stalks cutting repeatedly is the moving knife, which moves twice in the forward direction of the header. In short, when the forward speed is less than the cutting frequency of the cutter reciprocating, the stem will be repeatedly cut. So, a large number of stems will be repeatedly cut and form into broken stalks. The rice stems formed by repeated cutting are shown in Figure 21.

As shown in Figure 20(b), when the cutting speed is 0.8 m/s, the height of the rice stems cut by the cutter is relatively flat. The number of broken stems is small. Therefore, the forward speed of 0.8 m/s is an ideal advance speed of the cutter.

As shown in Figure 20(c), when the cutting speed of the cutter is 1.0 m/s, the rice stalk are cut neatly. There are fewer broken stalks on the ground. The cut end faces of rice stalks have different degrees of slopes. The results of cutting surface angle are shown in Figure 22.

As shown in Figure 21, the length of the repeatedly cut stems was normally distributed. The length of the cut stems was distributed between 14.20 and 45.40 mm, which the mean length was 23.60 mm. This length is inextricably linked to the up and down vibration of the header. As shown in Table 4, when the header was in the cutting work, the header was vibrated up and down by 25.36 mm. The peak-to-peak value of the upper and lower vibration of the header was similar to the length of the stem being repeatedly cut with an error of 7.46%. If the header does not vibrate up and down during cutting, the cutter will not produce short stalks. In the actual cutting process, the cutter was vibrating up and down, so the cutter produces short stalks. From the theoretical cutting, the length of the short stalk was the peak-to-peak (upper and lower) vibration value.

As shown in Figure 22, when the cutting head advance speed was 1.0 m/s, the cutting head forward speed was

faster than the cut frequencies. More stems were less likely to be cut or pushed to be cut. According to the stem oblique cutting principle shown in Figure 9, there were three types of bevel angles, 38° , 44° , and 62° , which were cut by the header. The cutting surface angle (62°) was mainly caused by the faster forward speed. The faster forward speed causes the slope to be cut when the stem was cut. The cutting surface 44° was caused by the repeated cutting zone II in the main cutting diagram. Stalk was also inclined when it was cut for the second time. The cutting surface 38° was caused by the missing cutting zone III in the main cutting diagram. So, the faster forward speed causes the stem to be cut obliquely.

4. Conclusion

- (1) The vibration amplitude of one side of header was 18.37~23.49 mm with the mean 0.02~0.04 mm. The mean vibration value is less than 0.04 mm, which can be considered that the balance of the vibration is zero at no-load state. The frame structure has a high natural frequency than the thin plate position.
- (2) When the header was cutting rice, the vibration amplitude, mean value, and variance of the first and second measurement points were the similar. The length of the cut stems was distributed between 14.20 and 45.40 mm; the mean length is 23.60 mm. This length is inextricably linked to the up and down vibration of the header 25.36 mm. The peak-to-peak value of the upper and lower vibration was similar to the length of the stems which were cut repeatedly.
- (3) The cutting surface angle (62°) was mainly caused by the faster forward speed. The cutting surface 44° was caused by the repeated cutting zone II in the main cutting diagram. The cutting surface 38° was caused by the missing cutting zone III in the main cutting diagram. The faster forward speed causes the stem



FIGURE 21: Interval length distribution and distribution of short stems of rice.

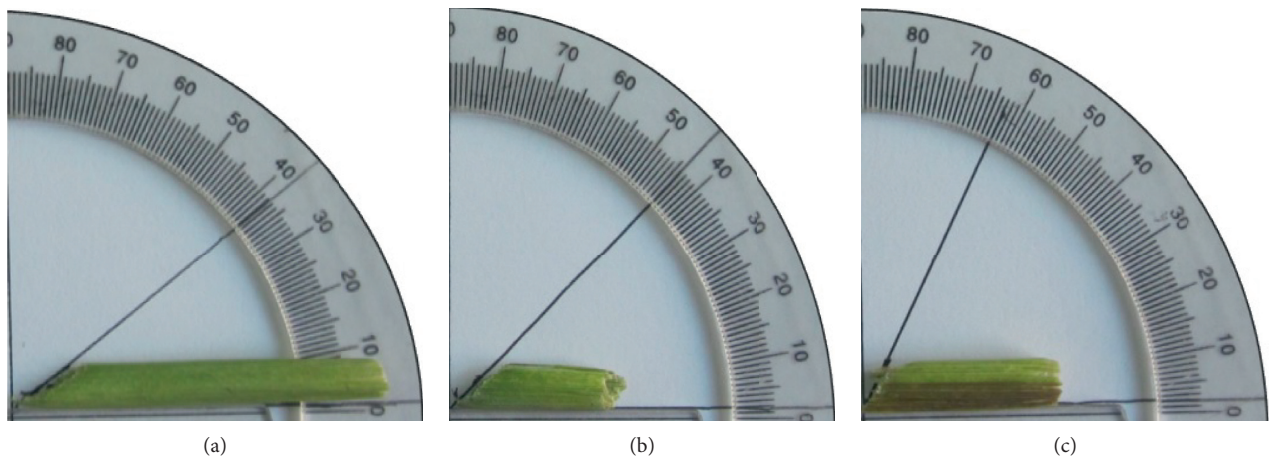


FIGURE 22: Cutting surface angle of stems at different forward speeds. (a) Surface angle 38° . (b) Surface angle 44° . (c) Surface angle 62° .

to be cut obliquely. If height of the rice stems cut by the cutter should be relatively flat, the forward speed of 0.8 m/s is an ideal advance speed of the cutter.

Data Availability

The data used to support the findings of this study are available from the corresponding author upon request.

Conflicts of Interest

The authors declare that they have no conflicts of interest.

Acknowledgments

This research work was supported by the National Natural Science Foundation of China (51705212), the Natural Science Foundation of Jiangsu Province (BK20170553), the National Key Research and Development Plan (2016YFD0702004), and a project funded by the Priority

Academic Program Development of Jiangsu Higher Education Institutions (PAPD).

References

- [1] Y. L. Wang, Y. Zeng, L. K. Xu, J. X. Sun, and M. Zhao, "Establishing the shafting vibration model under the condition of spindle torsional deformation," *Journal of Drainage and Irrigation Machinery*, vol. 37, no. 7, pp. 600–605, 2018.
- [2] S. Jiang, W. Yao, J. Chen, and T. Cai, "Finite element modeling of FRP-strengthened RC beam under sustained load," *Advances in Materials Science and Engineering*, vol. 2018, Article ID 7259424, 16 pages, 2018.
- [3] Z. Tang, Y. M. Li, R. Wang, and J. S. Chen, "Experimental study of multi-source dynamic load of combine harvester in rice harvesting," *International Agricultural Engineering Journal*, vol. 25, no. 3, pp. 46–52, 2016.
- [4] B. Bai and L. X. Zhang, "Dynamic response of hydro-turbine set shaft system under stochastic hydraulic excitation," *Journal of Drainage and Irrigation Machinery*, vol. 35, no. 5, pp. 398–403, 2017.

- [5] Q. Guo, X. L. Zhang, Y. F. Xu, P. P. Li, C. Chen, and H. W. Xie, "Simulation and experimental study on cutting performance of tomato cane straw based on EDEM," *Journal of Drainage and Irrigation Machinery*, vol. 30, no. 10, pp. 1017–1022, 2018.
- [6] R. Ebrahimi, M. Esfahanian, and S. Ziaei-Rad, "Vibration modeling and modification of cutting platform in a harvest combine by means of operational modal analysis (OMA)," *Measurement*, vol. 46, no. 10, pp. 3959–3967, 2013.
- [7] S. Chuan-Udom, "Development of a cutter bar driver for reduction of vibration for a rice combine harvester," *Asia-Pacific Journal of Science and Technology*, vol. 15, no. 7, pp. 572–580, 2017.
- [8] T. Fukushima, E. Inoue, M. Mitsuoka, T. Okayasu, and K. Sato, "Collision vibration characteristics with interspace in knife driving system of combine harvester," *Engineering in Agriculture, Environment and Food*, vol. 5, no. 3, pp. 115–120, 2012.
- [9] T. Fukushima, E. Inoue, M. Mitsuoka, M. Matsui, and T. Okayasu, "Vibration characteristics and modeling of knife driving system of combine harvester (Part 2)," *Journal of the Japanese Society of Agricultural Machinery*, vol. 68, no. 5, pp. 59–64, 2006.
- [10] Y. X. Yu, Q. D. Meng, Y. L. Li, and W. Mao, "Load spectrum test and fatigue analysis of cutting table frame of 4LZ-4.6 whole-feeding harvester," *Journal of Zhejiang Sci-Tech University (Natural Sciences)*, vol. 35, no. 5, pp. 720–725, 2016.
- [11] D. D. Kong, J. Yin, L. Xiao, and K. Zhang, "Simulation analysis and optimal design of the lifting header of combined harvester based on motion," *Machinery Design and Manufacture*, vol. 2, pp. 231–234, 2018.
- [12] Y. Liao, Y. Xiang, M. L. Wu, D. W. Liu, Y. Q. Cheng, and Y. L. Li, "Design and test of the adaptive height adjustment system for header of the combine-harvester," *Journal of Hunan Agricultural University (Natural Sciences)*, vol. 44, no. 3, pp. 326–329, 2018.
- [13] Y. N. Li, Y. W. Yi, S. W. Du, Q. S. Ding, and W. M. Ding, "Design and experiment on air blowing header of plot combine harvester for grain," *Transactions of the CSAE*, vol. 48, no. 6, pp. 79–87, 2017.
- [14] Y. Li, X. L. Zhang, Q. Dan, and B. Xu, "The finite element modal analysis of the frame of cutting table on 4LZ-2.0 rice and wheat combine harvester," *Journal of Agricultural Mechanization Research*, vol. 11, pp. 90–93, 2011.
- [15] Z. P. Gao, L. Z. Xu, Y. M. Li, Y. D. Wang, and P. P. Sun, "Vibration measure and analysis of crawler-type rice and wheat combine harvester in field harvesting condition," *Transactions of the Chinese Society of Agricultural Engineering*, vol. 33, no. 20, pp. 48–55, 2017.
- [16] M. T. Li, J. J. Liu, L. J. Zhu, J. Z. Zhao, and Z. Zha, "Vibration finite element modal analysis of combine harvester header and inclined conveyer," *Journal of Chinese Agricultural Mechanization*, vol. 38, no. 7, pp. 10–16, 2017.
- [17] X. J. He, "Upgrade of rice harvester hydraulic system," *Journal of Agricultural Mechanization Research*, vol. 11, pp. 74–79, 2018.
- [18] K. Lu, G. Z. Zhang, S. B. Peng et al., "Design and performance of tracked harvester for ratoon rice with double-headers and double threshing cylinders," *Journal of Huazhong Agricultural University*, vol. 36, no. 5, pp. 108–114, 2017.
- [19] S. Chuan-Udom, T. Srison, and W. Wiangwisad, "Comparative study on vibration of a combine harvester due to operation of cutter bar driver, reel, and auger," *TSAE Journal*, vol. 15, no. 1, pp. 3–6, 2009.
- [20] M. Liang, "Optimization design for structure reliability of cutting table wheat harvester based on improved particle swarm optimization algorithm," *Journal of Agricultural Mechanization Research*, vol. 2, pp. 52–56, 2017.
- [21] S. G. Ren, F. Jiao, M. L. Wu, S. Z. He, and S. Z. Tang, "Studies of united harvest machine cutting system structure parameters on the vibration impact," *Journal of Agricultural Mechanization Research*, vol. 11, pp. 38–43, 2018.
- [22] Z. Tang, Y. M. Li, and C. H. Wang, "Experiments on variable-mass threshing of rice in the tangential-longitudinal-flow combine harvester," *Journal of Agricultural Science and Technology*, vol. 15, no. 4, pp. 1319–1334, 2013.
- [23] Z. Tang, Y. Li, L. Xu, and F. Kumi, "Modeling and design of a combined transverse and axial flow threshing unit for rice harvesters," *Spanish Journal of Agricultural Research*, vol. 12, no. 4, pp. 973–983, 2014.
- [24] C. Y. Chen, X. Z. Wang, and Z. F. He, "Design of header for rape harvesting using grain combine harvester," *Transactions of the Chinese Society of Agricultural Engineering*, vol. 34, no. 5, pp. 54–60, 2003.
- [25] Z. Tang, H. T. Zhang, and Y. P. Zhou, "Unbalanced vibration identification of tangential threshing cylinder induced by rice threshing process," *Shock and Vibration*, vol. 2018, Article ID 4708730, 14 pages, 2018.
- [26] Y. Shi, X. Zhang, S. Cui, and K. Ma, "Contact forces in a screw feeding process," *Advances in Materials Science and Engineering*, vol. 2018, Article ID 4924582, 6 pages, 2018.
- [27] X. X. Xiao, H. Li, X. D. Qi, and M. Wang, "Modal and transient analysis of threshing cylinder based on ANSYS Workbench," *Journal of Agricultural Mechanization Research*, vol. 8, pp. 46–50, 2016.
- [28] L. J. Yao, W. D. Cao, X. Jiang, Q. Zhang, and Y. M. Xu, "FEA for rotor system of axial flow pump based on ANSYS," *Journal of Drainage and Irrigation Machinery*, vol. 37, no. 7, pp. 612–617, 2018.
- [29] L. Bai, Y. Li, M. Yang, Z. Yao, and Z. Yao, "Influences of process parameters and vibration parameters on the forming force in the ultrasonic-assisted incremental forming process," *Advances in Materials Science and Engineering*, vol. 2018, Article ID 5726845, 12 pages, 2018.
- [30] Z. Tang, Y. M. Li, and J. B. Liu, "Dynamic vibration test and analysis of 4LZ-2.5B combine harvester cutting table rack in wheat harvesting," *International Agricultural Engineering Journal*, vol. 26, no. 1, pp. 79–86, 2017.
- [31] Z. Tang, Y. Li, Z. Zhao, and T. Sun, "Structural and parameter design of transverse multi-cylinders device on rice agronomic characteristics," *Spanish Journal of Agricultural Research*, vol. 13, no. 4, article e0216, 2015.

Research Article

Effects of Welded Mechanical Heterogeneity on Interface Crack Propagation in Dissimilar Weld Joints

Fu-qiang Yang ¹, He Xue ², Ling-yan Zhao ¹ and Xiu-rong Fang ²

¹School of Science, Xi'an University of Science & Technology, Xi'an 710054, China

²School of Mechanical Engineering, Xi'an University of Science & Technology, Xi'an 710054, China

Correspondence should be addressed to Fu-qiang Yang; yang_afreet@163.com

Received 23 November 2018; Accepted 6 January 2019; Published 3 February 2019

Guest Editor: Dariusz Rozumek

Copyright © 2019 Fu-qiang Yang et al. This is an open access article distributed under the Creative Commons Attribution License, which permits unrestricted use, distribution, and reproduction in any medium, provided the original work is properly cited.

The stress and strain status associated with the material properties is one of the main factors affecting stress corrosion cracking (SCC) of structural components in nuclear power plants (NPPs). In many SCC prediction models, the stress intensity factor calculated with homogeneous materials is used to characterize the crack tip stress state. However, the mechanical and material properties in weld joints are heterogeneous, which will produce the discontinuous distribution of stress and strain nearby crack tip and affect the crack propagation. To understand the material mechanical heterogeneity effects on interface crack propagation, the specimens with ultimate tensile strength mismatch and elastic modulus mismatch were studied by using an extended finite element method (XFEM). The results indicate that the interface crack extension is easy to occur in the specimens with larger ultimate tensile strength mismatch, while the elastic modulus mismatch has little effects on crack extension. The different interface cracks in the dissimilar metal weld joints of the reactor pressure vessel used in NPPs tend to deviate from the initial direction into alloy 182, and the interface crack propagation path fluctuation is small.

1. Introduction

It is widely known that welding defects such as inclusions, pores, and incomplete penetration are common in welding zone, which will affect the integrity of weld structure. However, a weld structure exists in subcomponents of pressure vessels, pressurizers, steam generators, piping, and deaerators in primary water systems of pressurized water reactors (PWRs) [1]. A typical application of weld joints in PWRs is the dissimilar metal weld (DMW) joints connecting the low alloy steel (LAS) reactor pressure vessel (RPV) nozzles to austenitic stainless steel (SS) pipes, as shown in Figure 1; initially, the Ni-base alloy buttering is predeposited on the RPV nozzle face, then welding is carried out between the buttering layer and the pipe with Ni-base alloy [2]. The operating experience of nuclear power plants (NPPs) shows that the weld zone is more susceptible to stress corrosion cracking (SCC), which seriously threatens the safety of NPPs [3–5]. In order to avoid the sudden failure of components and structures caused by SCC in NPPs, efforts have been made to understand the mechanism of SCC [6–8], and many

SCC crack prediction models have been developed to predict the remaining life of main structures during the last three decades [9, 10]. Because the mechanical and material properties are key factors affecting SCC, in many SCC prediction models, the linear fracture mechanics are widely used to acquire the relationship between the crack propagation rate (da/dt) and the stress intensity factor (K) [11–14].

Since the materials are different at different positions in weld joints, especially in DMW joints, the mechanical and material heterogeneities of base metal, weld metal, and heat-affected zone (HAZ) are different; the different constraints induced by mechanical heterogeneity will lead to the discontinuity of stress and strain distribution nearby crack tip and affect the integrity of welded structures [15, 16]. Even the wide use of crack tip opening displacement (CTOD) and the J -integral as elastic-plastic fracture parameters in structural integrity assessment, this is relevant to the plastic constraint and the yield strength of material in the homogeneous case, there are no standard procedures for fracture mechanics testing of specimens with welds due to the difficulty to determine the CTOD from the crack mouth opening displacement (CMOD)

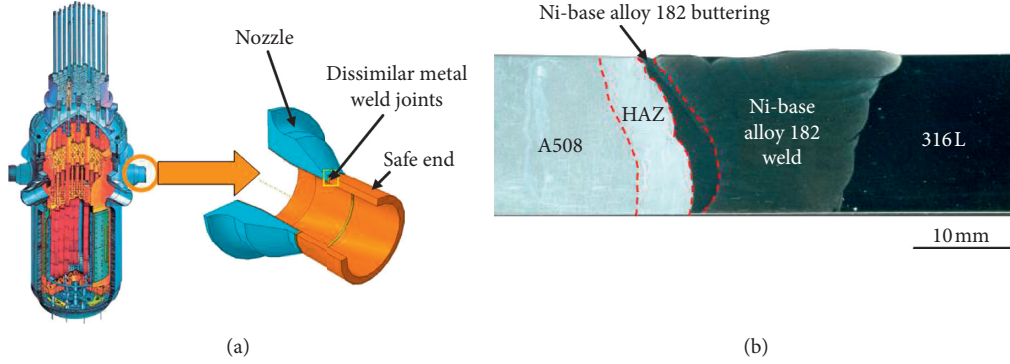


FIGURE 1: Dissimilar weld joints connecting the RPV nozzle and the hot-leg pipe in NPPs: (a) weld joint position and (b) sectional view of material composition of the weld joint.

with a heterogeneity welded joint. Thus, the relationship between the J -integral and the CTOD was investigated with different mismatch materials and crack depth by using an elastic-plastic finite element method, which supports the use of the J -integral instead of the CTOD [17]. The J - Q - M approach, where Q quantifies the geometry effect and M the material mismatch effects, was produced to estimate the influence of fracture toughness on the effect of mismatch without the discussion of competing failure criteria related to ductile crack growth and plastic collapse [18]. By the J - Q - M approach, it was concluded that the weld-metal strength overmatch results in higher constraint than evenmatch, and the critical stress level for initiating brittle fracture in the HAZ is reached at the lowest loads in the case of overmatching.

Even the mismatch of weldments has been much discussed, most of them focus on the effects of yield strength mismatch [15–19], and little concerns the ultimate tensile strength and elastic modulus differences of the welded metals. Thus, the ultimate tensile strength and elastic modulus differences of welded metals and their effects on the interface crack propagation were focused, and the propagation characteristic of interface crack in dissimilar weld joints was summarized by adopting an extended finite element method (XFEM) in this study.

2. Theory Model

2.1. Solution of Interface Crack. As shown in Figure 2, a finite length crack $2a$ along the interface of an infinite body composed of two different isotropic, homogeneous materials; a tensile stress σ_{22} normal to the crack faces and an in-plane shear stress τ_{12} are applied remote from the crack; a complex stress intensity factor K at the crack tip could be calculated as [20]

$$K = K_1 + iK_2 = (\sigma_{22} + i\tau_{12})\sqrt{\pi a}(1 + 2\epsilon i)(2a)^{-\epsilon i}, \quad (1)$$

where i denotes the imaginary term, $i = \sqrt{-1}$. K_1 and K_2 are real and denote the stress intensity factor of modes 1 and 2, respectively. ϵ is an oscillatory parameter given by

$$\epsilon = \frac{1}{2\pi} \ln \left(\frac{\kappa_1 \mu_2 + \mu_1}{\kappa_2 \mu_1 + \mu_2} \right), \quad (2)$$

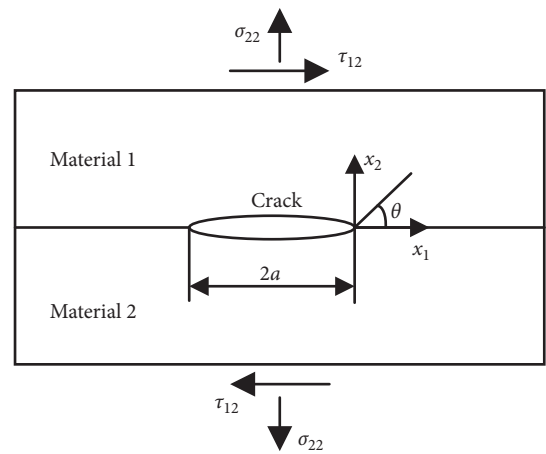


FIGURE 2: Interface crack tip geometry.

where

$$\kappa_k = \begin{cases} 3 - 4\nu_k, & \text{plane strain,} \\ (3 - \nu_k)/(1 + \nu_k), & \text{generalized plane stress,} \end{cases} \quad (3)$$

where μ_k ($k = 1, 2$) are the shear modulus of the two different materials, respectively, and ν_k are Poisson's ratios.

By means of Irwin's crack closure integral, the interface energy release rate G of an interface crack is given as [21]

$$G = \frac{K_1^2 + K_2^2}{2 \cosh^2(\pi\epsilon)} \left(\frac{1}{\bar{E}_1} + \frac{1}{\bar{E}_2} \right), \quad (4)$$

where

$$\frac{1}{\bar{E}_k} = \begin{cases} (1 - \nu_k^2)/E_k, & \text{plane strain,} \\ 1/E_k, & \text{generalized plane stress,} \end{cases} \quad (5)$$

where $k = 1, 2$ denotes the two different materials and E_k is the elastic modulus.

2.2. Damage Model in XFEM. When dealing with the numerical simulation of crack propagation, a damage model contains crack initiation criterion and crack propagation law should be involved; once the crack initiation criterion is met,

the crack can occur according to the defined crack propagation law.

2.2.1. Crack Initiation Criterion and Crack Extension Direction. The stress intensity factor K , which is mainly determined by the maximum principal stress of crack tip, has an important effect in the SCC process; the crack starts to propagate if the crack-tip stress intensity factor reaches the threshold value K_{ISCC} . Thus, the maximum principal stress criterion built in the XFEM models was selected to describe the initiation of crack [22]:

$$f = \left\{ \frac{\langle \sigma_{\max} \rangle}{\sigma_{\max}^0} \right\}, \quad (6)$$

$$\langle \sigma_{\max} \rangle = \begin{cases} 0, & \sigma_{\max} < 0, \\ \sigma_{\max}, & \sigma_{\max} \geq 0, \end{cases}$$

where σ_{\max}^0 is the maximum allowable principal stress; σ_{\max} is the maximum principal stress; the Macaulay brackets $\langle \rangle$ are used to signify that the crack does not initiate with a purely compressive stress state; f is the maximum principal stress ratio, and the crack is assumed to initiate when f reaches a value of one.

When the maximum principal stress is specified, the newly introduced crack is always orthogonal to the maximum principal stress direction when the fracture criterion is satisfied.

2.2.2. Crack Propagation Law. By defining the equivalent fracture energy release rate G_{equiv} , the power law based on energy was involved in this study to describe the crack propagation after the crack initiates [23]:

$$\frac{G_{\text{equiv}}}{G_{\text{equivC}}} = \left(\frac{G_I}{G_{IC}} \right)^{a_m} + \left(\frac{G_{II}}{G_{IIC}} \right)^{a_n} + \left(\frac{G_{III}}{G_{IIIC}} \right)^{a_o}, \quad (7)$$

where G_{equiv} is the equivalent fracture energy release rate and G_{equivC} is the critical equivalent fracture energy release rate; G_I , G_{II} , and G_{III} are critical energy release rates in Mode I, Mode II, and Mode III cracks, respectively; a_m , a_n , and a_o are damage exponents. In this study, the crack was Mode I, so only the first item in (7) was adopted.

The crack will propagate if G_{equiv} reaches G_{equivC} . According to Irwin, the fracture energy release rate in a two-dimensional crack is the energy that must be provided in order to break the material and create a cracked surface area ΔA [21]:

$$G = -\frac{d\Pi}{dA} = -\lim_{\Delta A \rightarrow 0} \frac{\Delta\Pi}{\Delta A} = -\lim_{\Delta A \rightarrow 0} \frac{\Delta\Pi}{B\Delta a}, \quad (8)$$

where G is the fracture energy release rate; $\Pi = U - W$ is potential energy, W is external work, and U is strain energy of the crack; a is the crack length, and B is the crack width.

According to (8), the calculation of G requires the crack increments Δa approaching zero, and it obviously cannot be reached in numerical simulation; thus the Virtual Crack Closure Technique (VCCT) with two steps is adopted. The

crack length equals to a in step 1, and the potential energy could be calculated as $\Pi_1 = U_1 - W_1$; the crack extends to $a + \Delta a$ in step 2, and the potential energy is $\Pi_2 = U_2 - W_2$; then, the fracture energy release rate G could be approximately calculated with a small enough increment of Δa as

$$G \approx \frac{\Pi_2 - \Pi_1}{B\Delta a}. \quad (9)$$

2.2.3. The Description of Crack Status. The crack status in the simulation is described by a variable STATUSXFEM; the element is completely cracked if STATUSXFEM equals to 1, and the element contains no crack if STATUSXFEM equals to 0. If the element is partially cracked, the value of STATUSXFEM is in the range of 0 and 1.

3. Finite Element Model of Interface Crack

3.1. Geometry Model and Mesh Model. A typical DMW joint in RPV has a pipe inner diameter of 735 mm and a wall thickness of 74 mm. When the inner diameter of pipe is far greater than the crack length, the welded joint could be simplified as a two-dimensional plane strain problem; a three-point bending specimen model was built according to ASTM E1820-05a [24], as shown in Figure 3. The initial crack length is 15 mm, and the precrack length is 3 mm.

The calculation of crack propagation is on the mesh model; even an accurate solution can be obtained with a coarser mesh with XFEM; the element size near the crack tip still affects the accuracy and stability of the numerical simulation. The element size in the crack propagation zone should satisfy the demands of

$$h \leq \frac{G_c E}{10(1-\nu^2)\sigma_0}, \quad (10)$$

where h is the element size along the crack propagation direction; G_c is the critical fracture energy release rate at crack tip; E is the elastic modulus; ν is Poisson's ratio; and σ_0 is yield strength.

The element size in a crack propagation zone is modeled as $0.05 \text{ mm} \times 0.05 \text{ mm}$, which satisfied the demands of (10), the element size far away from the crack propagation zone is $1 \text{ mm} \times 1 \text{ mm}$, and the element with a size of $0.05 \text{ mm} \sim 0.2 \text{ mm}$ is used in the transition zone. The finite element model was meshed to 38735 elements with 4-node biquadratic plane strain quadrilateral (CPE4), as shown in Figure 4. A small size blunt notch was designed at the crack tip with a radius of 0.05 mm to eliminate the calculation singularity. The geometric nonlinearity should be used to satisfy the computing demands when larger displacement and larger deformation appear in the simulation.

3.2. Material Model. The fracture mode of welded joints in nuclear power plants mainly manifests as ductile damage, and the materials of welded joints generally belong to a power hardening materials; thus the nonlinear relationship between stress and strain of power hardening materials can be described by the Ramberg-Osgood equation:

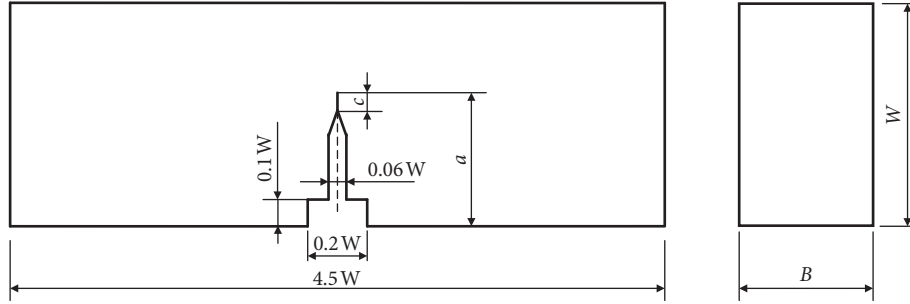


FIGURE 3: Geometry size of three-point bending specimen, where $W = 60$ mm, $a = 0.5W$, $c = 3$ mm, and $B = 0.5W$.

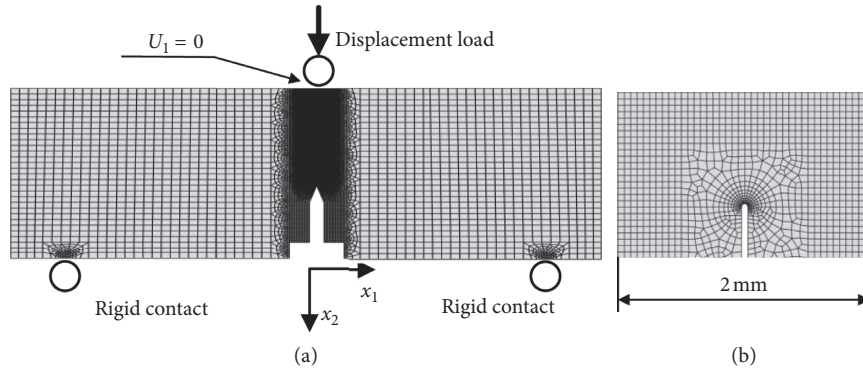


FIGURE 4: Mesh, load, and boundary condition of the specimen: (a) the global mesh model and (b) the mesh of crack tip.

$$\frac{\varepsilon}{\varepsilon_0} = \frac{\sigma}{\sigma_0} + \alpha \left(\frac{\sigma}{\sigma_0} \right)^n, \quad (11)$$

where ε is strain, σ is stress, σ_0 is the yield strength of the material, α is the yield offset, n is the hardening exponent for the plastic, and n can be calculated by [17]

$$n = \frac{1}{\kappa \cdot \ln(1390/\sigma_0)}, \quad (12)$$

where $\kappa = 0.163$ and σ_0 is the yield strength.

The materials are different at the two sides of interface crack, in order to quantitate the difference of material properties on both sides of the crack, defined

$$\gamma = \left| \frac{P_l - P_r}{P_r} \right| \times 100\%, \quad (13)$$

where γ is the material mismatch rate; the larger the value, the greater the differences of the two materials; it will be represented as γ_u and γ_E subsequently to denote the ultimate tensile strength mismatch rate and elastic modulus mismatch rate, respectively; P represents elastic modulus or ultimate tensile strength; subscripts l and r represent left and right, respectively.

Assuming that the specimen is made of A508 at the beginning, in order to obtain the effects of elastic modulus mismatch and ultimate tensile strength mismatch on the crack propagation, the elastic modulus and ultimate tensile strength of the material at the left side of interface are arbitrarily changed. The mechanical properties of A508 and other materials used in DMW joints of RPV are listed in

Table 1, and the three-point bending specimens built are listed in Table 2.

4. Effects of Material Properties Mismatch on Interface Crack Propagation

4.1. Ultimate Tensile Strength Mismatch. Under the condition of ultimate tensile strength mismatch, the load-displacement curves and displacement-crack extension curves are shown in Figures 5 and 6, respectively. It can be seen that the loads increase with the increase in applied displacement, followed by the crack extension during the first stage; this indicates that the short crack tends to propagation than the long crack under the same load condition. As the applied displacement increases, the loads increase to the maximum value and then decrease. With the increase in the ultimate tensile strength mismatch rate, the maximum load and the corresponding applied displacement decrease; this indicates that the increase in the ultimate tensile strength mismatch rate will reduce the load crack propagation needed; cracks are more likely to extend at the interface with large mismatch. With a certain crack extension length, the applied displacement also decreases with the increase in the ultimate tensile strength mismatch rate, which also indicates that the cracks are more likely to extend at the interface with large mismatch.

As shown in Figure 7, at the initiation of crack propagation, J -integral increases with the mismatch rate, which means that the crack initiation resistance is greater in interface crack with a larger mismatch rate. As the crack

TABLE 1: Mechanical properties of materials used in DMW joints of RPV [25–27].

Material type	Elastic modulus, E (GPa)	Poisson's ratio, ν	Yield strength, σ_0 (MPa)	Ultimate tensile strength, σ_u (MPa)	Fracture toughness, J_{IC} (kJ/m ²)
A508	183	0.30	345	560	224.2
Alloy 182	203	0.32	342	576	166.6
316L	176	0.30	309	485	170

TABLE 2: The material properties used to model the material mismatch (right metal is A508).

Specimens no.	Left material	Right material
1	$0.8\sigma_u$	σ_u
2	$0.9\sigma_u$	σ_u
3	$1.0\sigma_u$	σ_u
4	$0.8E$	E
5	$0.9E$	E
6	$1.0E$	E

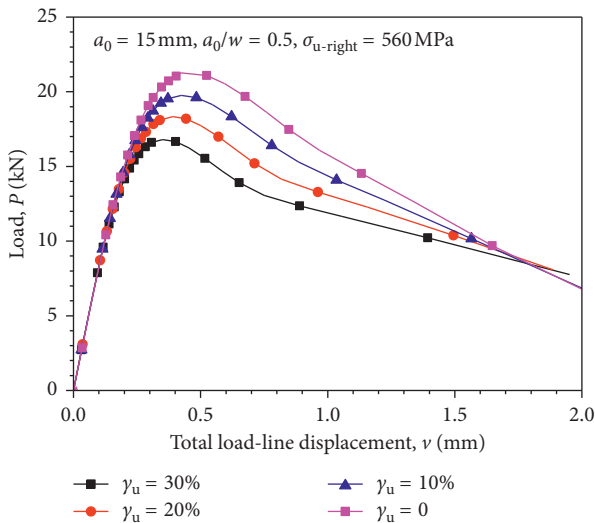


FIGURE 5: Load-applied displacement curve of ultimate tensile strength mismatch specimen.

extends, the J -integral reduces, and the largest reduction gradient appears in the specimen with a larger mismatch rate. When the crack propagates to 1 mm, the J -integral starts to increase with the extension of crack. In the specimens with different mismatch rates, the J -integral decreases with the increase of mismatch rate, and this also indicates that the crack tends to extend easily in the specimen with a larger mismatch rate.

Figure 8 illustrates the crack propagation path in the specimens with different mismatch rates; it can be seen that the crack propagation will deviate from the initiation direction. The crack extends to the left side of the specimens when mismatch rate exists, and the crack propagation path fluctuation is small in the specimen with a small mismatch rate, which indicates the larger the mismatch rate, the more unstable the interface crack propagation path is. Since the specimens all have a small ultimate tensile strength at the left side, the crack tends to propagate to the side with small ultimate tensile strength; the crack path fluctuation increases

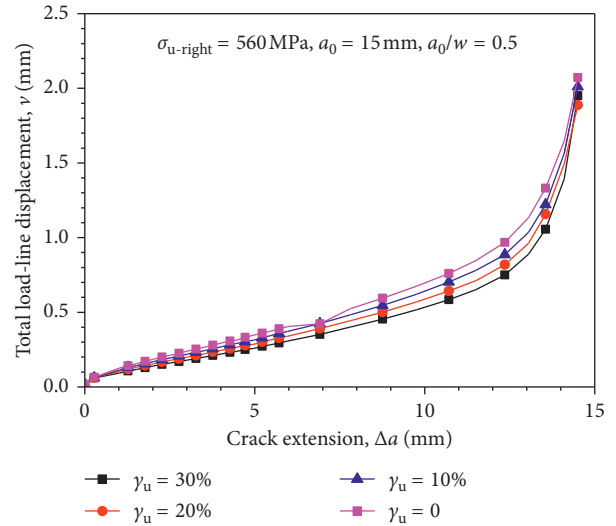


FIGURE 6: Applied displacement-crack extension curve of ultimate tensile strength mismatch specimen.

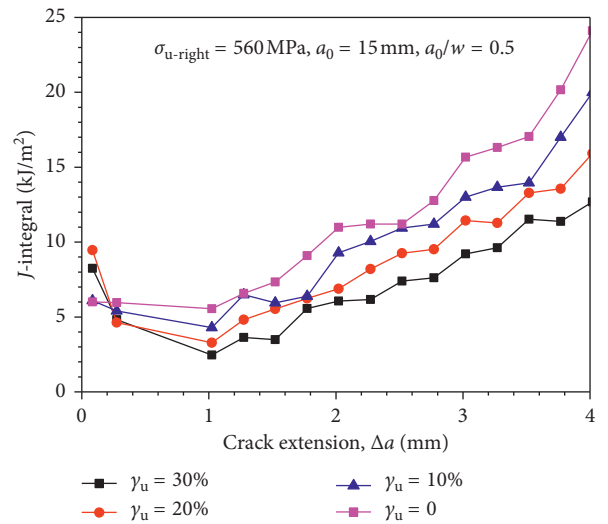


FIGURE 7: J - Δa curves of ultimate tensile strength mismatch specimen.

as the ultimate tensile strength mismatch increases. When the mismatch rate equals to 0, the crack direction will deviate from the initiation direction to the left or right side random.

4.2. *Elastic Modulus Mismatch.* The load-displacement curves in Figure 9 show the maximum load required for crack extension decreases with the increase in the elastic modulus mismatch rate, which indicates that the crack tends

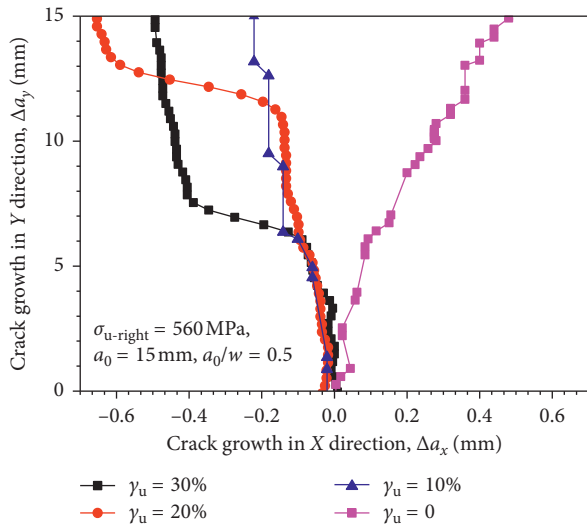


FIGURE 8: Crack extension paths of ultimate tensile strength mismatch specimen.

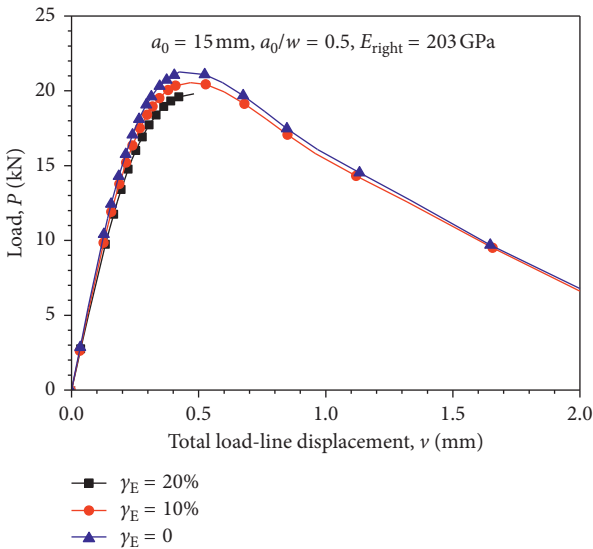


FIGURE 9: Load-applied displacement curve of elastic modulus mismatch specimen.

to extend at the interface with a larger elastic modulus mismatch rate. As the displacement-crack extension curves in Figure 10 are coincident with each other, the differences of J -integral- Δa curves shown in Figure 11 are also small; it could be concluded that the elastic modulus mismatch has little effects on the interface crack extension.

Figure 12 shows the crack propagation path in specimens with different elastic modulus mismatch rates; it can be seen that the crack propagation will deviate from the initiation direction to the side with larger elastic modulus. The crack extension direction seems to be the same if the crack extend length is smaller than 7 mm even if the elastic modulus mismatch exists. When the crack continues to extend, the crack path in the specimen with a small elastic modulus mismatch rate seems similar to the specimen of no mismatch, but the crack path has a big deflection in the

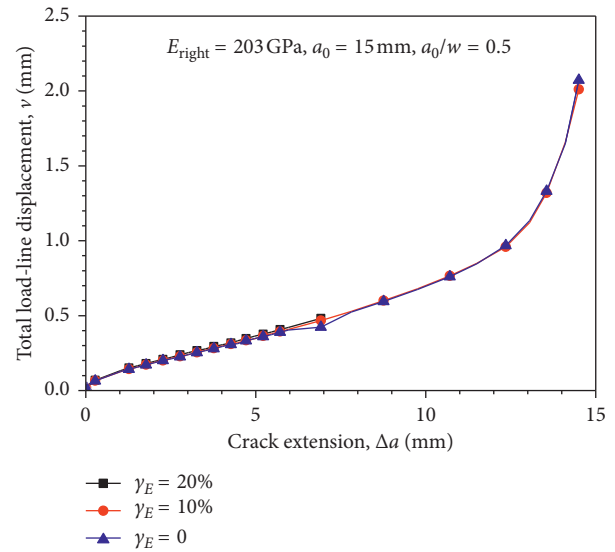


FIGURE 10: Applied displacement-crack extension curve of elastic modulus mismatch specimen.

specimen with a small elastic modulus mismatch rate; thus the crack extension path fluctuation increases as the elastic modulus mismatch rate increases.

5. Interface Crack Propagation in the Safe-Ends Weld Joints

Two specimens with austenite stainless steel 316L, nickel alloy 182, and low-alloy steel A508 are modeled to simulate the crack propagation in DMW joints. Of the two specimens, left and right materials are modeled with 316L and alloy 182, respectively, in one specimen, and another one is modeled using alloy 182 and A508 as left and right materials, respectively. Figure 13 illustrates the load-displacement curves of the two different weld joint specimens; although the maximum load is needed in the 316L-Alloy 182 specimen, the two curves have little differences. The applied displacement-crack extension curve and J -integral-crack extension curves in Figures 14 and 15 also coincide with each other; this indicates that the interface crack propagation resistances have little differences in two specimens.

The crack extension directions of the two specimens are shown in Figure 16; it can be seen that the two interface cracks both deviate from the initiation direction and both deviate into alloy 182 specimen. When the specimens fracture, the crack path offset in the X -direction is in the range of 0.2~0.3 mm, and the crack extend direction has little fluctuation.

6. Conclusion

The effects of material properties' mismatch on interface crack extension are calculated with XFEM. The crack extension resistance is larger in the specimens with a larger ultimate tensile strength mismatch rate initially, and the crack seems to easily initiate in specimens with small ultimate tensile strength mismatch. When the crack extends to a

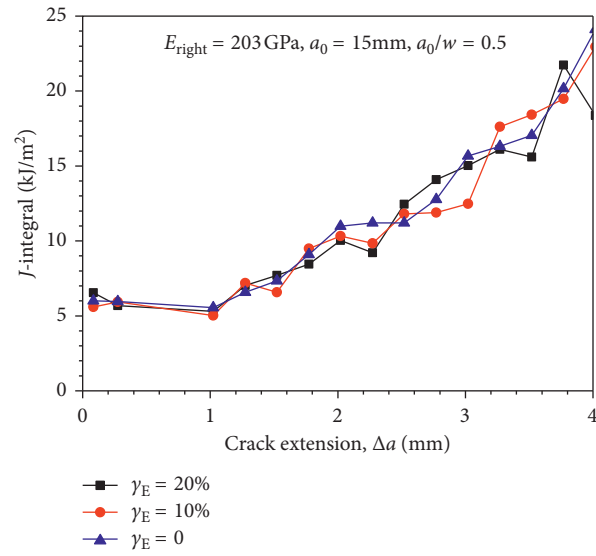


FIGURE 11: J - Δa curves of elastic modulus mismatch specimen.

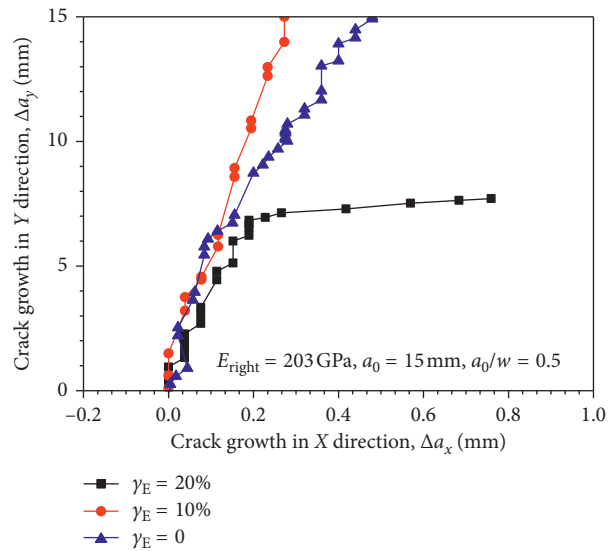


FIGURE 12: Crack extension paths of elastic modulus mismatch specimen.

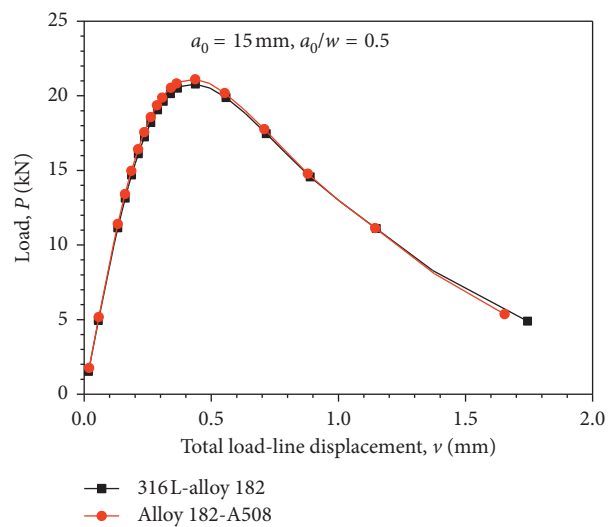


FIGURE 13: Load-applied displacement curve at different interfaces of DMW joints.

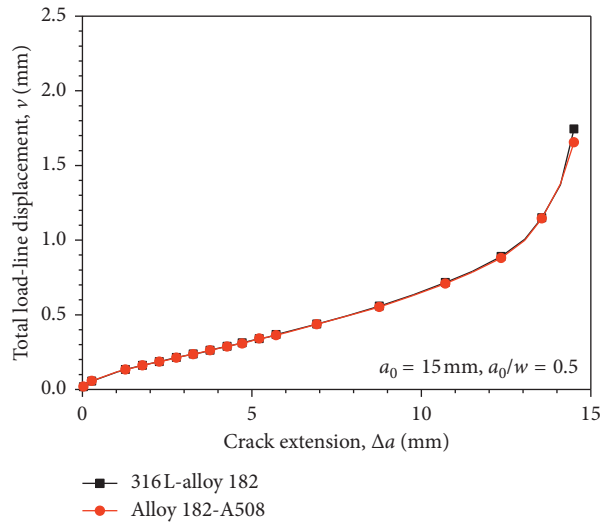


FIGURE 14: Applied displacement-crack extension curve at different interfaces of DMW joints.

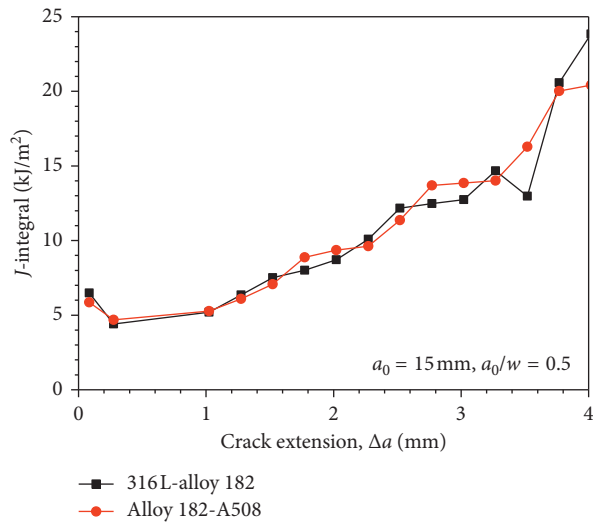


FIGURE 15: J - Δa curves at different interfaces of DMW joints.

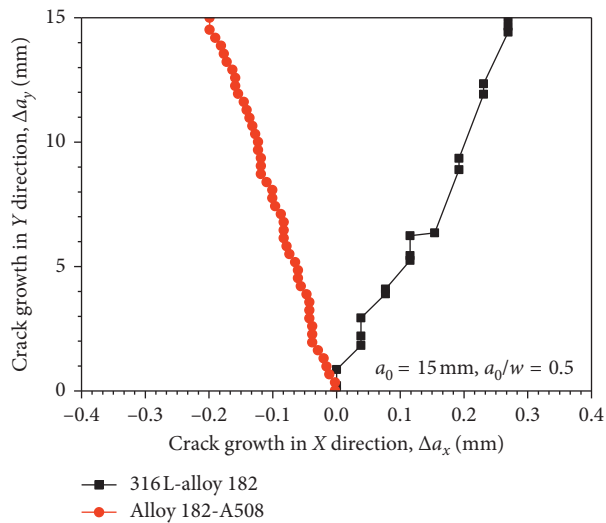


FIGURE 16: Crack extension paths at different interfaces of DMW joints.

certain length, the crack extension resistance is small in the specimen with larger ultimate tensile strength mismatch; the crack extends easily in the specimens with larger ultimate tensile strength mismatch. The elastic modulus mismatch has little effects on crack extension resistance. The crack extension resistances have little differences in the DMW bimaterial specimens, and the crack tends to deviate from the initial direction into alloy 182, and the crack path fluctuation is small.

Data Availability

The data used to support the findings of this study were calculated according to the finite element method, and they are included within the article. The parameters used in the calculation model were cited from references listed.

Conflicts of Interest

The authors declare that there are no conflicts of interest regarding the publication of this paper.

Acknowledgments

This work was supported by the Research Fund of State Key Laboratory for Marine Corrosion and Protection of Luoyang Ship Material Research Institute (LSMRI) under Contract No. 61429010102, the National Natural Science Foundation of China (Grant Nos. 11502195 and 51775427), the Key Research and Development Program of Shaanxi Province (Grant No. 2017GY-034), and the Natural Science Basic Research Plan in Shaanxi Province of China (Grant No. 2018JQ5193).

References

- [1] H. Hänninen, P. Aaltonen, A. Brederholm et al., "Dissimilar metal weld joints and their performance in nuclear power plant and oil refinery conditions," VTT Research Notes 2347, VTT Technical Research Centre of Finland, Espoo, Finland, 2006.
- [2] A. J. Cox, R. J. Olson, B. A. Young, P. M. Scott, and D. L. Rudland, "Dissimilar metal weld pipe fracture testing: experimental procedures and results," in *Proceedings of the ASME 2012 Pressure Vessels & Piping Conference*, Toronto, Ontario, Canada, 2012.
- [3] W. Bamford, B. Newton, and D. Seeger, "Recent experience with weld overlay repair of indications in alloy 182 butt welds in two operating PWRs," in *Proceedings of ASME 2006 Pressure Vessels and Piping/ICPVT-11 Conference*, pp. 427–434, Vancouver, BC, Canada, 2006.
- [4] G. F. Li and J. Congleton, "Stress corrosion cracking of a low alloy steel to stainless steel transition weld in PWR primary waters at 292°C," *Corrosion Science*, vol. 42, no. 5, pp. 1005–1021, 2000.
- [5] G. F. Li, G. J. Li, and K. W. Fang, "Stress corrosion cracking behavior of dissimilar metal weld A508/52M/316L in high temperature water environment," *Acta Metallurgica Sinica*, vol. 47, no. 7, pp. 797–803, 2011.
- [6] R. N. Parkins, "Predictive approaches to stress corrosion cracking failure," *Corrosion Science*, vol. 20, no. 2, pp. 147–166, 1980.
- [7] F. P. Ford, "Quantitative prediction of environmentally assisted cracking," *Corrosion*, vol. 52, no. 5, pp. 375–395, 1996.
- [8] F. Q. Yang, H. Xue, L. Y. Zhao, and X. R. Fang, "A quantitative prediction model of SCC rate for nuclear structure materials in high temperature water based on crack tip creep strain rate," *Nuclear Engineering and Design*, vol. 278, pp. 686–692, 2014.
- [9] J. Heldt and H. P. Seifert, "Stress corrosion cracking of low-alloy, reactor-pressure-vessel steels in oxygenated, high-temperature water," *Nuclear Engineering and Design*, vol. 206, no. 1, pp. 57–89, 2001.
- [10] O. K. Chopra, H. M. Chung, T. F. Kassner et al., "Current research on environmentally assisted cracking in light water reactor environments," *Nuclear Engineering and Design*, vol. 194, no. 2, pp. 205–223, 1999.
- [11] P. L. Andresen, "Similarity of cold work and radiation hardening in enhancing yield strength and SCC growth of stainless steel in hot water," in *Proceedings of Corrosion 2002*, Denver, CO, USA, 2002.
- [12] P. L. Andersen, P. W. Emigh, M. M. Morra, and R. M. Horn, "Effects of yield strength, corrosion potential, stress intensity factor, silicon and grain boundary character on the SCC of stainless steels," in *Proceedings of 11th International Conference on Environmental Degradation of Materials in Nuclear Systems*, pp. 816–833, Stevenson, WA, USA, 2003.
- [13] T. Shoji, G. Li, J. Kwon, S. Matsushima, and Z. Lu, "Quantification of yield strength effects on IGSCC of austenitic stainless steels in high temperature water," in *Proceedings of 11th International Conference on Environmental Degradation of Materials in Nuclear Systems*, pp. 834–844, Stevenson, WA, USA, 2003.
- [14] T. Moltubakk, C. Thaulow, and Z. L. Zhang, "Application of local approach to inhomogeneous welds. Influence of crack position and strength mismatch," *Engineering Fracture Mechanics*, vol. 62, no. 4-5, pp. 445–462, 1999.
- [15] H. Xue and Y. Shi, "CTOD design curve in consideration of material strain hardening," *International Journal of Pressure Vessels and Piping*, vol. 75, no. 7, pp. 567–573, 1998.
- [16] H. E. Xue and Y. Shi, "Effects of mechanical heterogeneity on plastic zones of welded three-point bend specimens," *International Journal of Pressure Vessels and Piping*, vol. 75, no. 7, pp. 575–580, 1998.
- [17] Y. Ueda, Y. Shi, and S. Sun, "Effects of crack depth and strength mismatching on the relation between J -integral and CTOD for welded tensile specimens," *Transactions of JWRI*, vol. 26, no. 2, pp. 133–140, 1997.
- [18] M. Daumling, C. Thaulow, M. Hauge, Z. L. Zhang, Ø Ranestad, and F. Fattorini, "On the interrelationship between fracture toughness and material mismatch for cracks located at the fusion line of weldments," *Engineering Fracture Mechanics*, vol. 64, no. 4, pp. 367–382, 1999.
- [19] W. B. Wang, H. Xue, F. Q. Yang, and X. S. Zhou, "Characteristic of interface crack propagation in dissimilar weld joints," *Advanced Materials Research*, vol. 988, pp. 249–252, 2014.
- [20] J. R. Rice, "Elastic fracture mechanics concepts for interfacial cracks," *Journal of Applied Mechanics*, vol. 55, pp. 98–103, 1988.
- [21] G. R. Irwin, "Fracture," in *Handbuch der Physik*, S. Flugge, Ed., vol. 6, pp. 551–590, Springer, Berlin, Germany, 1958.
- [22] Dassault Systèmes Simulia Corp., *Abaqus Analysis User's Manual 6.12*, Simulia, Johnston, RI, USA, 2012.

- [23] E. M. Wu and R. C. Reuter Jr., "Crack extension in fiberglass reinforced plastics," T & AM Report No. 275, University of Illinois, Champaign, IL, USA, 1965.
- [24] ASTM E1820-05a, *Standard Test Method for Measurement of Fracture Toughness*, ASTM International, West Conshohocken, PA, USA, 2005.
- [25] O. K. Chopra, E. E. Gruber, and W. J. Shack, "Fracture toughness and crack growth rates of irradiated austenitic stainless steels," Report No. ANL-03/22, Argonne National Laboratory, Lemont, IL, USA, 2003.
- [26] C. Jang, J. Lee, J. Eun Jin, and T. E. Jin, "Mechanical property variation within Inconel 82/182 dissimilar metal weld between low alloy steel and 316 stainless steel," *International Journal of Pressure Vessels and Piping*, vol. 85, no. 9, pp. 635–646, 2008.
- [27] J.-H. Liu, L. Wang, Y. Liu, X. Song, J. Luo, and D. Yuan, "Fracture toughness and fracture behavior of SA508-III steel at different temperatures," *International Journal of Minerals, Metallurgy, and Materials*, vol. 21, no. 12, pp. 1187–1195, 2014.

Research Article

Failure Analysis on 42CrMo Steel Bolt Fracture

Guo Hongfei,^{1,2} Jianwei Yan ,^{1,3} Ru Zhang,¹ Zhihui He,¹ Zengqi Zhao,⁴ Ting Qu,¹ Ming Wan,¹ Jingshun Liu,² and Congdong Li ¹

¹Institute of Physical Internet, Jinan University, Zhuhai 519070, China

²School of Materials, Inner Mongolia University of Technology, Hohhot 010051, China

³State Key Laboratory for Strength and Vibration of Mechanical Structures, Xi'an Jiaotong University, Xi'an 710049, Shanxi, China

⁴Baotou Research Institute of Rare Earths, Baotou 014010, China

Correspondence should be addressed to Jianwei Yan; tyanjianwei@jnu.edu.cn

Received 1 September 2018; Revised 12 October 2018; Accepted 17 October 2018; Published 1 January 2019

Guest Editor: Dariusz Rozumek

Copyright © 2019 Guo Hongfei et al. This is an open access article distributed under the Creative Commons Attribution License, which permits unrestricted use, distribution, and reproduction in any medium, provided the original work is properly cited.

Fracture behaviors of 42CrMo ultrahigh strength steel-based bolt have been experimentally studied including macroscopic and microscopic fracture observation, metallographic test, mechanical property testing, and energy spectrum analysis. The results show that a large amount of structure defects, such as sulfide inclusions, band, and carbon depletion, appear in the fracture origin region and matrix of the bolt. Such defects reduce fatigue strength of materials and easily yields fatigue fracture origin. In addition, sulfide inclusions provide easy access to crack growth, gradually reducing the effective cross section of the bolt accompanying with increasing stress and finally causes fracture when stress exceeds the material fracture strength. The fracture mechanism is also explored based on fracture failure criterion and fatigue crack growth curve.

1. Introduction

The 42CrMo steel has been widely used as forgings due to its ultrahigh strength, toughness, good hardenability, unobvious temper brittleness, and higher fatigue limit and resistance to multiple impacts after quenching and tempering [1–3]. Such a kind of steel-based forgings possesses higher strength and larger quenching and tempering section, which are promising for the engineering applications in large gears for locomotive traction, rear axles of pressure vessels, extremely loaded connecting rod, spring clips, as well as deep well drill pipe joint and 2000 m underwater fishing tools.

However, malfunction inevitably occurs, and thus, a good understanding of the failure mechanism plays an important role in the optimized design and circumvented action. In this research work, macro-observations and micro-observations are carried out to analyze the mechanical behaviors and metallographic structure of bolt fracture origin region and matrix. In addition, by introducing fracture failure criterion [4, 5], the crack growth onset and direction analysis are theoretically explored,

which provides a forecasting method and thus will be helpful in the engineering application.

The bolt is a fastening of the wind generator, with specification model of M30 × 435. The manufacturing process is described as follows: raw materials → fracturing materials → forging blanks → rough finish → heat treating → longitudinal mechanical property test → flaw detection → finish machining → finished products. When the bolt was installed and used, the customer found bolt fracture during routing inspection.

2. Test Process and Results

2.1. Macroscopic Observation of Fracture. The bolt fracture occurs at the position of 33 mm near the end of the bolt as shown in Figure 1. The bolt fracture is at the root of the thread. The morphology is as shown in Figure 2. Under macroscopic observation, obvious fatigue characteristics can be seen on the fracture. The fracture originates from the outer surface of the bolt. The fatigue origin area in the shape of semiellipse is relatively smooth. Clear fatigue lines can be



FIGURE 1: Macromorphology of fractured bolt.



FIGURE 2: Morphology of bolt fracture position.

observed in the extended area. The extended area covers most of the fracture, and the instantaneous fracture area is relatively small, with the morphology as shown in Figure 3. The surface of the bolt fracture is seriously worn out and shows different degrees of corrosion. The fracture morphology can no longer be observed. Based on the fracture morphology, instantaneous fracture area is close to the edge, indicating a low degree of bolt overload. If the bolt is a fracture caused by overload, the fiber zone is the location of the source of the fracture, and the fiber zone with the annular ridge pattern is always at the innermost volcano, not the edge.

2.2. Mechanical Property Test of Bolt Matrix. A set of tensile specimens and three impact specimens are taken on the fracture bolt for the mechanical property test, as shown in Table 1.

As shown in Table 1, the mechanical property of the fractured bolt meets the technical requirements of GB/T3077.

2.3. Metallographic Test of Bolt Matrix. Tests of nonmetallic inclusions, microstructure, and grain size have been conducted by sampling on bolt matrix. The metallographic test results are as shown in Table 2. The structure morphology is as shown in Figure 4, and the grain size is as shown in Figure 5.

As shown in Table 2, no obvious abnormality is observed in the test results of nonmetallic inclusions, microstructure, and grain size of this bolt.

2.4. Fracture Observation with a Scanning Electron Microscope and Energy Spectrum Analysis. Clean the bolt fracture with an ultrasonic oscillator, and observe microscopic fracture morphology with a scanning electron microscope (FEG-450). It is found that microscopic fracture of the bolt is severely scratched and rusted, and the fracture morphology cannot be clearly observed. However, a large number of

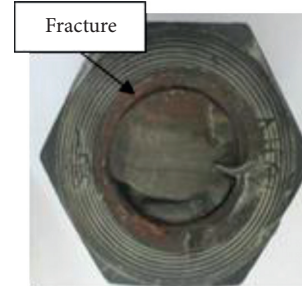


FIGURE 3: Morphology of bolt fracture.

TABLE 1: Results of mechanical property test.

Test result	RP0.2 (MPa)	Rm (MPa)	A (%)	Z (%)	Impact test result KV2 (J)	HRC
GB/T3077 (standard value)	≥930	≥1080	≥12	≥45	≥63	32–38
Test value	1055	1127	16.5	56	–20°C: 63.7 70.4 71.3	36.0

TABLE 2: The results of the metallographic test.

Bolt	Nonmetallic inclusions (level)	Microstructure	Grain size (level)
/	A2.0; B0; C0; D0.5e; DS1.0	Tempered sorbite + small amounts of bainite	8.5
Test standard	GB/T10561-2005	GB/T13298-1991	GB/T6394-2002

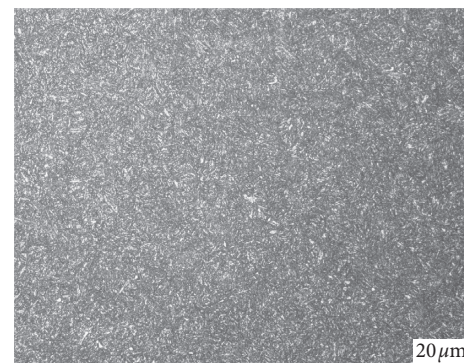


FIGURE 4: Metallographic structure of bolt matrix.

holes are observed in the fracture origin area (Figure 6). Less obvious fatigue striations are distributed in the extended area, with the morphology as shown in Figure 7. Under magnified observation, the fracture surface is relatively flat and a large number of secondary cracks are distributed on the fracture surface, with the morphology as shown in Figure 8. According to the semiquantitative analysis of energy spectrum performed on the gray products in the crack of metallographic specimen, the crack mainly contains elements including Os, Cr, Mn, and Fe. See Figure 9 for the energy spectrum.

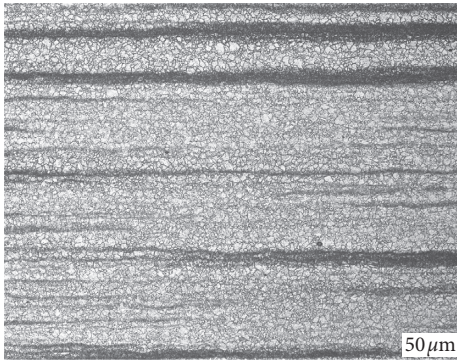


FIGURE 5: Grain size of bolt matrix.

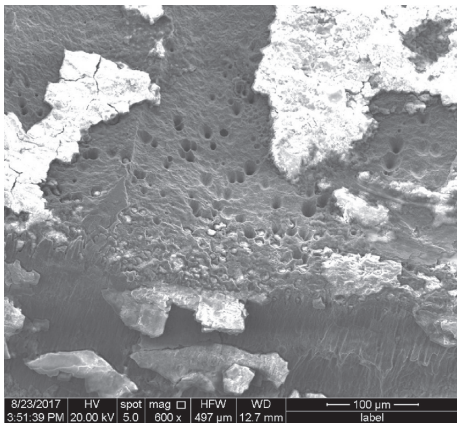


FIGURE 6: Micromorphology of fracture origin area.

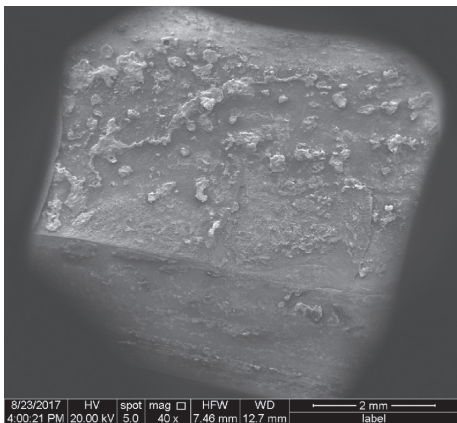


FIGURE 7: Micromorphology of fracture extended area.

According to the above results of electron microscopy and energy spectrum, it is known that there are a large number of hole defects in the fracture source region, which is the direct cause of the fracture of the whole bolt. The fatigue fringe distributed in the extended region is one of the important microscopic bases for the fatigue fracture of the part, because fatigue streaks appear in the second stage of fatigue crack propagation, where the crack growth rate is faster, and each stress cycle is on the order of microns. The gray product of the crack mouth is the oxidation product, and the crack

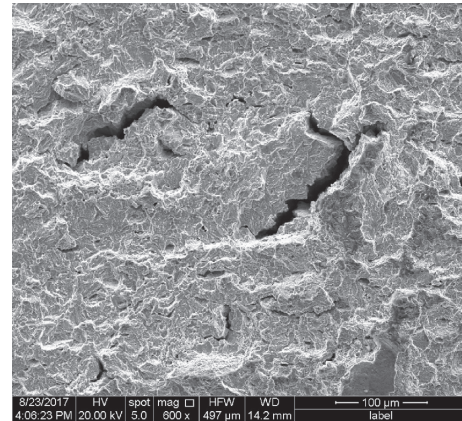


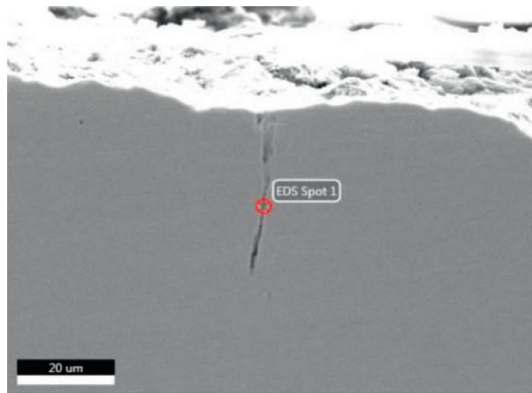
FIGURE 8: Macromorphology of secondary fracture crack.

tail is the manganese sulfide inclusion. The existence of these structures destroys the continuity of the surface of the material, causing the formation of cracks in the Hertz region of the subsurface, and especially the brittle oxide and the matrix are separated into voids. The stress concentration at the sharp corners of the cavity edges exceeds the elastic limit of the matrix, and the plastic deformation is large, causing the surface of the material to harden, thereby causing cracks.

2.5. Microscopic Observation of Fracture Origin. Cut the bolt at the fracture origin area longitudinally and grind it. Under the metalloscope, many small cracks extending from the fracture to the matrix can be observed. The deepest crack depth measures 0.10 mm, with the morphology shown in Figure 10. Under magnified observation, the cracks are filled with gray products (Figure 11). Concentratedly distributed manganese sulfide inclusions are found near the fracture origin (Figure 12). Many manganese sulfide inclusions are also observed in the matrix.

Upon corrosion of the sample in 4% nitric acid alcohol solution, carbon depletion is observed at the fracture origin. The deepest depth of the carbon-depleted layer is 0.40 mm, with the morphology shown in Figure 13. At the fracture origin, bands are distributed in the same direction as the crack propagation, and some microcracks extend along the banded structure, with the morphology as shown in Figure 14. Bands are also distributed in the matrix. According to GB/T13299-1991, the banded structure is rated as 3C2.5, with the morphology as shown in Figure 15. Carbon depletion is observed at addendum and both tooth sides of the bolt, with the morphology as shown in Figure 16.

It can be seen from the above microscopic results that the deepest crack depth in the fracture source region is 0.10 mm, and the crack initiation phase is 0.05–0.08 mm in the engineering. It is known that the deepest crack in the fracture source region has crossed the crack initiation stage to reach the crack. During the expansion phase, the presence of cracks causes stress and strain concentration on the surface of the bolt, forming a fatigue source at the crack and accelerating the initiation and propagation of fatigue cracks. There is carbon depletion at the source of the fracture, the



eZAF intelligent quantitative

Element	Weight %	Atom	Net	Error %
O K	2.71	8.45	65.18	11.45
S K	6.41	9.99	351.15	5.44
CrK	1.21	1.16	50.67	13.14
MnK	11.5	10.46	293.65	3.42
FeK	78.17	69.93	1665.52	1.92

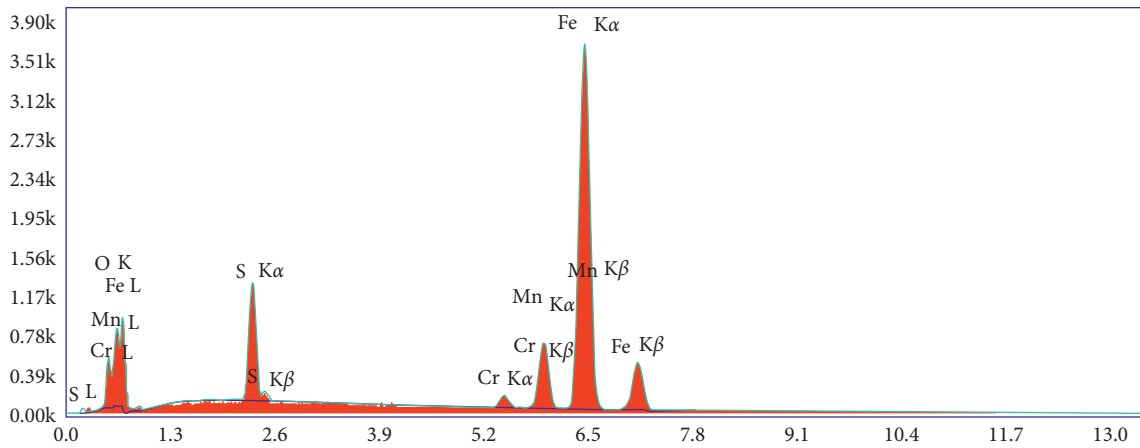


FIGURE 9: Energy spectrum.



FIGURE 10: Micromorphology of small cracks.



FIGURE 11: Magnified micromorphology of small distributed cracks in fracture origin area.

root of the bolt, and the sides of the tooth. The carbon depletion is partial decarburization. The decarburization causes the surface hardness to decrease; thus the yield strength of the material decreases and the plastic deformation is easy. The increase of surface friction coefficient promotes the formation of surface cracks. Defects in the band structure at the source of the fracture and in the matrix are also one of the causes of fatigue fracture. Due to the different microstructures of the adjacent bands of the banded structure, their properties are also different. The bands with low performance under external force are easily exposed, and stress concentration occurs between the strong

and weak bands, thus causing a decrease in overall mechanical properties. There is obvious anisotropy, thus reducing the fatigue properties of materials.

3. Fracture Failure Criterion

For brittle fracture of homogeneous materials, take the stress intensity factor and energy release rate as the crack propagation forces and fracture toughness as the fracture resistance parameter [6, 7]. Assuming that the energy release rate (G) reaches the fracture toughness of the material (I),



FIGURE 12: Micromorphology of nonmetallic.

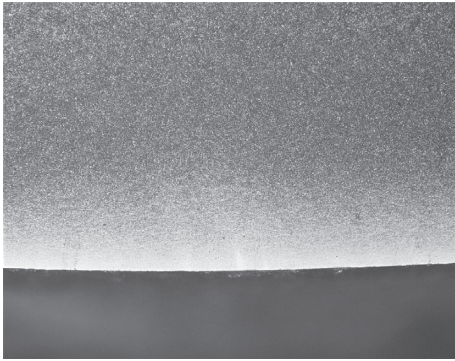


FIGURE 13: Micromorphology of carbon inclusions near the fracture surface depletion near the fracture origin.

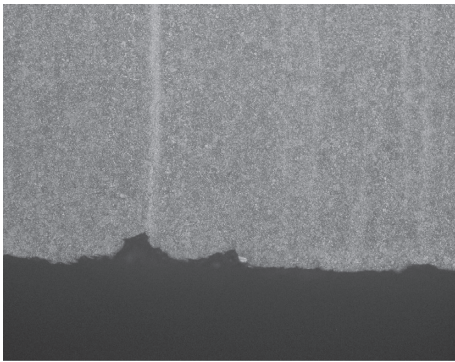


FIGURE 14: Micromorphology of the band.

the crack begins to grow. G is the function of K_{II}/K_I , crack propagation angle φ (angle between the crack propagation direction and the positive direction of the X axis $-\pi < \Phi < \pi$), external load, and elastic modulus. The fracture criterion can be expressed as

$$G = \Gamma, \quad (1)$$

$$\frac{\partial(G - \Gamma)}{\partial\Phi} = 0.$$

If the toughness value of the material in $\Phi \neq 0$ direction is greater than that in $F = 0$ direction, the fracture criterion can be expressed as

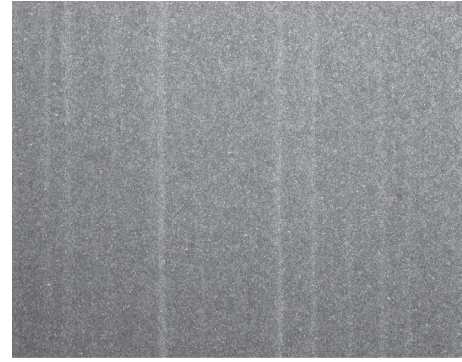


FIGURE 15: Micromorphology of the matrix band at the fracture origin.

$$G = \Gamma, \quad (2)$$

where Γ is a toughness value along $\Phi = 0$, obtained by the test and methods of mesomechanics. Based on the study of Gu and Asaro [8, 9] and the analysis on specimens of in-plane and antisymmetric loads, the following can be suggested:

- (1) The greater the material nonuniformity, the larger the type II stress intensity factor. The crack propagates in the direction in which the difference in energy release rate and fracture toughness is the greatest.
- (2) When the crack is located in the center of the specimen, the nonuniformity of the material has a great effect on the direction of crack propagation, and when the crack is close to the boundary of the specimen, the nonuniformity has little effect on it.

4. Mechanism Analysis and Discussion

The above test results suggest that the mechanical property of the bolt conforms to the technical requirements of GB/T3077 and the metallographic structure is a normal quenched and tempered structure. Under microscopic observation, the bolt has structural defects of many sulfide inclusions, indicating that the material has poor desulfurization in the desulfurization process. Meanwhile, fine cracks extending from the outer surface into the matrix are observed in the fracture origin area of the bolt. The cracks are filled with gray products. Based on the electron microscope and energy spectrum analysis, the gray products in the front part of the crack are oxidation products, and those in the rear part of the crack are manganese sulfide inclusions. Nonmetallic inclusions in steel, especially oxides, are coarse and unevenly distributed and are not deformed in a point shape, which greatly reduces the fatigue wear resistance of the material. Although the sulfide is less harmful than the oxide, if the sulfide content in the steel is high, the continuity of the surface of the material is also destroyed. This is because the sulfide has plasticity in the hot working state and the expansion coefficient is close to that of the steel, which is deformed together with the matrix. Fatigue crack sources are often generated in areas

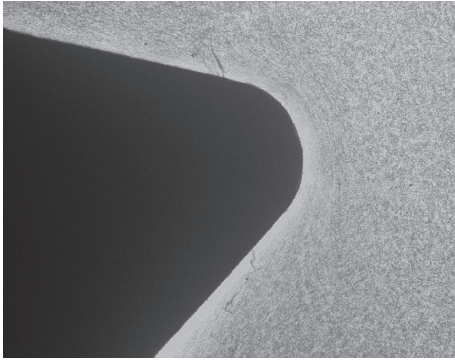


FIGURE 16: Micromorphology of carbon depletion at addendum and both tooth sides of the bolt.

with severe defects and stress concentrations. Therefore, in use, the bolt forms a stress concentration point at the hole and the inclusion defect in the fracture source region and then becomes a crack source. In the subsequent use, the crack further extends and expands and finally causes the bolt to be unstable and fractured.

The banded structure of the bolt is obvious, and the grow direction of the banded structure is consistent with the direction of crack propagation. The banded structure includes a primary banded structure and a secondary banded structure. The primary band structure is the original band shape, which is caused by the dendrite segregation generated when the steel ingot is cast; the secondary band structure is formed on the basis of the primary strip shape, which is generated along the rolling direction of the steel after rolling or heat treatment. The eutectoid ferrite band and the pearlite band are stacked on each other in a band structure. The secondary band structure can be alleviated or eliminated by a reasonable heat treatment process, and the primary band structure is difficult to be eliminated by common heat treatment. However, it is difficult to eliminate the primary banded structure by common heat treatment, which needs to be avoided or improved by electroslag remelting, liquid steel crystallization speed increasing, final rolling (forging) temperature increasing, forging ratio increasing or diffusion annealing, and other technologies. The presence of banded structure causes two structural stress differences and material anisotropy, providing a convenient channel for crack propagation.

There is carbon depletion at the source of bolt breakage, the root of the tooth, and both sides of the tooth. Although the carbon-poor layer is very shallow, only 0.40 mm, even negligible for large-size shafts, in practice the thin-layer decarburization of the surface is a fatal defect. Decarburization is a fatal flaw, and decarburization of 0.1 mm will significantly reduce the fatigue limit. In addition, the presence of the decarburization layer reduces the fatigue strength of the surface of the part. Under the action of alternating stress in the long-term use, the surface has fatigue cracks, and the existence of fatigue cracks causes stress concentration in the source region, also in actual use. If subjected to a large impact force, the crack will develop rapidly, causing the bolt to break.

The crack originates at the bottom of the first thread, and deformation mark is observed on the thread surface.

This mark should be formed during the process of pretightening the bolt. The morphology of the bolt fracture indicates that the crack initiation stress is large. In this aspect, it also shows that the bolt was subjected to pretightening force. Pretightening force refers to tightening force, which is also the shear stress [10–12]. Tensile load is the main work load. Pretightening force overlapping with service stress promotes the crack initiation. When the crack origin appears on the surface, the fatigue crack origin develops based on the microcrack nucleation [13–16]. These microcracks gradually and progressively grow with the repeated stress. When the fatigue cracks grow to a certain extent, the effective cross section of the part is greatly reduced while the stress is continuously increased. When the stress exceeds the fracture strength of the material, the fracture occurs.

According to the fracture criterion, when the energy release rate (G) of the homogeneous material reaches the fracture toughness of the material (Γ), the crack begins to grow. Corresponding to the crack initiation stage when the crack depth is 0.05–0.08 mm, it provides a theoretical basis for predicting the timing of crack initiation. The greater the nonuniformity of the material, the larger the stress intensity factor of type II, and the crack expands along the direction of the difference between the energy release rate and the fracture toughness. However, there are many structural defects in the fracture bolt, which leads to poor uniformity of the material. That is, the material nonuniformity is large, and the type II stress intensity factor is large, causing the crack to start cracking along the defects such as inclusions. When the crack is located in the center of the test piece, the material nonuniformity has a great influence on the direction of crack propagation. When the crack is close to the boundary of the test piece, the nonuniformity has little effect on the crack propagation direction and the fracture position of the bolt test piece in this paper. The fracture position of the bolt specimen is at the root of the thread; that is, the crack is close to the boundary of the specimen, so the nonuniformity of the material has little influence on the crack propagation direction.

In summary, the fracture property of the fault bolt is a typical fatigue fracture, involving three stages: crack initiation, crack propagation, and instantaneous fracture. The typical fatigue crack growth curve is shown in Figure 17. The three general causes of crack initiation are surface roughness due to slip band; crack source formed in the grain boundary due to serious misalignment of the strain; and surface inclusions, processing defects, and nucleation of the chemical segregation area. For the bolt in this paper, crack initiation is caused by surface inclusions, processing defects, and nucleation of the chemical segregation area. For industrial materials, defect areas involving inclusions, voids, surface processing defects, and microarea of chemical segregation can also become sites of fatigue crack initiation [17–19]. The mechanism of fatigue crack initiation at the defect site is related to a series of mechanical factors, microstructure factors, and environmental factors [20–23]. These factors include the slip characteristics of matrix, the relative strength of matrix and defect, the strength of matrix and inclusion

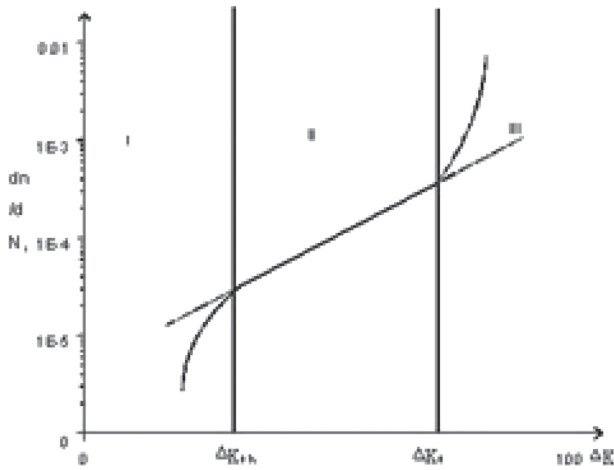


FIGURE 17: Typical fatigue crack growth curve.

interface, and the relative sensitivity of matrix and inclusions to corrosion in a fatigue environment. The fatigue submicroscopic cracks formed in the metal connect to form microscopic fatigue cracks [24, 25], which is called the first stage of crack formation. Then, the cracks continue to grow in the direction of the maximum shear stress that forms an angle of about 45° with the load, which is the second stage of fatigue crack formation. When the crack propagates perpendicular to the load direction, the normal stress has a great influence on the crack propagation and the crack propagation speed and depth are much greater than before. When the crack propagates to a certain critical length, the instability expansion causes rapid fracture.

5. Conclusions

- (1) Based on macroscopic and microscopic observation and analysis of the fractured bolt, the bolt fracture is determined as a fatigue fracture.
- (2) The mechanical property and the matrix microstructure of the bolt meet the technical requirements.
- (3) The fracture origin area and matrix of the bolt involve structure defects including a large amount of sulfide inclusions, segregation, and carbon depletion. The presence of defects reduces the fatigue strength of the material, and fatigue fracture origin is easily formed in the weak area of the material. Cracks continue to grow along the sulfide inclusions and gradually reduce the effective crosssection of the bolt while the stress increases. When the stress exceeds the fracture strength of the material, the fracture occurs.

Data Availability

The data used to support the findings of this study are available from the corresponding author upon request.

Conflicts of Interest

The authors declare that there are no conflicts of interest regarding the publication of this paper.

Acknowledgments

The research and publication of this article was supported by the Fundamental Research Funds for the Central Universities (No. 21618412), Inner Mongolia Autonomous Region Science and Technology Innovation Guide Award Fund Project (No. 103-413193), and Open Project of Key Laboratory for Strength and Vibration of Mechanical Structures (SV2017-KF-23).

Supplementary Materials

The Supplementary Materials contain all the original images of the paper. (*Supplementary Materials*)

References

- [1] Z. Yu, P. Jiang, Z. Yao, and Y. Xu, "Fracture analysis of bolt made of 42CrMo steel," *Heat Treatment of Metals*, vol. 37, no. 4, pp. 134-136, 2012.
- [2] Y. Xiong, C. Chen, X. Xie et al., "42CrMo steel bolt failure analysis," *Aerospace Materials and Technology*, vol. 47, no. 3, pp. 67-70, 2017.
- [3] S. Gao, Y. Xu, G. Sun, and J. Zhang, "Fracture analysis of high strength bolt," *Physical Testing and Chemical Analysis Part A: Physical Testing*, vol. 42, no. 6, pp. 306-308, 2006.
- [4] D. Yao, X. Yan, M. Chen, and J. He, "Elastic fracture mechanics analysis of functionally gradient materials," *Rare Metal Materials and Engineering*, vol. 34, no. 8, pp. 1191-1195, 2005.
- [5] D. Zhang, P. Zhong, C. Tao et al., *Failure Analysis*, National Defense Industry Press, Beijing, China, 2004.
- [6] Z. Wang, *Fatigue of Materials*, National Defense Industry Press, Beijing, China, 1993.
- [7] C. Chen, *Fatigue and Fracture*, Huazhong University of Science and Technology Press, Wuhan, China, 2002.
- [8] P. Gu and R. J. Asaro, "Cracks in functionally graded materials," *International Journal of Solids and Structures*, vol. 34, no. 1, pp. 1-17, 1997.
- [9] P. Gu and R. J. Asaro, "Crack deflection in functionally graded materials," *International Journal of Solids and Structures*, vol. 34, no. 24, p. 3085, 1997.
- [10] T. Zhang, Z. Zhao, L. Ni, and X. Xue, "Fracture failure analysis of hexagon head bolt," *Metal Products*, vol. 42, no. 4, pp. 719-721, 2016.
- [11] C. Hu, X. Liu, C. Tao et al., "Failure analysis on 0Cr17Ni4-Cu4Nb screw," *Journal of Materials Engineering*, vol. 12, pp. 21-23, 2012.
- [12] C. Hu, T. Jiang, and X. Liu, "Failure analysis of steel screws," *Heat Treatment of Metals*, no. 2, pp. 141-144, 2014.
- [13] Z. Han, H. Ma, and Y. Ding, "Fracture failure analysis of the high strength bolt," *Physical Testing and Chemical Analysis (Part A: Physical Testing)*, vol. 39, no. 9, pp. 477-480, 2003.
- [14] T. Zhou and J. Suo, "Failure analysis on 42CrMo steel connecting rod," *Chemical Engineering and Equipment*, no. 4, pp. 21-24, 2016.
- [15] W. Jiang, J. Gong, and S. Tu, "Analysis of fatigue fracture mechanism for brazed 304 stain-less steel plate-fin structure," *Transactions of the China Welding Institution*, vol. 31, no. 4, pp. 45-48, 2010.
- [16] L. Jiang, J. Zhang, S. Zhang et al., "High-cycle fatigue fracture mechanism for ZTC4 alloy," *Hot Working Technology*, vol. 42, no. 10, pp. 93-95, 2013.

- [17] M. Endo and A. J. McEvily, "An analysis of the fatigue strength of metals containing small defects," *Key Engineering Materials*, vol. 353–358, pp. 323–326, 2007.
- [18] W. C. Cui and X. P. Huang, "A general constitutive relation for fatigue crack growth analysis of metal structures," *Acta Metallurgica Sinica*, vol. 16, no. 5, pp. 342–354, 2003.
- [19] M. D. Chapetti, T. Tagawa, and T. Miyata, "Ultra-long cycle fatigue of high-strength carbon steels part I: review and analysis of the mechanism of failure," *Materials Science and Engineering: A*, vol. 356, no. 1-2, pp. 227–235, 2003.
- [20] X. Huang, G. Jia, W. Cui et al., "Unique crack growth rate curve model for fatigue life prediction of marine steel structures," *Journal of Ship Mechanics*, vol. 15, no. 1, pp. 118–125, 2011.
- [21] F. Wang, W. Cui, and X. Huang, "Evaluation of surface crack shape evolution using the improved fatigue crack growth rate model," *Journal of Ship Mechanics*, vol. 15, no. 6, pp. 660–668, 2011.
- [22] C. Santus and D. Taylor, "Physically short crack propagation in metals during high cycle fatigue," *International Journal of Fatigue*, vol. 31, no. 8-9, pp. 1356–1365, 2009.
- [23] K. Wang, F. Wang, W. C. Cui et al., "Prediction of short fatigue crack growth life by unified fatigue life prediction method," *Chuan Bo LI Xue/Journal of Ship Mechanics*, vol. 18, no. 6, pp. 678–689, 2014.
- [24] A. Abdullah, H. Alfawaz, Amani bin Rabba, A. Almutairi, S. Alnafaiy, and M. K. Mohammed, "Failure analysis and reliability of Ni–Ti-based dental rotary files subjected to cyclic fatigue," *Metals*, vol. 8, no. 1, p. 36, 2018.
- [25] J. Ina, M. Vallentyne, F. Hamandi et al., "Failure analysis of PHILOS plate construct used for pantalar arthrodesis paper I—analysis of the plate," *Metals*, vol. 8, no. 3, p. 180, 2018.

Research Article

Effect of PWHT on the Carbon Migration and Mechanical Properties of 2205DSS-Q235 LBW Joint

Fujun Cao ¹ and Chengchao Du ²

¹*Seksun Technology (Suzhou) Co.,Ltd, Suzhou 215100, China*

²*School of Power and Mechanical Engineering, Wuhan University, Wuhan 430072, China*

Correspondence should be addressed to Chengchao Du; lanshanchimu@126.com

Received 2 June 2018; Revised 7 September 2018; Accepted 6 November 2018; Published 2 December 2018

Guest Editor: Marek Smaga

Copyright © 2018 Fujun Cao and Chengchao Du. This is an open access article distributed under the Creative Commons Attribution License, which permits unrestricted use, distribution, and reproduction in any medium, provided the original work is properly cited.

The effect of postweld heat treatment (PWHT) on the carbon migration and mechanical properties of the 2205DSS-Q235 laser beam welding (LBW) joint was investigated. The carbon-rich zone (CRZ) and carbon-depleted zone (CDZ) generated at the welding seam/Q235 (WS-Q235) interface as the carbon migration occurred after heat-treated at 600°C, 700°C, and 800°C for 1 h. The softening was found in the CDZ. Only the CRZ in joints heat-treated at 800°C was hardened because of the retaining of high-carbon untempered martensite. The thick CDZ in joints heat-treated at 700°C and 800°C contributed to the tensile fracture and the low elongation. The strength of the joint was roughly determined by the hardness of the fracture zone.

1. Introduction

Dissimilar steel welding is common in pressure vessel manufacturing. Dissimilar joints, such as martensitic steel/martensitic steel [1], martensitic steel/austenitic steel [2–4], and Ni-based superalloy/austenitic steel [5], have been widely investigated. Among these dissimilar joints, carbon migration from carbon steel to high-Cr weld metal (WM) was usually observed. The carbon migration was in uphill diffusion, as the carbon atom continuously diffusing from the low-carbon steel to the CRZ. Many investigations revealed that the uphill diffusion depended on the higher Cr concentration in the WM [6–8]. Cr atoms combine with the carbon atoms from carbon steel and generate $M_{23}C_6$ and M_7C_3 (M stands for Cr, Fe, and Mn) in the WM near the WM/carbon steel interface [6]. Therefore, the CRZ forms in the WM near the WM/carbon steel interface. As the loss of carbon atom near the interface occurs, the CDZ generates in the carbon steel near the WM/carbon steel interface. Mas et al. [6] indicated that the diffusion of carbon atom to high-Cr region was driven by the high chemical potential gradient across the interface.

The generation of CDZ in the dissimilar joint always contributed to the change in mechanical properties. Ming

et al. [9] employed Inconel 52M as the transition layer to join the 316L and SA508 steel. They found that the hardest area was in the 1st layer of 52Mb just adjacent to the SA508-52Mb interface due to the CRZ. The CDZ just adjacent to the fusion boundary had the lowest hardness. Sarikka et al. [10] found that the PWHT improved the carbon migration, thus resulting in the wider and softer CDZ compared to the as-welded state in the SA508-Alloy 52 interface. Wu et al. [11] observed that the CDZ in the 9%Cr fusion zone induced the fracture during the high-cycle fatigue test at 470°C. It can be concluded that the generation of CDZ contributed to the poor performance of the dissimilar joint.

Laser beam welding (LBW) provides outstanding characteristics of high energy density and high welding speed [12]. It contributes to the rapid joining of aluminum alloys [13, 14], magnesium alloys [15, 16], and steel [17, 18]. In our previous study, 2205DSS and Q235 steel with a thickness of 6.5 mm was joined using LBW [19]. In order to improve the toughness of the LBW joint, the PWHT process was conducted. After the PWHT process, CDZ and CRZ were generated as the carbon migration [20]. In this investigation, the mechanical properties of the joints with

different PWHT processes were investigated. Based on these results, the effect of PWHT on the carbon migration and mechanical properties were derived.

2. Materials and Experiments

The 2205DSS and Q235 plates with a thickness of 6.5 mm were joined using LBW without filler metal. The power of the laser beam was 3.7 kW. The defocusing distance was 0 mm. The welding speed was 1.2 m/min. The shielded gas was Ar gas with a flow rate of 25 L/min. The joints were heat-treated at 500°C, 600°C, 700°C, and 800°C for 1 h. The cross-sectional specimen of the weld joint perpendicular to the WD was prepared using an electrical discharge machine (EDM). The specimens were mechanically polished using waterproof SiC emery papers of up to 7000 grit and mirror polished using a colloidal Al₂O₃ (100 nm) suspension. The mirror-polished specimens were then etched using a solution consisting of HNO₃(40 vol%) + C₂H₅OH for ~5 s and subjected to the optical microscopy (OM, Zeiss Axio Scope A1) observation, scanning electron microscopy (SEM, MIRA3 LMH) observation, and electron probe microanalysis (EPMA, EPMA-1600). The tests of SEM and EPMA were under the secondary electron imaging (SEI) mode. For the electron backscatter diffraction (EBSD, MIRA3 LMH + Oxford) observation, the specimens were mechanically polished in a similar manner and then electropolished in a solution consisting of 10 vol.% perchloric acid and 90 vol.% ethanol at 20 V for ~10 s at room temperature. The step size of 1 μm was set for EBSD observation. The results from the EBSD were analyzed using Channel 5 software. The films with a diameter of 3 mm were prepared using a twin-jet electropolishing device and observed using a transmission electron microscope (TEM, JEM-2100).

The microhardness was measured using a microhardness tester with a load of 200 g and a dwell time of 5 s. The tensile test was conducted using a tensile machine with the help of fixture. The tensile speed was 100 μm/min.

The schematic of the joint is shown in Figure 1(a). The cross section of the joint is shown in Figure 1(b). A narrow WS (approximately 1 mm) was observed from Figure 1(b). The chemical compositions of the WS, Q235 BM, and 2205DSS BM are listed in Table 1. The interface of the WS/Q235 is shown in Figure 1(c). The structure of the tensile sample is shown in Figure 1(d). The tensile sample and fixture are shown in Figures 1(d) and 1(e). The fractured samples are shown in Figure 1(f).

3. Results and Discussion

3.1. Microstructure after PWHT

3.1.1. WS Evolution. The microstructure of WS is shown in Figure 2 [20]. The microstructure of the as-welded WS is shown in Figures 2(a) and 2(g). High dislocation density can be observed in Figure 2(g). Moreover, a small amount of retained austenite is observed in Figure 2(g). The microstructure of as-welded WS was mainly untempered martensite [19, 20].

The phase diagram of the WS (Figure 2(f)) was calculated using JMatPro software. According to the phase fraction of the WS, the Ac₁ temperature (621°C) and Ac₃ temperature (772°C) were derived. In this investigation, the PWHT temperatures of 500°C and 600°C were lower than the Ac₁ temperature. The untempered martensite would become tempered martensite. The microstructures of the WS heat-treated at 500°C and 600°C are shown in Figures 2(b) and 2(c). The martensitic lath was clearer. The microstructure of the WS heat-treated at 600°C is revealed in Figure 2(h). It could be observed that the (Cr,Fe)₂₃C₆ particles precipitated in the martensitic lath boundary. The high dislocation density disappeared. The subgrain was observed. Moreover, the dislocation density declined.

When the PWHT temperature was increased to 700°C, part of martensite transformed into the γ phase. After cooled to the room temperature, the γ phase became the untempered martensite again. The martensite, which did not transform into the γ phase, became the deeply tempered martensite during the PWHT. Therefore, the microstructure of the WS heat-treated at 700°C was consisted of untempered martensite and tempered martensite.

When the PWHT temperature was increased to 800°C, the martensite totally transformed into the γ phase which can be observed from Figure 2(f). After cooled to the room temperature, the γ phase became the untempered martensite again. From the microstructure in Figure 2(e), the martensitic lath could not be clearly observed. It meant that carbide did not precipitate. The TEM image of the WS heat-treated at 800°C is revealed in Figure 2(i). The (Cr,Fe)₂₃C₆ particles on the grain boundaries disappeared. The martensitic lath with a high dislocation density was observed again.

From the above results and discussion, the untempered martensite transformed into the tempered martensite after heat-treated at 500°C and 600°C. The WS heat-treated at 700°C consisted of tempered martensite and part of untempered martensite. The WS heat-treated at 800°C was total untempered martensite.

3.1.2. Interface Evolution. The WS-Q235 interfaces after heat-treated are shown in Figure 3 [20]. From Figure 3(a), the carbon migration was not observed in the WS-Q235 interface heat-treated at 500°C. When the PWHT temperature was increased to 600°C, CRZ and CDZ were observed. When the PWHT temperature was raised to 700°C, CRZ and thick CDZ were observed (Figures 3(c) and 3(f)). However, when the PWHT temperature was increased to 800°C, only the CDZ was observed (Figures 3(d) and 3(e)). Moreover, the thickness of the CDZ heat-treated at 800°C was smaller than that heat-treated at 700°C.

In order to observe the CRZ in the WS-Q235 interface heat-treated at 800°C, the cross section was etched by FeCl₃ + HCl solution again. The optical image of the WS-Q235 interface is shown in Figure 3(g). The CRZ was distinguished.

The formation of the CDZ and CRZ was attributed to the Cr in the WS [6–8, 21]. During the PWHT process of

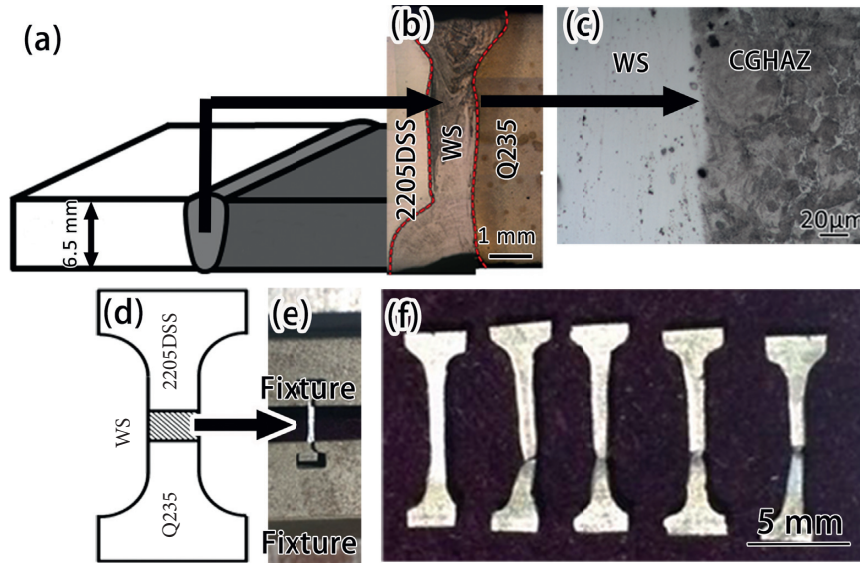


FIGURE 1: (a) Schematic of the joint; (b) cross section of the joint; (c) microstructure of the WS-Q235 interface; (d) structure of the tensile sample; (e) fixture of the tensile sample; (f) fractured tensile samples.

TABLE 1: Chemical compositions of WS, Q235 BM, and 2205DSS BM (wt.%).

Materials	C	Si	Mn	Ni	Cr	Mo	N	S	P	Fe
WS	0.107	0.350	0.823	2.067	8.800	1.186	0.055	0.013	0.03	Bal.
Q235	0.16	0.21	0.55	—	—	—	—	0.020	0.030	Bal.
2205DSS	0.025	0.570	1.250	5.300	22.570	3.040	0.14	0.002	0.030	Bal.

2205DSS-Q235 joint, the carbon atom continuously migrated from the Q235 BM to the WS. It combined with the Cr and Fe atoms and contributed to the generation of the $(Cr,Fe)_{23}C_6$ carbide in WS. Therefore, CDZ and CRZ generated in Q235 BM and WS, respectively. The thickness of CDZ and CRZ as a function of PWHT temperature is revealed in Figure 3(h). The CDZ thickened as the increase of temperature when the PWHT temperature was below 700°C. However, when the PWHT temperature was raised to 800°C, the thickness of the CDZ declined to approximately 130 μm. The rapid thickening of the CRZ is also marked in Figure 3(h).

3.1.3. Carbon-Depleted Zone Evolution. The A_{c1} temperature of Q235 BM was approximately 710°C as shown in Figure 4. Therefore, when the PWHT temperature was 500°C, 600°C, and 700°C, the phase in the CDZ was mainly the α -Fe phase. The generation of CDZ mainly relied on the migration of carbon atom from Q235 to WS. Therefore, the thickness of CDZ depended on the diffusion rate of carbon atom. When the temperature increased (below 710°C), the carbon migration gradually accelerated. Therefore, the thickness of the CDZ increased as the increase of PWHT temperature.

When the temperature was 800°C, the CDZ consisted of α -Fe and γ -Fe as shown in Figure 4. At the early stage of the PWHT at 800°C, the carbon concentration of Q235 near the WS/Q235 interface was 0.16 wt.%. The volume fraction of

γ -Fe was 54%. However, when the PWHT time extended to 1 h, the carbon concentration of CDZ was only approximately 0.087 wt.% (from EPMA result). According to Figure 4, the volume fraction of γ -Fe was 31% after heat-treated for 1 h. Huang et al. [21] indicated that the γ -Fe in the CDZ slowed the migration of carbon atom. Therefore, the CDZ in the joint heat-treated at 800°C was thinner than that heat-treated at 700°C.

The grain orientation (in the X direction) of WS/Q235 interface heat-treated at 700°C and 800°C is shown in Figure 5. The columnar α -Fe grain with a straight grain boundary was observed in the CDZ heat-treated at 700°C. However, the part of grain boundaries of the α -Fe grain in the CDZ heat-treated at 800°C was not straight anymore as indicated in Figure 5(b). It should be attributed to the transformation from γ -Fe to α -Fe when the joint cooled from 800°C to room temperature. The grain boundary of γ -Fe and α -Fe at 800°C should also be the straight. When the temperature declined, the α -Fe grains would nucleate in the grain boundary. The prior austenitic grain was partitioned by the new α -Fe grains. Therefore, the zigzag grain boundaries generated after heat-treated at 800°C.

The difference in the Fe_3C particle after heat-treated at 700°C and 800°C should also be discussed in this investigation. The Fe_3C particle is indicated in Figures 5(c) and 5(d). It can be observed from Figures 5(c) and 5(d) that the Fe_3C particle in the CDZ heat-treated at 700°C was less than that heat-treated at 800°C. The α -Fe phase in the CDZ heat-treated at 700°C exhibited a smaller solubility for carbon

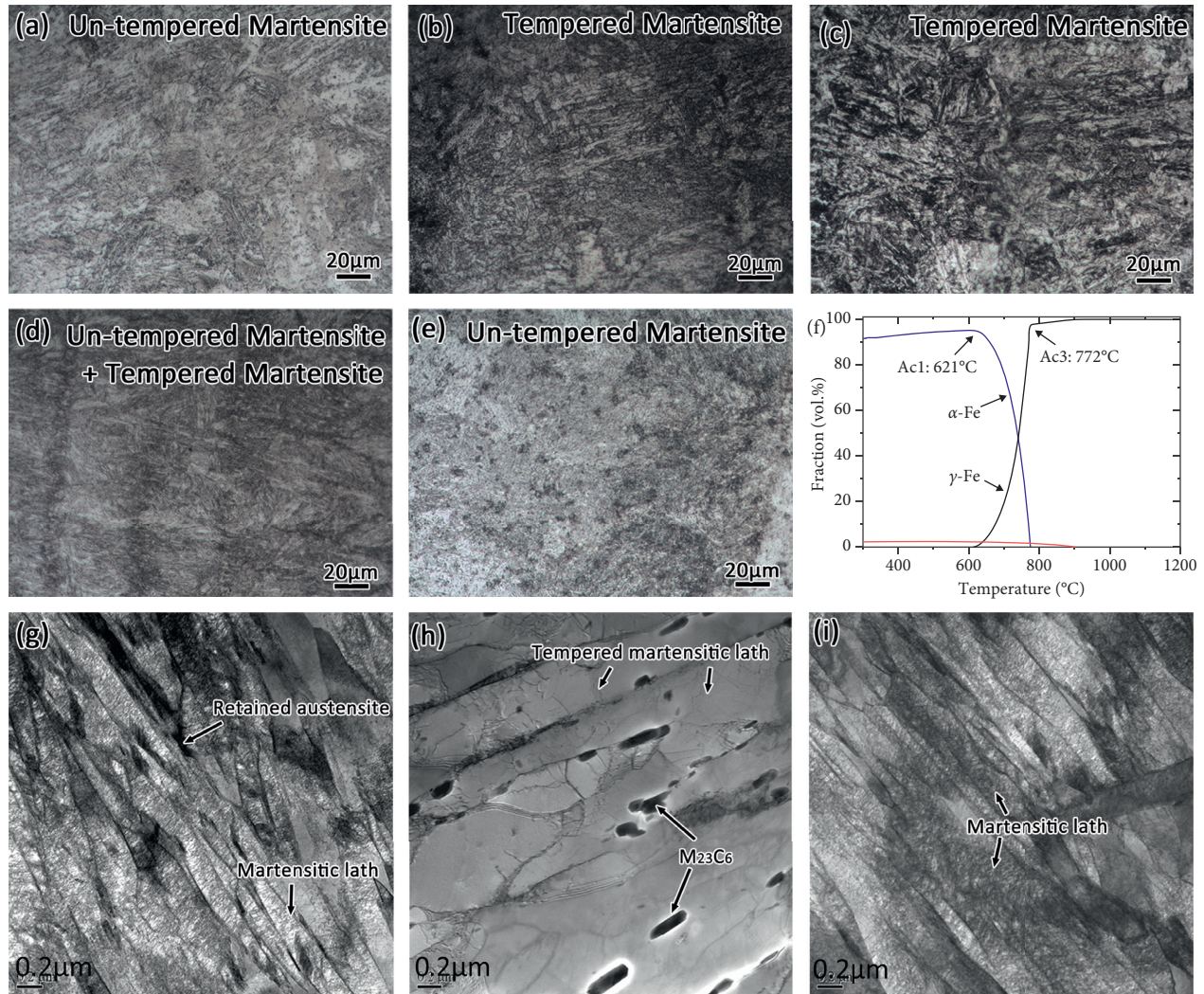


FIGURE 2: Microstructure and phase diagram of WS: (a, g) as-welded; (b) heat-treated at 500°C, (c, h) heat-treated at 600°C, (d) heat-treated at 700°C, (e, i) heat-treated at 800°C, (f) phase diagram.

atoms when compared with that heat-treated at 800°C. Moreover, the γ -Fe phase in the CDZ at 800°C exhibited a larger solubility for carbon atoms when compared with the α -Fe phase at 700°C. Therefore, more carbon atoms were dissolved in the CDZ at 800°C. After cooled to room temperature from 800°C, more Fe_3C particles precipitated from the CDZ.

3.1.4. Carbon-Rich Zone Evolution. The Ac_1 and Ac_3 temperatures of the WS as a function of carbon concentration are shown in Figure 6(a). From Figure 6(a), the microstructure of the WS at 700°C consisted of α -Fe and γ -Fe. The volume fraction of the γ -Fe in the as-welded WS was 21%. When heat-treated at 700°C for 1 h, the carbon concentration of the CRZ was approximately 0.47 wt.% (from EPMA). The volume fraction of the γ -Fe was 17% from Figure 6(a). The matrix of WS became pure γ -Fe at 800°C as shown in Figure 6(a).

$(\text{Cr,Fe})_{23}\text{C}_6$ carbide would generate at 700°C and 800°C. Its volume fraction is shown in Figure 6(b). The carbon

concentration of the CRZ in the joint heat-treated at 800°C was 0.22 wt.% (from EPMA). The volume fraction of the $(\text{Cr,Fe})_{23}\text{C}_6$ carbide at 800°C was only 3.3%. However, the volume fraction of $(\text{Cr,Fe})_{23}\text{C}_6$ carbide at 700°C reached 8.9%.

From the carbon concentration of the CRZ in the joint heat-treated at 700°C and 800°C, the wider CRZ with a lower carbon concentration was found in the joint heat-treated at 800°C. The formation of the wider CRZ relied on the long-distance diffusion of carbon atom. At 800°C, the grain boundary contained less $(\text{Cr,Fe})_{23}\text{C}_6$ carbide. The diffusion of the carbon atom along the grain boundary at 800°C was easier than that at 700°C as the weaker hindering effect of $(\text{Cr,Fe})_{23}\text{C}_6$. Therefore, the wider CRZ was generated at 800°C.

The CRZ in the joint heat-treated at 600°C consisted of tempered martensite and $(\text{Cr,Fe})_{23}\text{C}_6$. $(\text{Cr,Fe})_{23}\text{C}_6$ came from two sources. The first was the carbon from the WS. The second was the carbon from the Q235 BM. The CRZ in the joint heat-treated at 700°C consisted of tempered martensite, untempered martensite, and $(\text{Cr,Fe})_{23}\text{C}_6$. The

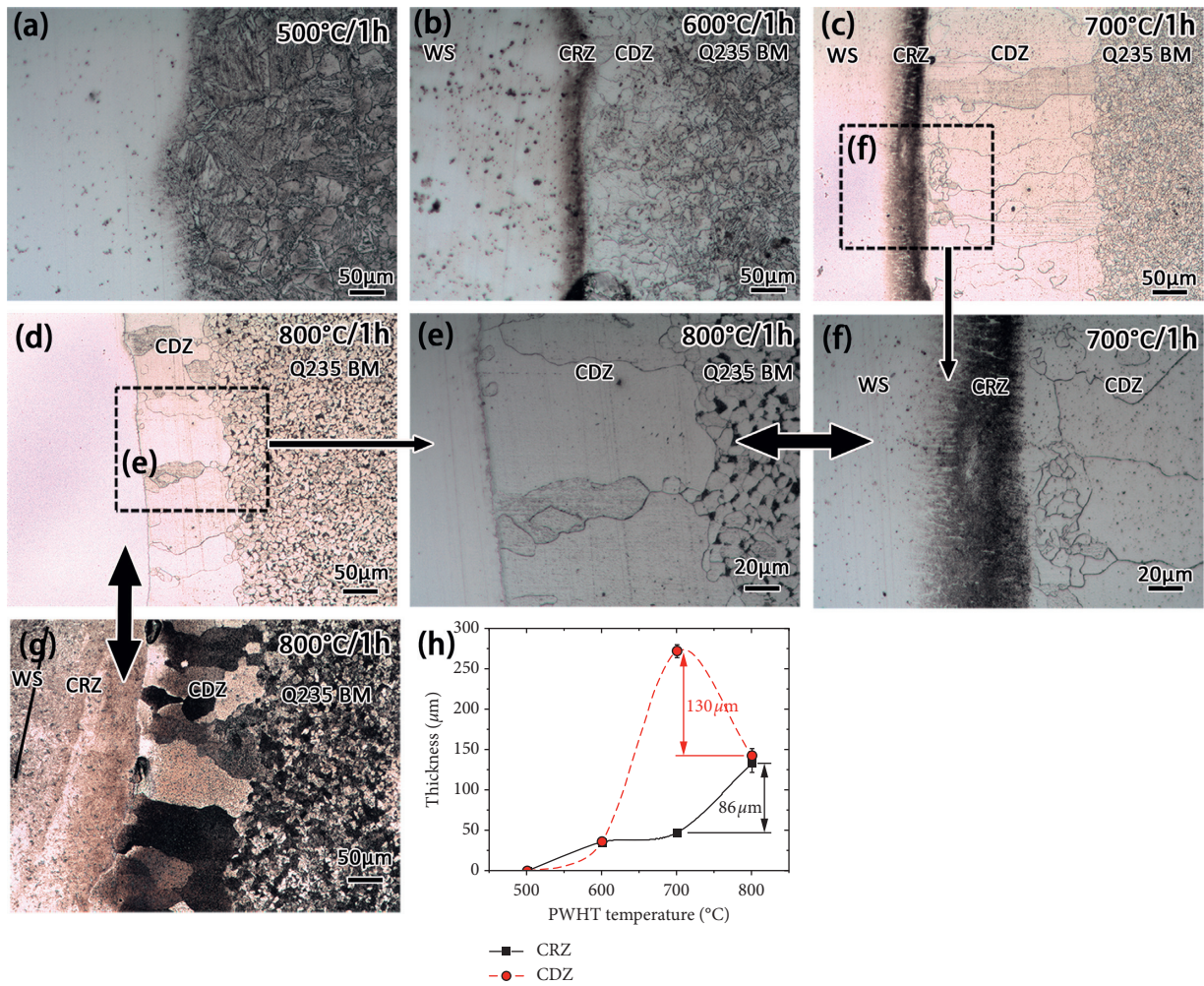


FIGURE 3: Microstructure of WS-Q235 interface and thickness of CDZ and CRZ: (a) heat-treated at 500°C; (b) heat-treated at 600°C; (c, f) heat-treated at 700°C; (d, e, g) heat-treated at 800°C; (h) thickness of CDZ and CRZ as a function of PWHT temperature.

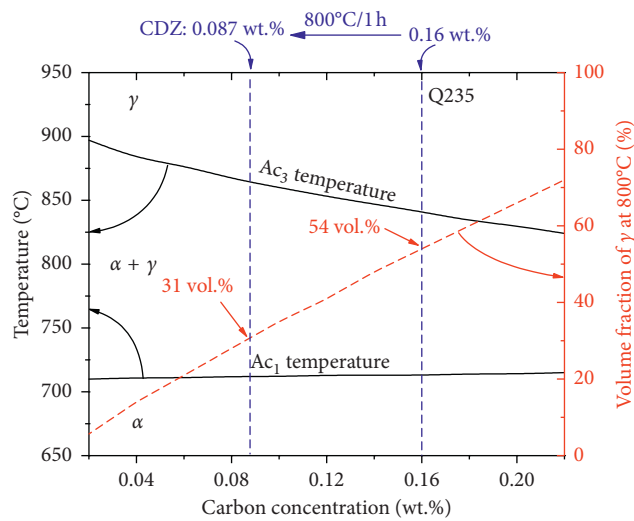


FIGURE 4: Ac₁ temperature; Ac₃ temperature; γ-Fe phase fraction of Q235 as a function of the carbon concentration.

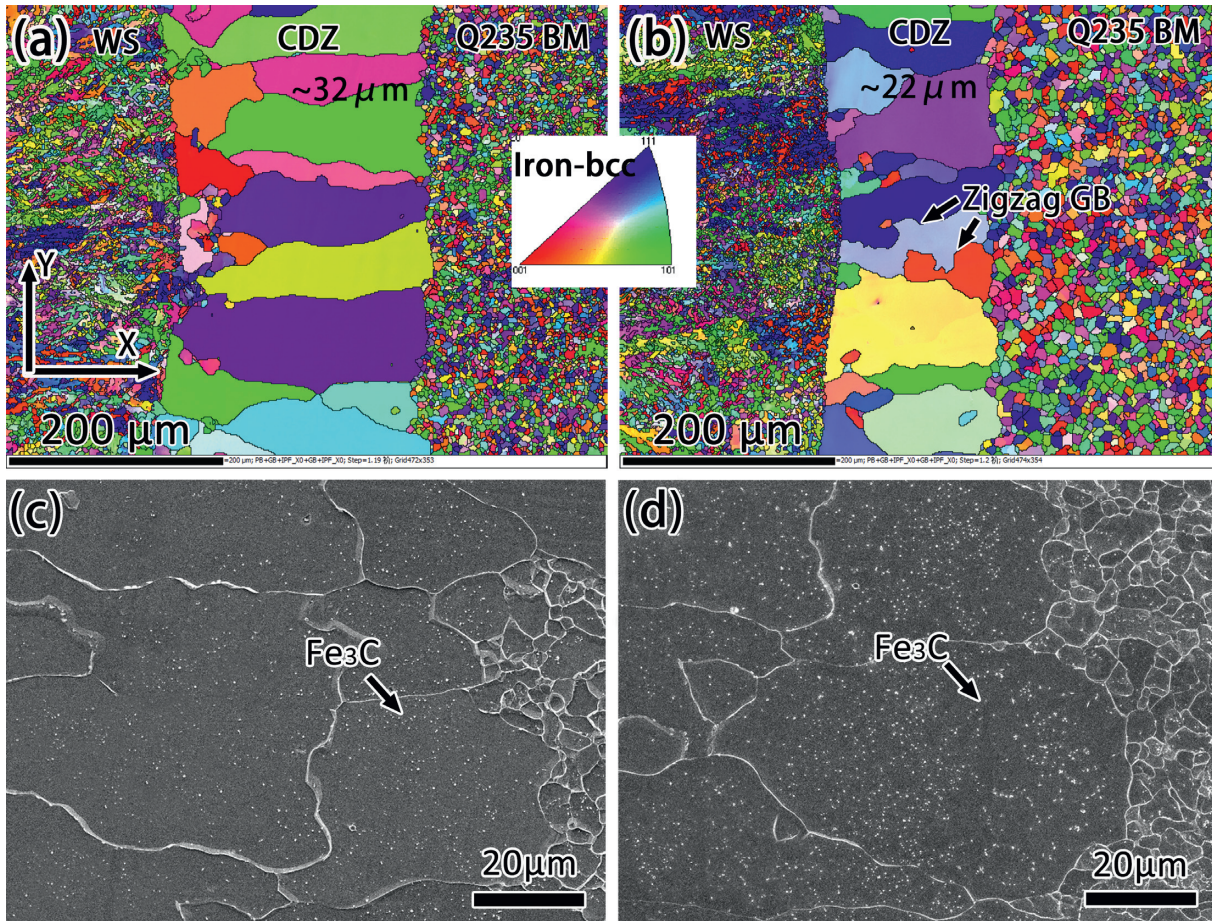


FIGURE 5: Microstructure of the CDZ; (a) grain orientation of the CDZ heat-treated at 700°C; (b) grain orientation of the CDZ heat-treated at 800°C; (c) CDZ heat-treated at 700°C; (d) CDZ heat-treated at 800°C.

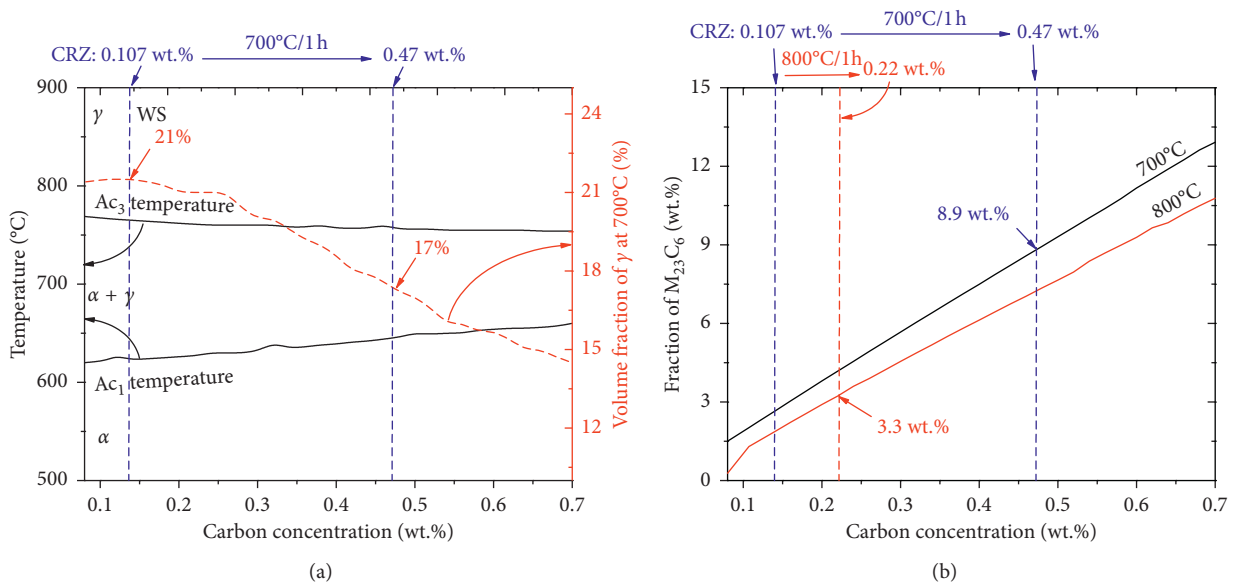


FIGURE 6: (a) Ac_1 , Ac_3 , and γ -Fe fraction as a function of carbon concentration; (b) $M_{23}C_6$ concentration as a function of carbon concentration.

formation of $(\text{Cr,Fe})_{23}\text{C}_6$ was similar to that at 600°C . The untempered martensite came from the $\gamma\text{-Fe}$ at 800°C . When the joints heat-treated at 600°C and 700°C were etched by $\text{HNO}_3(4\text{ wt.}\%) + \text{ethanol}$ solution, the $(\text{Cr,Fe})_{23}\text{C}_6$ carbide was etched easily. Therefore, the CRZ could be observed clearly in Figures 3(b)–3(f).

The CRZ in the joint heat-treated at 800°C was of untempered martensite and small amount of $(\text{Cr,Fe})_{23}\text{C}_6$ carbide. Therefore, it was hard to reveal the microstructure using $\text{HNO}_3(4\text{ wt.}\%) + \text{ethanol}$ as shown in Figures 3(e) and 3(f).

3.2. Mechanical Properties after PWHT

3.2.1. Hardness. The hardness distribution of the joints is shown in Figure 7(a). The hardness change of the 2205DSS and Q235 was small. In this investigation, the hardness evolution of 2205DSS BM and Q235 BM was not discussed as their small influence on the fracture behavior. The hardness evolution of WS, CRZ, and CDZ was discussed in detail. From Figures 7(a) and 7(b), the hardness of the as-welded WS was approximately 550 HV. The hardness of the WS declined slightly after heat-treated at 500°C . When the WS was heat-treated at 600°C and 700°C , the hardness was approximately 350 HV. When the PWHT temperature was increased to 800°C , the hardness increased to approximately 450 HV. Moreover, the hardness of the WS near the WS/Q235 interface significantly increased (approximately 570 HV) as shown in Figure 7.

In this investigation, the hardness decline of WS at 500°C , 600°C , and 700°C should be attributed to the formation of tempered martensite. The hardness increase at 800°C should be attributed to the regain of untempered martensite.

The hardness distribution near the WS/Q235 interface is shown in Figure 7(b). The high-hardness CRZ in the joint heat-treated at 800°C should be attributed to the high-carbon martensite which had a high hardness as discussed in Section 3.1.4. However, the hardness increment of the CRZ in the joints heat-treated at 500°C , 600°C , and 700°C was not observed in Figure 7(b). Although $(\text{Cr, Fe})_{23}\text{C}_6$ carbide or small amount of untempered martensite generated in the CRZ in the joints heat-treated at 500°C , 600°C , and 700°C , its strengthening effect could not balance the hardness reduction of the tempered martensite at all. Therefore, the hardness of the CRZ did not increase after heat-treated at 500°C , 600°C , and 700°C .

The hardness of the HAZ heat-treated at 500°C declined slightly compared with that of the HAZ of the as-welded joint as shown in Figure 7(b). When the PWHT temperature was increased to 600°C , the hardness of the CDZ was approximately 150 HV. The lowest hardness of the CDZ was only approximately 110 HV after heat-treated at 700°C . When heat-treated at 800°C , the lowest hardness of the CDZ was improved to approximately 135 HV.

The low hardness of the CDZ in the joint heat-treated at 700°C and 800°C should be contributed to the less Fe_3C particle and the coarse ferrite grain. The difference in CDZ hardness between the two joints should also be discussed. From the discussion about the Fe_3C in Section 3.1.3, the

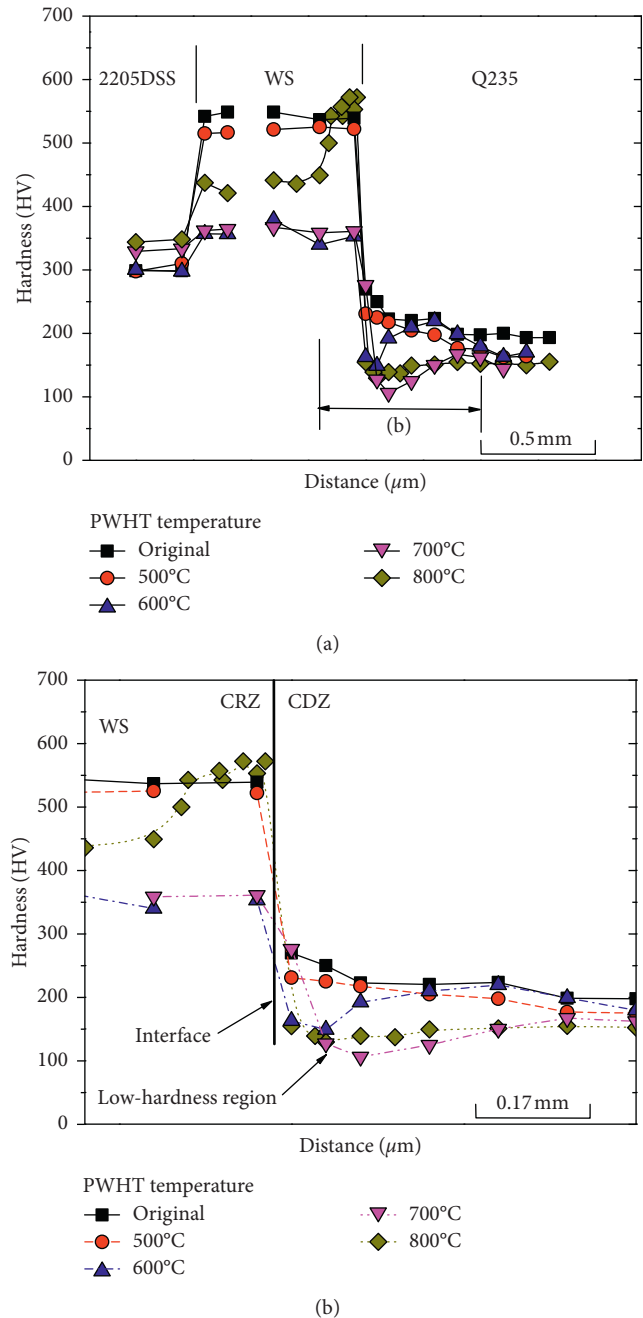


FIGURE 7: Hardness distribution of the as-welded and heat-treated 2205DSS-Q235 joints: (a) the whole joint; (b) the WS-Q235 interface.

fraction of Fe_3C in the CDZ heat-treated at 700°C was smaller than that heat-treated at 800°C . Moreover, the grain sizes of the CDZ in the joints heat-treated at 700°C and 800°C were $\sim 32\ \mu\text{m}$ and $\sim 22\ \mu\text{m}$ from the EBSD results. Therefore, the coarse grain and less Fe_3C of CDZ in the joint heat-treated at 700°C contributed to its lowest hardness.

3.2.2. Strength, Elongation, and Fracture Behavior. The stress-strain curves are shown in Figure 8(a). The

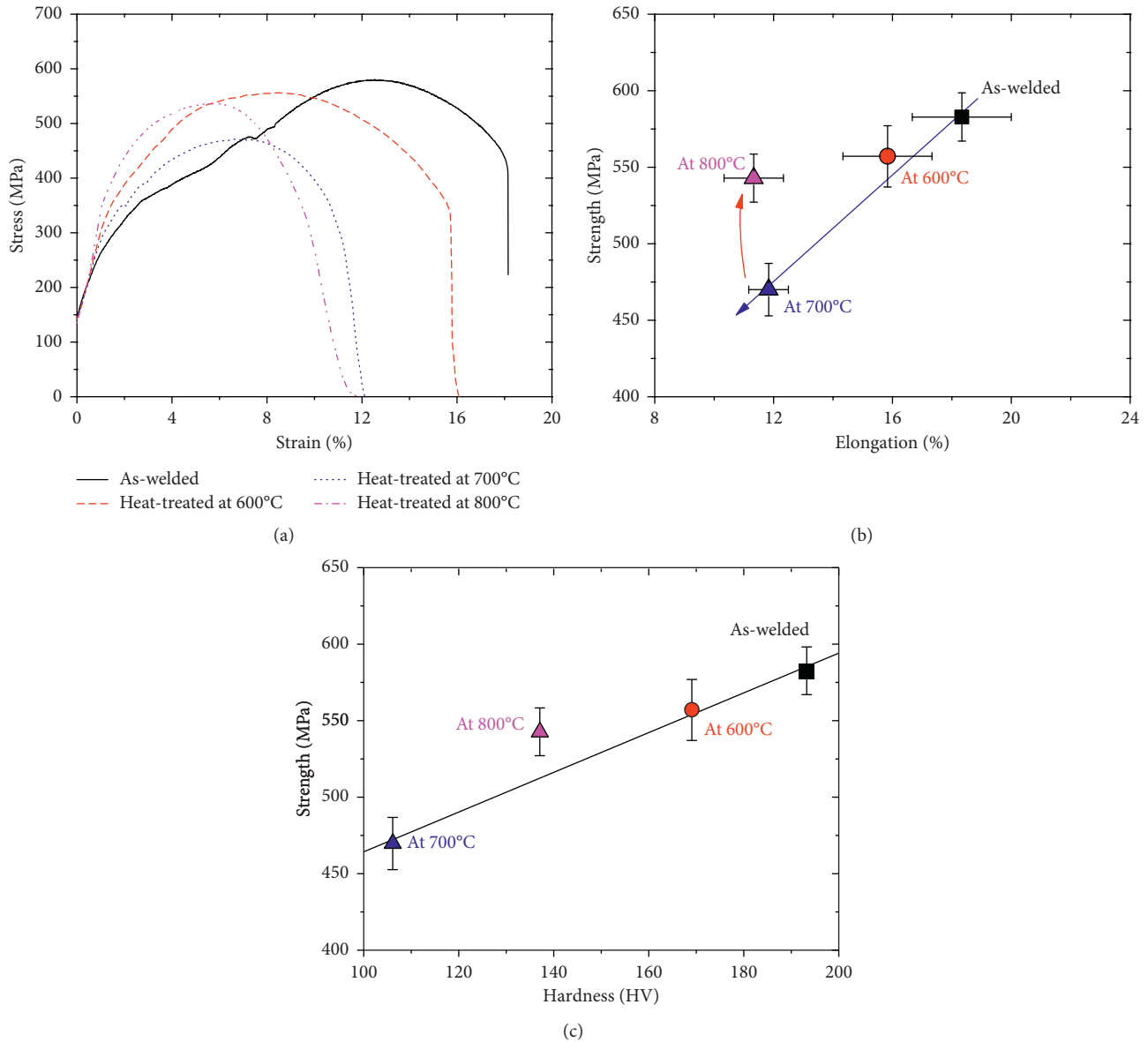


FIGURE 8: (a) Stress-strain curves; (b) strength vs. elongation; (c) strength vs. hardness.

strength as a function of elongation is shown in Figure 8(b). It was found that all of the strength and elongation gradually declined as the increase of PWHT temperature when the PWHT temperature was below 700°C. However, when the PWHT temperature was 800°C, the strength increased.

The microstructure of the cross section of fractured joints is shown in Figure 9. From Figures 9(a) and 9(b), the fracture location of the joints without PWHT and heat-treated at 600°C was in the Q235 BM. The fracture of the joints heat-treated at 700°C and 800°C was located in the CDZ as shown in Figures 9(c)–9(h). In this paper, the relationship between hardness of the fractured zone and strength of the joints was investigated as shown in Figure 8(c). It could be found that the strength of the joint was mainly determined by the hardness of the fracture zone.

From Figures 9(c) and 9(d), the CDZ in the joints heat-treated at 700°C and 800°C induced the fracture during tensile. However, the CDZ in the joint heat-treated at 600°C could not result in the fracture as shown in Figure 9(b). It should be attributed to the small thickness of the CDZ in the joint heat-treated at 600°C. During tensile, the strength of the WS and the Q235 near the CDZ in the joint heat-treated at 600°C was higher than the thin CDZ. The deformation of the CDZ was restricted. Therefore, the necking did not occur in the CDZ. On the contrary, the Q235 BM was stretched. When the true stress of the Q235 BM increased to a critical value, the necking occurred in the Q235 BM. Therefore, the fracture was located in the Q235 BM.

The plastic deformation of the Q235 BM contributed to the higher elongation of the joints without PWHT and heat-treated at 600°C. With regard to the joints heat-treated at 700°C and 800°C, the necking and fracture rapidly

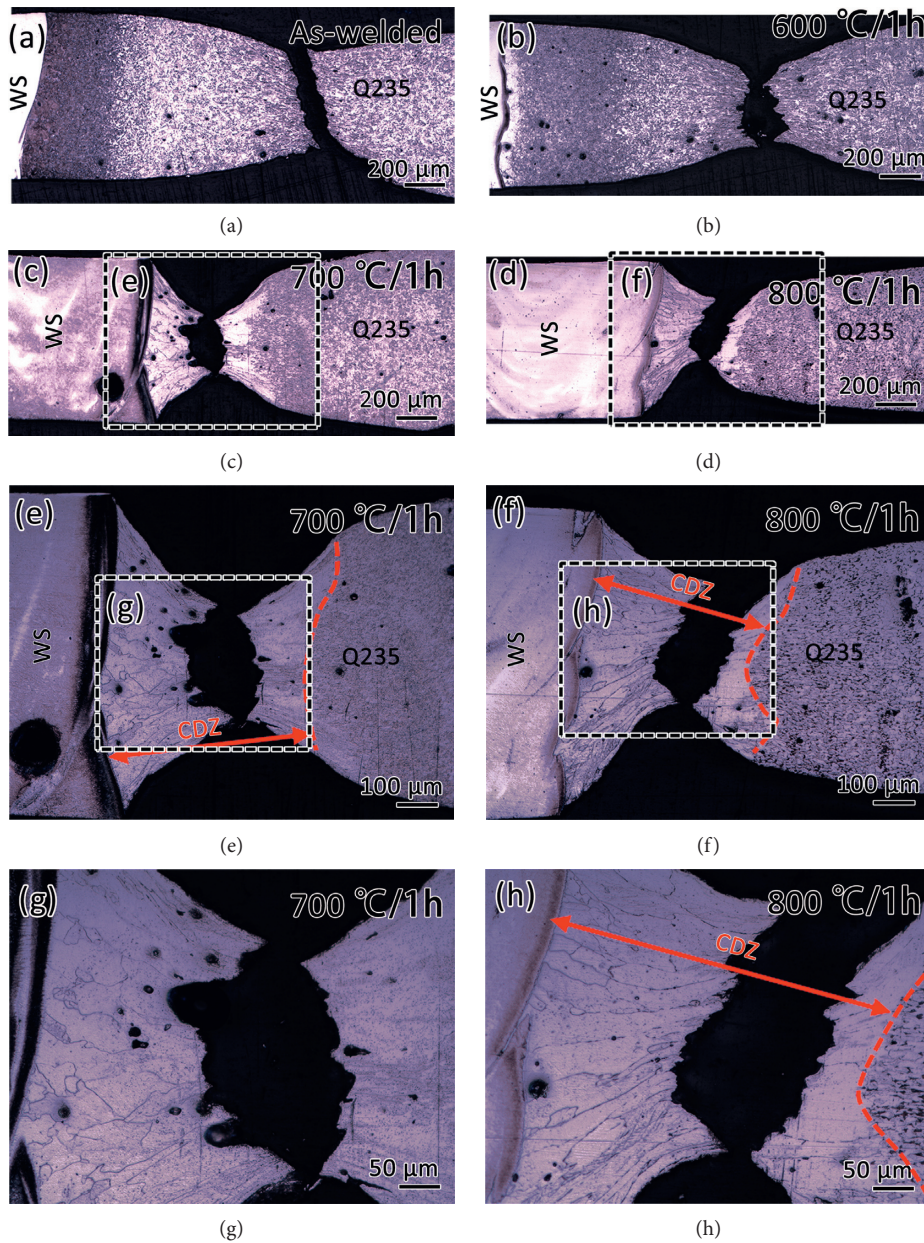


FIGURE 9: (a) Fractured as-welded joint; (b) fractured joint heat-treated at 600°C; (c, e, g) fractured joint heat-treated at 700°C; (d, f, h) fractured joint heat-treated at 800°C.

generated in the CDZ during tensile. The deformation of the Q235 BM was small. Therefore, the elongation of the joints heat-treated at 700°C and 800°C was small as shown in Figures 8(a) and 8(b).

4. Conclusions

- (1) Tempered martensite was obtained in the WS when heat-treated at 500°C and 600°C, as the generation of precipitates and decline of dislocation density. Untempered martensite was retained in the WS when heat-treated at 800°C which was higher than the A_{c3} temperature.
- (2) The CDZ and CRZ were generated on the WS/Q235 interface after heat-treated at 600°C, 700°C, and 800°C, as the carbon atoms diffused from Q235 BM to WS. The CDZ of the joint heat-treated at 800°C was thinner than that heat-treated at 700°C because of the generation of γ -Fe in Q235 BM during heat-treatment.
- (3) The hardness of the WS declined to ~ 350 HV after heat-treated at 600°C and 700°C as the tempered martensite formed. The hardness of the WS heat-treated at 800°C was ~ 450 HV as the untempered martensite was retained.
- (4) The softening was found in the CDZ. Only the CRZ of the joint heat-treated at 800°C was hardened as

high-carbon untempered martensite was generated which had a hardness of ~ 570 HV.

- (4) The strength of the joint was roughly determined by the hardness of the fracture zone. The CDZ in joints heat-treated at 700°C and 800°C contributed to the tensile fracture of the joints. The joint fractured in the CDZ exhibited the lower elongation.

Data Availability

All the data in the article came from our experiments.

Conflicts of Interest

The authors declare that they have no conflicts of interest.

References

- [1] C. Pandey, M. M. Mahapatra, P. Kumar, and N. Saini, "Comparative study of autogenous tungsten inert gas welding and tungsten arc welding with filler wire for dissimilar P91 and P92 steel weld joint," *Materials Science and Engineering A*, vol. 712, no. 17, pp. 720–737, 2018.
- [2] R. S. Vidyarthi, A. Kulkarni, and D. K. Dwivedi, "Study of microstructure and mechanical property relationships of A-TIG welded P91–316L dissimilar steel joint," *Materials Science and Engineering A*, vol. 695, no. 17, pp. 249–257, 2017.
- [3] L. Falat, J. Kepic, L. Ciripová, P. Ševc, and I. Dlouhý, "The effects of postweld heat treatment and isothermal aging on T92 steel heat-affected zone mechanical properties of T92/TP316H dissimilar weldments," *Journal of Materials Research*, vol. 31, no. 10, pp. 1532–1543, 2016.
- [4] G. Li, X. Lu, X. Zhu, J. Huang, L. Liu, and Y. Wu, "The interface microstructure, mechanical properties and corrosion resistance of dissimilar joints during multipass laser welding for nuclear power plants," *Optics and Laser Technology*, vol. 101, pp. 479–490, 2018.
- [5] P. Prabaharan, K. Devendranath Ramkumar, and N. Arivazhagan, "Characterization of microstructure and mechanical properties of Super Ni 718 alloy and AISI 316L dissimilar weldments," *Journal of Materials Research*, vol. 29, no. 24, pp. 3011–3023, 2014.
- [6] F. Mas, C. Tassin, N. Valle et al., "Metallurgical characterization of coupled carbon diffusion and precipitation in dissimilar steel welds," *Journal of Materials Science*, vol. 51, no. 10, pp. 4864–4879, 2016.
- [7] F. Mas, C. Tassin, F. Roch, M. Yescas, P. Todeschini, and Y. Brechet, "Growth morphologies and primary solidification modes in a dissimilar weld between a low-alloy steel and an austenitic stainless steel," *Metals*, vol. 8, no. 4, pp. 284–305, 2018.
- [8] R. Anand, C. Sudha, T. Karthikeyan, A. L. E. Terrance, S. Saroja, and M. Vijayalakshmi, "Effectiveness of Ni-based diffusion barriers in preventing hard zone formation in ferritic steel joints," *Journal of Materials Science*, vol. 44, no. 1, pp. 257–265, 2008.
- [9] H. Ming, R. Zhu, Z. Zhang et al., "Microstructure, local mechanical properties and stress corrosion cracking susceptibility of an SA508-52M-316LN safe-end dissimilar metal weld joint by GTAW," *Materials Science and Engineering A*, vol. 669, no. 4, pp. 279–290, 2016.
- [10] T. Sarikka, M. Ahonen, R. Mouginot et al., "Effect of mechanical mismatch on fracture mechanical behavior of SA 508 - alloy 52 narrow gap dissimilar metal weld," *International Journal of Pressure Vessels and Piping*, vol. 157, pp. 30–42, 2017.
- [11] Q. Wu, F. Lu, H. Cui, X. Liu, P. Wang, and Y. Gao, "Soft zone formation by carbon migration and its effect on the high-cycle fatigue in 9% Cr–CrMoV dissimilar welded joint," *Materials Letters*, vol. 141, no. 15, pp. 242–244, 2015.
- [12] M. Li, Z. Li, Y. Zhao, H. Li, Y. Wang, and J. Huang, "Influence of welding parameters on weld formation and microstructure of dual-laser beams welded T-joint of aluminum alloy," *Advances in Materials Science and Engineering*, vol. 2011, Article ID 767260, 6 pages, 2011.
- [13] A. Elbatahy and M. Kutsuna, "Laser beam welding of AA5052, AA 5083, and AA 6061 aluminum alloys," *Advances in Materials Science and Engineering*, vol. 2009, Article ID 974182, 9 pages, 2009.
- [14] M. Behúlová, E. Babalová, and M. Sahul, "Design of laser welding parameters for joining Ti grade 2 and AW 5754 aluminium alloys using numerical simulation," *Advances in Materials Science and Engineering*, vol. 2017, Article ID 3451289, 15 pages, 2017.
- [15] L. Commin, M. Dumont, R. Rotinat, F. Pierron, J. E. Masse, and L. Barrallier, "Texture evolution in Nd:YAG-laser welds of AZ31 magnesium alloy hot rolled sheets and its influence on mechanical properties," *Materials Science and Engineering A*, vol. 528, no. 4–5, pp. 2049–2055, 2011.
- [16] G. Padmanaban and V. Balasubramanian, "Fatigue performance of pulsed current gas tungsten arc, friction stir and laser beam welded AZ31B magnesium alloy joints," *Materials and Design*, vol. 31, pp. 3724–3732, 2010.
- [17] W. W. Zhang, S. Cong, S. B. Luo, and J. H. Fang, "Effects of energy density and shielding medium on performance of laser beam welding (LBW) joints on SAF2205 duplex stainless steel," *JOM*, vol. 70, pp. 1554–1559, 2018.
- [18] J. Xu, J. Chen, Y. Duan, C. Yu, J. Chen, and H. Lu, "Comparison of residual stress induced by TIG and LBW in girth weld of AISI 304 stainless steel pipes," *Journal of Materials Processing Technology*, vol. 248, pp. 178–184, 2017.
- [19] C. Du, X. Wang, and L. Hu, "Microstructure, mechanical properties and residual stress of a 2205DSS/Q235 rapidly formed LBW joint," *Journal of Materials Processing Technology*, vol. 256, pp. 78–86, 2018.
- [20] C. Du, X. Wang, and C. Luo, "Effect of post-weld heat treatment on the microstructure and mechanical properties of the 2205DSS/Q235 laser beam welding joint," *Journal of Materials Processing Technology*, vol. 263, pp. 138–150, 2019.
- [21] M. Huang and L. Wang, "Carbon migration in 5Cr-0.5Mo/21Cr-12Ni dissimilar metal welds," *Metallurgical and Materials Transactions A*, vol. 29, no. 12, pp. 3037–3046, 1998.